

**Alma Mater Studiorum  
Università degli Studi di Bologna**

---

**Facoltà di Scienze Matematiche, Fisiche e Naturali**

**Dipartimento di Astronomia**

**DOTTORATO DI RICERCA IN ASTRONOMIA**

**Ciclo XXIII**

**MAGNETIC FIELDS AROUND RADIO GALAXIES  
FROM FARADAY ROTATION MEASURE ANALYSIS**

**Dottoranda:**

**DARIA GUIDETTI**

**Coordinatore:**

**Chiar.mo Prof.**

**Lauro MOSCARDINI**

**Relatrice:**

**Chiar.ma Prof.ssa**

**Loretta GREGORINI**

**Co-relatori:**

**Chiar.mo Prof. Robert A. LAING**

**Dott.ssa Paola PARMA**

---

---

**Settore Scientifico Disciplinare: Area 02 - Scienze Fisiche**

**FIS/05 Astronomia e Astrofisica**

**Esame Finale Anno 2011**



This thesis has been carried out at:

European Southern Observatory (ESO, Garching)

and

Istituto di Radioastronomia (IRA-INAf, Bologna)

as part of the Institute research activity



To Hypatia from Alexandria in Egypt, mother of the observational method

And to all Warriors of the Light



*“There are two possible outcomes: if the result confirms the hypothesis, then you’ve made a discovery. If the result is contrary to the hypothesis, then you’ve made a discovery.”*

(Enrico Fermi)

*Let Light and Love and Power restore the Plan on Earth.*



# Contents

<b>Abstract</b>	<b>i</b>
<b>1 Physics of radio galaxies</b>	<b>1</b>
1.1 Active galaxies . . . . .	1
1.2 Non-thermal emission mechanisms of active galaxies . . . . .	2
1.2.1 Synchrotron radiation . . . . .	2
1.2.2 Polarization of synchrotron radiation . . . . .	3
1.2.3 Inverse Compton emission . . . . .	5
1.3 Radio galaxies . . . . .	6
1.3.1 Radio-galaxy morphologies . . . . .	6
1.3.2 Morphology and expansion of lobes and tails . . . . .	7
1.3.3 Internal physical conditions of radio galaxies . . . . .	8
1.3.4 Equipartition parameters . . . . .	8
1.3.5 Field and particle content of radio lobes and tails . . . . .	10
<b>2 The X-ray environment of radio galaxies</b>	<b>13</b>
2.1 Introduction . . . . .	13
2.2 The thermal component . . . . .	14
2.2.1 The continuum spectrum . . . . .	14
2.2.2 Morphology of the X-ray emitting gas . . . . .	15
2.3 Radio source – environment interactions . . . . .	17
2.3.1 X-ray cavities and their content . . . . .	17
2.3.2 Gas compression and heating by radio galaxies . . . . .	18

<b>3</b>	<b>Magnetic fields in the hot phase of the intergalactic medium</b>	<b>21</b>
3.1	Introduction . . . . .	21
3.1.1	Diffuse synchrotron sources in galaxy clusters . . . . .	22
3.1.2	Magnetic fields from diffuse radio sources . . . . .	24
3.1.3	Diffuse inverse Compton emission . . . . .	25
3.2	Faraday Rotation . . . . .	26
3.2.1	Internal Faraday Rotation . . . . .	27
3.2.2	Foreground RM contributions . . . . .	28
3.2.3	Galactic Faraday rotation . . . . .	30
3.3	Depolarization . . . . .	31
3.4	RM analysis . . . . .	32
3.5	The magnetic field profile . . . . .	33
3.6	Tangled magnetic field . . . . .	34
3.7	The magnetic field power spectrum . . . . .	36
3.7.1	Magnetic field power spectrum from two-dimensional analysis . . . . .	38
<b>4</b>	<b>Structure of the magneto-ionic medium around the Fanaroff-Riley Class I radio galaxy 3C 449</b>	<b>43</b>
4.1	The radio source 3C 449: general properties . . . . .	43
4.2	Total intensity and polarization properties . . . . .	46
4.3	The Faraday rotation in 3C 449 . . . . .	47
4.3.1	Rotation measure images . . . . .	47
4.3.2	The Galactic Faraday rotation . . . . .	50
4.4	Depolarization . . . . .	51
4.5	Two dimensional analysis . . . . .	54
4.5.1	General considerations . . . . .	54
4.5.2	Structure functions . . . . .	54
4.6	Three-dimensional analysis . . . . .	59
4.6.1	Models . . . . .	59
4.6.2	Magnetic field strength and radial profile . . . . .	60

4.6.3	The outer scale of the magnetic-field fluctuations . . . . .	64
4.7	Summary and comparison with other sources . . . . .	67
4.7.1	Summary . . . . .	67
4.7.2	Comparison with other sources . . . . .	70
<b>5</b>	<b>Ordered magnetic fields around radio galaxies: evidence for interaction with the environment</b>	<b>73</b>
5.1	The Sample . . . . .	74
5.1.1	0206+35 . . . . .	77
5.1.2	3C 270 . . . . .	77
5.1.3	3C 353 . . . . .	78
5.1.4	M 84 . . . . .	78
5.2	Analysis of RM and depolarization images . . . . .	79
5.3	Rotation measure images . . . . .	79
5.4	Depolarization . . . . .	84
5.5	Rotation measure structure functions . . . . .	86
5.6	Rotation-measure bands from compression . . . . .	88
5.7	Rotation-measure bands from a draped magnetic field . . . . .	95
5.7.1	General considerations . . . . .	95
5.7.2	Axisymmetric draped magnetic fields . . . . .	96
5.7.3	A two-dimensional draped magnetic field . . . . .	97
5.7.4	RM reversals . . . . .	97
5.8	Discussion . . . . .	99
5.8.1	Where do bands occur? . . . . .	99
5.8.2	RM bands in other sources . . . . .	99
5.8.3	Foreground isotropic field fluctuations . . . . .	100
5.8.4	Asymmetries in RM bands . . . . .	103
5.8.5	Enhanced depolarization and mixing layers . . . . .	104
5.9	Conclusions and outstanding questions . . . . .	104

<b>6 Faraday rotation in two extreme environments</b>	<b>109</b>
6.1 The sources . . . . .	109
6.1.1 B2 0755+37 . . . . .	109
6.1.2 M 87 . . . . .	110
6.2 Two-dimensional analysis: rotation measure and depolarization . . . . .	111
6.2.1 0755+37: images . . . . .	113
6.2.2 M 87: images . . . . .	116
6.3 Two-dimensional analysis: structure functions . . . . .	118
6.4 Preliminary conclusions . . . . .	121
<b>Summary and conclusions</b>	<b>125</b>
6.5 Summary . . . . .	125
6.5.1 The tailed source 3C 449 . . . . .	125
6.5.2 The lobed radio galaxies 0206+35, 3C 270, M 84 and 3C 353 . . . . .	126
6.5.3 The radio galaxies 0755+37 and M 87 . . . . .	127
6.6 General conclusions . . . . .	128
6.7 Future prospects . . . . .	131
<b>Appendix</b>	<b>133</b>
<b>Data reduction and imaging of lobed radio galaxies</b>	<b>135</b>
.1 Observations and VLA data reduction . . . . .	135
.2 Images . . . . .	138
.2.1 0206+35 . . . . .	140
.2.2 0755+37 . . . . .	140
.2.3 M 84 . . . . .	141
<b>Bibliography</b>	<b>143</b>
<b>Acknowledgments</b>	<b>153</b>

# Abstract

The existence of diffuse magnetic fields of  $\mu\text{G}$  strength in the hot intergalactic medium is now well established. Our knowledge about them has greatly improved over the last few decades, mainly thanks to radio continuum observations, which have detected synchrotron emission from cluster diffuse sources (halos and relics) and Faraday rotation of polarized emission from embedded and/or background radio galaxies. Such fields are not thought to be dynamically significant, since they provide typical magnetic pressures one or two orders of magnitude below thermal values. However, they are believed to strongly influence the heat conductivity in the intergalactic medium and to inhibit the spatial mixing of gas and propagation of cosmic rays. Therefore, in order to improve our knowledge of the physical processes in the gaseous environment of galaxies, accurate measurements of quantities such as magnetic field strength, spatial variation, topology and power spectrum are crucial. While most work until recently has been devoted to rich clusters of galaxies, little attention has been given to sparser environments, such as groups of galaxies, although similar physical processes are likely to be at work.

The purpose of this thesis is to investigate the strength and structure of the magnetized medium surrounding radio galaxies via observations of the Faraday effect. This study is based on an analysis of the polarization properties of radio galaxies selected to have a range of morphologies (elongated tails, or lobes with small axial ratios) and to be located in a variety of environments (from rich cluster core to small group). The targets include famous objects like M 84 and M 87. A key aspect of this work is the combination of accurate radio imaging with high-quality X-ray data for the gas surrounding the sources.

Although the focus of this thesis is primarily observational, I developed analytical models and performed two- and three-dimensional numerical simulations of magnetic fields.

The steps of the thesis are: (a) to analyze new and archival observations of Faraday rotation measure (RM) across radio galaxies and (b) to interpret these and existing RM images using sophisticated two and three-dimensional Monte Carlo simulations.

This thesis aims to pose and answer the following basic questions.

1. What is the origin of the bulk of the Faraday effect observed across radio galaxies? Two possible contributors have been discussed in the literature: the intergalactic medium as a whole and a local sheath formed through mixing layer surrounding the radio lobes.
2. How does the intergalactic magnetic field strength scale with the thermal density? Is there a connection with the richness of the environment? Is the magnetic field ever energetically important?
3. Can the intergalactic magnetic field always be described as an isotropic, Gaussian random variable? If so, what is its power spectrum? Is there evidence for Kolmogorov turbulence? What are the maximum and minimum scales? Is there evidence for a preferred direction or two-dimensionality?
4. How do embedded radio galaxies affect the surrounding plasma and the structure and strength of the field within it? What can be ascribed to the source morphology? Recent X-ray observations have detected regions of low emissivity (“cavities”) in the X-ray emitting gas at the position of the radio lobes. It appears that the radio sources have displaced the surrounding thermal medium rather than mixing with it. What might be the consequences for the magnetic field structure?
5. What is the content of the radio lobes and hence of cavities? In some cases, the relativistic plasma in the radio lobes can provide enough pressure to support them, but others require an additional pressure component – most likely from entrained and heated ( $kT > 10$  keV) intergalactic medium. This heated component should be detected through polarization studies since it may cause *internal* Faraday rotation.

The approach has been to select a few bright, very extended and highly polarized radio galaxies. This is essential to have high signal-to-noise in polarization over large enough areas to allow computation of spatial statistics such as the structure function (and hence the power spectrum) of rotation measure, which requires a large number of independent measurements. New and archival Very Large Array (VLA<sup>1</sup>) observations of the target sources have been analyzed in combination with high-quality X-ray data from the *Chandra*, *XMM-Newton* and *ROSAT* satellites. The work has been carried out by making use of:

1. Analytical predictions of the RM structure functions to quantify the RM statistics and to constrain the power spectra of the RM and magnetic field.

---

<sup>1</sup>The Very Large Array is a facility of the National Science Foundation, operated under cooperative agreement by Associated Universities, Inc.

2. Two-dimensional Monte Carlo simulations to address the effect of an incomplete sampling of RM distribution and so to determine errors for the power spectra.
3. Methods to combine measurements of RM and depolarization in order to constrain the magnetic-field power spectrum on small scales.
4. Three-dimensional models of the group/cluster environments, including different magnetic field power spectra and gas density distributions.

The thesis is organized as follows: Chapters 1–3 are introductory, while 4–6 contain the original work developed in the thesis.

Chapter 1 briefly outlines the essential physics required to understand the polarized emission and energetic of radio galaxies.

The gaseous environment of radio galaxies and implications for their interaction are described in Chapter 2.

Chapter 3 reviews the known properties of intergalactic magnetic fields and outlines different methods of analysis.

Chapter 4 presents a study of the magnetic field in the hot medium surrounding the radio galaxy 3C 449, located in the centre of a nearby galaxy group. High quality RM and depolarization images have been produced by making use of archival VLA data at seven frequencies in the range 1365 – 8385 MHz. Structure-function and simulation techniques have been used to model the magnetic field power spectrum over a wide range of spatial scales and to estimate both the minimum and maximum scale of the magnetic field variations. The central field strength and its dependence on density have been constrained. The work of this Chapter has been published in Guidetti et al. (2010), reported in the section *Highlighted papers* of the journal *Astronomy & Astrophysics*.

Chapter 5 concerns the analysis of the RM of the nearby radio galaxies 0206+35, 3C 270, 3C 353, and M 84. This represents the most innovative part of the thesis. The sources are embedded in different environments, but show the same double-lobed radio morphology. They all show highly anisotropic RM structures (RM bands) which are clearly different from the isotropic variations seen in previously-published RM images. This is a new RM phenomenon and a first attempt to interpret it as a consequence of source-environment interaction is presented. Analytical models for the magnetic field and simulations of the RM expected from expanding sources in the magnetized intergalactic medium are developed. This approach is entirely new and the main results are that a simple compression mechanism *cannot* produce all the observed properties of the RM bands, and a two-dimensional draped magnetic field provides a much better description of the data. The work of this Chapter will be published in Guidetti et al. (2011, in press).

Chapter 6 presents preliminary results from two-dimensional analyses of the polarization of two radio galaxies embedded in extremely different environments: 0755+37 in a very poor group and M87 at the centre of the cool core Virgo cluster. The work of this Chapter will be published in two forecoming papers: Guidetti et al. (in preparation), Guidetti et al. (in preparation).

Chapter 6.4 summarizes all the results presented and briefly lists some topics for further work. It is pointed out that this thesis has shown that the magnetized medium surrounding radio galaxies appears more complicated than was apparent from earlier work. Three distinct types of magnetic-field structure are identified: an isotropic component with large-scale fluctuations, plausibly associated with the intergalactic medium not affected by the presence of a radio source; a well-ordered field draped around the front ends of the radio lobes and a field with small-scale fluctuations in rims of compressed gas surrounding the inner lobes, perhaps associated with a mixing layer.

In the Appendix new VLA polarization data for the nearby radio galaxies 0206+35, 0755+37 and M84 are presented. This work will be published in the paper Laing, Guidetti et al. (2011, in prep).

Throughout the thesis I assume a cosmology with  $H_0 = 71 \text{ km s}^{-1} \text{ Mpc}^{-1}$ ,  $\Omega_m = 0.3$ , and  $\Omega_\Lambda = 0.7$ .

# Chapter 1

## Physics of radio galaxies

In this Chapter I will outline the essential physics required to understand the polarized emission of radio galaxies and their interactions with the local environment. Sec. 1.1 introduces radio sources in the context of active galaxies in general, and Sec. 1.2 discusses their principal emission mechanisms. The morphologies of radio galaxies, the physical parameters of their emitting regions and the implications for their interaction with the environment are described in Sec. 1.3.

### 1.1 Active galaxies

Active galactic nuclei (AGN) are the most powerful, persistent sources of luminosity in the Universe. Their luminosities range from about  $10^{40}$  up to  $10^{47}$  ergs  $s^{-1}$  and their emission is spread widely across the whole electromagnetic spectrum. AGN are so called because of the current accepted model explaining their nature. They are believed to be powered by accretion onto super-massive black holes ( $\sim 10^7 - 10^{10} M_{\odot}$ ) located at the nuclei of so-called “active galaxies”. Indeed, the radiation emitted by such nuclei cannot be explained just by starlight or normal supernova activity and can exceed the total emission of the rest of the galaxy by many order of magnitude. Moreover, the AGN emission is often variable on time-scales ranging from years down to hours or even minutes. Causality arguments imply that an object varying in a time  $t$  must be smaller than the light-crossing time  $ct$  (where  $c$  is the speed of light in the vacuum) and therefore must be spatially small. Accretion mechanisms onto a such small object with mass  $\simeq 10^8 M_{\odot}$  can efficiently convert potential and kinetic energy to radiation and bulk outflow, and therefore account for high luminosities and their rapid variations.

Since luminosity excesses have been observed across the entire electromagnetic waveband, there is no single observational signature of active galaxies, which can be classified in many

ways. This has often led to a confusing terminology. The distinctions between different types of AGN reflect historical differences in how objects were discovered or initially classified, rather than real physical differences. Although the spectrum of these objects can extend across the whole electromagnetic spectrum, the relative intensity between different wavebands and spectral lines features are extremely different and provide a basic classification for the AGN (*e.g.* radio galaxies, quasars, Seyfert galaxies, blazars). AGN are conventionally classified as either “radio-loud” or “radio-quiet”, depending on the ratio of their luminosities in the radio and optical bands. Physically, this distinction reflects the relative importance of relativistic jets and their associated non-thermal emission compared with radiation directly related to the accretion process. Jets are an important, and often dominant, energy loss channel for radio-loud AGN. The cause of the difference between radio-loud and radio-quiet AGN is a complicated and unresolved issue, which may involve the spin of the central black hole (*e.g.* Meier 2002) or the details of the accretion process.

A major simplification for radio-loud and radio-quiet objects is the “unified model”, which suggests that different classes of AGN are in fact the same objects seen at different angles to the line of sight. There are two physical mechanisms: beaming of radiation from relativistic jets (radio-loud only) and obscuration of the central regions of the AGN by a dusty torus (*e.g.* Barthel 1989; Antonucci 1993; Urry & Padovani 1995).

Since this thesis is based on the analysis of the polarization properties of extended radio galaxies, in the next sections I will concentrate on the main non-thermal emission mechanisms observed from radio-loud active galaxies and their implication about the energy content of radio galaxies.

## 1.2 Non-thermal emission mechanisms of active galaxies

The two main non-thermal radiation processes in radio-loud active galaxies are synchrotron radiation and Inverse-Compton (IC) scattering. Their relative importance depends on the observing frequency: IC emission from a given population of relativistic electrons is emitted at higher frequencies than the corresponding synchrotron component. For example, in the extended lobes of radio galaxies, synchrotron emission dominates at radio frequencies and IC in the X-ray band.

### 1.2.1 Synchrotron radiation

Synchrotron emission is generated by the acceleration of relativistic charged particles in a magnetic field  $\mathbf{B}$ . When detected, it provides therefore the more direct way to detect magnetic

---

fields in astrophysical sources. The synchrotron power emitted by a relativistic electron with Lorentz factor  $\gamma$  (electron energy  $\epsilon = \gamma m_e c^2$ ) is:

$$\frac{d\epsilon}{dt} \left[ \frac{\text{erg}}{s} \right] \simeq 1.6 \times 10^{-3} (B_{[\mu\text{G}]} \sin\theta)^2 \gamma^2 \quad (1.1)$$

where  $\theta$  is the pitch angle between the electron velocity and the magnetic field direction. This equation illustrates the degeneracy between particle energy and magnetic field: a given synchrotron power can be produced by a highly energetic particle in a low magnetic field or vice versa.

The spectral distribution for a single electron can be assumed to be approximately monochromatic since it peaks sharply at a frequency:

$$\nu_c[\text{GHz}] \simeq 4.2 \times 10^{-9} \gamma^2 (B_{[\mu\text{G}]} \sin\theta). \quad (1.2)$$

From Eq. 1.2, it is derived that electrons of  $\gamma \simeq 10^4$  in magnetic fields of  $B \simeq 10 \mu\text{G}$  produce synchrotron radiation in the radio band ( $\nu_c \sim 4 \text{ GHz}$ ), whereas electrons of  $\gamma \simeq 10^{7-8}$  in the same magnetic field radiate in the X-rays. A representative example is given by the nearby active galaxy Pictor A, where the spectrum of the jet from radio to X-ray wavelengths can be described as synchrotron emission from a population highly energetic particles with a distribution of Lorentz factors (Wilson, Young & Shopbell 2001).

For a homogeneous population of electrons with an isotropic pitch-angle distribution and a power-law energy spectrum with the particle density between energies  $\epsilon$  and  $\epsilon+d\epsilon$  given by

$$N(\epsilon)d\epsilon = N_0 \epsilon^{-\delta} d\epsilon, \quad (1.3)$$

the total intensity spectrum, in optically-thin regions has the functional form:

$$S(\nu) \propto \nu^{-\alpha}, \quad (1.4)$$

where the spectral index  $\alpha = (\delta - 1)/2$ . This spectrum of Eq. 1.4 is described as *non-thermal*, since the energy spectrum of the emitting particles is not Maxwellian - i.e. it does not have a single temperature.

### 1.2.2 Polarization of synchrotron radiation

In the optically-thin case, for a homogeneous and isotropic distribution of relativistic particles whose energy distribution follows the power law of Eq. 1.3 and in a uniform magnetic field, the

intrinsic degree of polarization has the value (Longair 1994):

$$P_{Int} = \frac{\delta + 1}{\delta + \frac{7}{3}}, \quad (1.5)$$

and the electric vector is perpendicular to the projection of the magnetic field onto the plane of the sky. For typical values of the index of the energy spectrum  $\delta = 2.5$ , the intrinsic polarization degree in an uniform field is expected to be  $\approx 70\%$ , which represents the maximum allowed value. Degrees of polarization  $\geq 0.1$  are often observed at 1.4 GHz; less commonly they exceed 0.3-0.4. A reduction of the expected degree of polarization might stem from an intrinsically complex magnetic field structure within the source and/or depolarization effects, as discussed in Secs. 3.2.1 and 3.3. If the magnetic field can be expressed as the superposition of two components, one uniform  $B_u$ , the other isotropic and random  $B_r$ , the observed degree of polarization is approximately given by (Burn 1966):

$$P_{Obs} = P_{Int} \frac{B_u^2}{B_u^2 + B_r^2}. \quad (1.6)$$

which gives the ratio of the energy in the uniform field over the energy in the total field, and is an indicator of the field uniformity and structure. However, random magnetic fields are likely to be anisotropic, in which case Eq. 1.6 does not hold.

A mathematically convenient way to describe the linear polarization state is given by the Stokes parameters  $I$ ,  $Q$  and  $U$  (Stokes, 1852).

The polarized intensity and the polarization angle of linearly polarized radiation can be described by:

$$P_\lambda = (Q_\lambda^2 + U_\lambda^2)^{1/2} \quad (1.7)$$

and

$$\Psi_\lambda = \frac{1}{2} \arctan \left( \frac{U_\lambda}{Q_\lambda} \right), \quad (1.8)$$

Images of polarized intensity  $P$ , degree of polarization  $P/I$  and position angle  $\Psi$  (and in turn magnetic field) can be derived across radio galaxies from the  $I$ ,  $Q$ , and  $U$  images through radio observations in full polarization mode.

Once corrected for the Faraday rotation (Sec. 3.2) the projected magnetic field in the plane of the sky appears to be tangential to the edges of the lobes in both low- and high-power radio sources. The field orientation in the jets differs between the two classes. Low-power jets usually show magnetic field parallel to the jet axis close to the core with a transition to perpendicular field as the jet expands. In contrast, in powerful sources the magnetic field is usually parallel to the jet axis for the whole length of the jets.

Therefore, the measurement of synchrotron emission from radio galaxies provides information about the index of the energy distribution of particles and the strength of magnetic fields inside the source, while the degree of polarization is an important indicator of the field uniformity and structure. The high degrees of linear polarization observed from radio-galaxy jets and lobes make them ideal probes of the foreground magnetised medium (Sec. 3.2).

### 1.2.3 Inverse Compton emission

Relativistic electrons in a radiation field can scatter low-energy photons to high energy through the inverse-Compton (IC) effect. The reason for the adjective “inverse” is that the electrons lose energy rather than the photons as in the usual Compton scattering. IC scattering increases the frequency of the scattered photons  $\nu_{ph}$  by a factor  $\frac{4}{3}\gamma^2$ , where  $\gamma$  is the Lorentz factor of the relativistic electrons (*e.g.* Rybicki & Lightman 1986). The low-energy scattered photons are often dominated by the ubiquitous 3K cosmic microwave background (CMB). In the presence of relativistic particles with  $\gamma \sim 10^{3-4}$ , CMB photons are scattered from the original frequency around  $10^{11}$  Hz to about  $10^{17-18}$  Hz, corresponding to the X-ray and  $\gamma$ -ray domains (0.8- 20 keV).

Since the power radiated via the IC process by an electron has the same functional dependence on the electron energy as in Eq. 1.1, if the synchrotron and IC emission originate from the same relativistic electron population their fluxes are related. For the electron energy distribution of Eq. 1.3, the two spectra share the same spectral index  $\alpha$ . The spectral index relates to the photon index of the IC emission as  $\Gamma_X = \alpha + 1$ .

Given that the synchrotron emissivity is proportional to the magnetic energy density  $U_B$ , while the IC emissivity is proportional to the energy density in the photon field  $U_{ph}$ , it follows that:

$$\frac{S_{syn}}{S_{IC}} \propto \frac{U_B}{U_{ph}}, \quad (1.9)$$

where  $S_{syn}$  and  $S_{IC}$  are the synchrotron and IC fluxes, respectively.

From the ratio between the IC and synchrotron fluxes, in principle one can derive an estimate of the total magnetic field, averaged over the emitting volume. In terms of observational parameters this is:

$$B[\mu G]^{1+\alpha} = h(\alpha) \frac{S_{syn}(\nu_r)[Jy]}{S_{IC(E_1-E_2)}[ergs^{-1}cm^{-2}]} (1+z)^{3+\alpha} (0.0545\nu_r[MHz])^\alpha \times \\ \times (E_2[keV]^{1-\alpha} - E_1[keV]^{1-\alpha}), \quad (1.10)$$

where  $S_{syn}(\nu_r)$  is the synchrotron flux at the radio frequency  $\nu_r$  and the flux  $S_{IC(E_1-E_2)}$  is integrated over the energy interval  $E_1 - E_2$ .

### 1.3 Radio galaxies

Radio galaxies are radio-loud AGN hosted by massive early type galaxies (visual magnitude  $M_v < -20$ ), with radio powers at 408 MHz spanning the range  $10^{23-28} \text{ WHz}^{-1}$ . Their radio spectra have approximately power-law forms with typical spectral indices  $\alpha = 0.8 \pm 0.2$ , consistent with synchrotron emission from relativistic particles with power-law energy spectra (Sec. 1.2.1). The electron Lorentz factors are  $\gamma \geq 100$  and magnetic field strengths are  $\sim \mu\text{G}$ . The synchrotron origin of the radio emission is confirmed by the smooth broad-band nature of the emission (10 MHz-10 GHz) and the high degree of linear polarization (commonly  $\geq 0.1$  averaged across the source, but reaching values of 0.7 in sub-regions).

The energy source for the relativistic particles and magnetic fields is thought to be the central black hole at the nucleus of the radio galaxy. The energy is transferred from this engine outwards by more or less collimated, initially relativistic, flows or beams, whose visible manifestations are the radio jets.

#### 1.3.1 Radio-galaxy morphologies

Radio galaxies show a wide range of structures and linear sizes, going from a few ten of pc up to Mpc (Bridle & Perley 1984; Laing 1993), and hence they can be more extended than the parent galaxy. The main morphological classification of extended radio galaxies is that made by (Fanaroff & Riley 1974). This was based on the sharp change in morphology of the sources in the 3C catalogue around the radio power  $10^{24.5} \text{ WHz}^{-1}$  at 1.4 GHz, close to the break in the radio luminosity function. Fanaroff & Riley pointed out that low-power sources tend to be brightest close to their nuclei (“edge-darkened”) whereas high-power ones are brightest at their outer extremities (“edge-brightened”). These are respectively classified as *Fanaroff-Riley I* and *Fanaroff-Riley II* sources, (or FR I and FR II sources). The prototypes of FR I and FR II sources are respectively 3C 31 and Cygnus A (Fig. 1.1). The sources discussed in detail in this thesis are mostly members of the FR I class.

The main morphological components of FR I and FR II radio galaxies observed with arcsecond resolution (e.g. Bridle & Perley 1984) are as follows.

- The “core” is an unresolved component coincident to within the observational errors with the optical nucleus. It represents the partially optically thick base of the jets (see below). Cores are relatively stronger in FR I sources.
- The “jets” are long narrow features, which emerge from the core and propagate generally in opposite directions. FR I jets are typically bright, with wide opening angles, while those of

FR II sources appear weak and well collimated, suggesting a more efficient energy transport than in FR Is. FR I jets are thought to decelerate to sub-relativistic speeds on kpc scales, while FR II jets remain relativistic over their whole lengths.

- The “hot-spots” are bright and compact regions observed only in FR II sources, close to the extremities of the radio structures. They are interpreted as the termination or major disruption of the jets at strong shocks (which requires that FR II jets are internally supersonic).
- The “lobes” are wide structures with small axial ratios which lie on either side of the parent galaxy and are often aligned across the nucleus on scales up to Mpc. Most of the radio emission is therefore seen between the end of the jets and the core. Synchrotron spectra of lobes show steepening towards the nucleus and it is therefore likely that lobes are formed from relativistic particles left behind at or back-flowing from the region where the jet impacts the external medium. Lobes are found in both FR I and FR II sources.
- The “tails” are elongated and sometimes irregular structures, mostly farther from the nucleus than the end of a jet. Their synchrotron spectra steepen away from the nucleus, suggesting that they are flowing outwards. They are found almost exclusively in FR I sources.

### 1.3.2 Morphology and expansion of lobes and tails

The physics of the interaction between a radio source and the surrounding IGM appears to be significantly different for lobes and tails. Also, as will become apparent in later Chapters, the magnetization of the IGM around a radio source appears to depend on the morphology of the extended emission. For these reasons, I briefly discuss the differences between lobes and tails.

The richness of the environment may play a role in the formation of tails rather than lobes. Most of the tailed sources are observed in galaxy clusters or rich groups and often show distorted morphologies which are likely to be caused by gas sloshing in the potential well of the cluster or by the high ram pressure exerted by the thermal gas on fast-moving galaxies (respectively Wide-angle tails, *e.g.* 3C 465, Eilek et al. 1984 and Narrow-angle tails, *e.g.* NGC 1265, O’Dea & Owen 1986). There is therefore clear evidence for jet/environment interaction in tailed sources. Indeed, tails are likely to be formed if the jet entrains enough material to slow it to below the external sound speed and/or if buoyancy causes the synchrotron plasma to be pushed outwards. For both these reasons, FR I tails are thought to be expanding *sub-sonically*, basically buoyantly, and in pressure equilibrium with their surroundings.

Lobes or bridges, on the other hand, do sometimes show evidence for shocks in the surrounding X-ray emitting gas, suggesting that they are expanding *supersonically* (Sec. 2.3.2).

So far, the best examples of strong shocks surrounding bridges are found only in two FR I sources (Centaurus A, Kraft et al. 2003; NGC 3801, Croston et al. 2007). Instead, weak shocks appear to occur more frequently and they are seen in both FR I (*e.g.* Perseus, Fabian et al. 2003; Hydra A, Nulsen et al. 2005a; M87, Forman et al. 2005) and FR II sources (*e.g.* Cygnus A, Wilson, Smith & Young 2006; Hercules A, Nulsen et al. 2005b; 3C 444, Croston et al. 2010). Therefore, standard models of supersonic radio-lobe expansion, which were originally thought to apply only to FR II sources (*e.g.* Scheuer 1974; Kaiser & Alexander 1997), are also likely to describe lobes in FR I's. It may be that the expansion of FR I lobes is supersonic only in the forward direction (driven by the ram pressure of the jets) and that the lobes are in static pressure equilibrium with their surroundings closer to the galaxy.

To conclude, the factors which determine the large-scale morphology of radio galaxies have not been disentangled yet, although the initial speeds of the jets and their density contrast with the external medium both seem to be important. Whether a lobe or a tail is formed clearly makes a substantial difference to the interaction between a source and its surroundings.

### 1.3.3 Internal physical conditions of radio galaxies

In order to understand the interaction of radio galaxies with their environments, we need to quantify the internal conditions in the extended emitting regions (lobes and tails). From the synchrotron emissivity alone, it is not possible to derive unambiguously the energy of the relativistic particles and magnetic field, because of the degeneracy between them (Eq. 1.1). Constraints on the energy density in relativistic electrons and magnetic field can be derived from synchrotron emission if IC emission from the same electron population is observed, in which case the degeneracy between particles and fields can be resolved (Eq. 1.10). The sum of particle and field energy densities can then be compared with the thermal pressure in the surroundings. If IC emission is lacking, in order to separate the magnetic and relativistic particles densities, one must make some assumptions about the relation between electrons and magnetic field. One commonly used approach is to assume energy equipartition between them: this is described in the next section.

### 1.3.4 Equipartition parameters

In the context of radio sources, the term “energy equipartition” is commonly used to mean that the energy densities in relativistic particles and magnetic field are equal. This is an assumption, with no rigorous justification, but has some empirical support from observations of FR II lobes. It is also close to the condition that the total energy density in particles and field is a minimum.

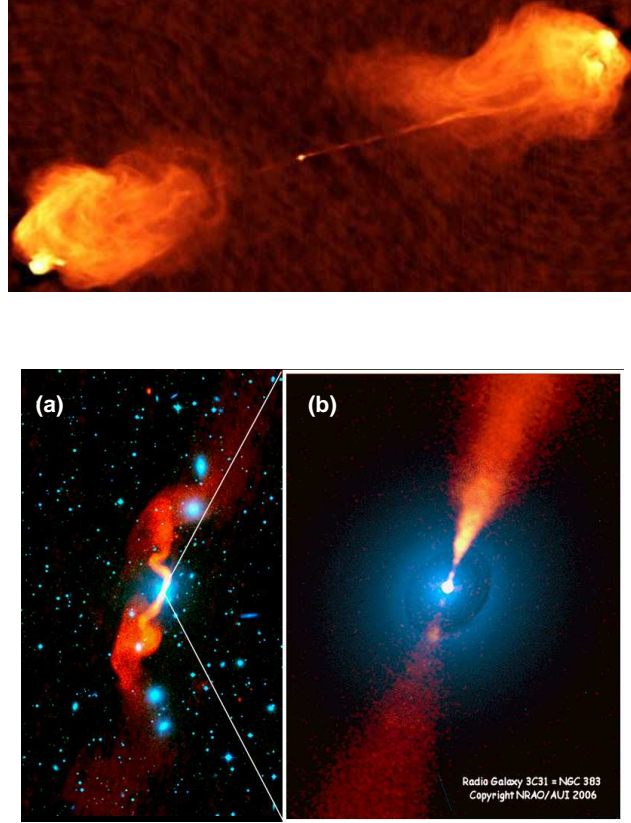


Figure 1.1: Examples of extended radio galaxies with lobes or plumes. Top panel: bridged radio galaxy Cygnus A (FR II) in a cluster of galaxy at  $z=0.056$ . This is the brightest extragalactic radio source in the sky. Bottom panels: montage by A.H. Bridle showing the tailed radio source 3C 31 (FRI, in red) at the center of a galaxy group at  $z=0.0169$ , superimposed on Hubble Space Telescope WFPC2 image (a) and on DSS image (b).

The field strength and pressure corresponding to the equipartition condition (e.g. Longair 1994) are:

$$B_{eq} [\mu G] \simeq 0.9 \cdot L_{[ergs^{-1}] }^{2/7} V_{[kpc^3]}^{-2/7} \zeta^{2/7} \Phi^{-2/7} \quad (1.11)$$

$$P_{eq} [dyne/cm^2] \propto L_{[ergs^{-1}] }^{4/7} V_{[kpc^3]}^{-4/7} \zeta^{4/7} \Phi^{-4/7}, \quad (1.12)$$

where  $L$  and  $V$  are the radio luminosity and the volume of the source,  $\zeta$  is the ratio of the total energy in particles to the energy in electrons alone, and  $\Phi$  is the so called “filling factor”, which is the fraction of the total source volume occupied by emitting material. For a relativistic plasma  $\Gamma = 4/3$ , so the total minimum energy density of the source is  $u_{min} \approx 3 \times P_{eq}$ . Since  $P_{eq}$  represents the pressure exerted by the synchrotron-emitting plasma, throughout the thesis it will be reported as  $P_{syn}$ .

The comparison of the pressure  $P_{eq}$  with the external one provided by the surrounding

medium (Chapter 2) is useful to understand the equilibrium conditions of radio galaxies. In both FR I and FR II radio sources,  $B_{eq}$  and  $P_{syn}$  are found to be a few  $\mu\text{G}$  and  $10^{-12}$ – $10^{-13}$  dyne/cm<sup>2</sup>, respectively.

However, all the equipartition estimates must be taken with caution, because each of the variables in Eqs. 1.11 and 1.12 is potentially a source of uncertainty. Indeed, the filling factor  $\Phi$  is unknown and often assumed to be 1 although in some radio galaxies there is evidence for filamentary structure. Some assumptions on the geometry of the source must also be made in order to compute the source volume  $V$ . The ratio  $\zeta$  is also subject to major uncertainties, since the energy density in relativistic protons is unconstrained. Moreover, the equipartition parameters are strongly related to the functional form of the particle energy spectrum and therefore to the synchrotron emission spectrum. Good constraints on the energy spectrum require wide frequency coverage. Indeed, even small changes in the lower limit of the relativistic particle energy can have a huge impact on the determination of  $B_{eq}$  and  $P_{min}$ . This is particularly true for steep radio spectra, where low energy particles contribute most of the total energy.

My personal conclusion is that minimum energy arguments are of limited usefulness. The best use of these estimates lies in making the most conservative assumptions and treating the resulting pressures as lower limits.

### 1.3.5 Field and particle content of radio lobes and tails

FR I radio galaxies with tails are believed to expand sub-sonically in pressure equilibrium with the surroundings, and to rise buoyantly in the intergalactic medium. On the other hand, some FR I sources with bridges appear to be surrounded by shocked X-ray emitting gas, which suggests supersonic expansion.

As already pointed out, when IC emission is detected from the radio sources, then the total energy density in relativistic electrons and fields can be estimated and compared with the external pressure, also derived from X-ray observations. For some FR II sources, this has been done (*e.g.* Kataoka & Stawarz 2005; Croston et al. 2004; Laskar et al. 2009; Isobe et al. 2011) The conclusion is that most FR II lobes are close to the minimum energy condition, in the sense that relativistic electron and field energy densities are comparable, and that their sum is in turn close to the external pressure, as expected for static thermal confinement (*e.g.* Hardcastle et al. 2002; Croston et al. 2004; Konar 2009). So far, there are no unambiguously detections of IC emission from FR I lobes. Instead, several studies have shown that the synchrotron equipartition pressure  $P_{syn}$  within the FR I radio lobes is often an order of magnitude smaller than the external pressure exerted by the hot surrounding gas (*e.g.* Morganti et al. 1988; Worrall & Birkinshaw 2000; Blanton et al. 2001; de Young 2006; Croston et al. 2003, 2008). Without a further source of internal

pressure, the radio sources would then collapse.

To solve the pressure balance problem for FRI sources we need to consider:

1. deviations from equipartition or
2. an additional source of pressure which is not detectable by current radio or X-ray observations.

Deviations from equipartition in the sense of electron dominance could be given by a large excess of low-energy electrons. These would be detectable via their IC radiation in at least some cases (*e.g.* Croston, Hardcastle & Birkinshaw 2005). Therefore deviations from equipartition would have to be in the direction of magnetic dominance.

An additional source of pressure could be provided by relativistic protons. These would have to be accelerated in the lobes, since a relativistic proton population in the jets would exert too high a pressure to allow collimation. Even cold protons cannot be transported by the jets in large enough numbers without violating constraints on the mass flux (Laing & Bridle 2002a). The best candidate to solve the pressure balance is therefore heated and entrained thermal material. This would have to be hot ( $kT \geq 10$  keV, *e.g.* Nulsen et al. 2002) but tenuous, to provide enough pressure without radiating sufficiently to erase the soft X-ray depressions (“cavities”), often observed at the position of radio lobes (Sec. 2.3.1).



## Chapter 2

# The X-ray environment of radio galaxies

### 2.1 Introduction

Early *Einstein* X-ray observations discovered that early-type galaxies, groups and clusters of galaxies are spatially-extended X-ray sources with luminosities in the range  $10^{39-43}$  erg s<sup>-1</sup> (*e.g.* Forman et al. 1979; Kriss et al. 1980; Biermann, Kronberg & Madore 1982). Subsequent more sensitive and detailed X-ray images provided by the *ROSAT*, *Asca*, *XMM-Newton* and *Chandra* satellites have led to the detection of components on several scales from several distinct emission mechanisms. These are:

- the end products of stellar evolution (point-like sources);
- emission spatially coincident with the bases of radio jets;
- the hot phase of the interstellar medium (ISM) of the galaxies and
- the hot and diffuse intergalactic medium (IGM) in groups and clusters of galaxies.

It is now well-established that the diffuse X-ray emission arises from hot and dilute plasma emitting via thermal bremsstrahlung (Sec. 2.2.2).

Radio emission from active galaxies therefore coexists with a complex, hot medium, with which it interacts in several ways.

- Radio jets can entrain the external medium, which is thought to be able to decelerate the initially relativistic flows in FR I sources on typical scales of a few kpc (*e.g.* Laing & Bridle 2002a).

- Both the lateral expansion of a radio source and the propagation of radio jets can do work against the external hot gas, displacing and compressing it. Energy can also be transferred, for example by shock heating or dissipation of sound waves.
- This transferred energy can prevent the cooling of hot gas and therefore suppress cooling flows and star formation in massive galaxies (*e.g.* Sarazin 1988; Binney & Tabor 1995; Mathews & Brighenti 2003).
- Conversely, hot gaseous atmospheres confine the radio emission, influencing its morphology.

Therefore, X-ray observations of the hot gas are crucial to an understanding of the dynamics and energetics of radio galaxies as well their impact on their environment. X-ray imaging can show signatures of interactions between the radio galaxies and hot gas, while X-ray spectroscopy can shed light on the mechanisms by which energy is transferred from the radio galaxy to the surrounding plasma.

## 2.2 The thermal component

### 2.2.1 The continuum spectrum

Any hot, fully-ionized plasma with a temperature above  $10^4$  K emits via thermal bremsstrahlung, which results from the acceleration of free electrons deflected in the Coulomb field of a ion. The thermal bremsstrahlung emissivity at frequency  $\nu$  for an optically-thin plasma in collisional equilibrium<sup>1</sup> can be expressed as :

$$J_X(\nu) \propto n_e n_{\text{ions}} g(\nu, T) T^{1/2} \exp^{-h\nu/K_B T} \text{ ergs}^{-1} \text{ cm}^{-3} \text{ Hz}^{-1} \text{ sr}^{-1} \quad (2.1)$$

where  $n_e$  and  $n_{\text{ions}}$  are the electron and ion number densities and  $T$  is the gas temperature.<sup>2</sup>  $g(\nu, T) \propto \ln(k_B T/h\nu \approx 1)$  is the Gaunt factor, which corrects for quantum mechanical effects and for the effects of distant collisions. The square-law density behavior in Eq. 2.1 reflects the collisional nature of the process. The emission of X-rays from ISM and IGM is well-described by Eq. 2.1.

X-ray data can therefore be used to derive the physical properties of the X-ray emitting gas such as central density, temperature profile and total mass. Fits to the X-ray spectra give average

<sup>1</sup>Collisional equilibrium takes place when processes of electron ionization are exactly balanced by recombination processes.

<sup>2</sup>The electrons and ions are thought to have a Maxwellian distribution with a common temperature  $T$ .

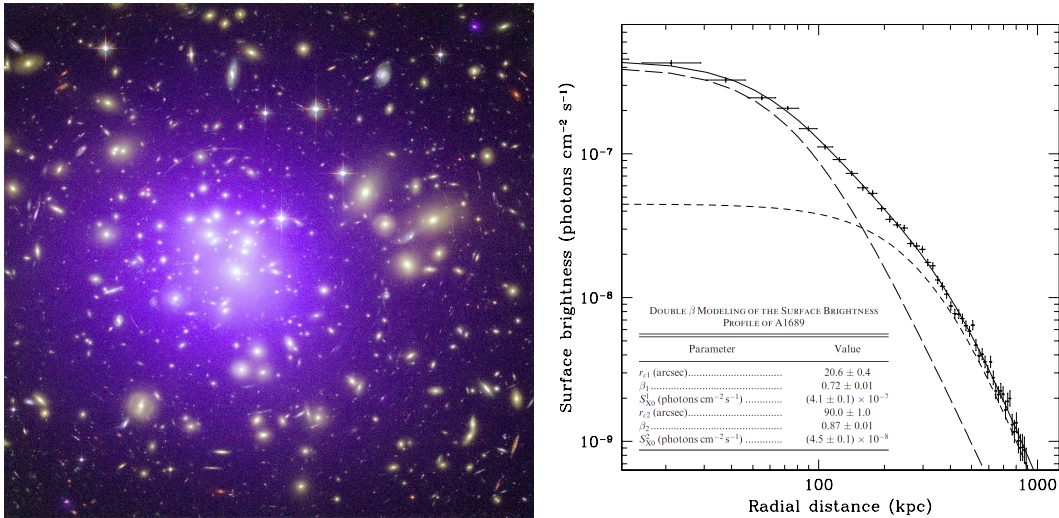


Figure 2.1: Panel (a): Chandra observation of the massive (regular) cluster of galaxies A 1689 (blue) superimposed on the optical image (yellow, Hubble Space Telescope). Panel (b): fitting of the surface brightness profile with a double  $\beta$  model described in the inset. Taken from Xue & Wu (2002).

gas temperatures increasing with the size and the mass of the environment. Typical temperatures for clusters, groups and individual galaxies are given in Table 2.1.

### 2.2.2 Morphology of the X-ray emitting gas

Imaging of the X-ray emission from massive ellipticals, groups and clusters of galaxies has shown that the morphologies of the emitting gas are quite heterogeneous, but that they can be related to the dynamical state of the systems. Much of work has been carried out for galaxy clusters, but the conclusions can be extended to sparser environments such as groups of galaxies and field galaxies, which can be regarded as scaled-down version of rich clusters.

Forman & Jones (1982) first proposed a classification into “regular” and “irregular” X-ray cluster morphologies, with a connection to the evolutionary state.

Essentially, regular clusters are those which show approximately round, centrally condensed X-ray brightness distributions, decreasing smoothly outwards. Their temperatures and X-ray luminosities are usually high and they often host a central dominant galaxy. Galaxy clusters belonging to this class are thought to be evolved systems which have undergone dynamical relaxation.

When the X-ray emission can be approximated as regular, its surface brightness profile is well parametrized by the function:

$$S(r) = S(0) \left[ 1 + \frac{r^2}{r_c^2} \right]^{-3\beta+1/2} \quad (2.2)$$

where  $r$  is the projected radial distance from the centroid of the X-ray surface brightness distribution,  $S(0)$  is the central surface brightness,  $r_c$  is the X-ray core radius and  $\beta = \frac{\mu m_p \sigma_r^2}{k_B T}$ . Here,  $\mu$  is the mean molecular weight,  $m_p$  is the proton mass, and  $\sigma_r$  is the radial velocity dispersion of the galaxies.

The model of Eq. 2.2 has the advantage that its shape is uniquely described by only two parameters: the core radius and the slope  $\beta$ . The latter determines the sharpness of the turnover beyond the core radius and the asymptotic slope of the scaling. Physically,  $\beta$  represents the ratio between the specific kinetic energy of the gravitationally bound galaxies and the specific thermal energy of the hot gas. Fits to the X-ray surface brightness profiles generally give  $\beta \sim 0.4-0.7$ , indicating that the energy per unit mass is higher in the hot gas than in the galaxies. The core radius  $r_c$  is highly correlated with the parameter  $\beta$ , in the sense that larger  $r_c$  corresponds to higher  $\beta$ : indeed, a given X-ray surface brightness can be reproduced by a concentrated distribution with a rapid decline (small  $r_c$  and high  $\beta$ ), or by a more diffuse one with a flatter decline (large  $r_c$  and low  $\beta$ ). Typical ranges for the fitted X-ray parameters are summarized in Table 2.1.

Assuming that the gas-density distribution is isothermal and hydrostatic, the surface brightness profile of Eq. 2.2 corresponds to the density profile called a  $\beta$  model and given by (Cavaliere & Fusco-Femiano 1976):

$$n_e(r) = n_e(0) \left[ 1 + \frac{r^2}{r_c^2} \right]^{-\frac{3}{2}\beta} . \quad (2.3)$$

where  $n_e(0)$  is the central electron density.

The  $\beta$  model adequately describes the surface brightness profiles of regular X-ray emission over a wide range of radii. However, it fails in reproducing the strongly peaked X-ray surface brightness distributions observed in some systems. This peak might be interpreted as emission due to the ISM of the central elliptical galaxy, superimposed on that from the intergalactic medium, or as an indication of the presence of a cooling flow (*e.g.* Trinchieri, Fabbiano & Kim 1997; Helsdon & Ponman 2000; Croston et al. 2008). In both cases, the fit to the X-ray surface brightness is significantly improved by using two distinct  $\beta$  models, one for each component (*e.g.* Croston et al. 2008). Analogously, fits to the temperature profile often require two-temperature models. Fig. 2.1 shows an example of X-ray emission from a relaxed galaxy cluster and the best fitting double  $\beta$  model describing the surface brightness profile.

Models of this type are used later in the thesis (Chapters 4 and 5) to parametrize the density distributions of hot gas around radio galaxies.

Table 2.1: Typical parameters describing the X-ray<sup>1</sup> emitting atmospheres in clusters, groups and massive ellipticals.

environment	$L_X$ [erg s <sup>-1</sup> ]	$n_e(0)$ [cm <sup>-3</sup> ]	$r_c$ [kpc]	$\beta$	$kT$ [keV]
cluster	10 <sup>43-45</sup>	10 <sup>-3</sup>	100-300	0.4-0.8	2-6
group	10 <sup>41-44</sup>	10 <sup>-3</sup> – 10 <sup>-4</sup>	20-200	0.3-0.9	0.3-2
elliptical	10 <sup>39-41</sup>	0.1	5-20	”	0.5-1.5

<sup>1</sup> in the soft X-ray energy band  $\approx 0.2-10$  keV.

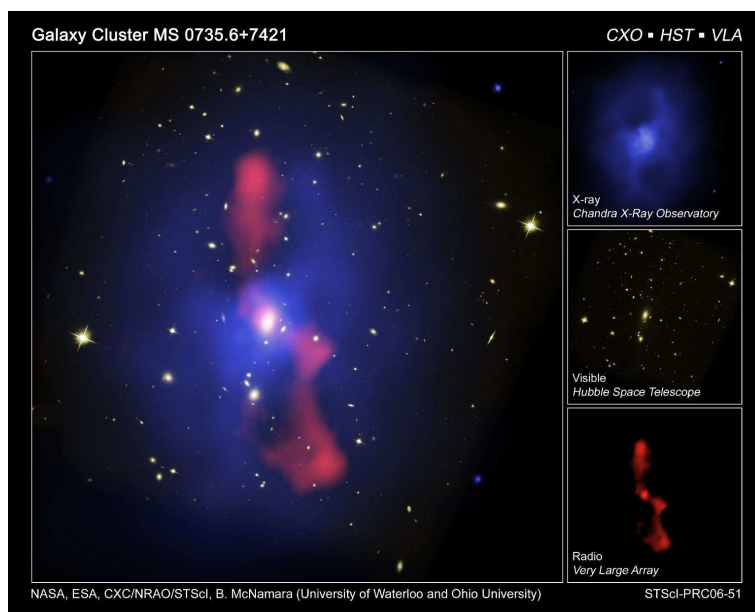


Figure 2.2: Composite image of the galaxy cluster MS0735.6 7421 Hubble Space Telescope (optical) superimposed on Chandra X-ray (blue) and Very Large Array at 330 MHz (red). The X-ray data show the emission of hot gas at  $\sim 5 \times 10^7$  K and two cavities, each roughly 200 kpc in diameter coincident with radio lobes. Taken from McNamara et al. (2005).

## 2.3 Radio source – environment interactions

### 2.3.1 X-ray cavities and their content

An increasing number of clusters, groups and giant ellipticals show regions of X-ray surface brightness depressions which appear as holes embedded in a brighter emission (see McNamara & Nulsen 2007 for a review).

The surface brightness of such holes is around 20-40% below that of the surroundings. They are commonly observed coincident with radio lobes and generally referred to as “cavities”. An example is given in Fig. 2.2: the *Chandra* image displays the soft X-ray emission of the cluster

MS0735.6 7421 with two large cavities, each roughly 20 kpc in diameter (McNamara et al. 2005). Other spectacular examples of cavities associated with cluster sources are Hydra A (McNamara et al. 2000), Centaurus A (Fabian et al. 2000) and Cygnus A (Carilli et al. 1994). Cavities are observed also in group environments of FR I sources (*e.g.* Croston et al. 2008; Giacintucci et al. 2011; Gitti et al. 2010). The cavities observed so far have an average radius of 10 kpc (*e.g.* Bîrzan et al. 2004), but there are examples with radii up to 100 kpc (Hydra A, Nulsen et al. 2005a).

The absence of soft X-ray emission from cavities shows that they cannot contain much thermal plasma, unless it is much hotter than the surroundings ( $kT \geq 10$  keV). One possibility is that cavities are filled entirely with synchrotron-emitting plasma associated with radio lobes (Nulsen et al. 2002; Bîrzan et al. 2008 and reference therein), but the inference of an apparent pressure deficit in the lobes of FR I radio galaxies (Sec. 1.3.5) suggests that there may also be a significant amount of heated and entrained thermal plasma.

The energy required to inflate a cavity  $E_{cav}$  adiabatically can be estimated roughly using only X-ray observations. For cavities containing only relativistic mono-atomic gas,  $E_{cav} = 4PV$ , where  $P$  is the pressure internal to the lobe and  $V$  is the volume of gas displaced by the radio lobe. A power-law relation is found between  $E_{cav}$  and the radio-source luminosity. However, this relation shows a large scatter (Bîrzan et al. 2004, 2008; Cavagnolo et al. 2010).  $E_{cav}$  is a lower limit to the energy supplied by the radio source, some of which may be dissipated (*e.g.* in shocks) or used to inflate further undetected cavities (*e.g.* McNamara & Nulsen 2007).  $E_{cav}$  estimates based only on enthalpy range from  $10^{55}$  up to  $10^{61}$  erg s<sup>-1</sup>, reaching the highest values in rich clusters. The energy deposition rates are high enough to prevent gas cooling below 2 keV in several systems (*e.g.* Bîrzan et al. 2008).

### 2.3.2 Gas compression and heating by radio galaxies

If radio lobes are expanding supersonically<sup>3</sup>, at least in the forward direction of the jets, then a bow shock is expected to form ahead of them (Fig. 2.3). The shock velocity is essentially the expansion velocity of the lobe. Shock waves are characterized by a discontinuous and very sharp change in the characteristics of the gas. Density and temperature jumps across the shock surface (Rankine-Hugoniot conditions) can be derived from conservation of mass, momentum and energy across the shock. In a perfect gas and for an adiabatic shock traveling normal to the gas flow the jump conditions for the density  $\rho$  and temperature  $T$  (Landau & Lifshitz 1987) are:

$$\frac{\rho_2}{\rho_1} = \frac{\gamma + 1}{\gamma - 1 + \frac{2}{M^2}} \quad (2.4)$$

<sup>3</sup>with respect to the sound speed of the X-ray emitting diffuse gas.

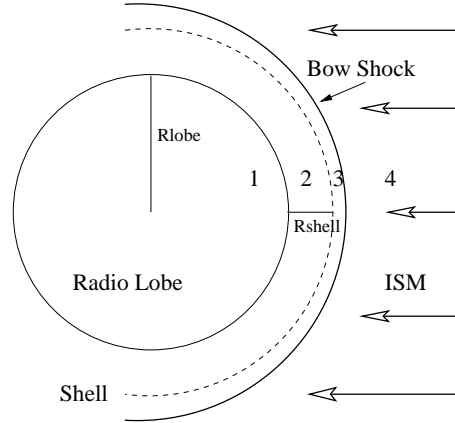


Figure 2.3: Schematic diagram of the regions around a supersonically expanding lobe in the ISM. Region 1 is the radio lobe, region 2 the observed X-ray enhancement region, region 3 is a physically thin layer where the Rankine-Hugoniot shock conditions are met, and region 4 is the ambient ISM. The figure is taken from Kraft et al. (2003).

$$\frac{T_2}{T_1} = \frac{2\gamma\mathcal{M}^2 - \gamma + 1}{\gamma + 1} \frac{\rho_1}{\rho_2} \quad (2.5)$$

where the subscripts 1 and 2 stand for the unshocked and shocked gas, and  $\mathcal{M}$  is the Mach number of the shock wave.  $\mathcal{M}$  is defined as the ratio between the shock velocity  $v$  and the sound speed in the un-shocked gas:  $\mathcal{M} = v/c_1$ .

In the limit of a very strong shock ( $\mathcal{M} \gg 1$ ), the two ratios become:

$$\frac{\rho_2}{\rho_1} = \frac{\gamma + 1}{\gamma - 1} \quad (2.6)$$

$$\frac{T_2}{T_1} = 2\gamma(\gamma - 1) \frac{\mathcal{M}^2}{(2\gamma + 1)^2}. \quad (2.7)$$

These show that for a very supersonic lobe expansion,  $T$  can be arbitrarily large, whereas the density jump attains a finite maximum value, which is 4 for a thermal mono-atomic plasma (a reasonable approximation for the hot IGM). The gas compression and heating take place over the mean free path of the gas and hence the shock front is expected to be narrow.

The presence of shocks surrounding radio lobes can be confirmed using deep X-ray observations by extracting surface brightness and spectra profiles. These allow the detection of density and temperature jumps, respectively, (Eqs.2.3 and 2.2) and from these the shock Mach number  $\mathcal{M}$  can be estimated. So far the two known cases of strong shocks associated with expanding radio-galaxy lobes are found in the FR I sources Cen A and NGC 3801. In these sources the shocked hot gas is 10 and 4-5 times hotter than the surroundings, corresponding respectively

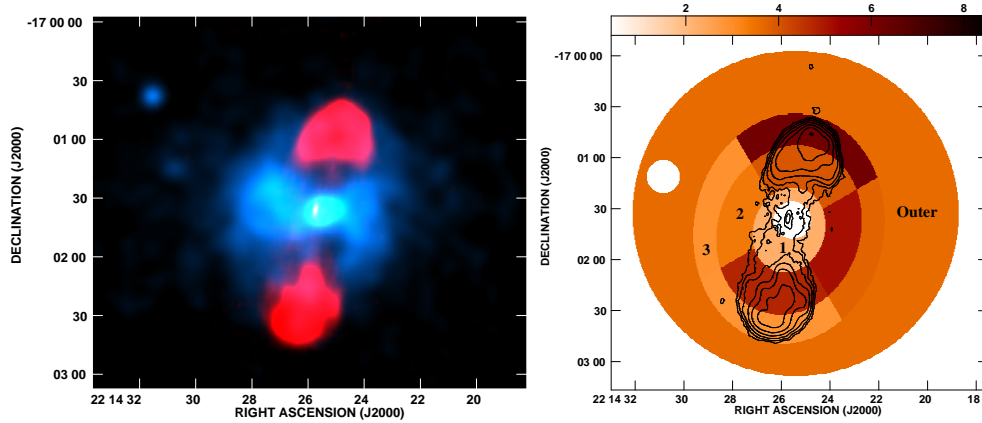


Figure 2.4: (Left): Overlay of a 5 GHz VLA map (red) of 3C 444 on 0.5 - 5.0 keV *Chandra* data (blue) indicating the relationship between the radio and X-ray structures, including cavities coincident with the radio lobes, and a sharp elliptical surface brightness drop surrounding the source. (right): temperature map in keV with 5 GHz contours overlaid. The spectral extraction regions are numbered. The figure is taken from (Croston et al. 2010).

to shock Mach numbers  $\mathcal{M}$  of about 8 and 4 respectively (Kraft et al. 2003; Croston et al. 2007). In both the cases, the total energies stored in the cavities are several times larger than the estimated  $PV$  work.

Weak shocks with  $\mathcal{M} \approx 1.2 - 1.7$  surrounding cavities associated with FR I and FR II sources are observed more frequently (*e.g.* McNamara et al. 2005; Nulsen et al. 2005a; Croston et al. 2008, 2010). Fig. 2.4 shows the case of the FR II radio galaxy 3C 444 where the surrounding intra-cluster medium is characterized by cavities and a temperature jump of a factor  $\sim 1.7$ , probably caused by a spheroidal shock (Croston et al. 2010).

The effects of these radio-galaxy shocks on the magnetic field in the IGM are analysed in detail in Chapter 5.

## Chapter 3

# Magnetic fields in the hot phase of the intergalactic medium

In this Chapter I will briefly review the state of our knowledge of intergalactic magnetic fields. Most attention is given to the results of the analysis of Faraday effect across radio galaxies, on which this thesis is based, while those from other techniques are summarized more briefly. In particular I will show that detailed radio observations of polarized radio galaxies indicate the presence of turbulent magnetic fields fluctuating over a wide range of spatial scales and provide a means of measuring their power spectra.

### 3.1 Introduction

The existence of magnetic fields in the extragalactic universe is now well established. Our knowledge about them has greatly improved over the last few decades, mainly thanks to radio continuum observations, which have detected magnetic fields at  $\mu\text{G}$  levels in objects such as galaxy disks and halos and intergalactic media in both groups and clusters of galaxies. It is also possible that intergalactic voids are permeated by a widespread magnetic field.

Despite their ubiquity, the role of extragalactic magnetic fields has often remained an ignored aspect of astrophysics, because of their low energy densities.  $\mu\text{G}$ -strength magnetic fields are now thought to be important for multiple reasons. Fields associated with the thermal IGM are not thought to be dynamically significant, since they provide typical magnetic pressures one or two orders of magnitude below thermal values. However, they are believed to strongly influence the IGM heat conductivity, inhibiting the spatial mixing of gas and propagation of cosmic rays (*e.g.* Balbus 2000; Bogdanović et al. 2009). Indeed, the IGM is so extremely dilute that is characterized by huge collisional mean free paths ( $\sim 20$  kpc). In this condition, even for

a weak magnetic field, the expected Larmor radius ( $\sim 10^8$  cm for  $T=10^8$  K and  $B=1\mu\text{G}$ ) is much smaller than the mean free path. It follows that the charged particles are channeled only around the magnetic field lines, so thermal conduction becomes anisotropic.

A detailed knowledge of the strength and structure (coherence lengths, fluctuations scales) of intergalactic magnetic fields is therefore important to a better understanding of the physical processes in the gaseous environment of galaxies.

Magnetic-field analysis has until recently been restricted to rich clusters of galaxies, while little attention has been given in the literature to sparser environments, such as groups of galaxies, although similar physical processes are likely to be at work. Intra-cluster magnetic fields have been measured using different techniques (*e.g.* Carilli & Taylor 2002) based mainly on the study of:

- diffuse radio synchrotron sources within clusters;
- inverse Compton emission and
- Faraday rotation of polarised radio sources both within and behind clusters.

These analyses have led to slightly discrepant estimates for the field strength, which in some cases could be reconciled taking into account the several and different assumptions on which the methods are based.

### 3.1.1 Diffuse synchrotron sources in galaxy clusters

The most direct proof of presence of magnetic fields mixed with the ICM is provided by the detection of diffuse radio synchrotron emission on scales up to Mpc in an increasing number of galaxy clusters (see *e.g.* Ferrari et al. 2008 for a review). Since this emission appears not to be associated with single active galaxies but to arise from the ICM itself, it indicates the presence of both relativistic particles and large-scale magnetic fields in such plasma. These are globally called the “non-thermal” component of galaxy clusters. Their radio spectra are well explained as synchrotron emission from ultra-relativistic electrons (Lorentz factor  $\geq 1000$ ) moving in magnetic fields of 0.1-1  $\mu\text{G}$  strength.

Diffuse cluster radio emission shows two types of morphology: radio *relics* and *halos*. While relics are irregular and polarized structures observed at the periphery of clusters, with size ranging from few tens of kpc up to  $10^3$  kpc (*e.g.* Harris et al. 1993; Clarke & Enßlin 2006; Bagchi et al. 2006; Bonafede et al. 2009a; van Weeren et al. 2010), radio halos are regular, distributed as the thermal X-ray emission of the ICM and typically showing low fractional polarization

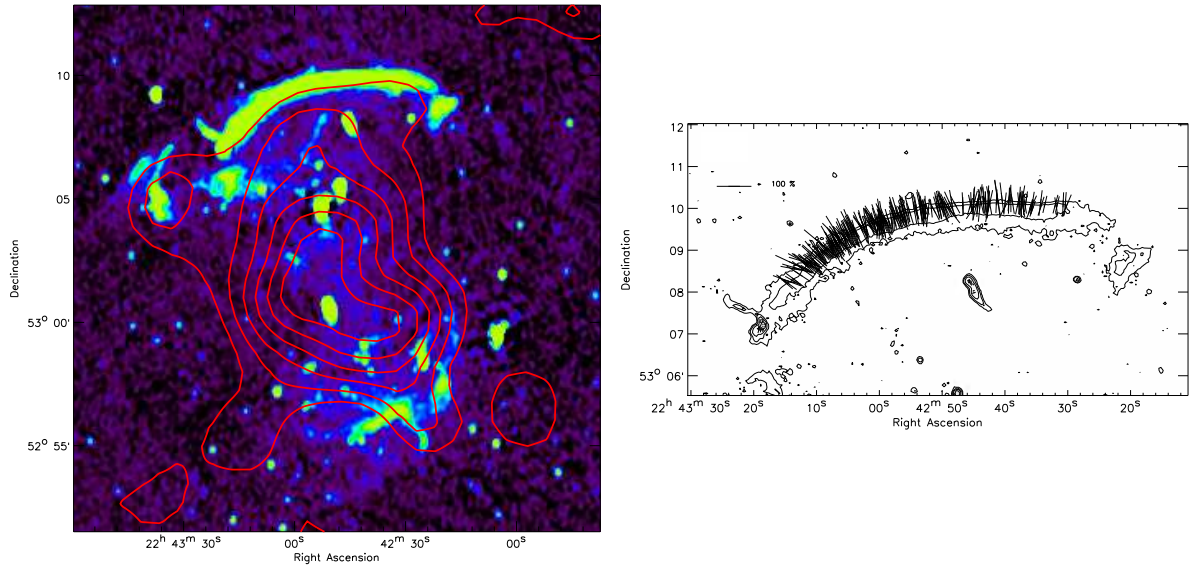


Figure 3.1: Example of a relic. **Left:** Westerbork Synthesis Radio Telescope (WSRT) image at 1.4 GHz overlaid on the X-ray emission from ROSAT showing the hot ICM (red contours). **Right:** Polarization electric field vectors at 4.9 GHz (corrected for the effects of Faraday rotation) and with lengths proportional to the fractional polarization at the same frequency. A reference vector for 100% polarization is drawn in the top left corner. Both figures are taken from van Weeren et al. (2010).

(e.g. Giovannini & Feretti 2002; Clarke & Enßlin 2006; Giacintucci et al. 2009. Both radio halos and relics show steep radio spectra ( $\alpha \geq 1$ ) and low surface brightness ( $\sim 10^{-6}$  Jy arcsec $^{-2}$  at 1.4 GHz).

The most widely accepted scenario for the origin of radio relics is that (primary) relativistic electrons are injected into the ICM from AGN activity and/or from star formation in galaxies. They are then accelerated by shocks or mergers (Enßlin et al. 1998; Röttiger, Burns & Stone 1999) or by adiabatic compression of fossil radio plasma (Ensslin & Gopal-Krishna 2001). This picture is supported by the typical high degree of polarization and the orientation of magnetic field vectors, which appear to be oriented along the major axis of elongated relics with coherence scales of several hundreds of kpc (Right panel of Fig. 3.1). Indeed, compression and/or shocks can locally amplify and align the field with their surfaces.

In contrast, the formation of radio halos is still debated. Since primary relativistic electrons lose energy on short timescales ( $\sim 10^{7-8}$  yrs), they cannot diffuse any significant distance in the cluster before ceasing to radiate. To explain the large extension, up to Mpc scales, of radio halos, continuous injection processes and/or particle re-acceleration are required. These might be due to gas turbulence, efficient in energetic mergers (*primary models*). Another possibility is that secondary electrons are continuously injected in the ICM by hadronic collisions between relativistic protons and ICM thermal protons (*secondary models*). Because of their higher mass,

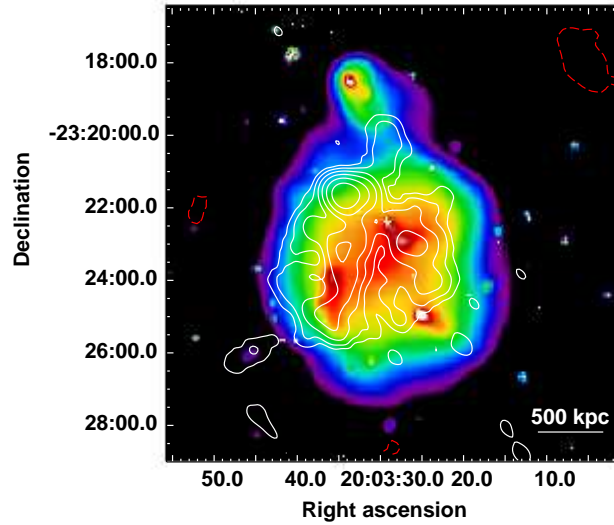


Figure 3.2: Example of a radio halo. *Chandra* image of the hot ICM in the cluster RXCJ 2003.5–2323 overlaid on contours of 235 MHz radio emission from the Giant Metrewave Radio Telescope (GMRT). Taken from Giacintucci et al. (2009).

relativistic protons have loss timescales of the order of the Hubble time, thus they are able to travel a large distance through the cluster.

The observed link between radio halos and relics and the unrelaxed state of clusters supports the scenario of re-acceleration *in situ* of particles by turbulence produced during cluster mergers *e.g.* Schlickeise, Sievers & Thiemann 1987; Brunetti et al. 2001; Petrosian 2001; Fujita, Takizawa & Sarazin 2003).

Cluster mergers are indeed able to drive turbulence, shocks and compression in the intra-cluster medium. The energy dissipated in cluster mergers can be channeled into the amplification of magnetic fields and particle acceleration (*e.g.* Carilli & Taylor 2002; Dolag et al. 2002; Brüggén et al. 2005; Brunetti & Lazarian 2007; Pfrommer, Enßlin & Springel 2008).

However, not all dynamically disturbed clusters possess radio halos. One of the reasons is that they are difficult to observe, due to their low surface brightness and steep spectrum. Cassano & Brunetti (2005) have shown that only the most massive clusters, where the energy density of the turbulence is high enough, should possess radio halos produced by primary models.

### 3.1.2 Magnetic fields from diffuse radio sources

Secondary models predict gamma-ray emission from neutral pion decay from the same hadronic collisions that create relativistic electrons. So far, such diffuse emission, which would corroborate the secondary models for the origin of radio halos, has not been detected from clusters, and only upper limits can be inferred (*e.g.* Ackermann et al. 2010). The expected gamma-ray flux is related

to the relativistic electron energy spectrum, which together with the magnetic field strength also determines the observed radio emission. Consequently, an upper limit to the gamma-ray flux corresponds to a lower limit on the intra-cluster field strength. To reproduce the observed radio halo emissivity, current gamma-ray upper limits give average field strength of the order of several  $\mu\text{G}$  (*e.g.* Jeltama & Profumo 2011).

When halos or relics are observed, minimum energy assumptions offer an alternative approach to estimate the magnetic field strength  $B_{eq}$  averaged over the whole halo/relic volume. This is the only estimate available for the preferred primary models. Multiple uncertainties affect this approach (Sec. 1.3.4). In particular, equipartition calculations can grossly underestimate the field strength as they are based on the assumption of a homogeneous magnetic field throughout the halo/relic volume, in contrast with evidence for its radial decline (Sec. 3.5). With standard assumptions ( $\zeta = 1$ ,  $\Phi = 1$ , emitting frequency range = 10 MHz  $\div$  10 GHz)  $B_{eq}$  ranges from 0.1 to  $2\mu\text{G}$  in cluster halos and from 0.5 up to  $6\mu\text{G}$  in relics (Ferrari et al. 2008 and reference therein, van Weeren et al. 2010).

### 3.1.3 Diffuse inverse Compton emission

As in radio galaxies, the observation of diffuse IC flux from radio halos and relics would allow a straightforward determination of both magnetic field strength and relativistic particle density (Sec. 1.2.3). IC emission from radio halos and relics, should be observable at hard X-ray energies (the ‘‘HXR excess’’) where the exponential decline of the thermal bremsstrahlung, dominating at soft keV energies, is steeper than the expected non-thermal spectrum (Rephaeli 1977).

So far, highly significant IC emission has been detected only in the Ophiuchus cluster (*e.g.* Eckert et al. 2008), which possesses a mini-halo and the implied averaged magnetic field is  $\approx 0.3\mu\text{G}$  (Murgia et al. 2010). Earlier, less significant, detections gave predicted magnetic fields strength in the range 0.1-0.7  $\mu\text{G}$ , reaching the higher values in relics (*e.g.* Slee et al. 2001; Rephaeli, Gruber & Arieli 2006; Eckert et al. 2008). Similar or slightly higher fields are derived as lower limits from non-detections of IC emission (*e.g.* Lutovinov et al. 2008; Wik et al. 2011).

Estimates of magnetic fields from IC emission in clusters are problematic for a number of reasons.

- It is difficult to distinguish the HXR excess from thermal emission. In some clusters, the observed spectrum can instead be reproduced by thermal model with a single or multiple gas temperatures (*e.g.* Lutovinov et al. 2008; Wik et al. 2011).
- An HXR excess might also be interpreted as synchrotron emission from highly relativistic electrons ( $\approx \text{PeV}$ , Timokhin et al. 2004) or non-thermal bremsstrahlung from supra-thermal

electrons (Blasi 2000; Ensslin & Gopal-Krishna 2001). However, the latter scenario is problematic because of the inefficiency of such process which converts most of the collisional energy into heat (Petrosian 2001, 2003).

- They assume the coincidence of IC and synchrotron emitting particles, which is poorly constrained if not unknown.

Taken at face value, IC detections predict slightly lower average field strengths than those which assume equipartition between relativistic electrons and field in halos and relics. These in turn are of about one order of magnitude below those derived from current upper limits on gamma-ray emission for secondary models (any improvement in the sensitivity of gamma-ray observations, will give even higher magnetic fields in this case). On the other hand, changes in assumptions about the relative number densities of relativistic protons and electrons can lead to increases in  $B_{eq}$  by factors of 2–3 (e.g. Beck & Krause 2005). Because of the various uncertainties and assumptions of all the methods outlined above, a detailed comparison of their results is not sensible. We can just say that all of them agree that  $\mu\text{G}$  average magnetic field strengths are present in clusters.

The Faraday effect across radio galaxies discussed in the next sections provides a much more detailed, and I would say surprising, picture of magnetic fields in the hot phase of the IGM.

## 3.2 Faraday Rotation

The Faraday effect (Faraday 1846) describes the rotation suffered by the plane of polarization of linearly polarized radiation traveling through a magnetized thermal plasma. The presence of magnetic fields induces different indices of refraction (circular birefringence) for the two circularly polarized components (left versus right) into which linearly polarized radiation can be decomposed. The different propagation speeds of the two components cause a shift between them and consequently a rotation of the plane of polarization. Such a situation occurs for example when polarized radio galaxies are located behind or embedded in magnetized intergalactic media.

The rotation  $\Delta\Psi$  of the  $\mathbf{E}$ -vector position angle of linearly polarized radiation by a magnetized thermal plasma is given by:

$$\Delta\Psi_{[\text{rad}]} = \Psi(\lambda)_{[\text{rad}]} - \Psi_0_{[\text{rad}]} = \lambda_{[\text{m}^2]}^2 \text{RM}_{[\text{rad m}^{-2}]}, \quad (3.1)$$

where  $\Psi(\lambda)$  and  $\Psi_0$  are the  $\mathbf{E}$ -vector position angle of linearly polarized radiation observed at wavelength  $\lambda$  and the intrinsic angle, respectively. RM is the *rotation measure*. For a fully resolved foreground Faraday screen, the  $\lambda^2$  relation of Eq. 3.1 holds exactly at any observing  $\lambda$ .

The RM can be expressed as:

$$\text{RM}_{[\text{rad m}^{-2}]} = 812 \int_0^{L_{[\text{kpc}]}} n_e_{[\text{cm}^{-3}]} B_z_{[\mu\text{G}]} dz_{[\text{kpc}]}, \quad (3.2)$$

where  $n_e$  is the electron gas density in the thermal plasma,  $B_z$  is the magnetic field along the line-of-sight and  $L$  is the integration path. Therefore the study of the Faraday effect across polarized radio sources allows us to probe the magnetic field strength along the line-of-sight. As already mentioned in Sec. 1.2.2, the polarization angle can be described by using the observables Stokes parameters  $Q$  and  $U$  (Stokes 1852):

$$\Psi_\lambda = \frac{1}{2} \arctan\left(\frac{U_\lambda}{Q_\lambda}\right), \quad (3.3)$$

and it can be measured at several wavelengths by multi-frequency polarimetric radio observations. Then, RM across radio sources can be derived through a linear fit of the observed polarization angles as a function of  $\lambda^2$  (Eq. 3.1). As is well known, the determination of RM is complicated because of the  $n\pi$  ambiguities in the observed  $\Psi_{obs}$ . Removal of these ambiguities requires observations at least at three different wavelengths, well-spaced in  $\lambda^2$ . An alternative is the method of RM synthesis using simultaneous polarization observations over a contiguous frequency range, which will be available with the new generation of wideband correlators (Brentjens & Bruyn 2005).

### 3.2.1 Internal Faraday Rotation

Internal RM occurs if thermal plasma and synchrotron emitting particles are mixed. In this case, together with the rotation of the polarization plane we observe a decrease of the degree of polarization with increasing wavelength. Indeed, emission arising from different depths within a source suffers differential Faraday rotation reducing the degree of polarization. The functional form of the expected depolarization is in general related to the geometry of the source. The simplest modeling for such phenomenon is the optically-thin slab with uniform density and magnetic field located entirely within the source. In this case, the degree of polarization is given by (Burn 1966):

$$P_{Obs}(\lambda) = P_{Int} \left| \frac{\sin(\text{RM}'\lambda^2)}{\text{RM}'\lambda^2} \right|, \quad (3.4)$$

where  $\text{RM}'$  is the *internal Faraday* RM and is equal to  $\frac{1}{2}$  of that expected for a foreground slab screen of the same thermal density and field strength.

Even in the case of internal RM,  $\lambda^2$  rotation holds at sufficiently short wavelengths. In particular, in the case of the slab model the  $\lambda^2$  rotation is observed over 90 degrees then shows

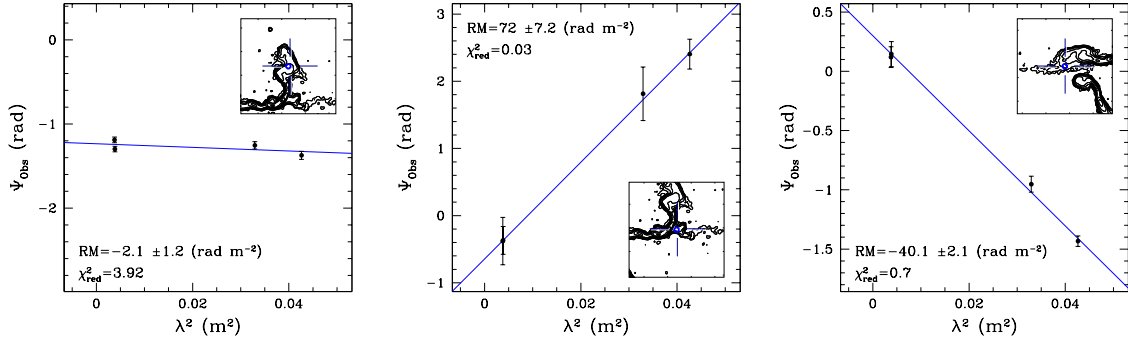


Figure 3.3: Examples of plots of the  $\mathbf{E}$ -vector position angle  $\Psi_{obs}$  against  $\lambda^2$  at different locations in PKS 2149-158. The exact position of the points in the sources is shown in the insets of the individual panels. The solid line represents the best fit of the  $\lambda^2$ -law to the data. Taken from Guidetti et al. (2008).

an abrupt  $90^\circ$  change. In more realistic geometries, it is the lack of significant deviations from  $\lambda^2$  rotation over  $\geq 45^\circ$  which allows us to exclude the presence of internal RM. So far, there is little evidence for RM occurring within the radio sources. This suggests that either that there is little thermal plasma in radio galaxies or that the internal fields are tangled on small scales.

Fig. 3.3 shows some examples of  $\lambda^2$  rotation of polarization positions angle for the extended radio galaxy PKS 2149-158 in A 2382 (Guidetti et al. 2008). This indicates a foreground origin for most of the RM across the source. The results from Faraday rotation and depolarization analyses presented in this thesis (Chapters 4, 5 and 6) are consistent with this scenario.

### 3.2.2 Foreground RM contributions

The RM occurring in front of radio galaxies can be thought of as the combined effect of multiple intervening magneto-ionic media along the line-of-sight:

1. thermal gas in a skin local to the source;
2. the interstellar and intergalactic media surrounding the radio source;
3. the same components associated with other galaxies located along the line-of-sight;
4. the ISM of our Galaxy and
5. the Earth's ionosphere.

A process able to form a magnetized local skin around the sources is the growth of Kelvin-Helmholtz instabilities at the surface of the radio lobes in contact with the surrounding medium (Bicknell, Cameron & Gingold 1990). These surface waves are expected to cause advection of the

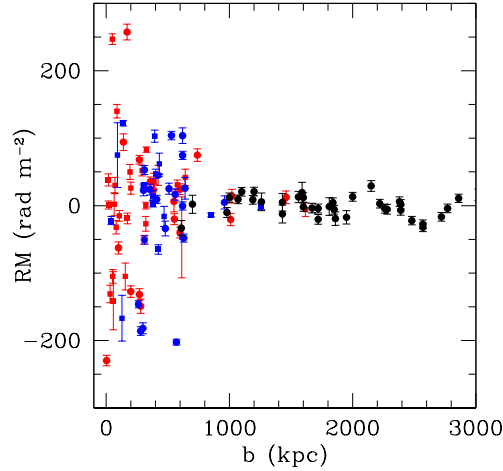


Figure 3.4: RM (corrected for the Galactic contribution) plotted as a function of source impact parameter in kpc for a sample of Abell clusters. The radio galaxies are split into clusters members (red), background (blue) sources and sources whose line-of-sight does not intercept the clusters X-ray emission (black). Taken from Clarke (2004).

magnetic field internal to the radio galaxies into the surrounding thermal gas with the consequent creation of a local Faraday screen. This model predicts magnetic field reversals and depolarization of emission from the surface layer.

Arguments in favour of an origin of the observed RM in the IGM of the radio source (item 2) are as follows.

- The detection of diffuse synchrotron emission in galaxy clusters (Sec. 3.1.1), implies that the IGM must be magnetized, so Faraday rotation is inevitable.
- The more distant radio lobe of a source shows higher depolarization than the approaching one (the Laing-Garrington effect; Laing 1988; Garrington et al. 1988). This is interpreted as resulting from a difference in the path length, and hence the Faraday depth, for the two lobes. Such an effect is not expected for a skin model (item 1) since in this case there is no reason for different path lengths between the two lobes.
- A statistical comparison of the RM's of point sources behind, embedded in and away from foreground galaxy clusters (Clarke 2004) has shown that those located behind clusters have a large RM dispersion (Fig. 3.4).
- Very large RM values are observed in cool core clusters.
- The dispersion in RM observed across individual sources is not correlated with Galactic coordinates, implying that the Galactic contribution is not dominant on small scales (although it will influence the mean).

- The presence of RM fluctuations on small angular scales also argues against a Galactic origin.

The latter two points suggest a generally small Galactic contribution, which nonetheless can become significant for radio sources located at low Galactic latitudes and when the Galactic magnetic field is almost aligned along the line-of-sight. To derive the properties of the RM local to the source, the Galactic contribution must be estimated and then properly removed; this is discussed more in detail in the next section. Finally, the RM due to the Earth's ionosphere at cm wavelengths is expected to be at most a few degrees (less at solar minimum) and is generally small compared with the fitting errors.

### 3.2.3 Galactic Faraday rotation

Our Galaxy has a magnetic field which can be thought as sum of an ordered component on kpc scale and a random one fluctuating on smaller scales. Both the two fields have mean strength of about  $2\mu\text{G}$  *e.g.* (Beck 1996).

Most extragalactic radio sources show Faraday rotation measures of the order of  $10\text{ rad m}^{-2}$  due to propagation of the emission through the magnetized interstellar medium of our Galaxy (Simard-Normandin et al. 1981). Diffuse and ionized Galactic feature in front of the sources, often associated with HII regions, represent another source of RM. At Galactic latitudes  $|b| \leq 5^\circ$ , radio sources can show Galactic RM's up to  $\pm 300\text{ rad m}^{-2}$ . The Galactic RM can be estimated by comparing the mean RM values of sources near the target, and assuming a smooth spatial variation of the Galactic field. Dineen & Coles (2005) have derived spherical harmonic models for the Galactic RM, by fitting to the RM values of large numbers of extragalactic sources.

There is evidence for linear gradients in Galactic RM on arcminute scales: Laing et al. (2006) found a gradient of  $0.025\text{ rad m}^{-2}\text{ arcsec}^{-1}$  along the jets of the radio galaxy NGC 315 ( $l = 124.6^\circ$ ,  $b = -32.5^\circ$ ). They argued that this gradient is almost certainly Galactic in origin, since the amplitude of the linear variation exceeds that of the small-scale fluctuations associated with NGC 315 (see also the case of 3C 449 presented in Chapter 4). Although the estimate of the Galactic RM might be highly uncertain in some cases, the angular size of radio galaxies are usually small enough so that it can be reasonably approximated as constant across them. In this case, the study of the RM local to the source is provided by statistical analysis techniques based on the use of the structure function (Sec. 3.7.1) which is a powerful tool independent of the mean level and (to first order) of structure on scales larger than the measurement area.

### 3.3 Depolarization

Faraday rotation generally leads to a decrease of the degree of polarization with increasing wavelength, or *depolarization* (DP) in different circumstances. We define  $DP_{\lambda_2}^{\lambda_1} = p(\lambda_1)/p(\lambda_2)$ , where  $p(\lambda)$  is the degree of polarization at a given wavelength  $\lambda$ . We adopt the conventional usage, in which *higher* depolarization corresponds to a *lower* value of DP.

Laing (1984) summarized the interpretation of polarization data. Faraday depolarization of radio emission from radio sources can occur in three principal ways:

1. thermal plasma is mixed with the synchrotron emitting material (*internal depolarization*, Sec. 3.2.1);
2. there are fluctuations of the foreground Faraday rotation across the beam (*beam depolarization*) and
3. the polarization angle varies across the finite band of the receiving system (*bandwidth depolarization*).

The last two terms are globally named as external depolarization and are due only to limitations of the instrumental capabilities.

The beam depolarization is due to the presence of unresolved inhomogeneities of thermal density and/or magnetic field which cause differential Faraday rotation of the polarization angle within the observing beam, and in turn a decrease of the observed degree of polarization with increasing wavelength. From a foreground Faraday screen with a small gradient of RM across the beam, it is still possible to observe  $\lambda^2$  rotation over a wide range of polarization angle. In this case, the wavelength dependence of the depolarization is expected to follow the Burn law (Burn 1966)

$$p(\lambda) = p(0) \exp(-k\lambda^4), \quad (3.5)$$

where  $p(0)$  is the intrinsic value of the degree of polarization and  $k=2|\nabla RM|^2\sigma^2$ , with  $\text{FWHM} = 2\sigma(2\ln 2)^{1/2}$ . Since  $k \propto |\nabla RM|^2$ , Eq. 3.5 clearly illustrates that higher RM gradients across the beam generate higher  $k$  values and hence higher depolarization. The variation of  $p$  with wavelength can potentially be used to estimate fluctuations of RM across the beam, which are below the resolution limit. We can determine the intrinsic polarization  $p(0)$  and the proportionality constant  $k$  by a linear fit to the logarithm of the observed fractional polarization as a function of  $\lambda^4$ .

To distinguish between the external and internal depolarization, sensitive polarization data at multiple frequencies and resolutions are needed. A decrease in depolarization with increasing

resolution, is expected from beam depolarization (Eq. 3.5). The external depolarization is correlated with the amount of the RM gradient, while that occurring internally is expected to be correlated with the geometry of the source and the RM values, in the sense that regions of small RM correspond to low depolarization.

Finally, bandwidth depolarization occurs when a significant rotation of the polarization angle of the radiation is produced across the finite bandwidth of the receiving system. The rotation of the polarization angle across the observing band is:

$$\Delta\Psi = -2RM\lambda^2\frac{\Delta\nu}{\nu} \quad (3.6)$$

where  $\Delta\nu$  is the bandwidth and  $\nu$  is the central frequency. This will reduce the observed polarization level by a quantity  $\sin(\Delta\Psi)/\Delta\Psi$  below that for monochromatic radiation. None of the observations used in this work are affected by significant bandwidth depolarization.

### 3.4 RM analysis

Observations of Faraday rotation variations across extended radio galaxies, once corrected for the contribution from our Galaxy (Sec 3.2.3), allow us to derive information about the integral of the density-weighted line-of-sight field component. The hot ( $T \simeq 10^7 - 10^8$  K) plasma emits in the X-ray energy band via thermal bremsstrahlung (Sec. 2.2.1). When high quality X-ray data for a radio-source environment are available, it is possible to infer the gas density distribution and therefore to separate it from that of the magnetic field (Eq. 3.2), subject to some assumptions about the relation of field strength and density. Consequently, uncertainties on these field estimates come from the assumed magnetic field topology and gas density profile.

Faraday rotation measure analysis has a number of advantages over other methods for estimating the magnetic field. RM studies can be carried out across radio galaxies hosted in less dense environments, allowing the study of magnetic fields in systems too sparse for radio halos to be detected. Moreover, the analysis of diffuse radio emission requires low-resolution and low-frequency observations, making it difficult to derive detailed information on the structure of the intergalactic magnetic field. These limitations do not affect RM maps, which can be produced even at sub-arcsec angular resolution at high frequencies ( $\geq 5$  GHz) as long as the radio galaxies are bright enough in polarized intensity.

A detailed study of intergalactic magnetic fields through the analysis of diffuse radio sources is also limited by the fact that these are affected by strong internal depolarization, intrinsically related to the nature of the diffuse synchrotron emission itself. In contrast, so far there is little evidence for internal depolarization in radio galaxies.

Faraday rotation studies also provide information about the direction of the magnetic field, being the positive (negative) when the magnetic field direction points towards (away from) the observer. One potential problem is that there could be numerous field reversals along the line of sight, which would be averaged out. The minimum field strength can be derived by assuming a constant magnetic field along the line-of-sight. Such estimates generally give fields of about  $1 \mu\text{G}$ .

Finally, through an extrapolation of Eq. 3.1 to zero wavelength, RM studies allow us to determine the intrinsic distribution of the projected magnetic field of radio galaxies, and its relation to the environment.

### 3.5 The magnetic field profile

In order to estimate the magnetic field strength, the equipartition and IC analyses assume a constant magnetic field through the whole halo or relic volume. This assumption is an oversimplified picture as is clear from a simple energy-balance argument: if the field was uniform on Mpc scales, the magnetic pressure would exceed the thermal pressure in the outskirts of the clusters. Jaffe (1980) first suggested that the magnetic field distribution in a cluster might be similar to those of the thermal gas density and the volume density of massive galaxies and therefore would decline with the cluster radius. Observations, analytical models and MHD simulations of galaxy clusters all suggest that the magnetic field intensity should scale with the thermal gas density (*e.g.* Brunetti et al. 2001; Dolag 2006; Dolag, Bykov & Diaferio 2008; Guidetti et al. 2008). Govoni et al. (2001a) found a two-point spatial correlation between the X-ray and radio halo surface brightness in the galaxy clusters of their sample suggesting that the thermal and non-thermal components might have similar radial scalings. Another indication of a radial decrease of the magnetic field strength comes from the radial steepening observed in a few radio halos (Coma, A665, A2163, Giovannini et al. 1993; Feretti et al. 2004a) which are expected in the modeling of radio halos formation including such a radial decrease.

Multiple works based on RM simulations (*e.g.* Murgia et al. 2004; Govoni et al. 2006; Guidetti et al. 2008; Laing et al. 2008; Kuchar & Enßlin 2009; Bonafede et al. 2010) have considered a radial field-strength variation of the form:

$$\langle B^2(r) \rangle^{1/2} = B_0 \left[ \frac{n_e(r)}{n_0} \right]^\eta \quad (3.7)$$

Here,  $B_0$  is the rms magnetic field strength at the group/cluster centre and  $n_e(r)$  is the thermal electron gas density. The results from the simulations are in favour of  $\eta$  in the range 0.5-1. This functional form is consistent with other observations, analytical models and numerical simulations. In particular,  $\eta = 2/3$  corresponds to flux-freezing and  $\eta = 1/2$  to equipartition between thermal

and magnetic energy. Dolag et al. (2001, 2006) found  $\eta \approx 1$  from the correlation between the observed rms RM and X-ray surface brightness in galaxy groups and clusters and showed that this is consistent with the results of MHD simulations.

### 3.6 Tangled magnetic field

Most of the published RM images of radio galaxies located in different environments show random structures with patches of different size, ranging from a few kpc up to tens of kpc (Fig. 3.5). From these RM distributions it is clear that the magnetic fields are not regularly ordered on cluster (Mpc) scales, but highly turbulent. It is indeed likely that anisotropies in the magnetic field would reflect themselves in the RM images, since the projection connecting field and RM conserves anisotropy.

Faraday rotation by tangled intergalactic magnetic fields was considered in several early theoretical papers (*e.g.* Lawler & Dennison 1982; Tribble 1991; Felten 1996). The simplest RM modeling invokes a Faraday screen in which the magnetic field fluctuates on a single scale  $\Lambda_c$ . The screen can be thought as made of cells of constant size and magnetic field strength, but random magnetic field direction. The RM from such a screen will be produced by a random walk along the line-of-sight. Because of the large number of cells, the RM distribution is expected to be described by a Gaussian function with zero mean and dispersion  $\sigma_{\text{RM}}$  given by:

$$\sigma_{\text{RM}}^2 = \langle \text{RM}^2 \rangle = 812^2 \Lambda_c \int (n_e B_z)^2 dz . \quad (3.8)$$

Considering a thermal density distribution which follows a  $\beta$ -profile (Eq. 2.3), and an isotropic field (so that  $B = \sqrt{3}B_z$ ), Eq. 3.8 can be integrated analytically and gives (Felten 1996)

$$\sigma_{\text{RM}}(r_{\perp}) = \frac{K B n_0 r_c^{1/2} \Lambda_c^{1/2}}{(1 + \frac{r_{\perp}}{r_c})^{(6\beta-1)/4}} \sqrt{\Gamma(3\beta - 0.5)\Gamma(3\beta)} \quad (3.9)$$

where  $\Lambda_c$  is the cell size,  $r_{\perp}$  is the projected distance of from the cluster center,  $\Gamma$  is the Gamma function, and  $K$  is a factor which depends on the location of the radio source along the line-of-sight (*e.g.* Carilli & Taylor 2002). The central field strength can be estimated by using Eq. 3.9:  $\sigma_{\text{RM}}(r_{\perp})$  can be measured from spatially resolved RM images and at a first level of approximation  $\Lambda_c$  can be assumed to be equal to the coherence length, deduced by-eye, of the RM map. It must however borne in mind that the magnetic fields in this model are not divergence-free (Enßlin & Vogt 2003).

This method has been applied to both statistical samples (Clarke 2004) and to single objects, *e.g.* Hydra A (Taylor & Perley 1993) 1993), A 119 (Feretti et al. 1999b), 3C 295 (Allen et al. 2001), A 514 (Govoni et al. 2001a), 3C 129 Taylor2001, A 400 and A 2634 (Eilek & Owen 2002). The magnetic field strengths deduced from these analyses are in the range 4-20  $\mu\text{G}$ , assuming  $\Lambda_c$

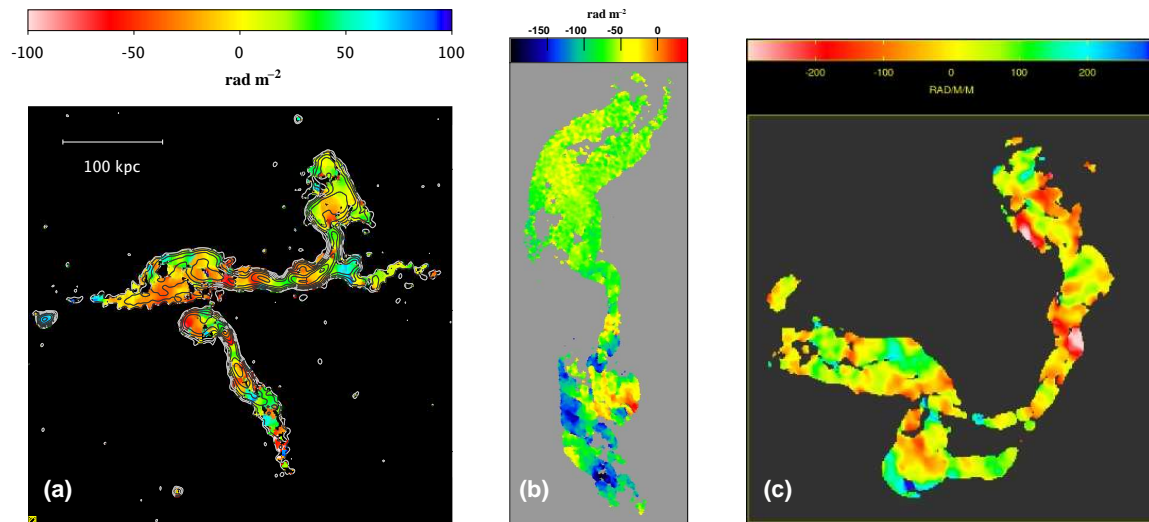


Figure 3.5: RM images of radio galaxies with tails: PKS 2149-158 and PKS 2149-158b **(a)**, 3C 31 **(b)**, and 3C 75 **(c)**. Figures respectively taken from: Guidetti et al. (2008), Laing et al. (2008), Eilek & Owen (2002).

of about 10 kpc, with the highest values found for radio galaxies in cooling-core clusters. None of these magnetic fields are thought to be dynamically important, since they provide negligible pressure compared with that of the thermal component.

Although RM images in general are not expected to show perfectly Gaussian distributions because of the partial sampling of large spatial scales, the Gaussian function is found to be a good representation for many RM distributions, supporting the scenario of a tangled and isotropic magnetic field component along the line-of-sight. However, in contrast with this scenario the majority of the RM distributions show non-zero means  $\langle \text{RM} \rangle$  if averaged over areas of size comparable with that of the radio source, even after removing the Galactic contribution. These  $\langle \text{RM} \rangle$ 's are thought to be due to large-scale magnetic field structure, whose fluctuations occur on scales larger than those producing the RM dispersion. Therefore, the magnetic field cannot be tangled only on a single scale, but it must have fluctuations over a wide range of spatial scales: small-scale components are necessary to produce the smallest structures observed in the RM images (Fig. 3.5) and structures on larger scales are needed to account for the non-zero RM mean. For this reason, the investigation of the magnetic field power spectrum has been object of many recent papers. Several studies (Enßlin & Vogt 2003; Enßlin & Vogt 2005; Murgia et al. 2004; Govoni et al. 2006; Guidetti et al. 2008; Laing et al. 2008; Kuchar & Enßlin 2009) have shown that detailed RM images of radio galaxies can be used to infer not only the strength of the cluster magnetic field, but also its power spectrum. All of these studies agree that random RM structures can be accurately reproduced if the magnetic field is isotropic and randomly variable with fluctuations on a wide range of spatial scales.

### 3.7 The magnetic field power spectrum

In order to derive the three-dimensional magnetic field power spectrum from the analysis of the RM images, it is necessary to assume statistical isotropy for the field, since only the component of the magnetic field along the line-of-sight contributes to the observed RM. It is important to underline that the turbulence in the intergalactic medium can be locally inhomogeneous, as expected in the MHD regime, particularly regarding small scales fluctuations. However, it is likely that the local anisotropies are isotropically distributed, so that whenever the volume sampled is large enough these anisotropies tend to average out along any line-of-sight. Therefore, the assumption of magnetic-field isotropy must be taken in the sense that the field has no preferred direction when averaged over a sufficiently large volume.

If the intergalactic magnetic field can be approximated as Gaussian random variable, then its spatial distribution can be described by the power spectrum of the component along the line-of-sight, or its Fourier transform (the autocorrelation function, Wiener-Khinchin Theorem). For intergalactic magnetic fields, these assumptions are justified by:

- the patchiness of most of the RM images across radio galaxies, consistent with isotropic random magnetic fields
- the fact that a sum of a large number of independent and identically-distributed random variables (*i.e.*, the field components) approaches a Gaussian distribution (Central Limit Theorem, Rice et al. 1955).

Following Laing et al. (2008), the three-dimensional magnetic field power spectrum can be expressed as  $\hat{\mathbf{w}}(f)$  such that  $\hat{\mathbf{w}}(f)df_xdf_ydf_z$  is the power in a volume  $df_xdf_ydf_z$  of frequency space, with  $\mathbf{f}$  (magnitude  $f$ ) representing a vector in the frequency space with the  $f_z$  coordinate along the line-of-sight. The other interesting property of the magnetic field is its auto-correlation length which in term of  $\hat{\mathbf{w}}(f)$  is given by:

$$\Lambda_B = \frac{1}{4} \frac{\int_0^\infty \hat{\mathbf{w}}(f) f df}{\int_0^\infty \hat{\mathbf{w}}(f) f^2 df} \quad (3.10)$$

The constant  $\frac{1}{4}$  differs by a factor of  $4\pi$  from that in the equivalent expressions in Enßlin & Vogt (2003, equation 39): a factor of  $2\pi$  is due to the use of spatial frequency  $f$  rather than wave-number  $k$  ( $k = 2\pi f$ ) and a factor of 2 is due to the different integration limits.<sup>1</sup>

Enßlin & Vogt (2003, 2005) have shown that typically  $\Lambda_{RM} > \Lambda_B$  since the former gives more weight to the largest spatial scales. In the literature, these scales have often been assumed to

<sup>1</sup>Enßlin & Vogt (2003) integrate from  $-\infty$  to  $+\infty$  in  $r$  and  $r_\perp$ .

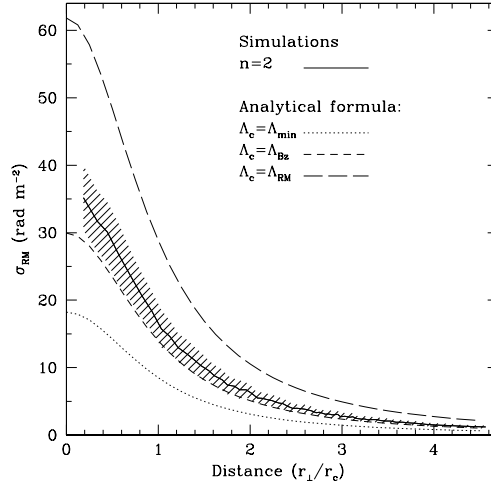


Figure 3.6: Comparison of the  $\sigma_{RM}$  profiles obtained from simulations of a Gaussian and random magnetic field (solid line) and the expectations from the analytical model of Eq. 3.9 by assuming three different  $\Lambda_c$ :  $\Lambda_{min}=6$  kpc,  $\Lambda_B = \Lambda_{Bz} = 16$  kpc,  $\Lambda_{RM}=69$  kpc (dashed and dotted lines). The best agreement is given by  $\Lambda_c = \Lambda_B$ . The simulated magnetic field power spectrum has slope  $n = 2$ . The source is assumed to be halfway through the cluster and the magnetic field strength and gas density have the same radial profiles in both the simulations and the analytical formulation. Taken from Murgia et al. (2004).

be identical and the approximation  $\Lambda_c = \Lambda_{RM}$  has been used in the single-scale model (Eq. 3.9), leading to underestimates of the magnetic field strength. Murgia et al. (2004) have shown that  $\Lambda_B$  is a good approximation for  $\Lambda_c$  in Eq. 3.9 and therefore that this length must be used to compare the analytical predictions from the single-scale model with RM analyses assuming a multi-scale field (Fig. 3.6). Since  $\Lambda_B$  depends on the underlying magnetic field power spectrum (Eq. 3.10), the latter must be estimated first.

Multiple different estimators of spatial statistics of the RM distributions such as structure and auto-correlation functions or a multi-scale statistic have been used to derive the field strength, its relation to the gas density and its power spectrum (Murgia et al. 2004; Govoni et al. 2006; Guidetti et al. 2008; Laing et al. 2008). The technique of Bayesian maximum likelihood has also been used for this purpose (Enßlin & Vogt 2005; Kuchar & Enßlin 2009). These studies have shown that the magnetic field power spectrum is well approximated by a power-law

$$\widehat{w}(f_{\perp}) \propto f_{\perp}^{-q} \quad (3.11)$$

over a range of spatial frequencies, corresponding respectively to the outer and inner fluctuation scales of the magnetic field<sup>2</sup>. Although the theory of intergalactic magnetic field fluctuations is still debated, a power-law functional form is expected if the turbulence is mostly hydrodynamic,

<sup>2</sup>Spatial frequency and scale are related in the sense:  $f = 1/\Lambda$

or in the

The analysis of Vogt & Enßlin (2003, 2005) suggests that the magnetic field power spectrum has a power law form with the slope appropriate for Kolmogorov turbulence and that the auto-correlation length of the magnetic field fluctuations is a few kpc. Also Adaptive Mesh Refinement (AMR) simulations by Brüggén et al. (2005) are consistent with the Kolmogorov slope. However, the Kolmogorov theory (1941), which assumes homogeneous and incompressible turbulence, cannot be rigorously applied because of the evidence in the intergalactic medium of gas radial scaling and in some cases of shells of compressed gas. Moreover, the deduction of a Kolmogorov slope could be premature: there is a degeneracy between the slope and the outer scale, which is difficult to resolve with current Faraday rotation data (Murgia et al. 2004; Guidetti et al. 2008; Laing et al. 2008). Indeed, Murgia et al. (2004) pointed out that shallower magnetic field power spectra are possible if the magnetic field fluctuations have structure on scales of several tens of kpc. Guidetti et al. (2008) showed that a power-law power spectrum with a Kolmogorov slope, and an abrupt long-wavelength cut-off at 35 kpc gave a very good fit to their Faraday rotation and depolarization data for the radio galaxies in A 2382, although a shallower slope extending to longer wavelengths was not ruled out.

In the next section I will describe the method used in this thesis to derive the magnetic power spectrum from our RM maps.

### 3.7.1 Magnetic field power spectrum from two-dimensional analysis

The relation between the magnetic field power spectrum and the observed RM distribution is in general quite complicated, depending on the fluctuations in the thermal gas density, the geometry of the source and the surrounding medium, and the effects of incomplete sampling. In order to derive the magnetic field power spectrum, one must make the following assumptions (*e.g.* Guidetti et al. 2008; Laing et al. 2008):

1. The observed Faraday rotation is due entirely to a foreground ionized medium. This can be addressed by lack of deviation from  $\lambda^2$  rotation over a wide range of polarization position angle and the lack of associated depolarization (Sec 3.2.1)
2. The magnetic field is an isotropic, Gaussian random variable
3. The form of the magnetic field power spectrum is independent of position
4. The magnetic field is distributed throughout the Faraday-rotating medium, whose density is a smooth, spherically symmetric function.

5. The amplitude of  $\widehat{w}(f)$  is spatially variable, but is a function only of the thermal electron density.

These assumptions guarantee that the spatial distribution of the magnetic field can be described entirely by its power spectrum  $\widehat{w}(f)$  and that for a medium of constant depth and density, the power spectra of magnetic field and RM are proportional (Enßlin & Vogt 2003).

If the RM fluctuations are isotropic, the RM power spectrum  $\widehat{C}(f_{\perp})$  is the Hankel transform of the auto-correlation function  $C(r_{\perp})$ , defined as

$$C(r_{\perp}) = \langle \text{RM}(\mathbf{r}_{\perp} + \mathbf{r}'_{\perp}) \text{RM}(\mathbf{r}'_{\perp}) \rangle, \quad (3.12)$$

where  $\mathbf{r}_{\perp}$  and  $\mathbf{r}'_{\perp}$  are vectors in the plane of the sky and  $\langle \rangle$  is an average over  $\mathbf{r}'_{\perp}$ . One could think of obtaining the magnetic field power spectrum directly by Fourier transforming Eq. 3.12. In reality, the observations are affected first by the effects of convolution with the beam, which modify the spatial statistics of RM, and secondly, by the limited size and irregular shape of the sampling region (the region of the source over which the RM has been derived), which results in a complicated window function (Enßlin & Vogt 2003) for computational work in the frequency space. Finally, most of the useful properties of the auto-correlation function are related to the outer scale at  $C(r_{\perp})$  approaches the zero-level, which in most cases is uncertain in the presence of large-scale fluctuations.

The alternative strategy proposed by Laing et al. (2008), and applied in the work of this thesis, first estimates the power spectrum of the RM,  $\widehat{C}(\mathbf{f}_{\perp})$ , where  $\widehat{C}(\mathbf{f}_{\perp})df_xdf_y$  is the power in the area  $df_xdf_y$ , and derives that of the three-dimensional magnetic-field  $\widehat{w}(\mathbf{f})$ . Laing et al. (2008) demonstrated a procedure that takes into account the convolution effects and minimises the effects of uncertainties in the zero-level. In particular, they showed that

1. in the short-wavelength limit (meaning that changes in Faraday rotation across the beam are adequately represented as a linear gradient), the measured RM distribution is closely approximated by the convolution of the true RM distribution with the observing beam
2. the *structure function* is a powerful and reliable statistical tool to quantify the two dimensional fluctuations of RM, given that it is independent of the zero-level and structure on scales larger than the area under investigation.

The structure function is defined by

$$S(r_{\perp}) = \langle [\text{RM}(\mathbf{r}_{\perp} + \mathbf{r}'_{\perp}) - \text{RM}(\mathbf{r}'_{\perp})]^2 \rangle \quad (3.13)$$

(Simonetti, Cordes & Spangler 1984; Minter & Spangler 1996). It is related to the autocorrelation function  $C(r_{\perp})$  for a sufficiently large averaging region by  $S(r_{\perp}) = 2[C(r_{\perp}) - C(0)]$ .

Laing et al. (2008) also derived the effects of convolution with the observing beam on the observed structure function. For the special case of a power-law power spectrum (their Eq. B2), they showed that the observed structure function after convolution can be heavily modified even at separations up to a few times the FWHM of the observing beam. Fig. 3.7 illustrates the effects of the convolution in two different power-law power spectra and corresponding structure function. After convolution the two power spectra are indistinguishable. This effect must be taken into account when comparing observed and predicted structure functions. However, because the suppression of power on high spatial frequencies due to the convolution, this analysis only constrains the power spectrum of the fluctuations on scales larger than the beam-width. Complementary information can be derived from numerical simulations of depolarization with fine spatial sampling (Laing et al. 2008; Guidetti et al. 2008) which constrain fluctuations of RM below the resolution limit. indeed, the use of the structure function together with the Burn law  $k$  represents a powerful technique to investigate the RM power spectrum over a wide range of spatial scales (Laing et al. 2008).

In this thesis we have derived very detailed images of Faraday rotation and depolarization across radio galaxies. The next Chapters will show that all of our observations are consistent with pure foreground Faraday rotation. Where the RM structures can be reasonably approximated as isotropic, the statistics of the magnetic-field fluctuations have been quantified by deriving rotation measure structure functions, fitted using models derived from theoretical power spectra. The minimum scale of the magnetic field variations have been derived from depolarization measurements. However, I will also show that not all Faraday rotation maps are consistent with an isotropic magnetic field. This forms the most important part of my thesis and describes an unexpected phenomenon in the RM world.

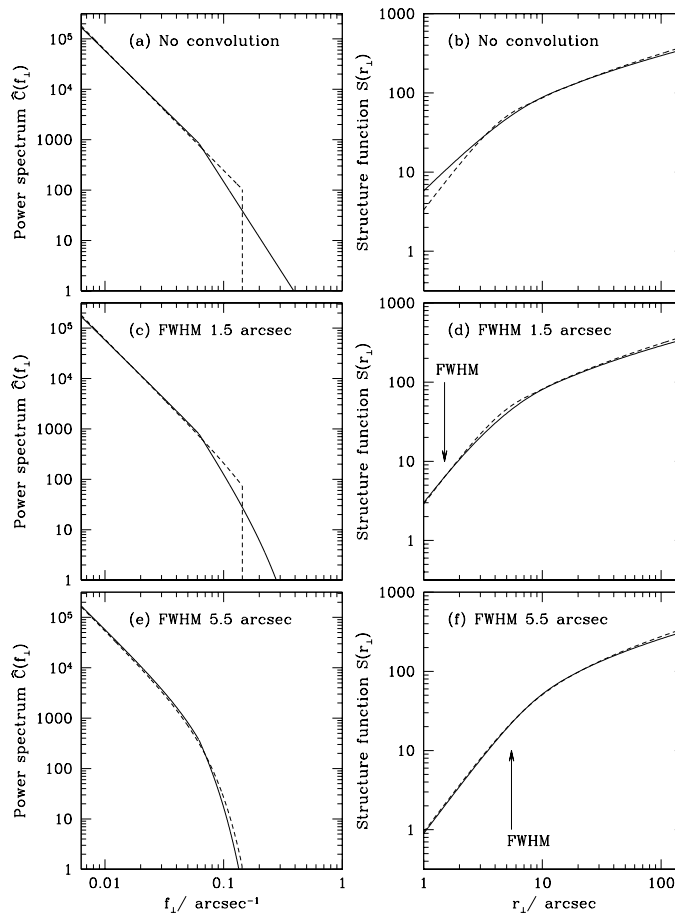


Figure 3.7: **(a), (c), (e)**: the two model RM power spectra discussed for the radio galaxy 3C 31 in Laing et al. (2008). Solid line, broken power-law power spectrum with indices  $q_{\text{high}} = 11/3$ ,  $q_{\text{low}} = 2.32$  and a break frequency of  $0.062 \text{ arcsec}^{-1}$  (their equation 8). Dashed line: power-law power spectrum with  $q = 2.39$  and a high-frequency cut-off at  $f_{\text{max}} = 0.144 \text{ arcsec}^{-1}$  (their equation 9). **(b), (d), (f)**: structure functions computed for the power spectra in panels (a), (c) and (d), with the same line codes. (a) and (b) no convolution; (c) and (d) 1.5 arcsec FWHM convolving beam; (e) and (f) 5.5 arcsec FWHM convolving beam.



## Chapter 4

# Structure of the magneto-ionic medium around the Fanaroff-Riley Class I radio galaxy 3C 449 \*

**M**agnetic fields associated with galaxy groups deserve to be investigated in more detail, since their environments are more representative than those of rich clusters. Moreover, observations, analytical models and MHD simulations of galaxy clusters all suggest that the magnetic-field intensity should scale with the thermal gas density (*e.g.* Brunetti et al. 2001; Dolag 2006; Guidetti et al. 2008; Bonafede et al. 2010). A key question is whether the relation between magnetic field strength and density in galaxy groups is a continuation of this trend. This Chapter presents a detailed analysis of Faraday rotation in 3C 449, a bright, extended radio source hosted by the central galaxy of a nearby group. With the aim of shedding new light on the environment around this source, I derive the statistical properties of the magnetic field from observations of Faraday rotation, following the method developed by Murgia et al. (2004). I use numerical simulations to predict the Faraday rotation for different strengths and power spectra of the magnetic field.

With the assumed cosmology, at the distance of 3C 449 1 arcsec corresponds to 0.342 kpc.

### 4.1 The radio source 3C 449: general properties

I image and model the Faraday rotation distribution across the giant FR I radio source 3C 449, whose environment is very similar to that of 3C 31. The optical counterpart of 3C 449, UGC 12064, is a dumb-bell galaxy and is the most prominent member of the group of galaxies

---

\*Guidetti et al. 2010, A&A, 514, 50

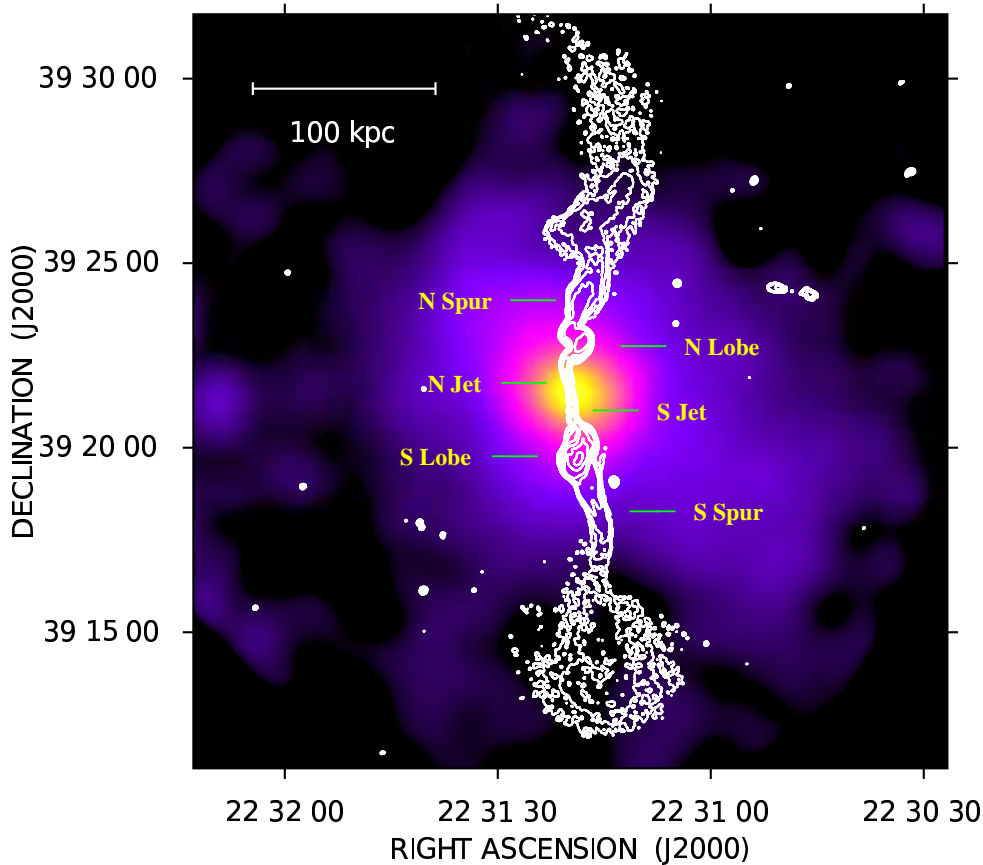


Figure 4.1: Radio contours of 3C 449 at 1.365 GHz superposed on the XMM-Newton X-ray image (courtesy of J. Croston, Croston et al. 2003). The radio contours start at  $3\sigma_l$  and increase by factors of 2. The restoring beam is 5.5 arcsec FWHM. The main regions of 3C 449 discussed in the text are labelled.

2231.2+3732 (Zwicky & Kowal 1968) The source is relatively nearby ( $z=0.017085$ , RC3.9, de Vaucouleurs et al. 1991) and quite extended, both in angular (30 arcmin) and linear size, so it is an ideal target for an analysis of the Faraday rotation distribution: detailed images can be constructed that can serve as the basis of an accurate study of magnetic field power spectra.

The source 3C 449 was one of the first radio galaxies studied in detail with the VLA (Perley, Willis & Scott 1979). High- and low-resolution radio data already exist and the source has been mapped at many frequencies. The radio emission of 3C 449 (Fig. 4.1) is elongated in the N–S direction and is characterized by long, two-sided jets with a striking mirror symmetry close to the nucleus. The jets terminate in well-defined inner lobes, which fade into well polarized tails (spurs), of which the southern one is more collimated. The spurs in turn expand to form diffuse outer lobes.

The brightness ratio of the radio jets is very nearly 1, implying that they are close to the plane of the sky if they are intrinsically symmetrical and have relativistic flow velocities similar to those

derived for other FR I jets (Perley, Willis & Scott 1979; Feretti et al. 1999a; Laing & Bridle 2002a). Therefore the jets are assumed to lie exactly in the plane of the sky, which simplifies the geometry of the Faraday-rotating medium.

Hot gas associated with the galaxy was detected on both the group and the galactic scales by X-ray imaging (Hardcastle, Worrall & Birkinshaw, 1998; Croston et al. 2003). These observations revealed deficits in the X-ray surface brightness at the positions of the outer radio lobes, suggesting interactions with the surrounding material. Figure 4.1 shows radio contours at 1.365 GHz overlaid on the X-ray emission as observed by the XMM-Newton satellite (Croston et al. 2003). The X-ray radial surface brightness profile of 3C 449 derived from these data can be fitted with the sum of a point-source convolved with the instrumental response and a  $\beta$  model (Cavaliere & Fusco-Femiano 1976):

$$n_e(r) = n_0(1 + r^2/r_c^2)^{-\frac{3}{2}\beta}, \quad (4.1)$$

where  $r$ ,  $r_c$  and  $n_0$  are the distance from the group X-ray center, the group core radius, and the central electron density, respectively. Croston et al. (2008) found a best fitting model with  $\beta = 0.42 \pm 0.05$ ,  $r_c = 57.1$  arcsec and  $n_0 = 3.7 \times 10^{-3} \text{cm}^{-3}$ . In these calculations, I assumed that the group gas density is described by the model of Croston et al. (2008). The X-ray depressions noted by Croston et al. (2003) are at distances larger than those at which it is possible to detect linear polarization, and there is no direct evidence of smaller cavities close to the nucleus. I therefore neglect any departures from the spherically-symmetrical density model, noting that this approximation may become increasingly inaccurate where the source widens (i.e. in the inner lobes and spurs).

The source 3C 449 resembles 3C 31 in environment and in radio morphology: both sources are associated with the central members of groups of galaxies, and their redshifts are very similar. The nearest neighbours are at a projected distances of about 30 kpc in both cases. Both radio sources have large angular extents, bending jets and long, narrow tails with low surface brightnesses and steep spectra, although 3C 31 appears much more distorted on large scales. There is one significant difference: the inner jets of 3C 31 are thought to be inclined by  $\approx 50^\circ$  to the line-of-sight (Laing & Bridle 2002a), whereas those in 3C 449 are likely to be close to the plane of the sky (Feretti et al. 1999a). It is therefore expected that the magnetized foreground medium will be very similar in the two sources, but that the geometry will be significantly different, leading to a much more symmetrical distribution of Faraday rotation in 3C 449 compared with that observed in 3C 31 by Laing et al. (2008).

## 4.2 Total intensity and polarization properties

The VLA observations and their reduction were presented by Feretti et al. (1999a). The high quality of these data make this source suited for a very detailed analysis of the statistics of the Faraday rotation.

I produced total intensity ( $I$ ) and polarization ( $Q$  and  $U$ ) images at frequencies in the range 1.365 – 8.385 GHz from the combined, self-calibrated u-v datasets described by Feretti et al. (1999a). The center frequencies and bandwidths are listed in Table 4.1. Each frequency channel was imaged separately, except for those at 8.245 and 8.445 GHz, which were averaged. The analysis below confirms that these frequency-bandwidth combinations lead to negligible Faraday rotation across the channels, as already noted by Feretti et al. (1999a). All of the datasets were imaged with Gaussian tapering in the u-v plane to give resolutions of 1.25 arcsec and 5.5 arcsec FWHM, and restored with circular Gaussian beams. The first angular resolution is the highest possible at all frequencies and provides good signal-to-noise for the radio emission within 150 arcsec ( $\approx 50$  kpc) of the radio core (the well defined radio jets and the inner lobes), while minimizing beam depolarization. The lower resolution of 5.5 arcsec allows imaging of the extended emission as far as 300 arcsec ( $\approx 100$  kpc) from the core at frequencies from 1.365 – 4.985 GHz (the 8.385-GHz dataset does not have adequate sensitivity to image the outer parts of the source). Therefore it is possible to study the structure of the magnetic field in the spur regions, which lie well outside the bulk of the X-ray emitting gas. Noise levels for both sets of images are given in Table 4.1. Note that the maximum scales of structure, which can be imaged reliably with the VLA at 8.4 and 5 GHz are  $\approx 180$  and  $\approx 300$  arcsec, respectively (Ulvestad, Perley & Chandler 2009). For this reason, I only use the Stokes  $I$  images for quantitative analysis within half these distances of the core. The  $Q$  and  $U$  images have much less structure on these large scales and are reliable to distances of  $\pm 150$  arcsec at 8.4 GHz and  $\pm 300$  arcsec at 5 GHz, limited by sensitivity rather than systematic errors due to missing flux as in the case of the  $I$  image.

Images of polarized intensity  $P = (Q^2 + U^2)^{1/2}$  (corrected for Ricean bias, following Wardle & Kronberg (1974), fractional polarization  $p = P/I$  and polarization angle  $\Psi = (1/2) \arctan(U/Q)$  were derived from the  $I$ ,  $Q$ , and  $U$  images.

All of the polarization images ( $P$ ,  $p$ ,  $\Psi$ ) at a given frequency were blanked where the rms error in  $\Psi > 10^\circ$  at any frequency. I then calculated the scalar mean degree of polarization  $\langle p \rangle$  for each frequency and resolution; the results are listed in Table 4.1. The values of  $\langle p \rangle$  are higher at 5.5 arcsec resolution than at 1.25 arcsec because of the contribution of the extended and highly polarized emission, which is not seen at the higher resolution. At 1.25 arcsec, where the beam depolarization is minimized, the mean fractional polarization shows a steady increase

Table 4.1: Parameters of the total intensity and polarization images.

$\nu$ (GHz)	Bandwidth (MHz)	1.25 arcsec			5.5 arcsec		
		$\sigma_I$ (mJy/beam)	$\sigma_{QU}$ (mJy/beam)	$\langle p \rangle$	$\sigma_I$ (mJy/beam)	$\sigma_{QU}$ (mJy/beam)	$\langle p \rangle$
1.365	12.5	0.037	0.030	0.24	0.018	0.014	0.26
1.445	12.5	0.021	0.020	0.25	0.020	0.011	0.27
1.465	12.5	0.048	0.049	0.25	0.019	0.013	0.25
1.485	12.5	0.035	0.027	0.21	0.014	0.010	0.26
4.685	50.0	0.017	0.017	0.32	0.017	0.013	0.37
4.985	50.0	0.018	0.017	0.33	0.017	0.016	0.39
8.385	100.0	0.014	0.011	0.31	0.015	0.013	–

Col. 1: Observation frequency. Col. 2: Bandwidth (note that the images at 8.385 GHz are derived from the average of two frequency channels, both with bandwidths of 50 MHz, centered on 8.285 and 8.485 GHz); Cols. 3, 4 : rms noise levels in total intensity ( $\sigma_I$ ) and linear polarization ( $\sigma_{QU}$ , the average of  $\sigma_Q$  and  $\sigma_U$ ) at 1.25 arcsec FWHM resolution; Col. 5: mean degree of polarization at 1.25 arcsec; Col. 6, 7: rms noise levels for the 5.5 arcsec images; Col. 8: mean degree of polarization at 5.5 arcsec. I estimate that the uncertainty in the degree of polarization, which is dominated by systematic deconvolution errors on the  $I$  images, is  $\approx 0.02$  at each frequency.

from 1.365 to 4.685 GHz, where it reaches an average value of 0.32 and then remains roughly constant at higher frequencies, suggesting that the depolarization between 4.685 and 8.385 GHz is insignificant.

### 4.3 The Faraday rotation in 3C 449

#### 4.3.1 Rotation measure images

I produced images of RM and its associated rms error by weighted least-squares fitting to the polarization angle maps (Eq. 3.1) with resolutions of 1.25 arcsec and 5.5 arcsec (Fig. 4.2a and b) using a version of the `task` modified by G. B. Taylor. The 1.25 arcsec-RM map was made by combining the maps of the polarization  $\mathbf{E}$ -vector ( $\Psi$ ) at all the seven available frequencies, so that the sampling of  $\lambda^2$  is very good. The RM map was calculated with a weighted least-squares fit at pixels with polarization angle uncertainties  $< 10^\circ$  at all frequencies. It is essentially the same as the RM image of Feretti et al. (1999a), but with more stringent blanking. The average fitting error is  $\approx 1.4 \text{ rad m}^{-2}$  and is almost constant over the whole RM image. The image of RM at 5.5 arcsec resolution was produced using the polarization position angles at the six frequencies between 1.365 and 4.985 GHz (see Table 4.1) with the same blanking criterion as at higher resolution.

Patches with different size are apparent in the 1.25 arcsec resolution map, with fluctuations down to scales of a few kpc. The RM values range from about  $-220 \text{ rad m}^{-2}$  up to  $-90 \text{ rad m}^{-2}$ ,

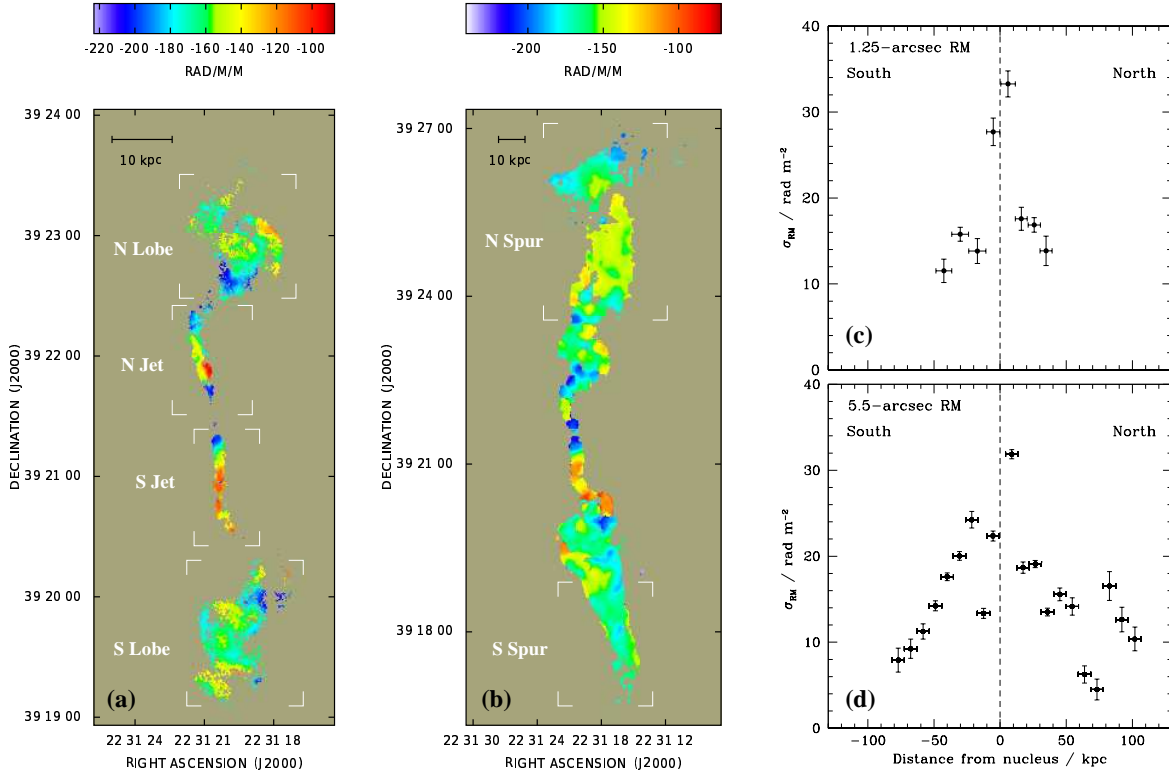


Figure 4.2: **(a)**: Image of the rotation measure of 3C 449 at a resolution of 1.25 arcsec FWHM, computed at the seven frequencies between 1.365 and 8.385 GHz. **(b)**: Image of the rotation measure of 3C 449 at a resolution of 5.5 arcsec FWHM, computed at the six frequencies between 1.365 and 4.985 GHz. In both of the RM images, the sub-regions used for the two-dimensional analysis of Sec. 4.5 are labelled. **(c)** and **(d)**: profiles of  $\sigma_{RM}$  as a function of the projected distance from the radio source center. The points represent the values of  $\sigma_{RM}$  evaluated in boxes as described in the text. The horizontal and vertical bars represent the bin widths and the rms on the mean expected from fitting errors, respectively. Positive distances are in the direction of the north jet and the vertical dashed lines show the position of the nucleus.

dominated by the Galactic contribution (see Sec. 4.3.2). The RM distribution peaks at  $-161.7 \text{ rad m}^{-2}$ , with a rms dispersion  $\sigma_{RM} = 19.7 \text{ rad m}^{-2}$ . Note that I have not corrected the values of  $\sigma_{RM}$  for the fitting error  $\sigma_{RM_{fit}}$ . A first order correction would be  $\sigma_{RM_{true}} = (\sigma_{RM}^2 - \sigma_{RM_{fit}}^2)^{1/2}$ . Given the low value for  $\sigma_{RM_{fit}}$ , the effect of this correction would be very small.

As was noted by Feretti et al. (1999a), the RM distribution in the inner jets is highly symmetric about the core with  $RM \approx -197 \text{ rad m}^{-2}$  at distances  $\lesssim 15 \text{ arcsec}$ . The symmetry of the RM distribution in the jets is broken at larger distances from the core: while the RM structure in the southern jet is homogeneous, with values around  $-130 \text{ rad m}^{-2}$ , fluctuations on scales of  $\approx 10 \text{ arcsec}$  ( $\approx 3 \text{ kpc}$ ) around a  $\langle RM \rangle$  of  $-160 \text{ rad m}^{-2}$  are present in the northern jet. The lobes are characterized by similar patchy RM structures with mean values  $\langle RM \rangle \approx -164 \text{ rad m}^{-2}$  and

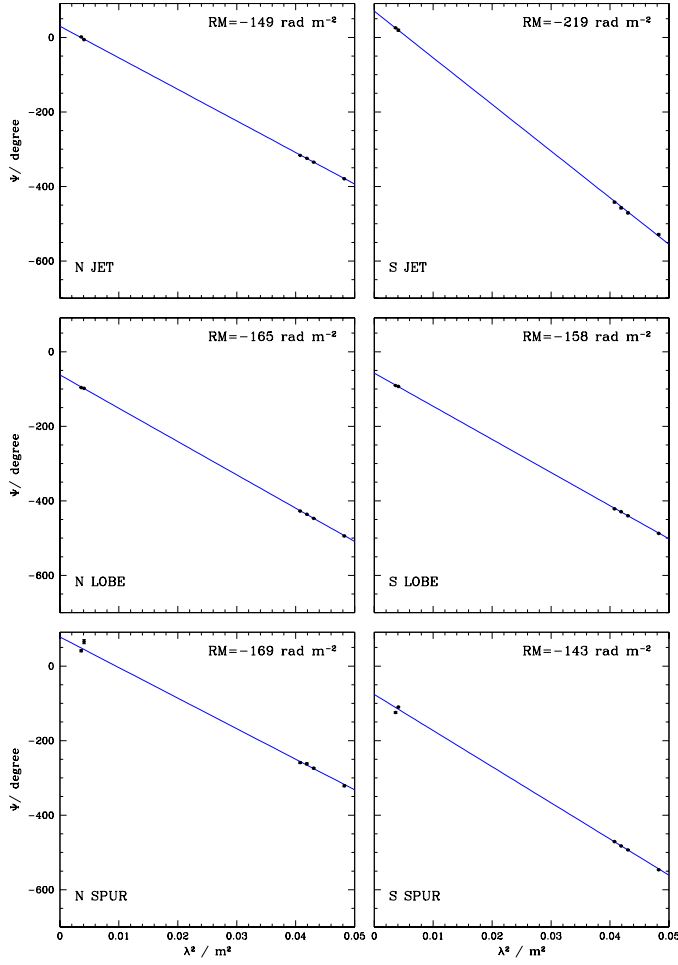


Figure 4.3: Plots of **E**-vector position angle  $\Psi$  against  $\lambda^2$  at representative points of the 5.5-arcsec RM map. Fits to the relation  $\Psi(\lambda) = \Psi_0 + \text{RM}\lambda^2$  are shown. The values of RM are given in the individual panels.

$$\sigma_{\text{RM}} \simeq 16 \text{ rad m}^{-2}.$$

At 5.5 arcsec resolution, more extended polarized regions of 3C 449 can be mapped with good sampling in  $\lambda^2$ . The average fitting error is  $\simeq 1.0 \text{ rad m}^{-2}$ . Both spurs are characterized by  $\langle \text{RM} \rangle \simeq -160 \text{ rad m}^{-2}$ , with  $\sigma_{\text{RM}} = 15$  and  $10 \text{ rad m}^{-2}$  in the north and south, respectively. The overall mean and rms for the 5.5 arcsec image,  $\langle \text{RM} \rangle = -160.7 \text{ rad m}^{-2}$  and  $\sigma_{\text{RM}} = 18.9 \text{ rad m}^{-2}$ , are very close to those determined at higher resolution and are consistent with the integrated value of  $-162 \pm 1 \text{ rad m}^{-2}$  derived by Simard-Normandin et al. (1981).

It was demonstrated by Feretti et al. (1999a) that the polarization position angles at 1.25 arcsec resolution accurately follow the relation  $\Delta\Psi \propto \lambda^2$  over a wide range of rotation. I find the same effect at lower resolution: plots of **E**-vector position angle  $\Psi$  against  $\lambda^2$  at representative points of the 5.5 arcsec-RM image are shown in Fig 4.3. As at the higher resolution, there are no significant deviations from the relation  $\Delta\Psi \propto \lambda^2$  over a range of rotation  $\Delta\Psi$  of  $600^\circ$ , confirming that a foreground magnetized medium is responsible for the majority of the Faraday rotation and extending this result to regions of lower surface brightness.

In Fig. 4.2(c) and (d), I show profiles of  $\sigma_{\text{RM}}$  for both low and high resolution RM images. The 1.25 arcsec profile was obtained by averaging over boxes with lengths ranging from 9 to 13 kpc along the radio axis; for the 5.5 arcsec profile I used boxes with a fixed length of 9 kpc (these sizes were chosen to give an adequate number of independent points per box). The boxes extend far enough perpendicular to the source axis to include all unblanked pixels. In both plots, there is clear evidence for a decrease in the observed  $\sigma_{\text{RM}}$  towards the periphery of the source, the value dropping from  $\approx 30 \text{ rad m}^{-2}$  close to the nucleus to  $\approx 10 \text{ rad m}^{-2}$  at 50 kpc. This is qualitatively as expected for foreground Faraday rotation by a medium whose density (and presumably also magnetic field strength) decreases with radius. The symmetry of the  $\sigma_{\text{RM}}$  profiles is consistent with the assumption that the radio source lies in the plane of the sky.

### 4.3.2 The Galactic Faraday rotation

For the purpose of this work, 3C 449 has an unfortunate line-of-sight within our Galaxy. Firstly, the source is located at  $l = 95.4^\circ$ ,  $b = -15.9^\circ$  in Galactic coordinates, where the Galactic magnetic field is known to be aligned almost along the line-of-sight. Secondly, there is evidence from radio and optical imaging for a diffuse, ionized Galactic feature in front of 3C 449, perhaps associated with the nearby HII region S126 (Andernach et al. 1992). Estimates of the Galactic foreground RM at the position of 3C 449 from observations of other radio sources are uncertain: Andernach et al. (1992) found a mean value of  $-212 \text{ rad m}^{-2}$  for six nearby sources, but the spherical harmonic models of Dineen & Coles (2005), which are derived by fitting to the RM values of large numbers of extragalactic sources, predict  $-135 \text{ rad m}^{-2}$ . Nevertheless, it is clear that the bulk of the mean RM of 3C 449 must be Galactic.

In order to investigate the magnetized plasma local to 3C 449, the value and possible spatial variation of this Galactic contribution must be constrained. The profiles of  $\sigma_{\text{RM}}$  (Fig. 4.2) show that the small-scale fluctuations of RM drop rapidly with distance from the nucleus. I might therefore expect the Galactic contribution to dominate on the largest scales. At low resolution, the RM can be accurately determined out to  $\approx 100 \text{ kpc}$  from the core. This is roughly 5 core radii for the X-ray emission and therefore well outside the bulk of the intra-group gas.

In order to estimate the Galactic RM contribution, I averaged the 5.5-arcsec RM image in boxes of length 20 kpc along the radio axis (the box size has been increased from that of Fig. 4.2 to improve the display of large-scale variations). The profile of  $\langle \text{RM} \rangle$  against the distance from the radio core is shown in Fig. 4.4. The large deviations from the mean in the innermost two bins are associated with the maximum in  $\sigma_{\text{RM}}$  and are almost certainly due to the intra-group medium. The dispersion in  $\langle \text{RM} \rangle$  is quite small in the south and the value of  $\langle \text{RM} \rangle = -160.7 \text{ rad m}^{-2}$  for the whole source is very close to that of the outer south jet. There are significant fluctuations in the

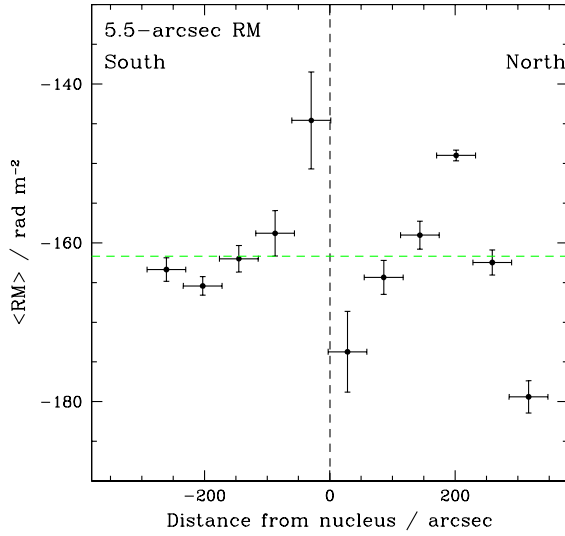


Figure 4.4: Profile of RM averaged over boxes of length 20 kpc along the radio axis for the 5.5 arcsec image. The horizontal bars represent the bin width. The vertical bars are the errors on the mean calculated from the dispersion in the boxes, the contribution from the fitting error is negligible and is not taken into account. Positive distances are in the direction of the north jet. The black vertical dashed line indicates the position of the nucleus; the green dashed line shows the adopted mean value for the Galactic RM.

north, however. Given their rather small scale ( $\sim 300$  arcsec), it is most likely that these arise in the local environment of 3C 449, and I include them in the statistical analysis given below.

There is some evidence for linear gradients in Galactic RM on arcminute scales (Laing et al. 2006a). In order to check the effect of a large-scale Galactic RM gradient on these results, I computed an unweighted least-squares fit of a function  $\langle \text{RM} \rangle = \text{RM}_0 + ax$ , where  $a$  and  $\text{RM}_0$  are constant and  $x$  is measured along the radio axis. The two innermost bins in Fig. 4.4 were excluded from the fit. The best estimate for the gradient is very small:  $a=0.0054 \text{ rad m}^{-2} \text{ arcsec}^{-1}$ . I have verified that subtraction of this gradient has a negligible effect on the structure-function analysis given in Sec. 4.6.3.

I therefore adopt a constant value of  $-160.7 \text{ rad m}^{-2}$  as the Galactic contribution.

## 4.4 Depolarization

I first estimated the bandwidth effects on the polarized emission of 3C 449 using the RM measurements from Sec. 4.3.1. In the worst case (the highest absolute RM value of  $-240 \text{ rad m}^{-2}$ ) at the lowest frequency of 1.365 GHz) the rotation across the band is  $\approx 10^\circ$ . This results in a depolarization of 0.017, negligible compared with errors due to noise.

The analysis of the depolarization of 3C 449 is based on the approach of Laing et al. (2008).

I made images of  $k$  at both standard resolutions by weighted least-squares fitting to the fractional polarization maps (Eq. 3.5), using the `fitfrac` code by M. Murgia. The same frequencies were used as for the RM images: 8.385 – 1.365 GHz and 4.985 – 1.365 GHz at 1.25 and 5.5 arcsec resolution, respectively. By simulating the error distributions for  $p$ , I established that the mean values of  $k$  were biased significantly at low signal-to-noise (cf. Laing et al. 2008), so only data

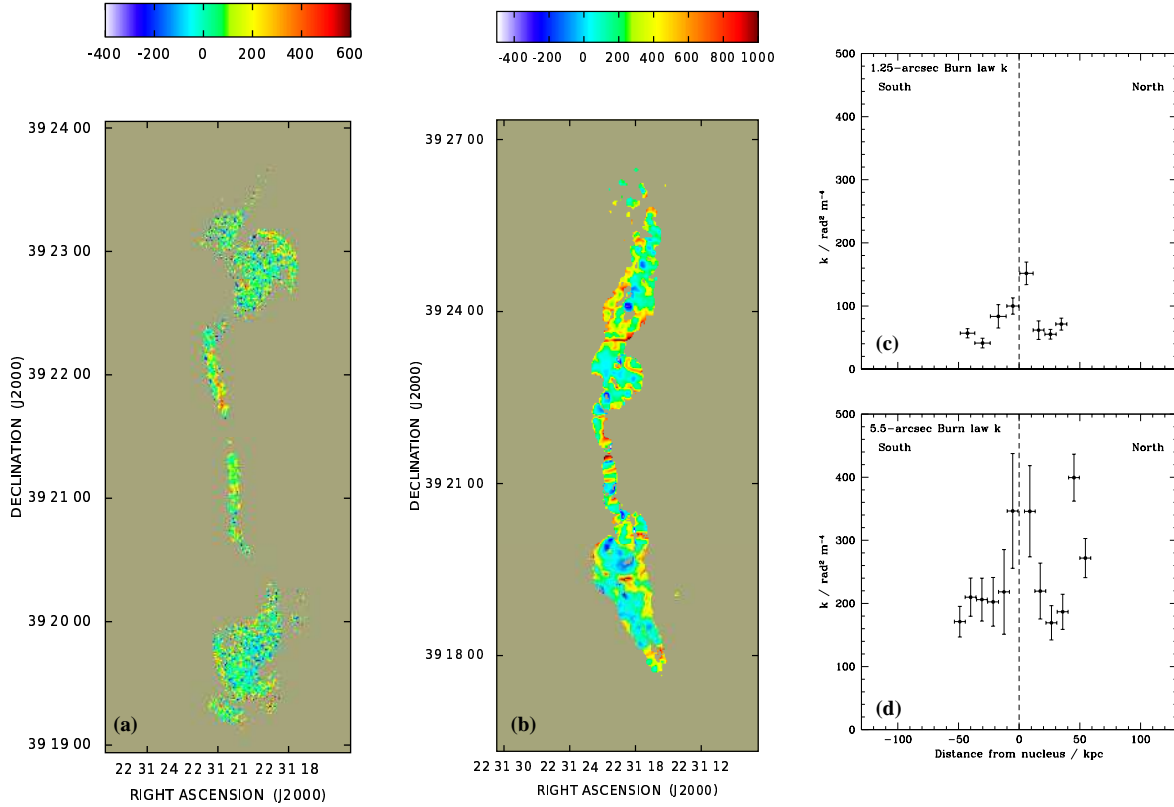


Figure 4.5: **(a)**: image of the Burn law  $k$  in  $\text{rad}^2 \text{m}^{-4}$  computed from a fit to the relation  $p(\lambda) = p(0)\exp(-k\lambda^4)$  for seven frequencies between 1.365 and 8.385 GHz. **(b)**: as (a), but the angular resolution is 5.5 arcsec FWHM, and the  $k$  image has been computed from the fit to the six frequencies between 1.365 and 4.985 GHz. **(c)** and **(d)**: profiles for  $k$  as functions of the projected distance from the radio source center (boxes as in Fig. 4.2). The horizontal and vertical bars represent the bin widths and the error on the mean, respectively. Positive distances are in the direction of the north jet, and the vertical dashed lines show the position of the nucleus.

with  $p > 4\sigma_p$  at each frequency are included in the fits. I estimate that any bias is negligible compared with the fitting error. I also derived profiles of  $k$  with the same sets of boxes as for the  $\sigma_{\text{RM}}$  profiles in Fig. 4.2.

The 1.25 arcsec resolution  $k$  map is shown in Fig. 4.5(a), together with the profile of the  $k$  values (Fig. 4.5c). The fit to a  $\lambda^4$  law is very good everywhere: examples of fits at selected pixels in the jets and lobes are shown in in Fig. 4.6. The symmetry observed in the  $\sigma_{\text{RM}}$  profiles is also seen in the 1.25 arcsec  $k$  image (Fig. 4.5): the mean values of  $k$  are  $\approx 50 \text{ rad}^2 \text{m}^{-4}$  for both lobes, 107 and  $82 \text{ rad}^2 \text{m}^{-4}$  for the northern and southern jet, respectively. The region with the highest depolarization is in the northern jet, very close to the core and along the west side. The integrated value of  $k$  at this resolution is  $\approx 56 \text{ rad}^2 \text{m}^{-4}$ , corresponding to a mean depolarization  $DP_{3\text{cm}}^{20\text{cm}} \approx 0.87$ .

The image and profile of  $k$  at 5.5-arcsec resolution are shown in Fig. 4.5(b) and (d). The fit

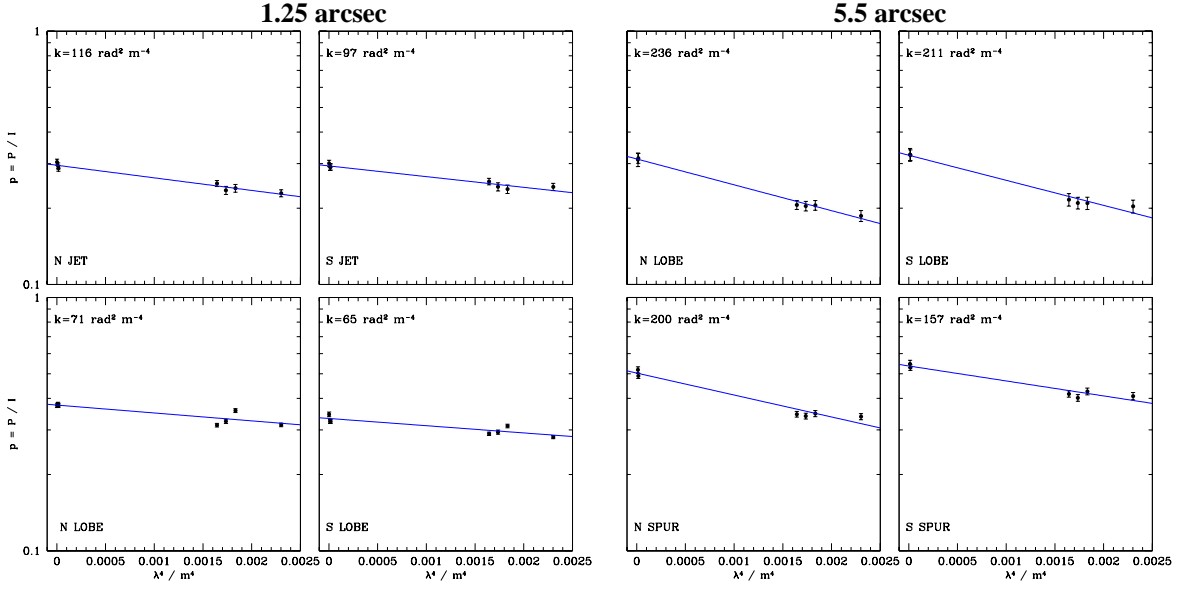


Figure 4.6: Plots of degree of polarization,  $p$  (log scale) against  $\lambda^4$  for representative points at 1.25-arcsec and 5.5-arcsec resolution. Burn law fits (Eq. 3.5) are also plotted. The values of  $k$  are quoted in the individual panels.

to a  $\lambda^4$  law is in general good and examples are shown in in Figs. 4.6. As mentioned earlier, the maximum scale of structure imaged accurately in total intensity at 5 GHz is  $\sim 300$  arcsec (100 kpc) and there are likely to be significant systematic errors in the degree of polarization on larger scales. I therefore show the profile only for the inner  $\pm 50$  kpc. Over this range, the  $k$  profiles are quite symmetrical, as at higher resolution. Note also that the small regions of very high  $k$  at the edge of the northern and southern spurs in the map shown in Fig. 4.5 are likely to be spurious.

The mean values of  $k$  are  $\simeq 184 \text{ rad}^2 \text{ m}^{-4}$  and  $178 \text{ rad}^2 \text{ m}^{-4}$  for the northern and southern lobes, respectively; and  $\simeq 238$  and  $174 \text{ rad}^2 \text{ m}^{-4}$  in the northern and in the southern spurs. The integrated value of  $k$  is  $\simeq 194 \text{ rad}^2 \text{ m}^{-4}$ , corresponding to a depolarization  $DP_{6\text{cm}}^{20\text{cm}} \simeq 0.64$ .

To summarize, depolarization between 20 cm and 3 cm is observed. Since I measure lower values of  $k$  at 1.25 arcsec than 5.5 arcsec, there is less depolarization at high resolution, as expected for beam depolarization. The highest depolarization is observed in a region of the northern jet, close to the radio core and associated with a steep RM gradient. Depolarization is significantly higher close to the nucleus, which is consistent with the higher path length through the group gas observed in X-rays. Aside from this global variation, I found no evidence for a detailed correlation of depolarization with source structure. Depolarization and RM data are therefore both consistent with a foreground Faraday screen. In Sec. 4.5.2 I show that the residual depolarization at 1.25-arcsec resolution can be produced by RM fluctuations on scales smaller than the beam-width, but higher-resolution observations are needed to establish this conclusively.

## 4.5 Two dimensional analysis

### 4.5.1 General considerations

In order to interpret the fluctuations of the magnetic field responsible for the observed RM and depolarization of 3C 449, I first discuss the statistics of the RM fluctuations in two dimensions. I use the notation of Laing et al. (2008) in which  $\mathbf{f} = (f_x, f_y, f_z)$  is a vector in the spatial frequency domain, corresponding to the position vector  $\mathbf{r} = (x, y, z)$ . The  $z$ -axis is taken to be along the line-of-sight, so that the vector  $\mathbf{r}_\perp = (x, y)$  is in the plane of the sky and  $\mathbf{f}_\perp = (f_x, f_y)$  is the corresponding spatial frequency vector. The goal is to estimate the RM power spectrum  $\widehat{C}(\mathbf{f}_\perp)$ , where  $\widehat{C}(\mathbf{f}_\perp)df_xdf_y$  is the power in the area  $df_xdf_y$  and in turn to derive the three-dimensional magnetic-field power spectrum  $\widehat{w}(\mathbf{f})$ , defined so that  $\widehat{w}(\mathbf{f})df_xdf_ydf_z$  is the power in a volume  $df_xdf_ydf_z$  of frequency space.

In order to derive the magnetic-field power spectrum, I make the simplifying assumptions discussed in Sec. 3.7.1, which can be summarized as follows: the observed Faraday rotation occurs in a foreground screen (in agreement with the results in Secs. 4.3 and 4.4) whose density is a spherically symmetric function; the magnetic field is distributed throughout the Faraday-rotating medium and it is an isotropic, Gaussian random variable, whose power spectrum is independent of position; the power spectrum amplitude is a function only of the thermal electron density. These assumptions guarantee that the spatial distribution of the magnetic field can be described entirely by its power spectrum  $\widehat{w}(f)$  and that for a medium of constant depth and density, the power spectra of magnetic field and RM are proportional (Enßlin & Vogt 2003)

In Sec. 4.3.2, I showed that the Galactic contribution to the 3C 449 RM is substantial and argued that a constant value of  $-160.7 \text{ rad m}^{-2}$  is the best estimate for its value. Fluctuations in the Galactic magnetic field on scales comparable with the size of the radio sources could be present; conversely, the local environment of the source might make a significant contribution to the mean RM. Both of these possibilities lead to difficulties in the use of the autocorrelation function. Therefore, following the approach of Laing et al. (2008), I initially used the RM structure function (Eq. 3.13) to determine the form of field power spectrum (Sec. 4.5.2), while for its normalization (determined by global variations of density and magnetic field strength), I made use of three-dimensional simulations (Sec. 4.6).

### 4.5.2 Structure functions

I calculated the structure function for discrete regions of 3C 449, over which the spatial variations of thermal gas density, rms magnetic field strength and path length are expected to be reasonably

small. For each of these regions, I first made unweighted fits of model structure functions derived from power spectra with simple, parametrized functional forms, accounting for convolution with the observing beam. I then generated multiple realizations of a Gaussian, isotropic, random RM field, with the best-fitting power spectrum on the observed grids, again taking into account the effects of the convolving beam. Finally, I made a weighted fit using the dispersion of the synthetic structure functions as estimates of the statistical errors for the *observed* structure functions, which are impossible to quantify analytically (Laing et al. 2008). These errors, which result from incomplete sampling, are much larger than those due to noise, but depend only weakly on the precise form of the underlying power spectrum. The measure of the goodness of fit is  $\chi^2$ , summed over a range of separations from  $r_{\perp} = \text{FWHM}$  to roughly half of the size of the region: there is no information in the structure function for scales smaller than the beam, and the upper limit is set by sampling. The errors are, of course, much higher at the large spatial scales, which are less well sampled. Note, however, that estimates of the structure function from neighbouring bins are not statistically independent, so it is not straightforward to define the effective number of degrees of freedom.

I selected six regions for the structure-function analysis, as shown in Fig. 4.2. These are symmetrically placed about the nucleus, consistent with the orientation of the radio jets close to the plane of the sky. For the north and south jets, I derived the structure functions only at 1.25-arcsec resolution, as the low-resolution RM image shows no additional structure and has poorer sampling. For the north and south lobes, I computed the structure functions at both resolutions over identical areas and compared them. The agreement is very good, and the low-resolution RM images do not sample significantly larger spatial scales, so I show only the 1.25-arcsec results. Finally, I used the 5.5-arcsec RM images to compute the structure functions for the north and south spurs, which are not detected at the higher resolution.

The structure function has a positive bias given by  $2\sigma_{\text{noise}}^2$ , where  $\sigma_{\text{noise}}$  is the uncorrelated random noise in the RM image (Simonetti, Cordes & Spangler 1984). The mean noise of the 1.25 and 5.5-arcsec RM maps is  $<1 \text{ rad m}^2$  and is essentially uncorrelated on scales larger than the beam. For each region I therefore subtracted  $2\sigma_{\text{noise}}^2$  from the structure functions, although this correction is always small. The noise-corrected structure functions are shown in Fig. 4.7.

The individual observed structure functions have approximately power-law forms. Given that the structure function for a power-law power spectrum with no frequency limits is itself a power law (Minter & Spangler 1996; Laing et al. 2008), I first tried to fit the observed data with a RM power spectrum of the form

$$\widehat{C}(f_{\perp}) \propto f_{\perp}^{-q} \quad (4.2)$$

over an infinite frequency range. This last assumption allows us to use the analytical solution of

the structure function, including convolution (Laing et al. 2008), and therefore to avoid numerical integration.

The fits were quite good, but systematically gave slightly too much power on small spatial scales and over-predicted the depolarization. I therefore fit a *cut-off power law* (CPL) power spectrum of the form

$$\begin{aligned}\widehat{C}(f_{\perp}) &= 0 & f_{\perp} < f_{\min} \\ &= C_0 f_{\perp}^{-q} & f_{\perp} \leq f_{\max} \\ &= 0 & f_{\perp} > f_{\max}.\end{aligned}\tag{4.3}$$

Initially, I consider values of  $f_{\min}$  sufficiently small that their effects on the structure functions over the observed range of separations are negligible. The free parameters of the fit in this case are the slope,  $q$ , the cut-off spatial frequency  $f_{\max}$  and the normalization of the power spectrum,  $C_0$ . In Table 4.2, I give the best-fitting parameters for CPL fits to all of the individual regions. The fitted model structure functions are plotted in Fig. 4.7(a)–(f), together with error bars derived from multiple realizations of the power spectrum as in Laing et al. (2008).

In order to constrain RM structure on spatial scales below the beam-width, I estimated the depolarization expected from the best power spectrum for each of the regions with 1.25-arcsec RM images, following the approach of Laing et al. (2008). To do this, multiple realizations of RM images have been made on an  $8192^2$  grid with fine spatial sampling. I then derived the  $Q$  and  $U$  images at our observing frequencies, convolved to the appropriate resolution and compared the predicted and observed mean degrees of polarization. These values are given in Table 4.4. The uncertainties in the expected  $\langle k \rangle$  in Table 4.4 represent statistical errors determined from multiple realizations of RM images with the same set of power spectrum parameters. The predicted and observed values are in excellent agreement. A constant value of  $f_{\max} = 1.67 \text{ arcsec}^{-1}$  predicts very similar values, also listed in Table 4.4. I have not compared the depolarization data at 5.5-arcsec resolution in the spurs because of limited coverage of large spatial scales in the  $I$  images (Sec. 4.2), which is likely to introduce systematic errors at 4.6 and 5.0 GHz.

I performed a joint fit of the CPL power spectra, minimizing the  $\chi^2$  summed over all six sub-regions, giving equal weight to each and allowing the normalizations to vary independently. In this case the free parameters of the fit are the six normalizations (one for each sub-region), the slope, and the maximum spatial frequency. The joint best-fitting single power-law power spectrum has  $q = 2.68$ .

A single power law slope does not give a good fit to all of the regions simultaneously, however. It is clear from Fig. 4.7 and Table 4.2 that there is a flattening in the slope of the observed structure

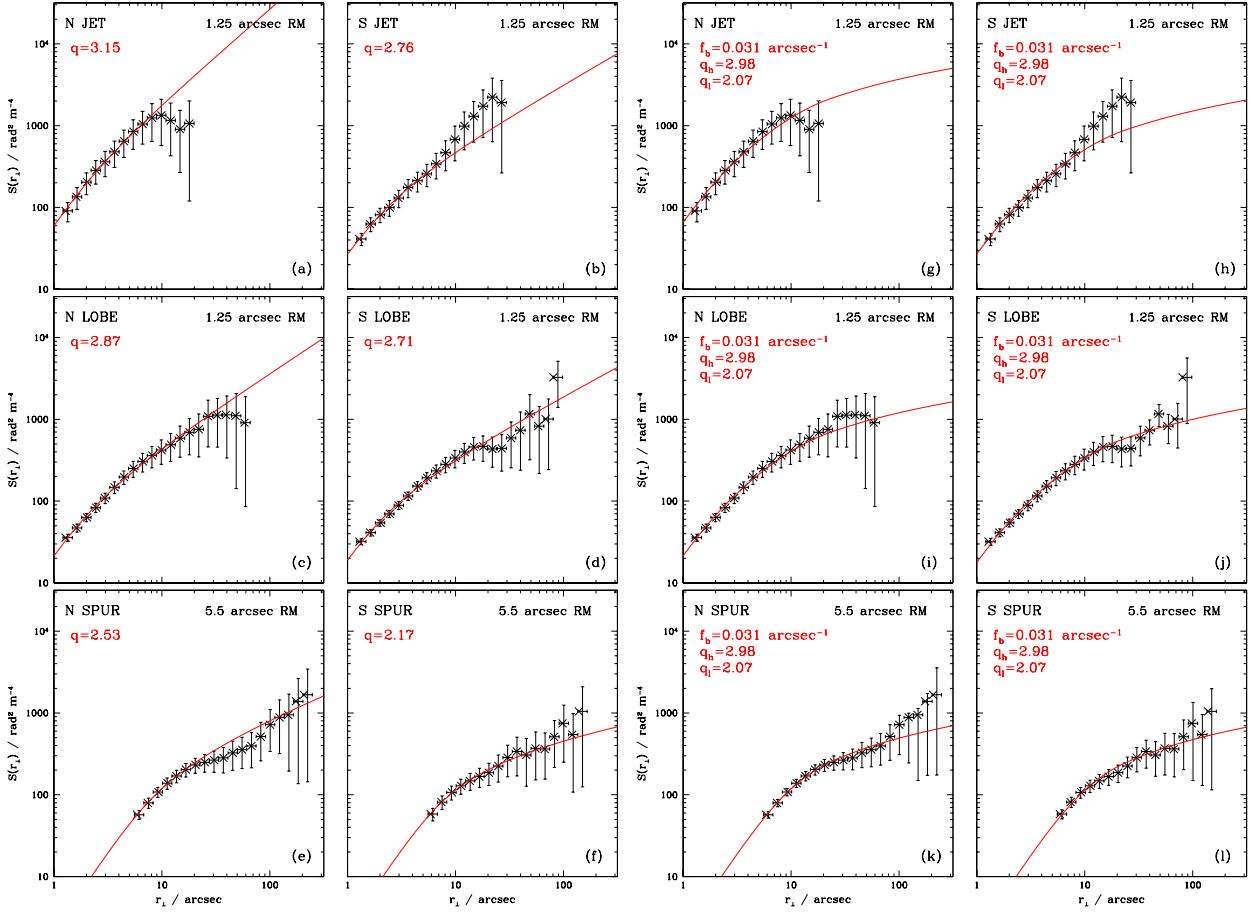


Figure 4.7: **(a)-(f)**: Plots of the RM structure functions for the sub-regions showed in Fig.4.2. The horizontal bars represent the bin widths and the crosses the centroids for data included in the bins. The red lines are the predictions for the CPL power spectra described in the text, including the effects of the convolving beam. The vertical error bars are the rms variations for the structure functions derived using a CPL power spectrum with the quoted value of  $q$  on the observed grid of points for each sub-region. **(g)-(l)**: as (a)-(f), but using a BPL power spectra with fixed slopes and break frequency, but variable normalization.

functions on the largest scales (which are sampled primarily by the spurs). In order to fit all of the data accurately with a single functional form for the power spectrum, I adopt a *broken power law* form (BPL) for the RM power spectrum:

$$\begin{aligned}
 \widehat{C}(f_{\perp}) &= 0 & f_{\perp} < f_{\min} \\
 &= D_0 f_b^{(q_l - q_h)} f_{\perp}^{-q_l} & f_b \geq f_{\perp} \\
 &= D_0 f_{\perp}^{-q_h} & f_{\max} \geq f_{\perp} > f_b \\
 &= 0 & f_{\perp} > f_{\max} .
 \end{aligned} \tag{4.4}$$

I performed a BPL joint fit in the same way as for the CPL power spectra. In this case

Table 4.2: CPL power spectrum parameters for the six individual sub-regions of 3C 449.

Region	FWHM (arcsec )	CPL					
		Best Fit		Min Slope		Max Slope	
		$q$	$f_{\max}$	$q^-$	$f_{\max}$	$q^+$	$f_{\max}$
N SPUR	5.50	2.53	1.96	1.58	0.23	3.44	$\infty$
N LOBE	1.25	2.87	1.60	2.31	0.55	3.35	$\infty$
N JET	1.25	3.15	1.21	2.29	0.30	4.27	$\infty$
S JET	1.25	2.76	1.95	2.02	0.3	3.69	$\infty$
S LOBE	1.25	2.71	1.68	2.36	0.65	3.05	$\infty$
S SPUR	5.50	2.17	1.53	0.20	0.12	3.95	0.12

Lower and upper limits are quoted at  $\sim 90\%$  confidence.

Table 4.3: Best-fitting parameters for the joint CPL and BPL fits to all six sub-regions of 3C449.

	Best Fit			Min Slope			Max Slope	
	$q$	$f_{\max}$	$\chi^2$	$q^-$	$f_{\max}$	$q^+$	$f_{\max}$	
joint CPL	2.68	1.67	33.5	2.55	1.30	2.81	2.00	

	Best Fit				Min Slope				Max Slope	
	$q_l$	$f_b$	$q_h$	$\chi^2$	$q_l^-$	$f_b$	$q_h^-$	$q_l^+$	$f_b$	$q_l^+$
joint BPL	2.07	0.031	2.97	17.7	1.99	0.044	2.91	2.17	0.021	3.09

Lower and upper limits are quoted at  $\sim 90\%$  confidence. The values of  $q$  and  $f_{\max}$  for the joint CPL fit and  $q_h$ ,  $q_l$  and  $f_b$  for the joint BPL fit are the same for all sub-regions, while the normalizations are varied to minimize the overall  $\chi^2$ . In the joint BPL fit, the maximum frequency is fixed at  $f_{\max} = 1.67 \text{ arcsec}^{-1}$ .

the free parameters of the fit are the six normalizations,  $D_0$ , one for each sub-region, the high and low-frequency slopes,  $q_h$  and  $q_l$ , and the break and maximum spatial frequencies  $f_b$  and  $f_{\max}$ . I found best fitting parameters of  $q_l = 2.07$ ,  $q_h = 2.98$ ,  $f_b = 0.031 \text{ arcsec}^{-1}$ . As noted earlier, I also fixed  $f_{\max} = 1.67 \text{ arcsec}^{-1}$  to ensure consistency with the observed depolarizations at 1.25-arcsec resolution. The corresponding structure functions are plotted in Fig.4.7(g)–(l) and the normalizations for the individual regions are given in Table 4.4. As for the CPL fits, the errors bars are derived from the rms scatter of the structure functions of multiple convolved RM realizations.

It is evident from Fig.4.7 that the structure functions corresponding to the BPL power spectrum, which gives less power on large spatial scales, agree much better with the data. The joint BPL fit has a  $\chi^2$  of 17.7, compared with 33.5 for the joint CPL fit (the former has only two extra parameters), which confirms this result.

I have so far ignored the effects of any outer scale of the magnetic-field fluctuations. This is justified because the structure functions for the spurs continue to rise at the largest observed separations, indicating that the outer scale must be  $\gtrsim 10 \text{ arcsec}$  ( $\approx 30 \text{ kpc}$ ). The model structure

Table 4.4: Normalizations and expected depolarization for the individual CPL, joint CPL and joint BPL fit parameters at 1.25 arcsec.

Region	Observed $\langle k \rangle$ [rad <sup>2</sup> m <sup>-4</sup> ]	CPL			JOINT CPL		JOINT BPL	
		$C_0$	$f_{\max}$ [arcsec <sup>-1</sup> ]	$\langle k \rangle$ [rad <sup>2</sup> m <sup>-4</sup> ]	$C_0$	$\langle k \rangle$ [rad <sup>2</sup> m <sup>-4</sup> ]	$D_0$	$\langle k \rangle$ [rad <sup>2</sup> m <sup>-4</sup> ]
N LOBE	61±6	0.96	1.60	63±3	1.52	66±3	1.91	52±4
N JET	106±12	1.34	1.21	106±5	4.76	110±5	0.5	109±5
S JET	91±11	1.50	1.95	70±5	1.94	73±5	1.52	65±4
S LOBE	50±5	1.18	1.68	53±2	1.28	50±2	2.20	45±3

Col.1: region; Col. 2: observed Burn law  $\langle k \rangle$ . Col. 3, 4 and 5: normalization constant  $C_0$ , fitted maximum spatial frequency  $f_{\max}$  for the best CPL power spectrum of each region and the predicted  $\langle k \rangle$  for each power spectrum. Col. 6, 7 as Col. 3 and 5 but for the joint fit to each CPL power spectrum; Col. 8 and 9 as Col. 3, and 5 but for the joint BPL power spectrum. For both the joint CPL and BPL fits, the maximum frequency is fixed at  $f_{\max} = 1.67 \text{ arcsec}^{-1}$ . In calculating each value of  $\langle k \rangle$  only data with  $p > 4\sigma_p$  are included.

functions fit to the observations assume that the outer scale is infinite and the realizations are generated on sufficiently large grids in Fourier space that the effects of the implicit outer scale are negligible over the range of scales here sampled. I used structure-function data for the entire source to determine an approximate value for the outer scale in Sec. 4.6.3.

I now adopt the BPL power spectrum with these parameters and investigate the spatial variations of the RM fluctuation amplitude using three-dimensional simulations.

## 4.6 Three-dimensional analysis

### 4.6.1 Models

I used the software package `RMsim` (Murgia et al. 2004) to compare the observed RM with simulated images derived from three-dimensional multi-scale magnetic-field models. Given a field model and the density distribution of the thermal gas, `RMsim` calculates an RM image by integrating Eq. 3.2 numerically. As in Sec. 4.5, the fluctuations of RM were modeled on the assumption that the magnetic field responsible for the foreground rotation is an isotropic, Gaussian random variable and therefore characterized entirely by its power spectrum. Each point in a cube in Fourier space was first assigned components of the magnetic vector potential. The amplitudes were selected from a Rayleigh distribution of unit variance, and the phases were random in  $[0, 2\pi]$ . The amplitudes were then multiplied by the square root of the power spectrum of the vector potential, which is simply related to that of the magnetic field. The corresponding components of the magnetic field along the line-of-sight were then calculated and transformed to real space. This procedure ensured that the magnetic field was divergence-free. The field components in real

Table 4.5: Summary of magnetic field power spectrum and density scaling parameters.

BPL power spectrum	
$q_l = 2.07$	low-frequency slope
$q_h = 2.98$	high-frequency slope
$f_b = 0.031 \text{ arcsec}^{-1}$	break frequency ( $\Lambda_b = 1/f_b = 11 \text{ kpc}$ )
$f_{\max} = 1.67 \text{ arcsec}^{-1}$	maximum frequency ( $\Lambda_{\min} = 1/f_{\max} = 0.2 \text{ kpc}$ )
$f_{\min}$ fitted	minimum frequency ( $\Lambda_{\max} = 1/f_{\min}$ )
Scaling of the magnetic field	
$B_0$ fitted	Average magnetic field at group center
$\eta$ fitted	Magnetic field exponent of the radial profile: $\langle B \rangle(r) = B_1 1860 \left[ \frac{n_e(r)}{n_0} \right]^\eta$

space were then multiplied by the model density distribution and integrated along the line of sight to give a synthetic RM image at the full resolution of the simulation, which was then convolved to the observing resolution.

For 3C 449, I assumed that the source is in a plane perpendicular to the line-of-sight, which passes through the group center and simulated the field and density structure using a  $2048^3$  cube with a real-space pixel size of 0.1 kpc. I used the best-fitting BPL power spectrum found in Sec. 4.5.2, but with a spatially-variable normalization, as described below (Sec. 4.6.2), and a low-frequency cut-off  $f_{\min}$ , corresponding to a maximum scale of the magnetic field fluctuations,<sup>1</sup>  $\Lambda_{\max}$  ( $= f_{\min}^{-1}$ ). The power spectrum of Eq. 4.4 was then set to 0 for  $f < f_{\min}$ . I fixed the minimum scale of the fluctuations  $\Lambda_{\min} = 0.2 \text{ kpc}$ . This is equivalent to the value  $f_{\max} = 1.67 \text{ arcsec}^{-1}$  found in Sec. 4.5.2 and also consistent with the requirement that the minimum scale can be no larger than twice the pixel size for adequate sampling.

Multiple synthetic RM images were produced at resolutions of 1.25 and 5.5 arcsec over the fields of view of the observations for each combination of parameters. In order to estimate the spatial variation of the magnetic-field strength, I first made a set of simulations with a large, fixed value of  $\Lambda_{\max}$  and compared the predicted and observed profiles of  $\sigma_{\text{RM}}$  (Sec. 4.6.2). I then fixed the radial variation of the field at its best-fitting form and estimated the value of  $\Lambda_{\max}$  with a structure-function analysis for the whole source (Sec. 4.6.3).

#### 4.6.2 Magnetic field strength and radial profile

In order to estimate the radial variation of field strength, I first fixed the value of the outer scale to be  $\Lambda_{\max} = 205 \text{ kpc}$ , the longest allowed by the simulation grid. The approach was to make a large

<sup>1</sup>Here I refer to the scale length  $\Lambda$  as a complete wavelength, i.e.  $\Lambda = 1/f$ . This differs by a factor of 2 from the definition in Guidetti et al. (2008), where  $\Lambda$  is the reversal scale of the magnetic field, so  $\Lambda = 1/2f$ .

number of simulations for each combination of field strength and radial profile and to compare the predicted and observed values of  $\sigma_{\text{RM}}$  evaluated over the boxes used in Sec. 4.3.1 (Fig. 4.2). I used  $\chi^2$  summed over the boxes as a measure of the goodness of fit. This procedure is independent of the precise value of the outer scale, provided that it is much larger than the averaging boxes. I express the results in terms of  $\chi_{\text{red}}^2$ , which is the value of  $\chi^2$  divided by the number of degrees of freedom.

I initially tried a radial field-strength variation of the form

$$\langle B^2(r) \rangle^{1/2} = B_0 \left[ \frac{n_e(r)}{n_0} \right]^\eta \quad (4.5)$$

as used by Guidetti et al. (2008) and Laing et al. (2008). Here,  $B_0$  is the rms magnetic field strength at the group center and  $n_e(r)$  is the thermal electron gas density, assumed to follow the  $\beta$ -model profile derived by Croston et al. (2008) (Sec. 4.1). As mentioned in Sec. 3.5, the field scaling of Eq. 4.5 is consistent with other observations, analytical models and numerical simulations. In particular,  $\eta = 2/3$  corresponds to flux-freezing and  $\eta = 1/2$  to equipartition between thermal and magnetic energy.

I produced simulated RM images for each combination of  $B_0$  and  $\eta$  in the ranges  $0.5 - 10 \mu\text{G}$  in steps of  $0.1 \mu\text{G}$  and  $0 - 2$  in steps of  $0.01$ , respectively. I then derived the synthetic  $\sigma_{\text{RM}}$  profiles and, by comparing them with the observed one, calculated the unweighted  $\chi^2$ . I repeated this procedure 35 times at each angular resolution, noting the  $(B_0, \eta)$  pair that gave the lowest  $\chi^2$  in each case. These values are plotted in Fig. 4.8. As in earlier work (Murgia et al. 2004; Guidetti et al. 2008; Laing et al. 2008), I found a degeneracy between the values of  $B_0$  and  $\eta$  in the sense that the fitted values are positively correlated, but there are clear minima in  $\chi^2$  at both resolutions. I therefore adopted the mean values of  $B_0$  and  $\eta$ , weighted by  $1/\chi^2$ , as the best overall estimates. These are also plotted in Fig. 4.8 as blue crosses. Although the central magnetic field strengths derived for the two RM images are consistent at the  $1\sigma$  level ( $B_0 = 2.8 \pm 0.5 \mu\text{G}$  and  $B_0 = 4.1 \pm 1.2 \mu\text{G}$  at 5.5 and 1.25-arcsec resolution, respectively), the values of  $\eta$  are not. The best-fitting values are  $\eta = 0.0 \pm 0.1$  at 5.5 arcsec FWHM and  $\eta = 0.8 \pm 0.4$  at 1.25 arcsec FWHM.

I next produced 35 RM simulations at each angular resolution by fixing  $B_0$  and  $\eta$  at their best values for that resolution. The weighted  $\chi^2$ 's for the  $\sigma_{\text{RM}}$  profiles were calculated evaluating the errors for each box by summing in quadrature the rms due to sampling (determined from the dispersion in the realizations) and the fitting-error of the observations. These values are listed in Table 4.6. The observed and best-fitting model profiles at both angular resolutions are shown in Fig. 4.9.

A model with  $\eta \simeq 0$  at all radii is a priori unlikely: previous work has found values of

$0.5 \lesssim \eta \lesssim 1$  in other sources (Dolag 2006; Guidetti et al. 2008; Laing et al. 2008). The most likely explanation for the low value of  $\eta$  inferred from the low-resolution image is that the electron density distribution is not well represented by a  $\beta$ -model (which describes a spherical and smooth distribution) at large radii. In support of this idea, Fig. 4.1 shows that the morphology of the X-ray emission is not spherical at large radii, but quite irregular. Croston et al. (2003, 2008) pointed out that the quality of the fit of a single  $\beta$ -model to the X-ray surface brightness profile was poor in the outer regions, suggesting small-scale deviations in the gas distribution. The single  $\beta$ -model gave a better fit to the inner region of the X-ray surface brightness profile, where the polarized emission of 3C 449 can be observed at 1.25-arcsec resolution. The aim is to fit the  $\sigma_{\text{RM}}$  profiles at both resolutions with the same distribution of  $n_e(r)\langle B(r)^2 \rangle^{1/2}$ . In the rest of this subsection I assume that the density profile  $n_e(r)$  is still represented by the single  $\beta$ -model, even though I have argued that it might not be appropriate in the outer regions of the hot gas distribution. Although the resulting estimates of field strength at large radii may be unreliable, the fit is still necessary for the calculation of the outer scale described in Sec. 4.6.3, which depends only on the combined spatial variation of density and field strength.

The best-fitting model at 1.25-arcsec resolution, which is characterized by a more physically reliable  $\eta$ , gives a very bad fit to the low resolution profile at almost all distances from the core (Fig. 4.9a). Conversely, the model determined at 5.5-arcsec resolution gives a very poor fit to the sharp peak in  $\sigma_{\text{RM}}$  observed within 20 kpc of the nucleus at 1.25-arcsec resolution, where the radio and X-ray data give the strongest constraints (Fig. 4.9b). I also verified that no single intermediate value of  $\eta$  gives an adequate fit to the  $\sigma_{\text{RM}}$  profiles at all distances from the nucleus.

A better description of the observed  $\sigma_{\text{RM}}$  profile is provided by the empirical function

$$\begin{aligned} \langle B^2(r) \rangle^{1/2} &= B_0 \left[ \frac{n_e(r)}{n_0} \right]^{\eta_{\text{int}}} & r \leq r_{\text{m}} \\ &= B_0 \left[ \frac{n_e(r)}{n_0} \right]^{\eta_{\text{out}}} & r > r_{\text{m}}, \end{aligned} \quad (4.6)$$

where  $\eta_{\text{int}}$ ,  $\eta_{\text{out}}$  are the inner and outer scaling index of the magnetic field and  $r_{\text{m}}$  is the break radius.

I fixed  $\eta_{\text{int}}=1.0$  and  $\eta_{\text{out}}=0.0$ , consistent with the initial results, in order to reproduce both the inner sharp peak and the outer flat decline of the  $\sigma_{\text{RM}}$  observed at the two resolutions, keeping  $r_{\text{m}}$  as a free parameter. I made three sets of three-dimensional simulations for values of the outer scale  $\Lambda_{\text{max}} = 205, 65$  and 20 kpc. Anticipating the result of Sec. 4.6.3, I plotted the results only for  $\Lambda_{\text{max}} = 65$  kpc, but the derived  $\sigma_{\text{RM}}$  profiles are in any case almost independent of the value of the outer scale in this range. The new simulations were made only at a resolution of 5.5 arcsec, since

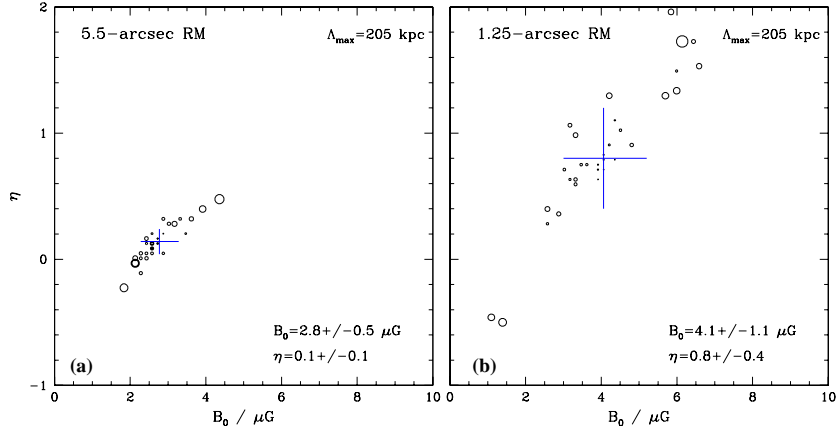


Figure 4.8: **(a)** and **(b)**: Distributions of the best-fitting values of  $B_0$  and  $\eta$  from 35 sets of simulations, each covering ranges of  $0.5 - 10 \mu\text{G}$  in  $B_0$  and  $0 - 2$  in  $\eta$ , at 5.5 and 1.25 arcsec respectively. The sizes of the circles are proportional to  $\chi^2$  for the fit and the blue crosses represent the means of the distributions weighted by  $1/\chi^2$ . The plot shows the expected degeneracy between  $B_0$  and  $\eta$ .

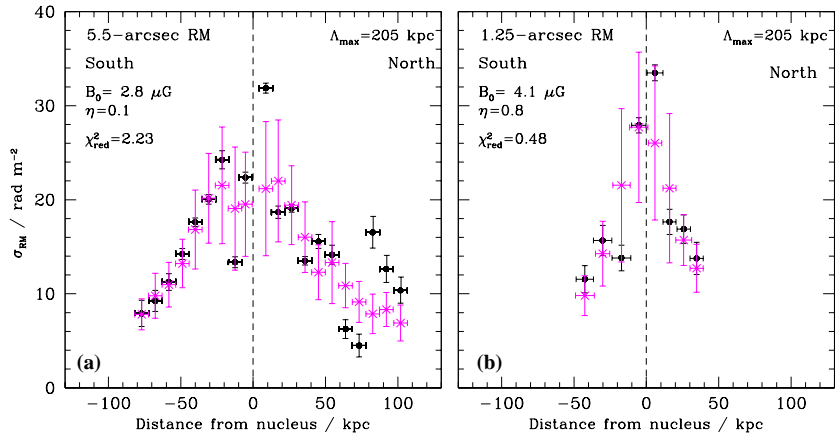


Figure 4.9: **(a)**: Observed and synthetic radial profiles for rms Faraday  $\sigma_{\text{RM}}$  at 5.5 arcsec as functions of the projected distance from the radio source center. The outer scale is  $\Lambda_{\text{max}}=205$  kpc. The black points represent the data with vertical bars corresponding to the rms error of the RM fit. The magenta crosses represent the mean values from 35 simulated profiles and the vertical bars are the rms scatter in these profiles due to sampling. **(b)** as **(a)**, but at 1.25 arcsec.

the larger field of view at this resolution is essential to define the change in slope of the profile.

In order to determine the best-fitting break radius,  $r_m$  in Eq. 4.6, I produced 35 sets of synthetic RM images for a grid of values of  $B_0$  and  $r_m$  for each outer scale, noting the pair of values which gave the minimum unweighted  $\chi^2$  for the  $\sigma_{\text{RM}}$  profile for each set of simulations. These values are plotted in Fig. 4.10, which shows that there is a degeneracy between the break radius  $r_m$  and  $B_0$ . As with the similar degeneracy between  $B_0$  and  $\eta$  noted earlier, there is a clear minimum in  $\chi^2$ , and I therefore adopted the mean values of  $B_0$  and  $r_m$  weighted by  $1/\chi^2$  as the best estimates of the magnetic-field parameters.

Table 4.6: Results from the three-dimensional fits at both the angular resolutions of 1.25 and 5.5 arcsec.

FWHM (arcsec)	$\Lambda_{\max}$ (kpc)	single $\eta$			broken $\eta$		
		$B_0$ ( $\mu\text{G}$ )	$\eta$	$\chi_{\text{red}}^2$	$B_0$ ( $\mu\text{G}$ )	$r_m$ (kpc)	$\chi_{\text{red}}^2$
1.25	205	$4.1 \pm 1.1$	$0.8 \pm 0.4$	0.48	-	-	-
5.50	205	$2.8 \pm 0.5$	$0.1 \pm 0.1$	2.2	$3.5 \pm 0.7$	$17 \pm 9$	1.9
5.50	65	-	-	-	$3.5 \pm 1.2$	$16 \pm 11$	1.8
5.50	20	-	-	-	$3.5 \pm 0.8$	$11 \pm 8$	2.1

I then made 35 simulations with the best-fitting values of  $B_0$  and  $\eta$  for each outer scale and evaluated the weighted  $\chi^2$ 's for the resulting  $\sigma_{\text{RM}}$  profiles. All three values of  $\Lambda_{\max}$  under investigation give reasonable fits to the observed  $\sigma_{\text{RM}}$  profile along the whole radio source. The fit for  $\Lambda_{\max} = 65$  kpc is marginally better than for the other two values ( $\chi_{\text{red}}^2 = 1.8$ ), consistent with the results of Sec. 4.6.3 below. In this case the central magnetic field strength is  $3.5 \pm 1.2 \mu\text{G}$  and the break radius is  $16 \pm 11$  kpc. For the power spectrum with  $\Lambda_{\max} = 65$  kpc and these best-fitting parameters, I also produced three-dimensional simulations at a resolution of 1.25 arcsec. Even though the fitting procedure is based only on the low-resolution data, this model also reproduces the 1.25-arcsec profile very well ( $\chi_{\text{red}}^2 = 0.7$ ). Combining the values of  $\chi^2$  for the two resolutions, using the 1.25-arcsec profile close to the core and the 5.5-profile at larger distances, I find  $\chi_{\text{red}}^2 = 1.8$ .

Figure 4.11 shows a comparison of the observed radial profiles for rms Faraday  $\sigma_{\text{RM}}$  and  $\langle \text{RM} \rangle$  with the synthetic ones derived for this model. The synthetic  $\sigma_{\text{RM}}$  profile plotted in Fig. 4.11 is the mean over 35 simulations and may be compared directly with the observations. In contrast, the  $\langle \text{RM} \rangle$  profile is derived from a single example realization. It is important to emphasize that the latter is *one example of a random process*, and is not expected to fit the observations; rather, I aim to compare the fluctuation amplitude as a function of position.

The values of  $B_0$  and  $\chi_{\text{red}}^2$  for all of the three-dimensional simulations, together with  $\eta$  and  $r_m$  for the single and double power-law profiles, respectively, are summarized in Table 4.6.

### 4.6.3 The outer scale of the magnetic-field fluctuations

The theoretical RM structure function for uniform field strength, density and path length and a power spectrum with a low-frequency cut-off should asymptotically approach a constant value ( $2\sigma_{\text{RM}}^2$  for a large enough averaging region) at separations  $\gtrsim \Lambda_{\max}$ . The observed RM structure function of the whole source is heavily modified from this theoretical one by the scaling of the electron gas density and magnetic field at large separations, which acts to suppress power on large spatial scales. In Sec. 4.5 I therefore limited the study of the structure function to sub-regions of 3C 449 where uniformity of field strength, density and path length (and therefore of the power-

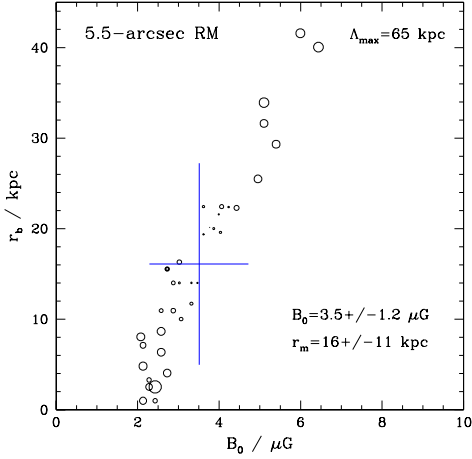


Figure 4.10: Distribution of the best-fitting values of  $B_0$  and  $r_m$  from 35 sets of simulations, each covering ranges of  $0.5 - 10 \mu\text{G}$  in  $B_0$  and  $0 - 50 \text{ kpc}$  in  $r_m$ . The sizes of the circles are proportional to  $\chi^2$  and the blue cross represents the means of the distribution weighted by  $1/\chi^2$ . The plot shows the degeneracy between  $B_0$  and  $r_m$  described in the text.

spectrum amplitude) is a reasonable assumption, inevitably limiting our ability to constrain the power spectrum on the largest scales.

Now that I have an adequate model for the variation of  $n_e(r)\langle B^2(r) \rangle^{1/2}$  with radius (Eq. 4.6), I can correct for it to derive what I call the pseudo-structure function – that is the structure function for a power-spectrum amplitude, which is constant over the source. This can be compared directly with the structure functions derived from the Hankel transform of the power spectrum. To evaluate the pseudo-structure function, I divided the observed 5.5-arcsec RM image by the function

$$\left[ \int_0^L n_e(r)^2 B(r)^2 dl \right]^{1/2} \quad (4.7)$$

(Enßlin & Vogt 2003), where the radial variations of  $n_e$  and  $B$  are those of the best-fitting model (Sec. 4.6) and the upper integration limit  $L$  has a length of 10 times the core radius. The integral was normalized to unity at the position of the radio core: this is equivalent to fixing the field and gas density at their maximum values and holding them constant everywhere in the group. The normalization of the pseudo-structure function should then be quite close to that of the two central jet regions.

The pseudo-structure function is shown in Fig. 4.12(a) together with the predictions for the BPL power spectra with  $\Lambda_{\text{max}}=205, 65$  and  $20 \text{ kpc}$ . As expected, the normalization of the pseudo-structure function is consistent with that of the jets (Fig. 4.7a and b).

The comparison between the synthetic and observed pseudo-structure functions indicates firstly that they agree very well at small separations, independent of the value of  $\Lambda_{\text{max}}$ . This confirms that the best BPL power spectrum found from a combined fit to all six sub-regions is a very good fit over the entire source. Secondly, despite the poor sampling on very large scales, the asymptotic values of the predicted structure functions for the three values of  $\Lambda_{\text{max}}$  are sufficiently different from each other that it is possible to determine an approximate outer

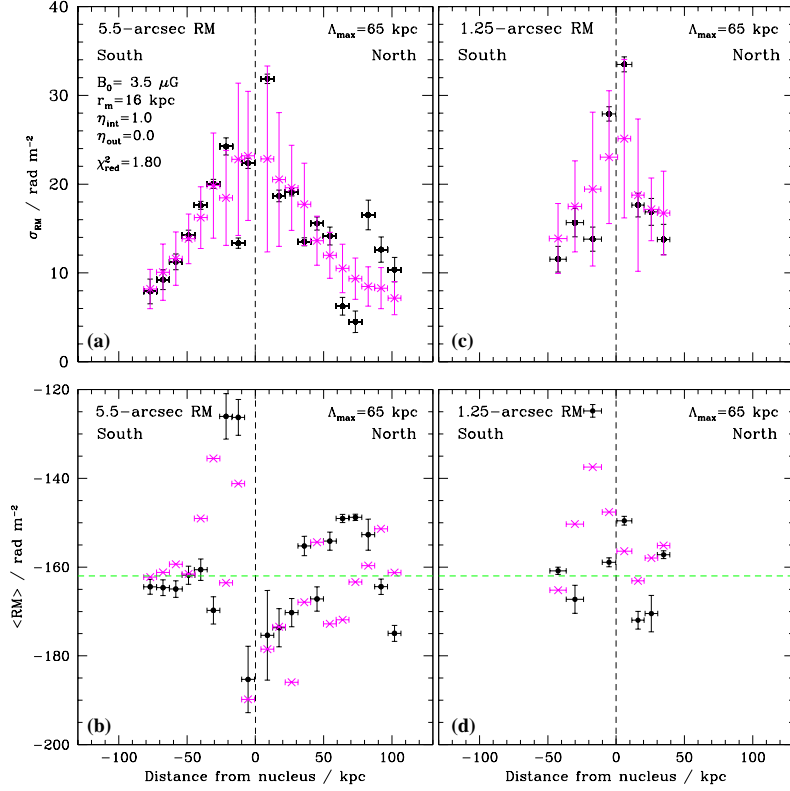


Figure 4.11: Comparison between observed and synthetic profiles of rms and mean Faraday rotation at resolutions of 5.5 arcsec (a and b) and 1.25 arcsec (c and d). The synthetic profiles are derived from the best-fitting model with  $\Lambda_{\text{max}} = 65 \text{ kpc}$ . The black points represent the data with vertical bars corresponding to the rms fitting error. **(a)** and **(c)**: Profiles of  $\sigma_{\text{RM}}$ . The magenta crosses represent the mean values from 35 simulations at 5.5-arcsec resolution, and the vertical bars are the rms scatter in these profiles due to sampling. **(b)** and **(d)**: Profiles of  $\langle \text{RM} \rangle$  derived from single example realizations at 5.5 and 1.25-arcsec resolutions.

scale. The model with  $\Lambda_{\text{max}}=65 \text{ kpc}$  gives the best representation of the data. The fit is within the estimated errors except for a marginal discrepancy at the very largest (and therefore poorly sampled) separations. That with  $\Lambda_{\text{max}}=20 \text{ kpc}$  is inconsistent with the observed pseudo-structure function for any separation  $\gtrsim 20 \text{ arcsec}$  ( $\approx 6 \text{ kpc}$ ) where the sampling is still very good, and is firmly excluded. The model with  $\Lambda_{\text{max}}=205 \text{ kpc}$  has slightly, but significantly too much power on large scales.

I emphasize that such estimate of the outer scale of the RM fluctuations is essentially independent of the functional form assumed for the variation of field strength with radius in the central region, which affects the structure function only for small separations. The results are almost identical if I fit the field-strength variation with either the profile of Eq. 4.5 (with  $\eta \approx 0$ ) or that of Eq. 4.6.

As for the structure functions of individual regions, the pseudo-structure function at large

separations is clearly affected by poor sampling: this increases the errors, but does not produce any bias in the derived values. At large radii, however, the integral in Eq. 4.7 becomes small, so the noise on the RM image is amplified. This is a potential source of error, and I therefore checked the results using numerical simulations. I calculated the mean and rms structure functions for sets of realizations of RM images generated with the `rm_sim` code for different values of  $\Lambda_{\max}$ . These structure functions are plotted in Figs. 4.12(b) and (c).

The main difference between the model structure functions derived from simulations and the pseudo-structure functions described earlier is that the former show a steep decline in power on large scales in place of a plateau. This occurs because the smooth fall-off in density and magnetic field strength with distance from the nucleus suppresses the fluctuations in RM on large scales.

The results of the simulations confirm the analysis using the pseudo-structure function. The mean model structure function with  $\Lambda_{\max} = 65$  kpc again fits the data very well, except for a marginal discrepancy at the largest scales. In view of the deviations from spherical symmetry on large scales evident in the X-ray emission surrounding 3C 449 (Fig. 4.1), I do not regard this as a significant effect.

In order to check that the best-fitting density and field model also reproduces the data at small separations, I repeated the analysis at 1.25-arcsec resolution. The observed pseudo-structure function is shown in Fig. 4.12(d), together with the the predictions for the BPL power spectrum with  $\Lambda_{\max} = 205, 65$  and  $20$  kpc. The observed structure function is compared with the mean from 35 simulations with  $\Lambda_{\max} = 65$  kpc in Fig. 4.12(e). In both cases, the agreement for  $\Lambda_{\max} = 65$  kpc is excellent.

In Fig. 4.13, example realizations of this model with the best-fitting field variation are shown for resolutions of 1.25 and 5.5 arcsec alongside the observed RM images.

## 4.7 Summary and comparison with other sources

### 4.7.1 Summary

In this work I have studied the structure of the magnetic field associated with the ionized medium around the radio galaxy 3C 449. I have analysed images of linearly polarized emission with resolutions of 1.25 arcsec and 5.5 arcsec FWHM at seven frequencies between 1.365 and 8.385 GHz, and produced images of degree of polarization and rotation measure. The RM images at both the angular resolutions show patchy and random structures. In order to study the spatial statistics of the magnetic field, I used a structure-function analysis and performed two- and three-dimensional RM simulations. I can summarize the results as follows.

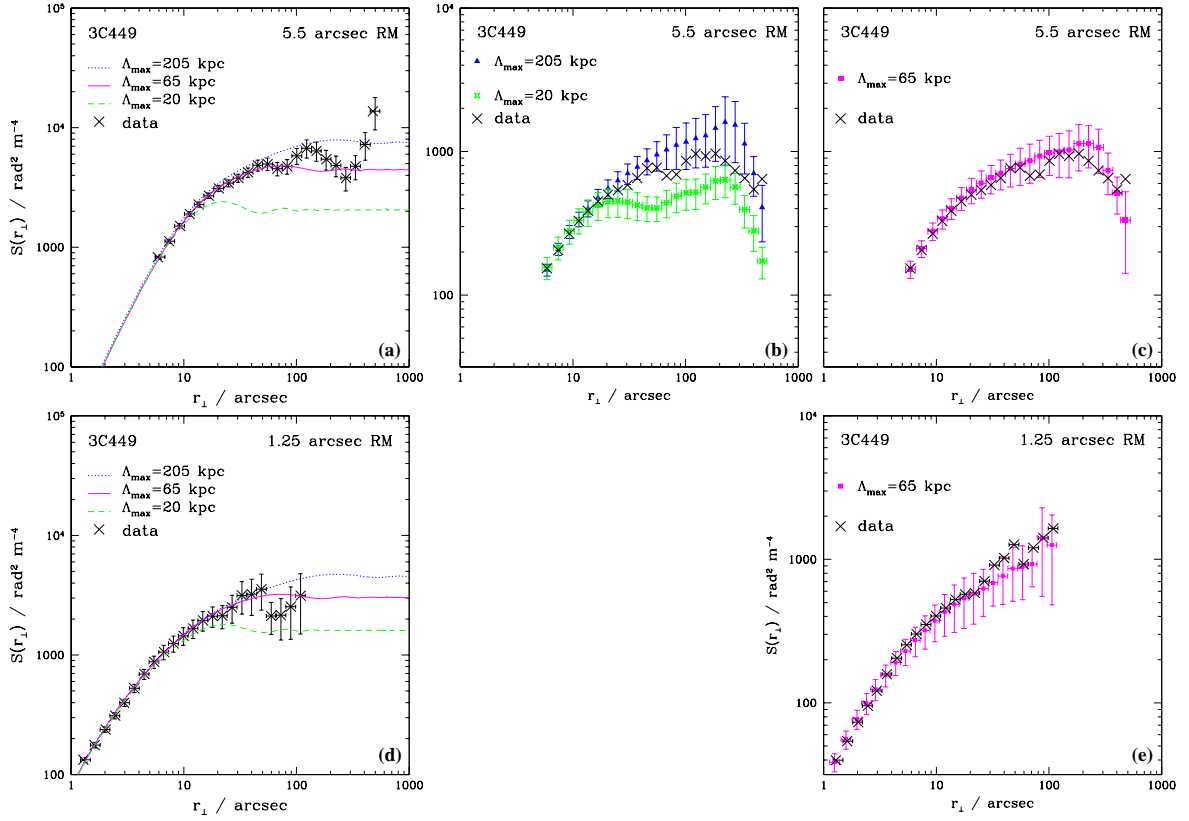


Figure 4.12: **(a)**: Comparison of the observed pseudo-structure function of the 5.5-arcsec RM image as described in the text (points) with the predictions of the BPL model (curves, derived using a Hankel transform). The predicted curves are for  $\Lambda_{\max}=205$  (blue dotted), 65 (continuous magenta) and 20 kpc (green dashed). **(b)** and **(c)**: structure functions of the observed (points) and synthetic 5.5-arcsec RM images produced with the  $\Lambda_{\max}=205, 20$  kpc and  $\Lambda_{\max}=65$  kpc, respectively. **(d)** and **(e)** as **(a)** and **(c)** respectively, but at 1.25-arcsec resolution. The error bars are the rms from 35 structure functions at a given  $\Lambda_{\max}$ , in **(a)** and **(d)** are representative error bars from the model with  $\Lambda_{\max}=65$  kpc.

1. The absence of deviations from  $\lambda^2$  rotation over a wide range of polarization position angle implies that a pure foreground Faraday screen with no mixing of radio-emitting and thermal electrons is a good approximation for 3C 449 (Sec. 4.3).
2. The best estimate for the Galactic contribution to the RM of 3C 449 is a constant value of  $-160.7 \text{ rad m}^{-2}$  (Sec. 4.3.2).
3. The dependence of the degree of polarization on wavelength is well fitted by a Burn law. This is also consistent with pure foreground rotation, with the residual depolarization observed at the higher resolution being due to unresolved RM fluctuations across the beam (Sec. 4.4). There is no evidence for a detailed correlation of radio-source structure with either RM or depolarization.
4. There is no obvious anisotropy in the RM distribution, consistent with the assumption that the magnetic field is an isotropic, Gaussian random variable.
5. The RM structure functions for six different regions of the source are consistent with the hypothesis that only the amplitude of the RM power spectrum varies across the source.
6. A broken power-law spectrum of the form given in Eq. 4.4 with  $q_l = 2.07$ ,  $q_h = 2.98$ ,  $f_b = 0.031 \text{ arcsec}^{-1}$  and  $f_{\text{max}} = 1.67 \text{ arcsec}^{-1}$  (corresponding to a spatial scale  $\Lambda_{\text{min}} = 0.2 \text{ kpc}$ ) is consistent with the observed structure functions and depolarizations for all six regions. No single power law provides a good fit to all of the structure functions.
7. The high-frequency cut-off in the power spectrum is required to model the depolarization data.
8. The profiles of  $\sigma_{\text{RM}}$  strongly suggest that most of the fluctuating component of RM is associated with the intra-group gas, whose core radius is comparable with the characteristic scale of the profile (Sec. 4.3.1). The symmetry of the profile is consistent with the idea that the radio source axis is close to the plane of the sky.
9. I therefore simulated the RM distributions expected for an isotropic, random magnetic field in the hot plasma surrounding 3C 449, assuming the density model derived by Croston et al. (2008).
10. These three-dimensional simulations show that the dependence of magnetic field on density is best modeled by a broken power-law function with  $B(r) \propto n_e(r)$  close to the nucleus and  $B(r) \approx \text{constant}$  at larger distances.
11. With this density model, the best estimate of the central magnetic field strength is  $B_0 = 3.5 \pm 1.2 \mu\text{G}$ .

12. Assuming these variations of density and field strength with radius, a structure-function analysis can be used to estimate the outer scale  $\Lambda_{\max}$  of the magnetic-field fluctuations. I find excellent agreement for  $\Lambda_{\max} \approx 65$  kpc ( $f_{\min} = 0.0053$  arcsec $^{-1}$ ).

#### 4.7.2 Comparison with other sources

These results are qualitatively similar to those of Laing et al. (2008) on 3C 31. The maximum RM fluctuation amplitudes are similar in the two sources, as are their environments. For spherically-symmetric gas density models, the central magnetic fields are almost the same:  $B_0 \approx 2.8\mu\text{G}$  for 3C 31 and  $3.5\mu\text{G}$  for 3C 449. Both results are consistent with the idea that the RM fluctuation amplitude in galaxy groups and clusters scales roughly linearly with density, ranging from a few rad m $^{-2}$  in the much sparsest environments (e.g. NGC 315; Laing et al. 2006a), through intermediate values  $\approx 30 - 100$  rad m $^{-2}$  in rich groups such as 3C 31 and 3C 449 to  $\sim 10^4$  rad m $^{-2}$  in the centers of clusters with cool cores.

The RM distribution of 3C 31 is asymmetrical, the northern (approaching) side of the source showing a much lower fluctuation amplitude, consistent with the inclination of  $\approx 50^\circ$  estimated by Laing & Bridle (2002a). Detailed modeling of the RM profile led Laing et al. (2008) to suggest that there is a cavity in the X-ray gas, but this would have to be significantly larger than the observed extent of the radio lobes and is, as yet, undetected in X-ray observations. A broken power-law scaling of magnetic field with density, similar to that found for 3C 449 in the present work, would also improve the fit to the  $\sigma_{\text{RM}}$  profile for 3C 31; alternatively, the effects of cavities around the inner lobes and spurs of 3C 449 might be significant. Deeper X-ray observations of both sources are needed to resolve this issue. In neither case is the magnetic field dynamically important: for 3C 449 the ratio of the thermal and magnetic-field pressures is  $\approx 30$  at the nucleus and  $\approx 400$  at the core radius of the group gas,  $r_c = 19$  kpc. The magnetic field is therefore not dynamically important, as in 3C 31.

The magnetic-field power spectrum in both sources can be fit by a broken power-law form. The low-frequency slopes are 2.1 and 2.3 for 3C 449 and 3C 31 respectively. In both cases, the power spectrum steepens at higher spatial frequencies, but for 3C 31 a Kolmogorov index (11/3) provides a good fit, whereas I find that the depolarization data for 3C 449 require a cut-off below a scale of 0.2 kpc and a high-frequency slope of 3.0. The break scales are  $\approx 5$  kpc for 3C 31 and  $\approx 11$  kpc for 3C 449. It is important to note that the simple parametrized form of the power spectrum is not unique, and that a smoothly curved function would fit the data equally well.

The gas-density structure on large scales in the 3C 31 group is uncertain, so Laing et al. (2008) could only give a rough lower limit to the outer scale of magnetic-field fluctuations,  $\Lambda_{\max} \gtrsim 70$  kpc. For 3C 449, we find  $\Lambda_{\max} \approx 65$  kpc. The projected distance between 3C 449 and its nearest

neighbour is  $\approx 33$  kpc (Birkinshaw et al. 1981), similar to the scale on which the jets first bend through large angles (Fig. 4.1). As in 3C 31, it is plausible that the outer scale of magnetic-field fluctuations is set by interactions with companion galaxies in the group.

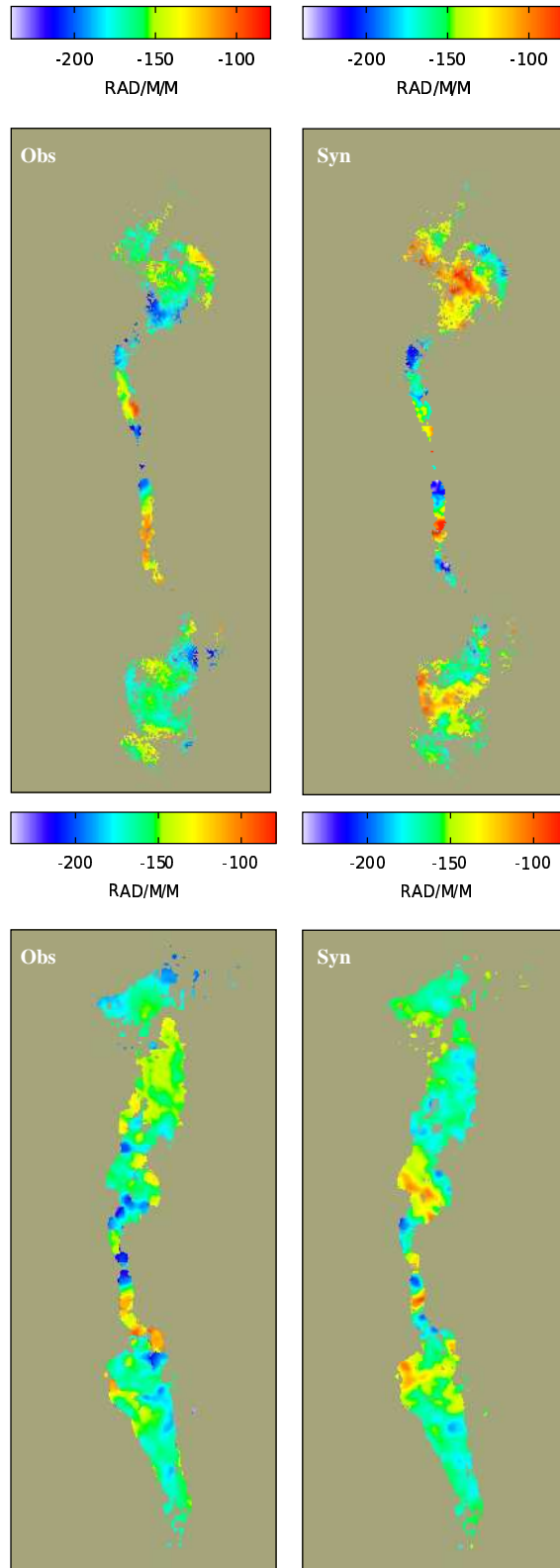


Figure 4.13: Comparison of observed and representative synthetic distribution of Faraday RM at 1.25 arcsec and 5.5 arcsec. The synthetic images have been produced for the best-fitting model with  $\Lambda_{\text{max}} = 65$  kpc. The colour scale is the same for all displays.

## Chapter 5

# Ordered magnetic fields around radio galaxies: evidence for interaction with the environment <sup>†</sup>

Most of the RM images of radio galaxies published so far show patchy structures with no clear preferred direction, consistent with isotropic foreground fluctuations over a range of linear scales ranging from tens of kpc to  $\lesssim 100$  pc (e.g. 3C 449, Chapter 4; see also Govoni et al. 2006; Guidetti et al. 2008; Laing et al. 2008; Kuchar & Enßlin 2009; Bonafede et al. 2010). Numerical modelling has demonstrated that this type of complex RM structure can be accurately reproduced if the magnetic field is randomly variable with fluctuations on a wide range of spatial scales, and is spread throughout the whole group or cluster environment (Chapter 4; see also Murgia et al. 2004; Govoni et al. 2006; Guidetti et al. 2008; Laing et al. 2008; Bonafede et al. 2010). These authors used forward modelling, together with estimators of the spatial statistics of the RM distributions (structure and autocorrelation functions or a multi-scale statistic) to estimate the field strength, its relation to the gas density and its power spectrum. The technique of Bayesian maximum likelihood has also been used for this purpose (Enßlin & Vogt 2005; Kuchar & Enßlin 2009).

In order to derive the three-dimensional magnetic field power spectrum, all of these authors had to assume statistical isotropy for the field, since only the component of the magnetic field along the line-of-sight contributes to the observed RM. This assumption is consistent with the absence of a preferred direction in most of the RM images.

In contrast, the present Chapter reports on *anisotropic* RM structures, observed in lobed radio galaxies located in different environments, ranging from a small group to one of the richest clusters

---

<sup>†</sup>Guidetti et al. 2011, MNRAS, in press

of galaxies. The RM images of radio galaxies presented in this Chapter show clearly anisotropic “banded” patterns over part or all of their areas. In some sources, these banded patterns coexist with regions of isotropic random variations. The magnetic field responsible for these RM patterns must, therefore, have a preferred direction.

One source whose RM structure is dominated by bands is already known: M 84 (Laing & Bridle 1987). In addition, there is some evidence for RM bands in sources which also show strong irregular fluctuations, such as Cygnus A (Carilli & Taylor 2002). It is possible, however, that some of the claimed bands could be due to imperfect sampling of an isotropic RM distribution with large-scale power, and I return to this question in Section 5.8.1.

In this Chapter I present new RM images of three sources which show spectacular banded structures, together with improved data for M 84. The environments of all four sources are well characterized by modern X-ray observations, and I give the first comprehensive description of the banded RM phenomenon. I present an initial attempt to interpret the phenomenon as a consequence of source-environment interactions and to understand the difference between it and the more usual irregular RM structure.

The RM images reported are derived from new or previously unpublished archive Very Large Array data for the nearby radio galaxies 0206+35, M 84 (Laing et al. in preparation), 3C 270 (Laing, Guidetti & Bridle in preparation) and 3C 353 (Swain, private communication; see Swain 1996).

## 5.1 The Sample

High quality radio and X-ray data are available for all of the sources. In this Section I summarize those of their observational properties which are relevant to this RM study. A list of the sources and their general parameters is given in Table 5.1, while Table 5.2 shows the X-ray parameters taken from the literature and equipartition parameters derived from radio observations in this work.

The sources were observed with the VLA at several frequencies, in full polarization mode and with multiple configurations so that the radio structure is well sampled. The VLA observations, data reduction and detailed descriptions of the radio structures are given for 0206+35 and M 84 by Laing, Guidetti et al. (in preparation), for 3C 270 by Laing, Guidetti & Bridle (in preparation), and for 3C 353 by Swain (1996). All of the radio maps show a core, two sided jets and a double-lobed structure with sharp brightness gradients at the leading edges of both lobes. The synchrotron minimum pressures are all significantly lower than the thermal pressures of the external medium (Table 5.2).

All of the sources have been observed in the soft X-ray band by more than one satellite,

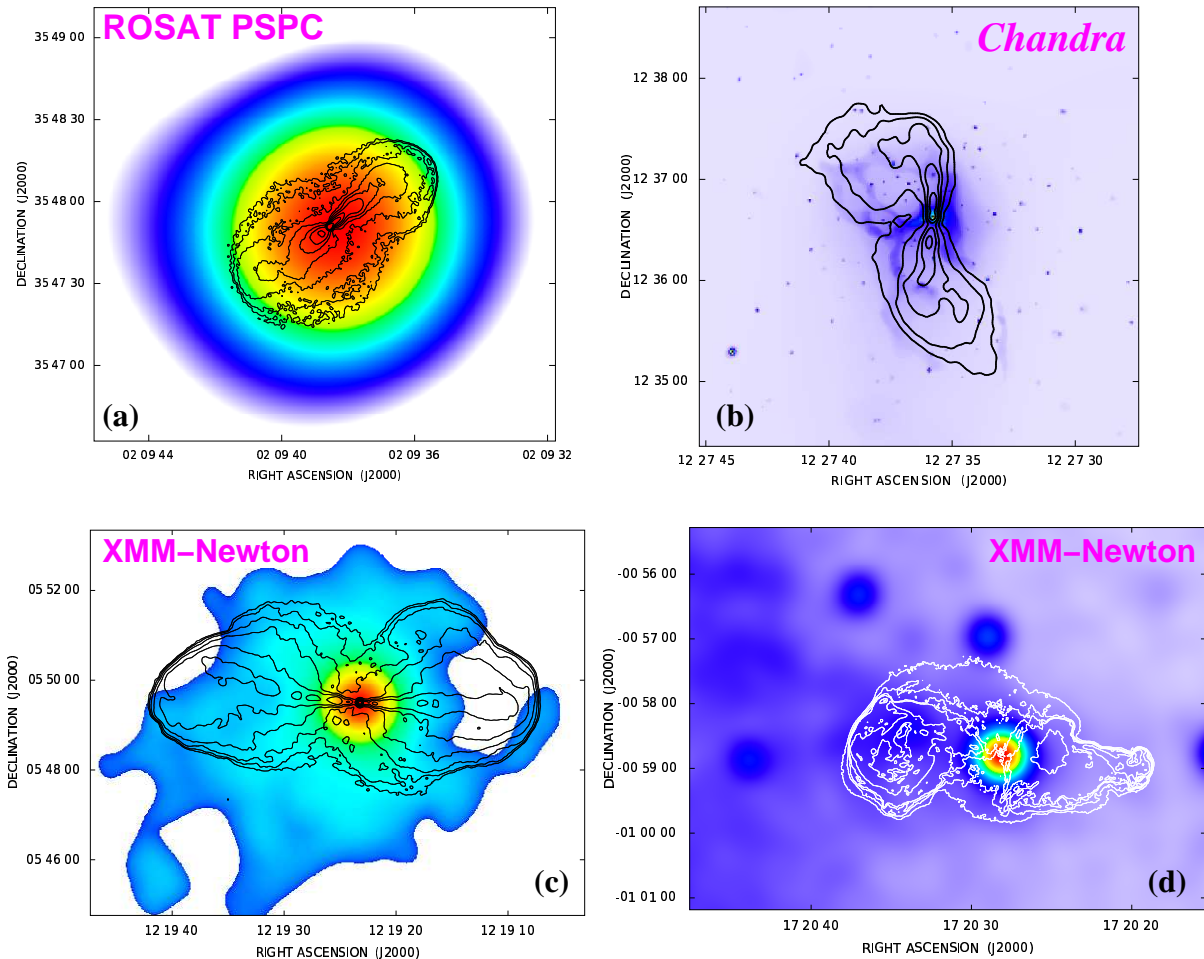


Figure 5.1: X-ray images overlaid with radio contours for all sources: **(a)** 0206+35: 1385.1 MHz VLA radio map with 1.2 arcsec FWHM; the contours are spaced by factor of 2 between 0.06 and 15 mJy beam<sup>-1</sup>. The ROSAT PSPC image (Worrall & Birkinshaw 2000), is smoothed with a Gaussian of  $\sigma = 30$  arcsec. **(b)** M84: 1413.0 MHz VLA radio map with 4.5 arcsec FWHM; the contours are spaced by factor of 2 between 1 and 128 mJy beam<sup>-1</sup>. The Chandra (Finoguenov & Jones 2001) image is a wavelet reconstruction on angular scales from 4 up to 32 arcsec. **(c)** 3C 270: 1365.0 MHz VLA radio map with 5.0 arcsec FWHM; the contours are spaced by factor of 2 between 0.45 and 58 mJy beam<sup>-1</sup>. The XMM-Newton image (Croston, Hardcastle & Birkinshaw 2005) is smoothed with a Gaussian of  $\sigma = 26$  arcsec. **(d)** 3C 353: 1385.0 MHz VLA radio map with 1.3 arcsec FWHM; the contours are spaced by factor of 2 between 0.35 and 22 mJy beam<sup>-1</sup>. The XMM-Newton image (Goodger et al. 2008) is smoothed with a Gaussian of  $\sigma = 30$  arcsec. The Chandra image of 3C 270 is displayed in logarithmic scale.

Table 5.1: General optical and radio properties: Col. 1: source name; Cols. 2&3: position; Col. 4: redshift; Col. 5: conversion from angular to spatial scale with the adopted cosmology; Col. 6: Fanaroff-Riley class; Col. 7: the largest angular size of the radio source; Col. 8: radio power at 1.4 GHz; Col. 9: angle to the line of sight of the jet axis; Col. 10: environment of the galaxy; Col. 11: reference.

source	RA [J2000]	DEC [J2000]	z	kpc/arcsec	FR class	LAS [arcsec]	$\log P_{1.4}$ [W Hz <sup>-1</sup> ]	$\theta$ [degree]	env.	ref.
0206+35	02 09 38.6	+35 47 50	0.0377	0.739	I	90	24.8	40	group	1
3C 353	17 20 29.1	-00 58 47	0.0304	0.601	II	186	26.3	90	poor cluster	2
3C 270	12 19 23.2	+05 49 31	0.0075	0.151	I	580	24.4	90	group	3
M 84	12 25 03.7	+12 53 13	0.0036	0.072	I	150	23.2	60	rich cluster	3

References for the environmental classification: (1) Miller et al. (2002); (2) de Vaucouleurs et al. (1991); (3) Trager et al. (2000).

Table 5.2: X-ray and radio equipartition parameters for all the sources. Col. 1: source name; Col. 2: X-ray energy band; Col. 3: average thermal temperature; Cols. 4,5,6 and 7,8,9 best-fitting core radii, central densities and  $\beta$  parameters for the outer and inner  $\beta$  models, respectively; Col. 10: average thermal pressure at the midpoint of the radio lobes; Cols. 11&12: minimum synchrotron pressure and corresponding magnetic field; Col.13: references for the X-ray models.

source	band [keV]	$kT$ [keV]	$r_{cx_{out}}$ [kpc]	$n_{0_{out}}$ [cm <sup>-3</sup> ]	$\beta_{out}$	$r_{cx_{in}}$ [kpc]	$n_{0_{in}}$ [cm <sup>-3</sup> ]	$\beta_{in}$	$P_0$ [dyne cm <sup>-2</sup> ]	$P_{min}$ [dyne cm <sup>-2</sup> ]	$B_{Pmin}$ $\mu G$	ref.
0206+35	0.2-2.5	$1.30^{+1.30}_{-0.30}$	22.2	$2.4 \times 10^{-3}$	0.35	0.85	0.42	0.70	$9.6 \times 10^{-12}$	$4.31 \times 10^{-13}$	5.70	1, 2
3C 353	"	$4.33^{+0.25}_{-0.24}$								$1.66 \times 10^{-12}$	11.2	3
3C 270	0.3-7.0	$1.45^{+0.23}_{-0.01}$	36.8	$7.7 \times 10^{-3}$	0.30	1.1	0.34	0.64	$5.75 \times 10^{-12}$	$1.64 \times 10^{-13}$	3.71	4
M 84	0.6-7.0	$0.60^{+0.05}_{-0.05}$				$5.28 \pm 0.08$	0.42	$1.40 \pm 0.03$	$1.70 \times 10^{-11}$	$1.07 \times 10^{-12}$	9.00	5

References: (1) Worrall & Birkinshaw (2000); (2) Worrall, Birkinshaw & Hardcastle (2001); (3) Iwasawa et al. (2000); (4) Croston et al. (2008); (5) Finoguenov & Jones (2001).

allowing the detection of multiple components on cluster/group and sub-galactic scales. The X-ray morphologies are characterized by a compact source surrounded by extended emission with low surface brightness. The former includes a non-thermal contribution, from the core and the inner regions of the radio jets and, in the case of 0206+35 and 3C 270, a thermal component which is well fitted by a small core radius  $\beta$  model. The latter component is associated with the diffuse intra-group or intra-cluster medium. Parameters for all of the thermal components, derived from X-ray observations, are listed in Table 5.2. Because of the irregular morphology of the hot gas surrounding 3C 353 and M 84, it has not been possible to fit  $\beta$  models to their X-ray radial surface brightness profiles.

### 5.1.1 0206+35

0206+35 is an extended Fanaroff-Riley Class I (FRI; Fanaroff & Riley 1974) radio source whose optical counterpart, UGC 1651, is a D-galaxy, a member of a dumb-bell system at the centre of a group of galaxies. At a resolution of 1.2 arcsec the radio emission shows a core, with smooth two-sided jets aligned in the NW-SE direction and surrounded by a diffuse and symmetric halo. Laing & Bridle (in preparation) have estimated that the jets are inclined by  $\approx 40^\circ$  with respect to the line of sight, with the main (approaching) jet in the NW direction.

0206+35 has been observed with both the *ROSAT* PSPC and HRI instruments (Worrall & Birkinshaw 1994, 2000; Trussoni et al. 1997) and with *Chandra* (Worrall, Birkinshaw & Hardcastle 2001). The X-ray emission consists of a compact source surrounded by a galactic atmosphere which merges into the much more extended intra-group gas. The radius of the extended halo observed by the *ROSAT* PSPC is  $\approx 2.5$  arcmin (Fig. 5.1a). The *ROSAT* and *Chandra* X-ray surface brightness profiles are well fit by the combination of  $\beta$  models with two different core radii and a power-law component (Hardcastle, private communication; Table 5.2).

### 5.1.2 3C 270

3C 270 is a radio source classified as FRI in most of the literature, although in fact, the two lobes have different FR classifications at low resolution (Laing, Guidetti & Bridle in preparation). The optical counterpart is the giant elliptical galaxy NGC 4261, located at the centre of a nearby group. The radio source has a symmetrical structure with a bright core and twin jets, extending E-W and completely surrounded by lobes. The low jet/counter-jet ratio indicates that the jets are close to the plane of the sky, with the Western side approaching (Laing, Guidetti & Bridle in preparation).

The XMM-Newton image (Fig. 5.1c) shows a disturbed distribution with regions of low surface-brightness (cavities) at the positions of both radio lobes. A recent *Chandra* observation (Worrall et al. 2010) shows “wedges” of low X-ray surface brightness surrounding the inner jets (see also Croston, Hardcastle & Birkinshaw 2005, Finoguenov et al. 2006, Jetha et al. 2007, Croston et al. 2008). The overall surface brightness profile is accurately reproduced by a point source convolved with the *Chandra* point spread function plus a double  $\beta$  model (Croston et al. 2008, *projb* model). Croston et al. 2008 found no evidence for a temperature gradient in the hot gas. The group is characterized by high temperature and low luminosity (Finoguenov et al. 2006), which taken together provide a very high level of entropy. This might be a further sign of a large degree of impact of the AGN on the environment.

### 5.1.3 3C 353

3C 353 is an extended FR II radio source identified with a D-galaxy embedded at the periphery of a cluster of galaxies. The best estimate for the inclination of the jets is  $\approx 90^\circ$  (Swain, Bridle & Baum 1998). The eastern jet is slightly brighter and ends in a well-defined hot spot. The radio lobes have markedly different morphologies: the eastern lobe is round with sharp edges, while the western lobe is elongated with an irregular shape. The location of the source within the cluster is of particular interest for this work and might account for the different shapes of the lobes. Fig. 5.1(d) shows the XMM-Newton image overlaid on the radio contours. The image shows only the NW part of the cluster, but it is clear that the radio source lies on the edge of the X-ray emitting gas distribution. so that the round eastern lobe is encountering a higher external density and is probably also behind a larger column of Faraday-rotating material (Iwasawa et al. 2000, Goodger et al. 2008). In particular, the image published by Goodger et al. (2008) shows that the gas density gradient persists on larger scales.

### 5.1.4 M 84

M 84 is a giant elliptical galaxy located in the Virgo Cluster at about 400 kpc from the core. Optical emission-line imaging shows a disk of ionized gas around the nucleus, with a maximum detected extent of  $20 \times 7 \text{ arcsec}^2$  (Hansen, Norgaard-Nielsen & Jorgensen 1985; Baum et al. 1988; Bower et al. 1997, 2000). The radio emission of M 84 (3C 272.1) has an angular extension of about 3 arcmin ( $\approx 11 \text{ kpc}$ ) and shows an unresolved core in the nucleus of the galaxy, two resolved jets and a pair of wide lobes (Laing & Bridle 1987; Laing et al. in preparation). The inclination to the line-of-sight of the inner jet axis is  $\sim 60^\circ$ , with the northern jet approaching, but there is a noticeable bend in the counter-jet very close to the nucleus, which complicates modelling (Laing & Bridle in preparation). After this bend, the jets remain straight for  $\approx 40 \text{ arcsec}$ , then both of them bend eastwards by  $\sim 90^\circ$  and fade into the radio emission of the lobes.

The morphology of the X-ray emission has a H-shape made up of shells of compressed gas surrounding cavities coincident with both the radio lobes (Finoguenov et al. 2008; Finoguenov et al. 2006; Finoguenov & Jones 2001). This shape, together with the fact that the initial bending of the radio jets has the same direction and is quite symmetrical, suggests a combination of interaction with the radio plasma and motion of the galaxy within the cluster (Finoguenov & Jones 2001). The ratio between the X-ray surface brightness of the shells of the compressed gas and their surroundings is  $\approx 3$  and is almost constant around the source. The shells are regions of enhanced pressure and density and low entropy: the amplitude of the density enhancements (a factor of  $\approx 3$ ) suggests that they are produced by weak shock waves (Mach number  $\mathcal{M} \sim 1.3$ ) driven by the

expanding lobes (Finoguenov et al. 2006).

## 5.2 Analysis of RM and depolarization images

The observational analysis is based on the following procedure. I first produced RM and Burn law  $k$  images at two different angular resolutions for each source and searched for regions with high  $k$  or correlated RM and  $k$  values, which could indicate the presence of internal Faraday rotation and/or strong RM gradients across the beam (Secs. 3.2 and 3.3). In regions with low  $k$  where the variations of RM are plausibly isotropic and random, I then used the structure function (defined in Eq. 3.13) to derive the power spectrum of the RM fluctuations. Finally, to investigate the depolarization in the areas of isotropic RM, and hence the magnetic field power on small scales, I made numerical simulations of the Burn law  $k$  using the model power spectrum with different minimum scales and compared the results with the data.

I assumed RM power spectra of the form:

$$\begin{aligned}\hat{C}(f_{\perp}) &= C_0 f_{\perp}^{-q} & f_{\perp} \leq f_{\max} \\ &= 0 & f_{\perp} > f_{\max}\end{aligned}\tag{5.1}$$

where  $f_{\perp}$  is a scalar spatial frequency and fit the observed structure function (including the effect of the observing beam) using the Hankel-transform method described by Laing et al. (2008) to derive the amplitude,  $C_0$  and the slope,  $q$ . To constrain the RM structure on scales smaller than the beamwidth, I estimated the minimum scale of the best fitted field power spectrum,  $\Lambda_{\min} = 1/f_{\max}$ , which predicts a mean value of  $k$  consistent with the observed one.

In this work, I am primarily interested in estimating the RM power spectrum over limited areas, and I made no attempt to determine the outer scale of fluctuations.

## 5.3 Rotation measure images

The RM images and associated rms errors were produced by weighted least-squares fitting to the observed polarization angles  $\Psi(\lambda)$  as a function of  $\lambda^2$  (Eq. 3.1) at three or four frequencies (Table 5.3, see also the Appendix) using the `rmfit` task in the `RMFIT` package.

Each RM map was calculated only at pixels with rms polarization-angle uncertainties  $<10^\circ$  at all frequencies. I refer only to the lower-resolution RM and  $k$  images for 3C 270 and M 84 (Table 5.3), as they show more of the faint, extended regions of these sources and are fully consistent with the higher-resolution versions. The RM image of M 84 is consistent with that

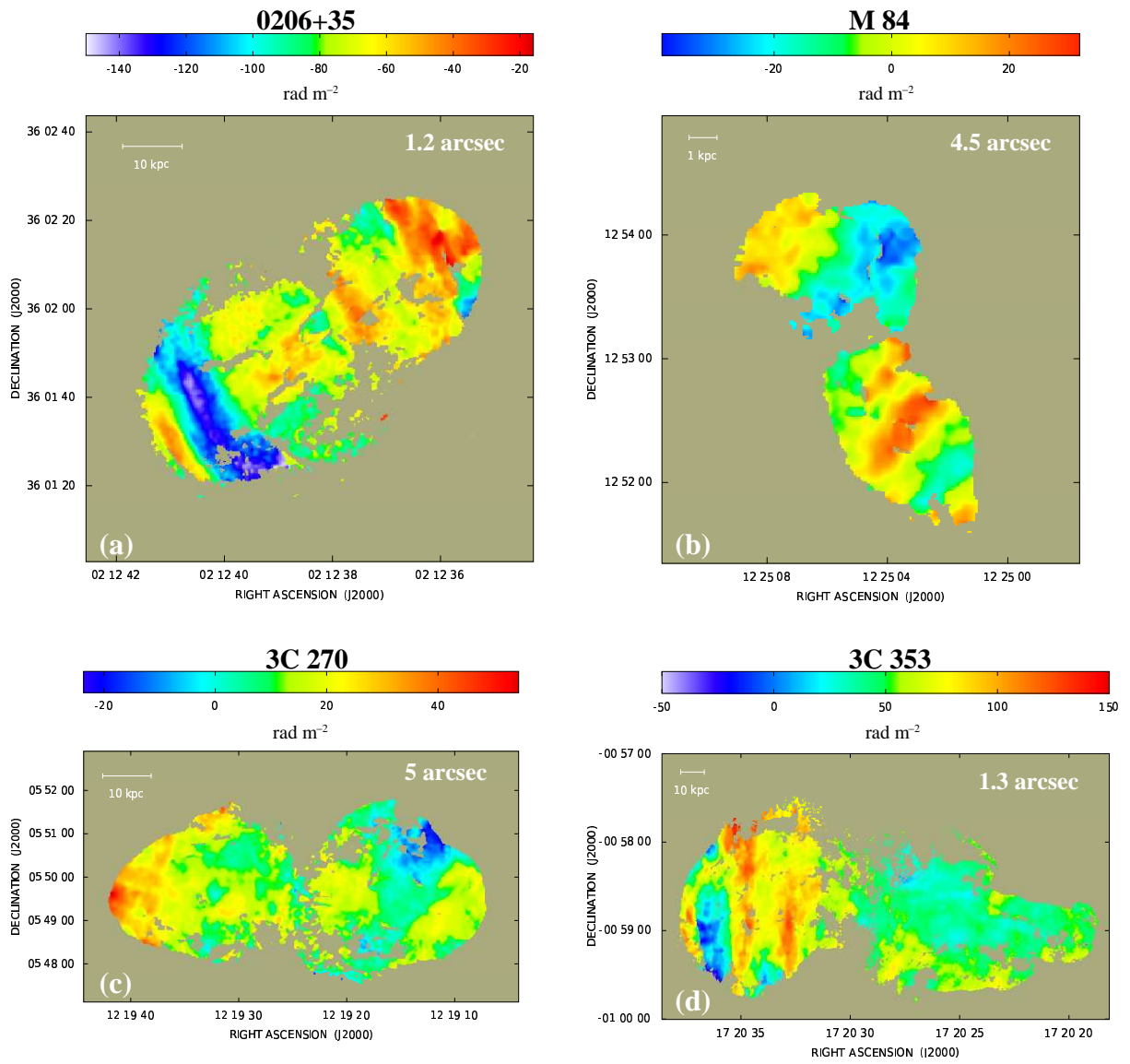


Figure 5.2: RM images for all sources: (a) 0206+35; (b) M 84; (c) 3C 270; (d) 3C 353. The angular resolution and the linear scale of each map are shown in the individual panels.

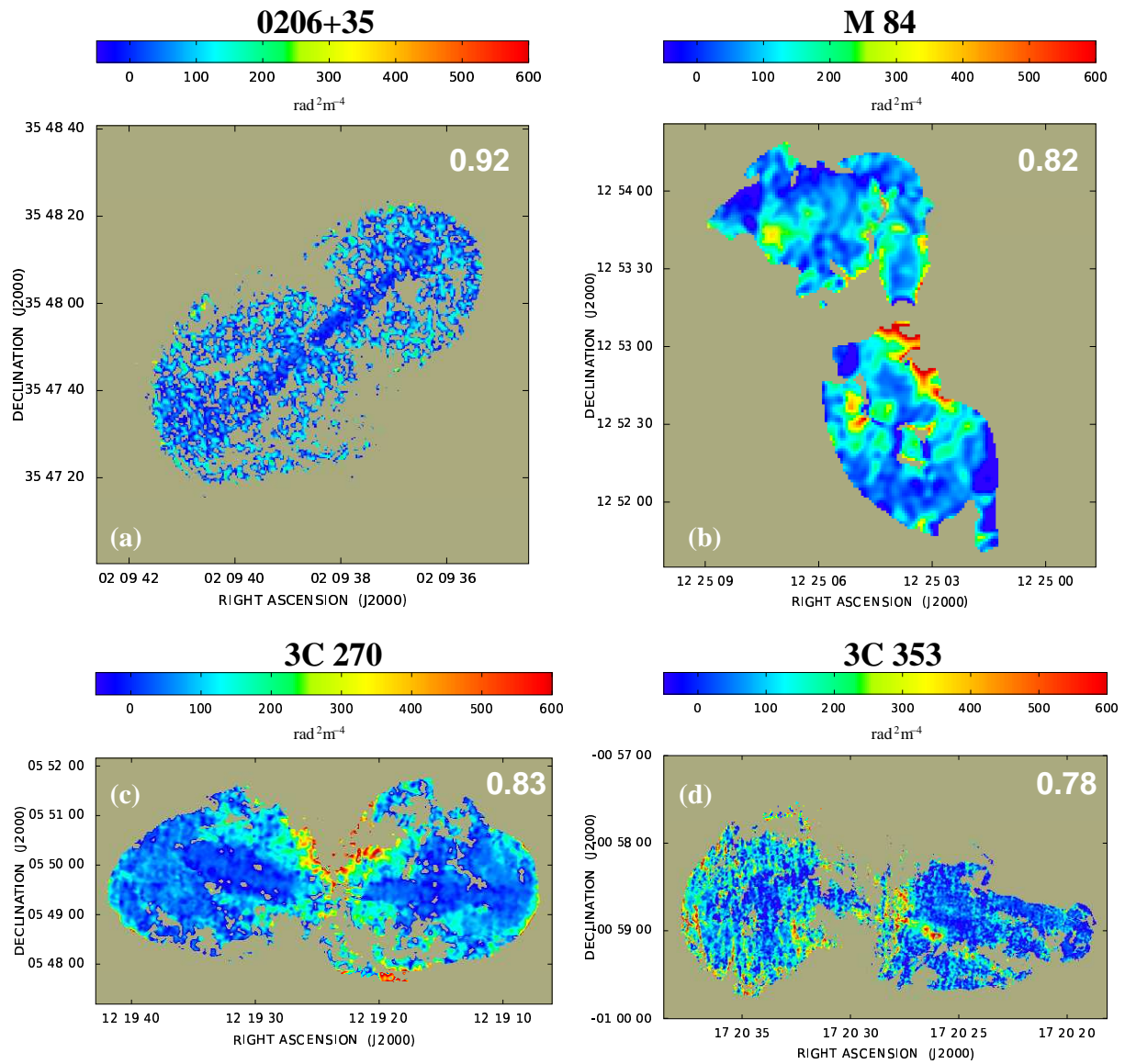


Figure 5.3: Burn law  $k$  images for all sources at the same angular resolutions as for the RM images: **(a)** 0206+35 at 1.2 arcsec FWHM; **(b)** M 84 at 4.5 arcsec FWHM; **(c)** 3C 270 at 5 arcsec FWHM; **(d)** 3C 353 at 1.3 arcsec FWHM. The corresponding integrated depolarization (DP; Section 5.4) is indicated on the top right angle of each panel. The colour scale is the same for all displays.

Table 5.3: Frequencies, bandwidths and angular resolutions used in the RM and Burn law  $k$  images discussed in Sects. 5.3 and 5.4, respectively.

source	$\nu$ [MHz]	$\Delta\nu$ [MHz]	beam [arcsec]	
0206+35	1385.1	25	1.2	
	1464.9	25		
	4885.1	50		
3C 353	1385.0	12.5	1.3	
	1665.0	12.5		
	4866.3	12.5		
	8439.9	12.5		
3C 270	1365.0	25	1.65	
	1412.0	12.5		
	4860.1	100	5.0	
	1365.0	25		
	1412.0	12.5		
	1646.0	25		
M 84	4860.1	100	1.65	
	1413.0	25		
	4885.1	50		
	1385.1	50		4.5
	1413.0	25		
	1464.9	50		
	4885.1	50		

shown by Laing & Bridle (1987), but is derived from four-frequency data and has a higher signal-to-noise ratio.

In the fainter regions of 0206+35 (for which only three frequencies are available and the signal-to-noise ratio is relatively low), the task occasionally failed to determine the  $n\pi$  ambiguities in position angle correctly. In order to remove these anomalies, I first produced a lower-resolution, but high signal-to-noise RM image by convolving the 1.2 arcsec RM map to a beamwidth of 5 arcsec FWHM. From this map I derived the polarization-angle rotations at each of the three frequencies and subtracted them from the observed 1.2 arcsec polarization angle maps at the same frequency to derive the residuals at high resolution. Then, I fit the residuals without allowing any  $n\pi$  ambiguities and added the resulting RM's to the values determined at low resolution. This procedure allowed us to obtain an RM map of 0206+35 free of significant deviations from  $\lambda^2$  rotation and fully consistent with the 1.2-arcsec measurements.

I have verified that the polarization angles accurately follow the relation  $\Delta\Psi \propto \lambda^2$  over the full range of position angle essentially everywhere except for small areas around the optically-thick cores: representative plots of  $\Psi$  against  $\lambda^2$  for 0206+35 are shown in Fig. 5.4. The lack of deviations from  $\lambda^2$  rotation in all of the radio galaxies is fully consistent with the assumption that the Faraday rotating medium is mostly external to the sources.

The RM maps are shown in Fig. 5.2. The typical rms error on the fit is  $\approx 2 \text{ rad m}^{-2}$ . No

correction for the Galactic contribution has been applied.

All of the RM maps show two-dimensional patterns, *RM bands*, across the lobes with characteristic widths ranging from 3 to 12 kpc. Multiple bands parallel to each other are observed in the western lobe of 0206+35, the eastern lobe of 3C 353 and the southern lobe of M 84.

In all cases, the iso-RM contours are straight and perpendicular to the major axes of the lobes to a very good approximation: the very straight and well-defined bands in the eastern lobes of both 0206+35 (Fig. 5.2a) and 3C 353 (Fig. 5.2d) are particularly striking. The entire area of M 84 appears to be covered by a banded structure, while in the central parts of 0206+35 and 3C 270 and the western lobe of 3C 353, regions of isotropic and random RM fluctuations are also present.

I also derived profiles of  $\langle \text{RM} \rangle$  along the radio axis of each source, averaging over boxes a few beamwidths long (parallel to the axes), but extended perpendicular to them to cover the entire width of the source. The boxes are all large enough to contain many independent points. The profiles are shown in Fig. 5.5. For each radio galaxy, I also plot an estimate of the Galactic contribution to the RM derived from a weighted mean of the integrated RM's for non-cluster radio sources within a surrounding area of  $10 \text{ deg}^2$  (Simard-Normandin et al. 1981). In all cases, both positive and negative fluctuations with respect to the Galactic value are present.

In 0206+35 (Fig. 5.2a), the largest-amplitude bands are in the outer parts of the lobes, with a possible low-level band just to the NW of the core. The most prominent band (with the most negative RM values) is in the eastern (receding) lobe, about 15 kpc from the core (Fig. 5.5a). Its amplitude with respect to the Galactic value is about  $40 \text{ rad m}^{-2}$ . This band must be associated with a strong ordered magnetic field component along the line of sight. If corrected for the Galactic contribution, the two adjacent bands in the eastern lobe would have RM with opposite signs and the field component along the line of sight must therefore reverse.

M 84 (Fig. 5.2b) displays an ordered RM pattern across the whole source, with two wide bands of opposite sign having the highest absolute RM values. There is also an abrupt change of sign across the radio core (see also Laing & Bridle 1987). The negative band in the northern lobe (associated with the approaching jet) has a larger amplitude with respect to the Galactic value than the corresponding (positive) feature in the southern lobe (Fig. 5.5c).

3C 270 (Fig. 5.2c) shows two large bands: one on the front end of the eastern lobe, the other in the middle of the western lobe. The bands have opposite signs and contain the extreme positive and negative values of the observed RM. The peak positive value is within the eastern band at the extreme end of the lobe (Fig. 5.5e).

The RM structure of 3C 353 (Fig. 5.2d) is highly asymmetric. The eastern lobe shows a strong pattern, made up of four bands, with very straight iso-RM contours which are almost

Table 5.4: Properties of the RM bands: Col. 1 source name; Cols. 2&3: overall  $\langle \text{RM} \rangle$  and  $\sigma_{\text{RM}}$ ; Col. 4: Galactic  $\langle \text{RM} \rangle$ ; Col. 5:  $\langle \text{RM} \rangle$  for each band; Col. 6: distance of the band midpoint from the radio core (positive distances are in the western direction for all sources, except for M 84, where they are in the northern direction); Col. 7: width of the band; Col. 8: maximum band amplitude.

source	$\langle \text{RM} \rangle$	$\sigma_{\text{RM}}$	$\text{RM}_{\text{G}}$ [rad m <sup>-2</sup> ]	band $\langle \text{RM} \rangle$ [rad m <sup>-2</sup> ]	$d_{\text{c}}$ [kpc]	width [kpc]	$A$ [rad m <sup>-2</sup> ]
0206+35	-77	23	-72	-140	-15	10	40
				-60	-27	4	
				34	22	6	
				51	8	4	
3C 353	-56	24	-69	122	-12	5	50
				102	-19	4	
				-40	-23	4	
				100	-26	4	
3C 270	14	10	12	-8	20	12	10
				32	37	11	
M 84	-2	15	2	-27	1	3	10
				22	-6	6	

exactly perpendicular to the source axis. As in 0206+35, adjacent bands have RM with opposite signs once corrected for the Galactic contribution (Fig. 5.5g). In contrast, the RM distribution in the western lobe shows no sign of any banded structure, and is consistent with random fluctuations superimposed on an almost linear profile. It seems very likely that the differences in RM morphology and axial ratio are both related to the external density gradient (Fig. 5.1d).

In Table 5.4 the relevant geometrical features (size, distance from the radio core,  $\langle \text{RM} \rangle$ ) for the RM bands are listed.

## 5.4 Depolarization

In this section, I use “depolarization” in its conventional sense to mean “decrease of degree of polarization with increasing wavelength” and define  $\text{DP} = p_{1.4\text{GHz}}/p_{4.9\text{GHz}}$ . Using the code (Murgia et al. 2004), I produced images of Burn law  $k$  by weighted least-squares fitting to  $\ln p(\lambda)$  as a function of  $\lambda^4$  (Eq. 3.5). Only data with signal-to-noise ratio  $>4$  in  $P$  at each frequency were included in the fits. The Burn law  $k$  images were produced with the same angular resolutions as the RM images. The 1.65 arcsec resolution Burn law  $k$  maps for M 84 and 3C 270 are consistent with the low-resolution ones, but add no additional detail and are quite noisy. This could lead to significantly biased estimates for the mean values of  $k$  over large areas (Laing et al. 2008).

Therefore, as for the RM maps, I used only the Burn law  $k$  images at low resolution for these two sources.

The Burn law  $k$  maps are shown in Fig. 5.3. All of the sources show low average values of  $k$  (i.e. slight depolarization), suggesting little RM power on small scales. With the possible exception of the narrow filaments of high  $k$  in the eastern lobe of 3C 353 (which might result from partially resolved RM gradients at the band edges), none of the images show any obvious structure related to the RM bands. For each source, I have also compared the RM and Burn law  $k$  values derived by averaging over many small boxes covering the emission, and I find no correlation between them.

I also derived profiles of  $k$  (Fig. 5.5b, d, f and h) with the same sets of boxes as for the RM profiles in the same Figure. These confirm that the values of  $k$  measured in the centres of the RM bands are always low, but that there is little evidence for any detailed correlation.

The signal-to-noise ratio for 0206+35 is relatively low compared with that of the other three sources, particularly at 4.9 GHz (a small beam is necessary to resolve the bands), and this is reflected in the high proportion of blanked pixels on the  $k$  image. The most obvious feature of this image (Fig. 5.3a), an apparent difference in mean  $k$  between the high-brightness jets (less depolarized) and the surrounding emission, is likely to be an artefact caused by the adopted blanking strategy: points where the polarized signal is low at 4.9 GHz are blanked preferentially, so the remainder show artificially high polarization at this frequency. For the same reason, the apparent minimum in  $k$  at the centre of the deep, negative RM band (Fig. 5.5a and b) is probably not significant. The averaged values of  $k$  for 0206+35 are already very low, however, and are likely to be slightly overestimated, so residual RM fluctuations on scales below the 1.2-arcsec beamwidth must be very small.

M 84 shows one localised area of very strong depolarization ( $k \sim 500 \text{ rad}^2 \text{ m}^{-4}$ , corresponding to  $\text{DP} = 0.38$ ) at the base of the southern jet (Fig. 5.3b). There is no corresponding feature in the RM image (Fig. 5.2b). The depolarization is likely to be associated with one of the shells of compressed gas visible in the *Chandra* image (Fig. 5.1b), implying significant magnetization with inhomogeneous field and/or density structure on scales much smaller than the beamwidth, apparently independent of the larger-scale field responsible for the RM bands. This picture is supported by the good spatial coincidence of the high  $k$  region with a shell of compressed gas, as illustrated in the overlay of the 4.5 arcsec Burn law  $k$  image on the contours of the *Chandra* data (Fig. 5.6(a)). Cooler gas associated with the emission-line disk might also be responsible, but there is no evidence for spatial coincidence between enhanced depolarization and  $\text{H}\alpha$  emission (Hansen, Norgaard-Nielsen & Jorgensen 1985). Despite the complex morphology of the X-ray emission around M 84, its  $k$  profile is very symmetrical, with the highest values at the centre (Fig. 5.5(d)).

3C 270 also shows areas of very strong depolarization ( $k \sim 550 \text{ rad}^2 \text{ m}^{-4}$ , corresponding to  $DP = 0.35$ ) close to the core and surrounding the inner and northern parts of both the radio lobes. As for M 84, the areas of high  $k$  are coincident with ridges in the X-ray emission which form the boundaries of the cavity surrounding the lobes (Fig. 5.6(b)). The inner parts of this X-ray structure are described in more detail by Worrall et al. (2010), whose recent high-resolution *Chandra* image clearly reveals “wedges” of low brightness surrounding the radio jets. As in M 84, the most likely explanation is that a shell of denser gas immediately surrounding the radio lobes is magnetized, with significant fluctuations of field strength and density on scales smaller than the 5-arcsec beam, uncorrelated with the RM bands. The  $k$  profile of 3C 270 (Fig. 5.5(f)) is very symmetrical, suggesting that the magnetic-field and density distributions are also symmetrical and consistent with an orientation close to the plane of the sky. The largest values of  $k$  are observed in the centre, coincident with the features noted earlier and with the bulk of the X-ray emission (the high  $k$  values in the two outermost bins have low signal-to-noise and are not significant).

In the Burn law  $k$  image of 3C 353, there is evidence for a straight and knotty region of high depolarization  $\approx 20$  kpc long and extending westwards from the core. This region does not appear to be related either to the jets or to any other radio feature. As in M 84 and 3C 270, the RM appears quite smooth over the area showing high depolarization, again suggesting that there are two scales of structure, one much smaller than the beam, but producing zero mean RM and the other very well resolved. In 3C 353, there is as yet no evidence for hot or cool ionized gas associated with the enhanced depolarization (contamination from the very bright nuclear X-ray emission affects an area of 1 arcmin radius around the core; Iwasawa et al. 2000, Goodger et al. 2008).

The  $k$  profile of 3C 353 (Fig. 5.5(h)) shows a marked asymmetry, with much higher values in the East. This is in the same sense as the difference of RM fluctuation amplitudes (Fig. 5.5(g)) and is also consistent with the eastern lobe being embedded in higher-density gas. The relatively high values of  $k$  within 20 kpc of the nucleus in the Western lobe are due primarily to the discrete region identified earlier.

## 5.5 Rotation measure structure functions

I calculated RM structure function (Eq. 3.13) for discrete regions of the sources where the RM fluctuations appear to be isotropic and random and for which we expect the spatial variations of foreground thermal gas density, rms magnetic field strength and path length to be reasonably small. These are: the inner 26 arcsec of the receding (Eastern) lobe of 0206+35, the inner 100 arcsec of 3C 270 and the inner 40 arcsec of the western lobe of 3C 353. The selected areas of 0206+35 and 3C 270 are both within the core radii of the larger-scale beta models that describe the group-

Table 5.5: Power spectrum parameters for the individual sub-regions. Col. 1: source name; Col. 2: angular resolution; Col. 3: slope  $q$ ; Col. 4: amplitude  $C_0$ ; Col. 5: minimum scale; Col. 6: amplitude of the large scale isotropic component; Col. 7: observed mean  $k$ ; Col. 8: predicted mean  $k$ . The power spectrum has not been computed for M 84 (see Section 5.5).

source	FWHM [arcsec]	$q$	$\log C_0$	$\Lambda_{min}$ [kpc]	$A_{iso}$ [rad m <sup>-2</sup> ]	$k^{obs}$ [rad <sup>2</sup> m <sup>-4</sup> ]	$k^{syn}$ [rad <sup>2</sup> m <sup>-4</sup> ]
0206+35	1.2	2.1	0.77	2	10	37	40
3C 270	1.65	2.7	0.90	0.1	5	30	26
	5.0	2.7	0.90	0.1	5	71	64
3C 353	1.3	3.1	0.99	0.1	10	38	33
M 84	1.65			<0.1		25	
	4.5			<0.1		43	

scale X-ray emission and the galaxy-scale components are too small to affect the RM statistics significantly (Table 5.2). In 3C 353, the selected area was chosen to be small compared with the scale of X-ray variations seen in Fig. 5.1(d). In all three cases, the foreground fluctuations should be fairly homogeneous. There are no suitable regions in M 84, which is entirely covered by the banded RM pattern.

The structure functions, corrected for uncorrelated random noise by subtracting  $2\sigma_{noise}^2$  (Simonetti, Cordes & Spangler 1984), are shown in Fig. 5.7. All of the observed structure functions correspond to power spectra of approximately power-law form over all or most of the range of spatial frequencies here sampled. I initially assumed that the power spectrum was described by Eq. 5.1 with no high-frequency cut-off ( $f_{max} \rightarrow \infty$ ) and made least-squares fits to the structure functions, weighted by errors derived from multiple realizations of the power spectrum on the observing grid, as described in detail by Laing et al. (2008) and in Sec. 4.5.2.

The best-fitting slopes  $q$  and amplitudes  $C_0$  are given in Table 5.5. All of the fitted power spectra are quite flat and have low amplitudes, implying that there is little power in the isotropic and random component of rotation measure. Indeed, the amplitudes of the largest-scale RM fluctuations sampled in this analysis is a few times less than that of the bands (see Tables 5.4 and 5.5). This suggests that the field responsible for the bands is stronger as well as more ordered than that responsible for the isotropic fluctuations.

The structure functions for 0206+35 and 3C 353 rise monotonically, indicating that the outer scale for the random fluctuations must be larger than the maximum separations here sampled. For 3C 270, the structure function levels out at  $r_{\perp} \approx 100$  arcsec (15 kpc; Fig. 5.7d). This could be the outer scale of the field fluctuations, but a better understanding of the geometry and external density distribution would be needed before ruling out the effects of large-scale variations in path length or field strength (cf. 3C 449, Sec. 4.6.3).

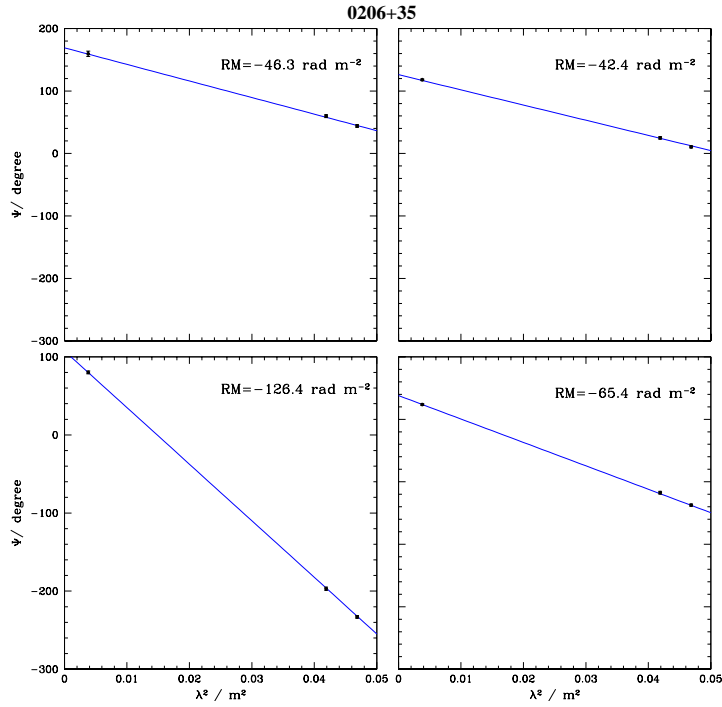


Figure 5.4: Plots of  $\mathbf{E}$ -vector position angle  $\Psi$  against  $\lambda^2$  at representative points of the 1.2 arcsec RM map of 0206+35. Fits to the relation  $\Psi(\lambda) = \Psi_0 + \text{RM}\lambda^2$  are shown. The values of RM are given in the individual panels.

In order to constrain RM structure on spatial scales below the beamwidth, I estimated the depolarization as described in Section 5.2. The fitted  $k$  values are listed in Table 5.5. I stress that these values refer only to areas with isotropic fluctuations, and cannot usefully be compared with the integrated depolarizations quoted in in Fig. 5.2.

For M 84, using the Burn law  $k$  analysis and assuming that variation of Faraday rotation across the 1.65-arcsec beam causes the residual depolarization, I find that  $\Lambda_{\min} \lesssim 0.1$  kpc for any reasonable RM power spectrum.

## 5.6 Rotation-measure bands from compression

It is clear from the fact that the observed RM bands are perpendicular to the lobe axes that they must be associated with an interaction between an expanding radio source and the gas immediately surrounding it. One inevitable mechanism is enhancement of field and density by the shock or compression wave surrounding the source.<sup>1</sup> The implication of the presence of cavities in the X-ray gas distribution coincident with the radio lobes is that the sources are interacting strongly

<sup>1</sup>An alternative mechanism is the generation of non-linear surface waves (Bicknell, Cameron & Gingold 1990). It is unlikely that this can produce large-scale bands, for the reasons given in Section 5.8.5.

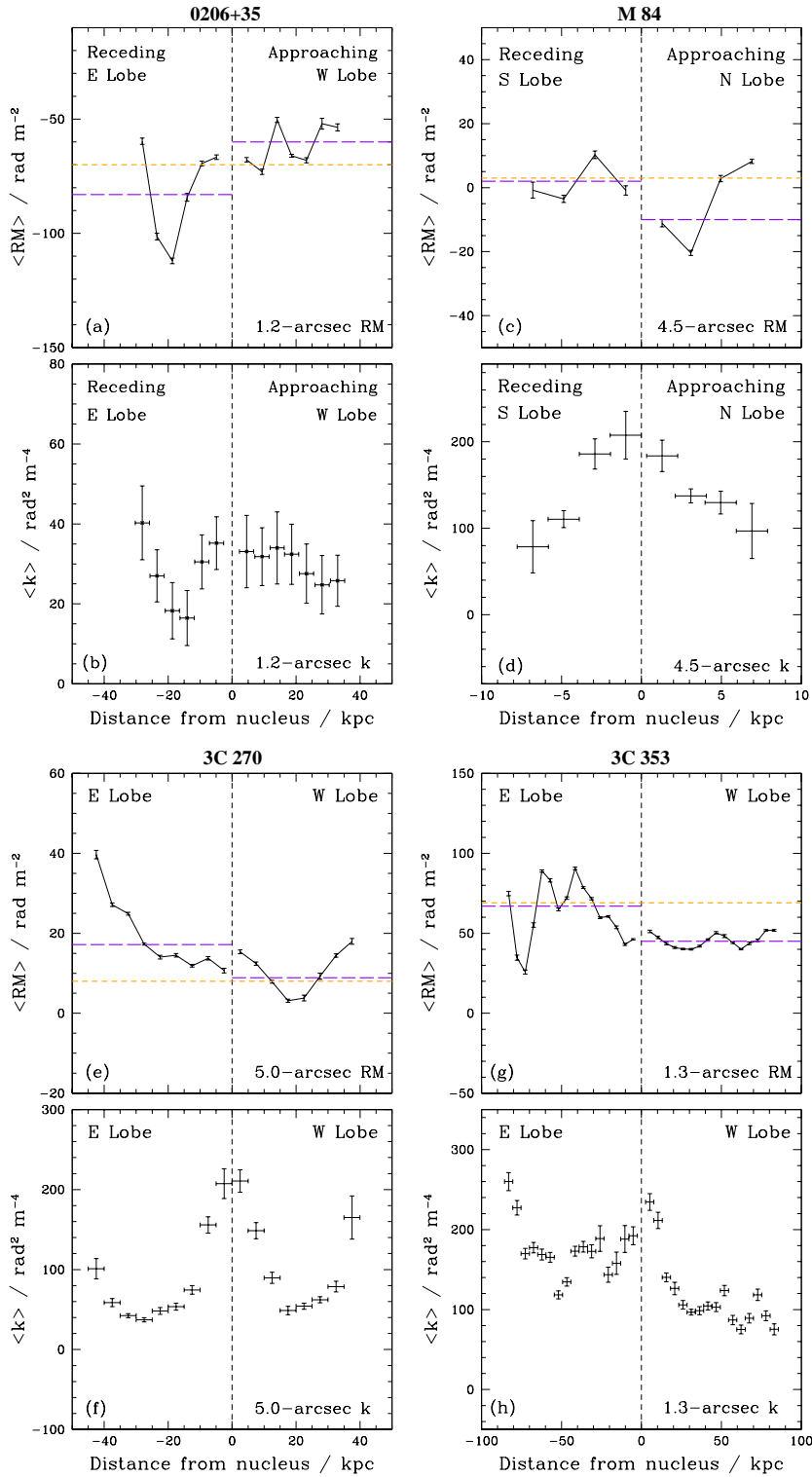


Figure 5.5: Profiles of mean and rms RM and Burn law  $k$  along the radio axis. The profiles have been derived by averaging over boxes perpendicular to the radio axis of length 5 kpc for all sources except M 84, for which the box length is 2 kpc. The orange (dashed) and violet (long-dashed) lines represent the Galactic RM contribution and the  $\langle \text{RM} \rangle$  of the lobes, respectively. All unblanked pixels are included.

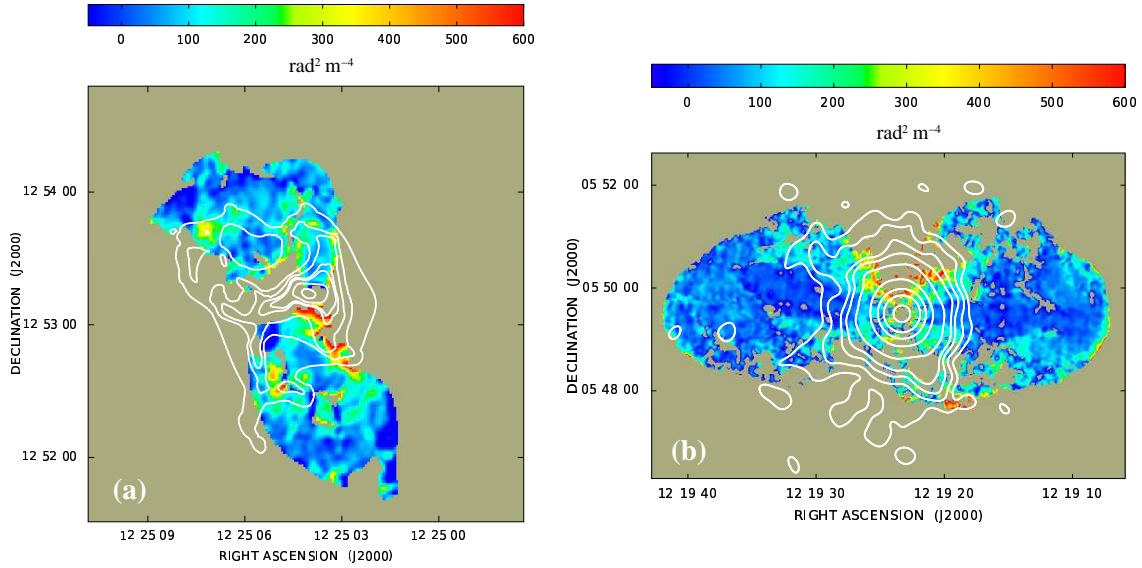


Figure 5.6: Burn law  $k$  images of M 84 (a) and 3C 270 (b) overlaid on X-ray contours derived from *Chandra* and XMM-Newton data, respectively.

with the thermal gas, displacing rather than mixing with it (see McNamara & Nulsen 2007 for a review). For the sources here presented, the X-ray observations of M 84 (Finoguenov et al. 2008, Fig.5.1b) and 3C 270 (Croston et al. 2008, Fig.5.1c) show cavities and arcs of enhanced brightness, corresponding to shells of compressed gas bounded by weak shocks. The strength of any pre-existing field in the IGM, which will be frozen into the gas, will also be enhanced in the shells. Therefore a significant enhancement in RM is expected. A more extreme example of this effect will occur if the expansion of the radio source is highly supersonic, in which case there will be a strong bow-shock ahead of the lobe, behind which both the density and the field become much higher. Regardless of the strength of the shock, the field is modified so that only the component in the plane of the shock is amplified and the post-shock field tends to become ordered parallel to the shock surface.

The evidence so far suggests that shocks around radio sources of both FR classes are generally weak (e.g. Forman et al. 2005, Wilson, Smith & Young 2006, Nulsen et al. 2005a). There are only two examples in which highly supersonic expansion has been inferred: the southern lobe of Centaurus A ( $\mathcal{M} \approx 8$ ; Kraft et al. 2003) and NGC 3801 ( $\mathcal{M} \approx 4$ ; Croston et al. 2007). There is no evidence that the sources here described are significantly over-pressured compared with the surrounding IGM (indeed, the synchrotron minimum pressure is systematically lower than the thermal pressure of the IGM; Table 5.2). The sideways expansion of the lobes is therefore unlikely to be highly supersonic. The shock Mach number estimated for all the sources from ram pressure balance in the forward direction is also  $\approx 1.3$ . This estimate is consistent with that for M 84 made by Finoguenov et al. (2006) and also with the lack of detection of strong shocks in the X-ray data

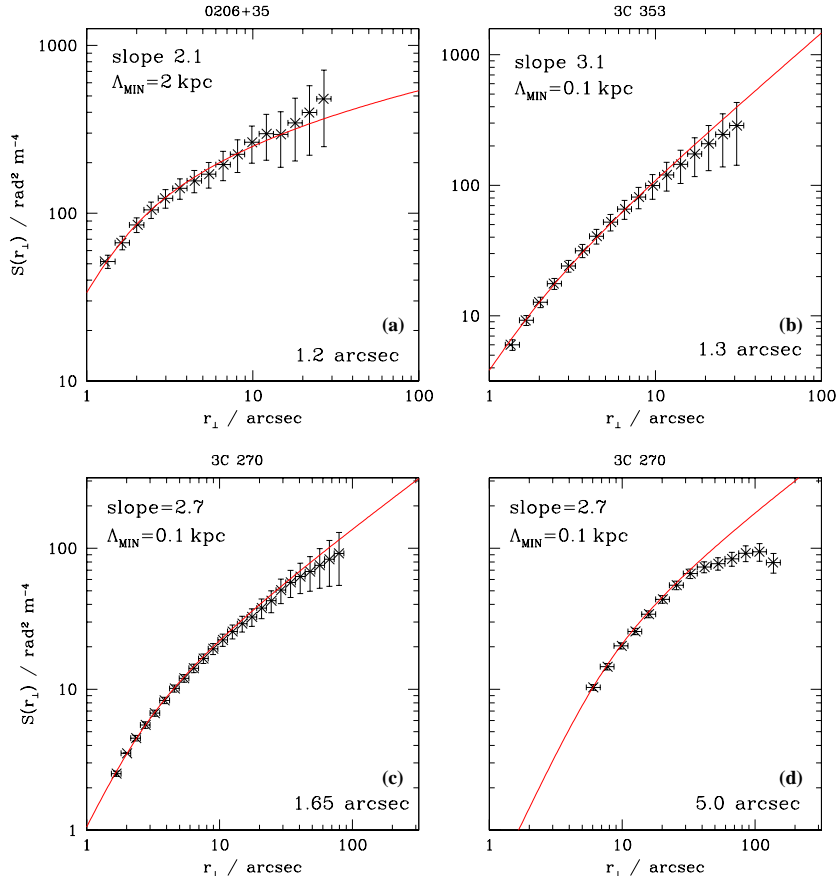


Figure 5.7: Plots of the RM structure functions for the isotropic sub-regions of 0206+35, 3C 353 and 3C 270 described in the text. The horizontal bars represent the bin width and the crosses the centroids for data included in the bins. The red lines are the predictions for power law power spectra, including the effects of the convolving beam. The vertical error bars are the rms variations for the structure functions derived for multiple realizations of the data. The fitted structure functions for 3C 270 are derived for the same power spectrum parameters.

for the other sources.

In this section, I investigate how the RM could be affected by compression. I consider a deliberately oversimplified picture in which the radio source expands into an IGM with an initially uniform magnetic field,  $B$ . This is the most favourable situation for the generation of large-scale, anisotropic RM structures: in reality, the pre-existing field is likely to be highly disordered, or even isotropic, because of turbulence in the thermal gas. I stress that I have *not* tried to generate a self-consistent model for the magnetic field and thermal density, but rather to illustrate the generic effects of compression on the RM structure.

In this model the radio lobe is an ellipsoid with its major axis along the jet and is surrounded by a spherical shell of compressed material. This shell is centred at the mid-point of the lobe (Fig. 5.8) and has a stand-off distance equal to 1/3 of the lobe semi-major axis at the leading

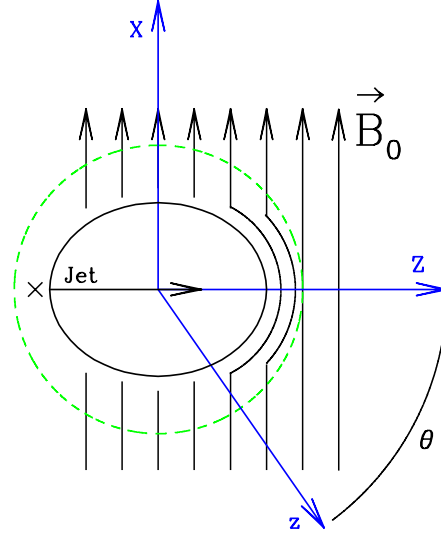


Figure 5.8: Amplification and sweeping up of the magnetic field lines inside the compression region defined by the projected circular green and dashed line. The driving expansion is along the Z-axis and the z-axis represents a generic line-of-sight.

edge (the radius of the spherical compression is therefore equal to  $4/3$  of the lobe semi-major axis). In the compressed region, the thermal density and the magnetic field component in the plane of the spherical compression are amplified by the same factor, because of flux-freezing. I use a coordinate system  $xyz$  centred at the lobe mid-point, with the  $z$ -axis along the line of sight, so  $x$  and  $y$  are in the plane of the sky. The radial unit vector is  $\hat{\mathbf{r}}=(\hat{\mathbf{x}}, \hat{\mathbf{y}}, \hat{\mathbf{z}})$ .  $\mathbf{B}=(B_x, B_y, B_z)$  and  $\mathbf{B}'=(B'_x, B'_y, B'_z)$  are respectively the pre- and post-shock magnetic-field vectors. Then, I consider a coordinate system  $XYZ$  still centred at the lobe mid-point, but rotated with respect to the  $xyz$  system by the angle  $\theta$  about the  $y$  ( $Y$ ) axis, so that  $Z$  is aligned with the major axis of the lobe. With this choice,  $\theta$  is the inclination of the source with respect to the line-of-sight (Fig. 5.8).

After a spherical compression, the thermal density and field satisfy the equations:

$$\begin{aligned} n'_e &= \gamma n_e \\ \mathbf{B}'_{\perp} &= \mathbf{B}_{\perp} = (\mathbf{B} \cdot \mathbf{r}) \hat{\mathbf{r}} \\ \mathbf{B}'_{\parallel} &= \gamma \mathbf{B}_{\parallel} = \gamma [\mathbf{B} - (\mathbf{B} \cdot \mathbf{r}) \hat{\mathbf{r}}] \end{aligned} \quad (5.2)$$

where  $n_e$ ,  $\mathbf{B}_{\perp}$  and  $\mathbf{B}_{\parallel}$  represent the initial thermal density and the components of the field perpendicular and parallel to the compression surface. The same symbols with primes stand for post-shock quantities and  $\gamma$  is the compression factor. The total compressed magnetic field is:

$$\mathbf{B}' = \mathbf{B}'_{\parallel} + \mathbf{B}'_{\perp} = \gamma \mathbf{B} + (1 - \gamma)(\mathbf{B} \cdot \mathbf{r}) \hat{\mathbf{r}} \quad (5.3)$$

The field strength after compression depends on the the angle between the compression surface and the initial field. Maximum amplification occurs for a field which is parallel to the surface, whereas a perpendicular field remains unchanged. The post-shock field component along the line-of-sight becomes:

$$B'_z = \mathbf{B}' \cdot \hat{\mathbf{z}} = \gamma \mathbf{B} \cdot \hat{\mathbf{z}} + (1 - \gamma)(\mathbf{B} \cdot \mathbf{r})(\mathbf{r} \cdot \hat{\mathbf{z}}) \quad (5.4)$$

I assumed that the compression factor,  $\gamma = \gamma(Z)$ , is a function of distance  $Z$  along the source axis from the centre of the radio lobe, decreasing monotonically from a maximum value  $\gamma_{\max}$  at the leading edge to a constant value from the centre of the lobe as far as the core. I investigated values of  $\gamma_{\max}$  in the range 1.5 – 4 ( $\gamma = 4$  corresponds to the asymptotic value for a strong shock). Given that there is no evidence for strong shocks in the X-ray data for any of the sources under investigation, I have typically assumed that the compression factor is  $\gamma_{\max} = 3$  at the front end of the lobe, decreasing to 1.2 at the lobe mid-point and thereafter remaining constant as far as the core. A maximum compression factor of 3 is consistent with the transonic Mach numbers  $\mathcal{M} \approx 1.3$  estimated from ram-pressure balance for all of the sources and this choice is also motivated by the X-ray data of M 84, from which there is evidence for a compression ratio  $\approx 3$  between the shells and their surroundings (Section 5.1.4).

I produced synthetic RM images for different combinations of source inclination and direction of the pre-existing uniform field, by integrating the expression

$$\text{RM}^{\text{syn}} = \int_{\text{lobe}}^{R0} n'_e B'_z dz. \quad (5.5)$$

numerically. I assumed a constant value of  $n_e = 2.4 \times 10^{-3} \text{ cm}^{-3}$  for the density of the pre-shock material (the central value for the group gas associated with 0206+35; Table 5.2), a lobe semi-major axis of 21 kpc (also appropriate for 0206+35) and an initial field strength of  $1 \mu\text{G}$ . The integration limits were defined by the surface of the radio lobe and the compression surface. This is equivalent to assuming that there is no thermal gas within the radio lobe, consistent with the picture suggested by the inference of foreground Faraday rotation and the existence of X-ray cavities and that Faraday rotation from uncompressed gas is negligible.

As an example, Fig. 5.9 shows the effects of compression on the RM for the receding lobe of a source inclined by  $40^\circ$  to the line of sight. The initial field is pointing towards us with an inclination of  $60^\circ$  with respect to the line-of-sight; its projection on the plane of the sky makes an angle of  $30^\circ$  with the  $x$ -axis. Fig. 5.9(a) displays the RM produced without compression ( $\gamma(Z) = 1$  everywhere): the RM structures are due only to differences in path length across the lobe. Fig. 5.9(b) shows the consequence of adding a modest compression of  $\gamma_{\max} = 1.5$ : structures similar to bands are generated at the front end of the lobe and the range of the RM values is

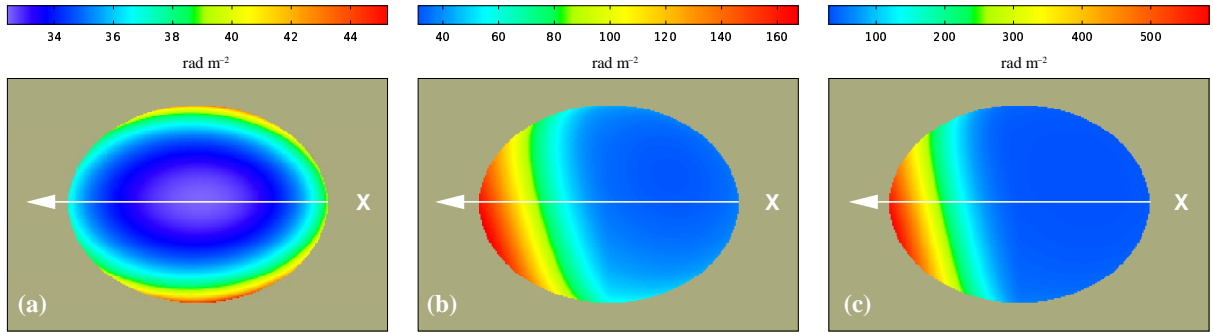


Figure 5.9: Panel (a): synthetic RM for a receding lobe inclined by  $40^\circ$  to the line-of-sight and embedded in a uniform field inclined by  $60^\circ$  to the line-of-sight and by  $30^\circ$  to the lobe axis on the plane of the sky. Panels (b) and (c): as (a) but with a weak compression ( $\gamma_{\max} = 1.5$ ) and a strong compression ( $\gamma_{\max} = 4$ ) of the density and field. The crosses and the arrows indicate the position of the core and the lobe advance direction, respectively.

increased. Fig. 5.9(c) illustrates the RM produced in case of the strongest possible compression,  $\gamma_{\max} = 4$ : the RM structure is essentially the same as in Fig. 5.9(b), with a much larger range.

This very simple example shows that RM bands with amplitudes consistent with those observed can plausibly be produced even by weak shocks in the IGM, but the iso-RM contours are neither straight, nor orthogonal to the lobe axis and there are no reversals. These constraints require specific initial conditions, as illustrated in Fig. 5.10, where I show the RM for a lobe in the plane of the sky. I considered three initial field configurations: along the line-of-sight (Fig. 5.10a), in the plane of the sky and parallel to the lobe axis (Fig. 5.10b) and in the plane of the sky, but inclined by  $45^\circ$  to the lobe axis (Fig. 5.10c). The case closest to reproducing the observations is that displayed in Fig. 5.10(b), in which reversals and well defined and straight bands perpendicular to the jet axis are produced for both of the lobes. In Fig. 5.10(a), the structures are curved, while in Fig. 5.10(c) the bands are perpendicular to the initial field direction, and therefore inclined with respect to the lobe axis.

For a source inclined by  $40^\circ$  to the line of sight, I found structures similar to the observed bands only with an initial field in the plane of the sky and parallel to the axis in projection (Figs 5.11a and b; note that the synthetic RM images in this example have been made for each lobe separately, neglecting superposition).

I can summarize the results of the spherical pure compression model as follows.

1. An initial field with a component along the line-of-sight does not generate straight bands.
2. The bands are orthogonal to the direction of the initial field projected on the plane of the sky, so bands perpendicular to the lobe axis are only obtained with an initial field aligned with the radio jet in projection.

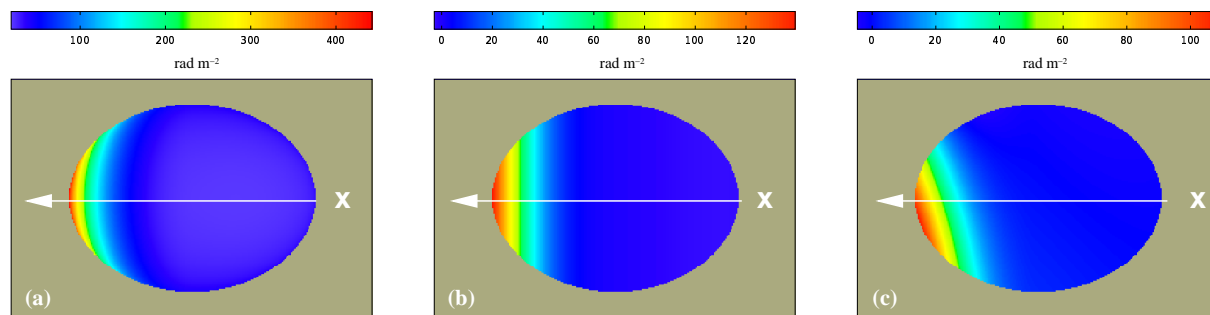


Figure 5.10: Synthetic RM images for a lobe in the plane of the sky with an ambient field which is uniform before compression. In panels (a) and (b), the field is along the axis of the lobe in projection and inclined to the line-of-sight by (a)  $45^\circ$  and (b)  $90^\circ$ . In panel (c), the field is in the plane of the sky and misaligned by  $45^\circ$  with respect to the lobe axis. The crosses and the arrows represent the radio core position and the lobe advance direction, respectively.

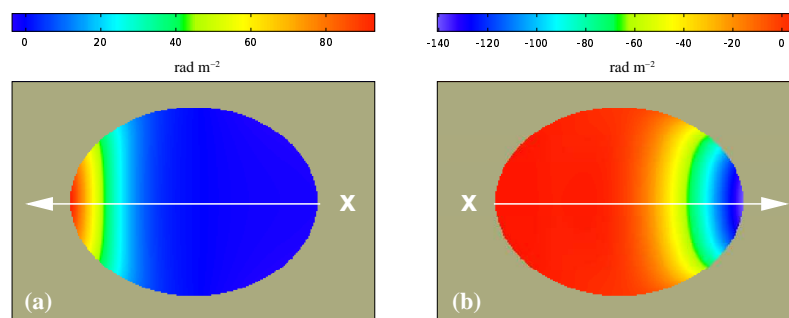


Figure 5.11: Synthetic RM images of the receding (a) and approaching lobe (b) of a source inclined by  $40^\circ$  with respect to the line-of-sight, in the case of a uniform ambient field. The field is aligned with the radio jets in projection and inclined with respect to the line-of-sight by  $90^\circ$ . The crosses and the arrows represent the radio core position and the lobe advance direction, respectively.

3. The path length (determined by the precise shape of the radio lobes) has a second-order effect on the RM distribution (compare Figs. 5.9a and b).

Thus, a simple compression model can generate bands with amplitudes similar to those observed but reproducing their geometry requires implausibly special initial conditions, as I discuss in the next section.

## 5.7 Rotation-measure bands from a draped magnetic field

### 5.7.1 General considerations

That the pre-existing field is uniform, close to the plane of the sky and aligned with the source axis in projection is implausible for obvious reasons:

1. the pre-existing field cannot know anything about either the radio-source geometry or our line-of-sight and
2. observations of Faraday rotation in other sources and the theoretical inference of turbulence in the IGM both require disordered initial fields.

This suggests that the magnetic field must be aligned *by* rather than *with* the expansion of the radio source. Indeed, the field configurations which generate straight bands look qualitatively like the “draping” model proposed by Dursi & Pfrommer (2008), for some angles to the line-of-sight. The analysis of Sections 5.2, 5.4 and 5.5 suggests that the magnetic fields causing the RM bands are well-ordered, consistent with a stretching of the initial field that has erased much of the small-scale structure while amplifying the large-scale component. I next attempt to constrain the geometry of the resulting “draped” field.

### 5.7.2 Axisymmetric draped magnetic fields

A proper calculation of the RM from a draped magnetic-field configuration (Dursi & Pfrommer 2008) is outside the scope of this work, but we can start to understand the field geometry using some simple approximations in which the field lines are stretched along the source axis. I assumed initially that the field around the lobe is axisymmetric, with components along and radially outwards from the source axis, so that the RM pattern is independent of rotation about the axis. It is important to stress that such an axisymmetric field is *not physical*, as it requires a monopole and unnatural reversals, it is nevertheless a useful benchmark for features of the field geometry that are needed to account for the observed RM structure. I first considered field lines which are parabolae with a common vertex on the axis ahead of the lobe. For field strength and density both decreasing away from the vertex, I found that RM structures, with iso-contours similar to arcs, rather than bands, were generated only for the approaching lobe of an inclined source. Such anisotropic RM structures were not produced in the receding lobes, nor for sources in the plane of the sky. Indeed, in order to generate any narrow, transverse RM structures such as arcs or bands, the line-of-sight must pass through a foreground region in which the field lines show significant curvature, which occurs only for an approaching lobe in case of a parabolic field geometry. This suggested to consider field lines which are families of ellipses centred on the lobe, again with field strength and density decreasing away from the leading edge. This indeed produced RM structures in both lobes for any inclination, but the iso-RM contours were arcs, not straight lines. Because of the non-physical nature of these axisymmetric field models, the resulting RM images are deliberately not shown. In order to quantify the departures from straightness of the iso-RM contours, I measured the ratio of the predicted RM values at the centre and edge of the lobe at constant  $Y$ , at different

distances along the source axis,  $X$ , for both of the example axisymmetric field models. The ratio, which is 1 for perfectly straight bands, varies from 2 to 3 in both cases, depending on distance from the nucleus. This happens because the variations in line-of-sight field strength and density do not compensate accurately for changes in path length. I believe that this problem is generic to any axisymmetric field configuration.

The results of this section suggest that the field configuration required to generate straight RM bands perpendicular to the projected lobe advance direction has systematic curvature in the field lines (in order to produce a modulation in RM) without a significant dependence on azimuthal angle around the source axis). I therefore investigated a structure in which elliptical field lines are wrapped around the front of the lobe, but in a two-dimensional rather than a three-dimensional configuration.

### 5.7.3 A two-dimensional draped magnetic field

I considered a field with a two-dimensional geometry, in which the field lines are families of ellipses in planes of constant  $Y$ , as sketched in Fig. 5.12. The field structure is then independent of  $Y$ . The limits of integration are given by the lobe surface and an ellipse whose major axis is  $4/3$  of that of the lobe. Three example RM images are shown in Fig. 5.13. The assumed density ( $2.4 \times 10^{-3} \text{ cm}^{-3}$ ) and magnetic field ( $1 \mu\text{G}$ ) were the same as the pre-shock values for the compression model of Section 5.6 and the lobe semi-major axis was again 21 kpc. Since the effect of path length is very small (Section 5.6), the RM is also independent of  $Y$  to a good approximation. The combination of elliptical field lines and invariance with  $Y$  allows us to produce straight RM bands perpendicular to the projected lobe axis for any source inclination. Furthermore, this model generates more significant reversals of the RM (e.g. Fig. 5.13c) than those obtainable with pure compression (e.g. Fig. 5.11b).

I conclude that a field model of this generic type represents the simplest way to produce RM bands with the observed characteristics in a way that does not require improbable initial conditions. The invariance of the field with the  $Y$  coordinate is an essential point of this model, suggesting that the physical process responsible for the draping and stretching of the field lines must act on scales larger than the radio lobes in the  $Y$  direction.

### 5.7.4 RM reversals

The two-dimensional draped field illustrated in the previous section reproduces the geometry of the observed RM bands very well, but can only generate a single reversal, which must be very close to the front end of the approaching lobe, where the elliptical field lines bend most rapidly. A

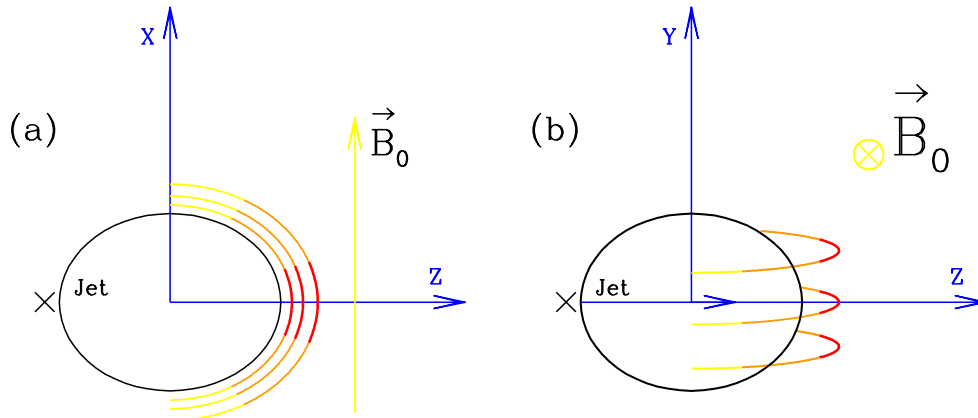


Figure 5.12: Geometry of the two-dimensional draped model for the magnetic field, described in Sec. 5.7.3. Panel **(a)**: seen in the plane of the direction of the ambient magnetic field. Panel **(b)**: seen in the plane perpendicular to the ambient field; only the innermost family of ellipses is plotted. For clarity, field lines behind the lobe are omitted. The colour of the curves indicates the strength of the field, decreasing from red to yellow. The crosses represent the radio core position. The coordinate system is the same as in Fig. 5.8 and the line of sight is in the  $X - Z$  plane.

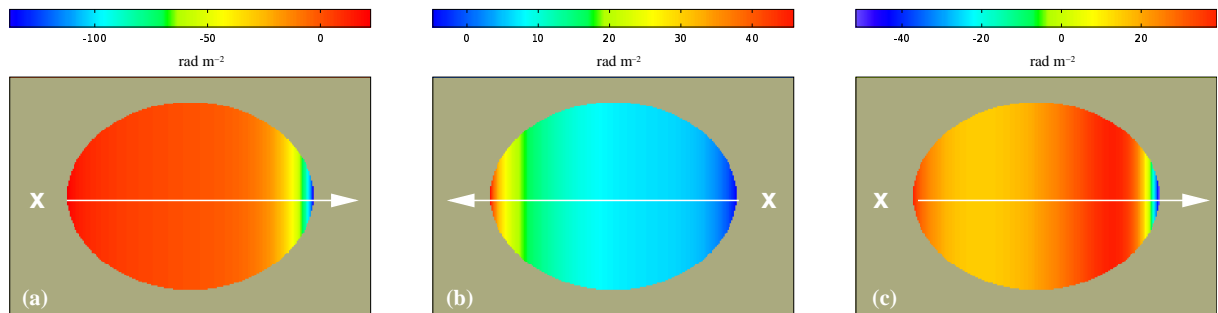


Figure 5.13: Synthetic RM images produced for a two-dimensional draped model as described in Section 5.7.3. The field lines are a family of ellipses draped around the lobe as in Fig. 5.12. Panel **(a)**: lobe inclined at  $90^\circ$  to the line-of-sight. **(b)** receding and **(c)** approaching lobes of a source inclined by  $40^\circ$  to the line-of-sight. The crosses and the arrows represent the radio core position and the lobe advance direction.

prominent reversal is apparent in the receding lobe of 0206+35 (Fig. 5.2a) and multiple reversals across the eastern lobe of 3C 353 and in M 84 (Fig. 5.2b and d). The simplest way to reproduce these is to assume that the draped field also has reversals, presumably originating from a more complex initial field in the IGM. One realization of such a field configuration would be in the form of multiple toroidal eddies with radii smaller than the lobe size, as sketched in Fig. 5.14. Whatever the precise field geometry, I stress that the straightness of the observed multiple bands again requires a two-dimensional structure, with little dependence on  $Y$ .

## 5.8 Discussion

### 5.8.1 Where do bands occur?

The majority of published RM images of radio galaxies do not show bands or other kind of anisotropic structure, but are characterized by isotropic and random RM distributions (*e.g.* Laing et al. 2008, 3C 449, Chapter 4). On the other hand, I have presented observations of RM bands in four radio galaxies embedded in different environments and with a range of jet inclinations with respect to the line-of-sight. These sources are not drawn from a complete sample, so any quantitative estimate of the incidence of bands is premature, but it is possible to draw some preliminary conclusions.

The simple two-dimensional draped-field model developed in Section 5.7.3 only generates RM bands when the line-of-sight intercepts the volume containing elliptical field lines, which happens for a restricted range of rotation around the source axis. At other orientations, the RM from this field configuration will be small and the observed RM may well be dominated by material at larger distances which has not been affected by the radio source. I therefore expect a minority of sources with this type of field structure to show RM bands and the remainder to have weaker, and probably isotropic, RM fluctuations. In contrast, the three-dimensional draped field model proposed by Dursi & Pfrommer (2008) predicts RM bands *parallel* to the source axis for a significant range of viewing directions: these have not (yet) been observed.

The prominent RM bands here described occur only in *lobed* radio galaxies. In contrast, well-observed radio sources with tails and plumes seem to be free of bands or anisotropic RM structure (*e.g.* 3C 31, 3C 449; Laing et al. 2008, Chapter 4). Furthermore, the lobes which show bands are all quite round and show evidence for interaction with the surrounding IGM. It is particularly striking that the bands in 3C 353 occur only in its eastern, rounded, lobe. The implication is that RM bands occur when a lobe is being actively driven by a radio jet into a region of high IGM density. Plumes and tails, on the other hand, are likely to be rising buoyantly in the group or cluster and I do not expect significant compression, at least at large distances from the nucleus.

### 5.8.2 RM bands in other sources

The fact that RM bands have so far been observed only in a few radio sources may be a selection effect: much RM analysis has been carried out for galaxy clusters, in which most of the sources are tailed (*e.g.* Blanton et al. 2003). With a few exceptions like Cyg A (see below, Section 5.8.2), lobed FR I and FR II sources have not been studied in detail.

### Cygnus A

Cygnus A is a source in which we might expect to observe RM bands, by analogy with the sources discussed in the present work: it has wide and round lobes and *Chandra* X-ray data have shown the presence of shock-heated gas and cavities (Wilson, Smith & Young 2006). RM bands, roughly perpendicular to the source axis, are indeed seen in both lobes (Dreher et al. 1987; Carilli & Taylor 2002), but interpretation is complicated by the larger random RM fluctuations and the strong depolarization in the eastern lobe. A semi-circular RM feature around one of the hot-spots in the western lobe has been attributed to compression by the bow-shock (Carilli, Perley & Dreher 1988).

### Hydra A

Carilli & Taylor (2002) have claimed evidence for RM bands in the northern lobe of Hydra A. The *Chandra* image (McNamara et al. 2000) shows a clear cavity with sharp edges coincident with the radio lobes and an absence of shock-heated gas, just as in the sources analysed in this work. Despite the classification as a tailed source, it may well be that there is significant compression of the IGM. Note, however, that the RM image is not well sampled close to the nucleus.

### 3C 465

The RM image of the tailed source 3C 465 published by Eilek & Owen (2002) shows some evidence for bands, but the colour scale was deliberately chosen to highlight the difference between positive and negative values, thus making it difficult to see the large gradients in RM expected at band edges. The original RM image (Eilek, private communication) suggests that the band in the western tail of 3C 465 is similar to those I have identified. It is plausible that magnetic-field draping happens in wide-angle tail sources like 3C 465 as a result of bulk motion of the IGM within the cluster potential well, as required to bend the tails. It will be interesting to search for RM bands in other sources of this type and to find out whether there is any relation between the iso-RM contours and the flow direction of the IGM.

### 5.8.3 Foreground isotropic field fluctuations

The coexistence in the RM images of the sources here analysed of anisotropic patterns with areas of isotropic fluctuations suggests that the Faraday-rotating medium has at least two components: one local to the source, where its motion significantly affects the surrounding medium, draping the field, and the other from material on group or cluster scales which has not felt the effects

---

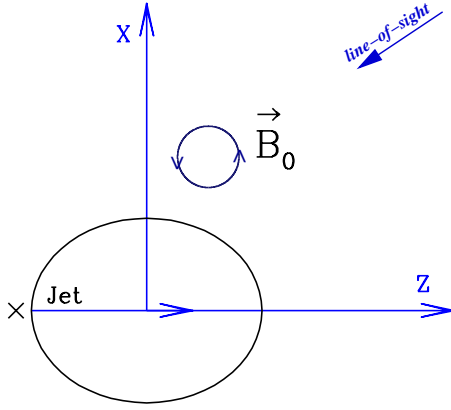


Figure 5.14: Geometry of a two-dimensional toroidal magnetic field as described in Section 5.7.3, seen in the plane normal to its axis. The cross represents the radio core position.

of the source. This raises the possibility that turbulence in the foreground Faraday rotating medium might “wash out” RM bands, thereby making them impossible to detect. The isotropic RM fluctuations observed across the sources are all described by quite flat power spectra with low amplitude (Table 5.5). The random small-scale structure of the field along the line-of-sight essentially averages out, and there is very little power on scales comparable with the bands. If, on the other hand, the isotropic field had a steeper power spectrum with significant power on scales similar to the bands, then its contribution might become dominant.

I first produced synthetic RM images for 0206+35 including a random component derived from the best-fitting power spectrum (Table 5.5) in order to check that the bands remained visible. I assumed a minimum scale of 2 kpc from the depolarization analysis for 0206+35 (Sec. 5.4), and a maximum scale of  $\Lambda_{\max} = 40$  kpc, consistent with the continuing rise of the RM structure function at the largest sampled separations, which requires  $\Lambda_{\max} \gtrsim 30$  arcsec ( $\approx 20$  kpc). The final synthetic RM is given by:

$$\text{RM}^{\text{syn}} = \text{RM}^{\text{drap}} + \text{RM}^{\text{icm}} = \int n'_e B'_z dz + \int n_e B_z dz \quad (5.6)$$

where  $\text{RM}^{\text{drap}}$  and  $\text{RM}^{\text{icm}}$  are the RM due to the draped and isotropic fields, respectively. The terms  $n'_e$  and  $B'_z$  are respectively the density and field component along the line-of-sight in the draped region. The integration limits of the term  $\text{RM}^{\text{drap}}$  were defined by the surface of the lobe and the draped region, while that of the term  $\text{RM}^{\text{icm}}$  starts at the surface of the draped region and extends to 3 times the core radius of the X-ray gas (Table 5.2). For the electron gas density  $n_e$  outside the draped region I assumed the beta-model profile of 0206+35 (Table 5.2) and for the field strength a radial variation of the form (Laing et al. 2008, and references therein)

$$\langle B^2(r) \rangle^{1/2} = B_0 \left[ \frac{n_e(r)}{n_0} \right]^\eta \quad (5.7)$$

where  $B_0$  is the rms magnetic field strength at the group centre. I took a draped magnetic field strength of  $1.8 \mu\text{G}$ , in order to match the amplitudes for the RM bands in both lobes of 0206+35,

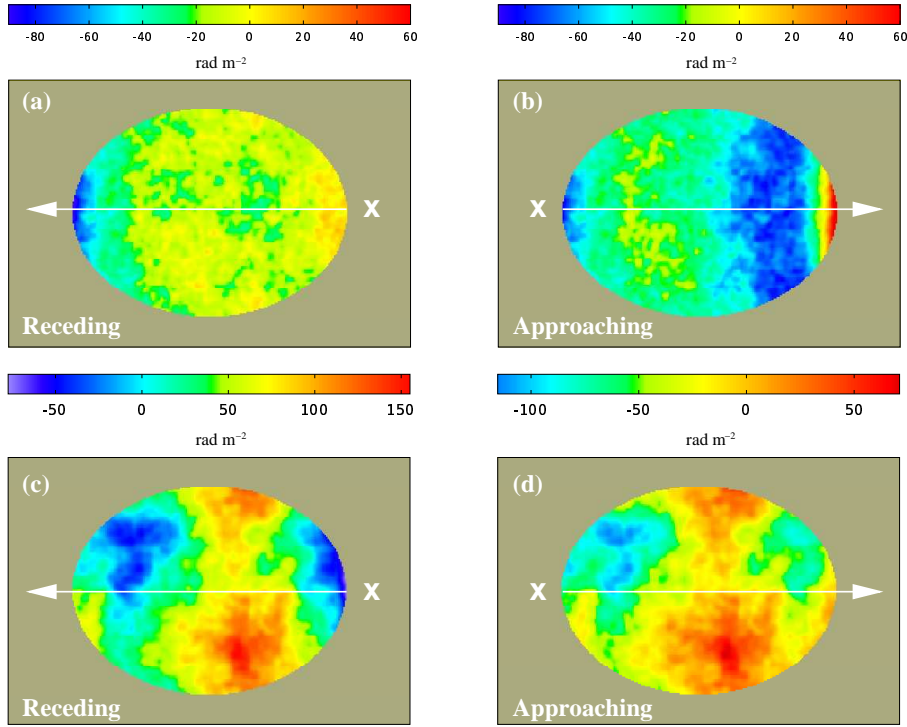


Figure 5.15: Synthetic RM images of the lobes of 0206+35, produced by the sum of a draped field local to the source and an isotropic, random field spread through the group volume with the best-fitting power spectrum found in Sec. 5.5 (panels (a) and (b)) and with a Kolmogorov power spectrum (panels (c) and (d)). Both power spectra have the same high and low-frequency cut offs and the central magnetic field strengths are also identical. The crosses and the arrows represent the radio core position and the lobe advance direction.

and assumed the same value for  $B_0$ .

Example RM images, shown in Figs. 5.15(a) and (b), should be compared with those for the draped field alone (Figs. 5.13b and c, scaled up by a factor of 1.8 to account for the difference in field strength) and with the observations (Fig. 5.2a) after correction for Galactic foreground (Table 5.4). The model is self-consistent: the flat power spectrum found for 0206+35 does not give coherent RM structure which could interfere with the RM bands, which are still visible.

I then replaced the isotropic component with one having a Kolmogorov power spectrum ( $q = 11/3$ ). I assumed identical minimum and maximum scales (2 and 40 kpc) as for the previous power spectrum and took the same central field strength ( $B_0 = 1.8 \mu\text{G}$ ) and radial variation (Eq. 5.7). Example realizations are shown in Fig. 5.15(c) and (d). The bands are essentially invisible in the presence of foreground RM fluctuations with a steep power spectrum out to scales larger than their widths.

It may therefore be that the RM bands in the sources here presented are especially prominent because the power spectra for the isotropic RM fluctuations have unusually low amplitudes and

flat slopes. I have established these parameters directly for 0206+35, 3C 270 and 3C 353; M 84 is only 14 kpc in size and is located far from the core of the Virgo cluster, so it is plausible that the cluster contribution to its RM is small and constant.

I conclude that the detection of RM bands could be influenced by the relative amplitude and scale of the fluctuations of the isotropic and random RM component compared with that from any draped field, and that significant numbers of banded RM structures could be masked by isotropic components with steep power spectra.

#### 5.8.4 Asymmetries in RM bands

The well-established correlation between RM variance and/or depolarization and jet sidedness observed in FR I and FR II radio sources is interpreted as an orientation effect: the lobe containing the brighter jet is on the near side, and is seen through less magneto-ionic material (e.g. Laing 1988; Morganti et al. 1997). For sources showing RM bands, it is interesting to ask whether the asymmetry is due to the bands or just to the isotropic component.

In 0206+35, whose jets are inclined by  $\approx 40^\circ$  to the line-of-sight, the large negative band on the receding side has the highest RM (Fig. 5.5). This might suggest that the RM asymmetry is due to the bands, and therefore to the local draped field. Unfortunately, 0206+35 is the only source displaying this kind of asymmetry. The other “inclined” source, M 84, ( $\theta \approx 60^\circ$ ) does not show such asymmetry: on the contrary the RM amplitude is quite symmetrical. In this case, however, the relation between the (well-constrained) inclination of the inner jets, and that of the lobes could be complicated: both jets bend by  $\approx 90^\circ$  at distances of about 50 arcsec from the nucleus (Laing et al. in preparation), so that we cannot establish the real orientation of the lobes with respect to the plane of the sky. The low values of the jet/counter-jet ratios in 3C 270 and 3C 353 suggest that their axes are close to the plane of the sky, so that little orientation-dependent RM asymmetry would be expected. Indeed, the lobes of 3C 270 show similar RM amplitudes, while the large asymmetry of RM profile of 3C 353 is almost certainly due to a higher column density of thermal gas in front of the eastern lobe. Within this small sample, there is therefore no convincing evidence for higher RM amplitudes in the bands on the receding side, but neither can such an effect be ruled out.

In models in which an ordered field is draped around the radio lobes, the magnitude of any RM asymmetry depends on the field geometry as well as the path length (cf. Laing et al. 2008 for the isotropic case). For instance, the case illustrated in Figs 5.13(b) and (c) shows very little asymmetry even for  $\theta = 40^\circ$ . The presence of a systematic asymmetry in the banded RM component could therefore be used to constrain the geometry.

### 5.8.5 Enhanced depolarization and mixing layers

A different mechanism for the generation of RM fluctuations was suggested by Bicknell, Cameron & Gingold (1990). They argued that large-scale nonlinear surface waves could form on the surface of a radio lobe through the merging of smaller waves generated by Kelvin-Helmholtz instabilities and showed that RM's of roughly the observed magnitude would be produced if a uniform field inside the lobe was advected into the mixing layer. This mechanism is unlikely to be able to generate large-scale bands, however: the predicted iso-RM contours are only straight over parts of the lobe which are locally flat, even in the unlikely eventuality that a coherent surface wave extends around the entire lobe.

The idea that a mixing layer generates high Faraday rotation may instead be relevant to the anomalously high depolarizations associated with regions of compressed gas around the inner radio lobes of M84 and 3C 270 (Section 5.4 and Fig. 5.6). The fields responsible for the depolarization must be tangled on small scales, since they produce depolarization without any obvious effects on the large-scale Faraday rotation pattern. It is unclear whether the level of turbulence within the shells of compressed gas is sufficient to amplify and tangle a pre-existing field in the IGM to the level that it can produce the observed depolarization; a plausible alternative is that the field originates within the radio lobe and mixes with the surrounding thermal gas.

## 5.9 Conclusions and outstanding questions

In this work I have analysed and interpreted the Faraday rotation across the lobed radio galaxies 0206+35, 3C 270, 3C 353 and M 84, located in environments ranging from a poor group to one of the richest clusters of galaxies (the Virgo cluster). The RM images have been produced at resolutions ranging from 1.2 to 5.5 arcsec FWHM using Very Large Array data at multiple frequencies. All of the RM images show peculiar banded patterns across the radio lobes, implying that the magnetic fields responsible for the Faraday rotation are anisotropic. The RM bands coexist and contrast with areas of patchy and random fluctuations, whose power spectra have been estimated using a structure-function technique. I have also analysed the variation of degree of polarization with wavelength and compared this with the predictions for the best-fitting RM power spectra in order to constrain the minimum scale of magnetic turbulence. I have investigated the origin of the bands by making synthetic RM images using simple models of the interaction between radio galaxies and the surrounding medium and have estimated the geometry and strength of the magnetic field.

The results of this work can be summarized as follows.

1. The lack of deviation from  $\lambda^2$  rotation over a wide range of polarization position angle and the lack of associated depolarization together suggest that a foreground Faraday screen with no mixing of radio-emitting and thermal electrons is responsible for the observed RM in the bands and elsewhere (Section 5.3).
2. The dependence of the degree of polarization on wavelength is well fitted by a Burn law, which is also consistent with (mostly resolved) pure foreground rotation (Section 5.4).
3. The RM bands are typically 3 – 10 kpc wide and have amplitudes of 10 – 50  $\text{rad m}^{-2}$  (Table 5.4). The maximum deviations of RM from the Galactic values are observed at the position of the bands. Iso-RM contours are orthogonal to the axes of the lobes. In several cases, neighbouring bands have opposite signs compared with the Galactic value and the line-of-sight field component must therefore reverse between them.
4. An analysis of the profiles of  $\langle \text{RM} \rangle$  and depolarization along the source axes suggests that there is very little small-scale RM structure within the bands.
5. The lobes against which bands are seen have unusually small axial ratios (i.e. they appear round in projection; Fig. 5.2). In one source (3C 353) the two lobes differ significantly in axial ratio, and only the rounder one shows RM bands. This lobe is on the side of the source for which the external gas density is higher.
6. Structure function and depolarization analyses show that flat power-law power spectra with low amplitudes and high-frequency cut-offs are characteristic of the areas which show isotropic and random RM fluctuations, but no bands (Section 5.5).
7. There is evidence for source-environment interactions, such as large-scale asymmetry (3C 353) cavities and shells of swept-up and compressed material (M 84, 3C 270) in all three sources for which high-resolution X-ray imaging is available.
8. Areas of strong depolarization are found around the edges of the radio lobes close to the nuclei of 3C 270 and M 84. These are probably associated with shells of compressed hot gas. The absence of large-scale changes in Faraday rotation in these features suggests that the field must be tangled on small scales (Section 5.4).
9. The comparison of the amplitude of  $\langle \text{RM} \rangle$  with that of the structure functions at the largest sampled separations is consistent with an amplification of the large scale magnetic field component at the position of the bands.
10. I produced synthetic RM images from radio lobes expanding into an ambient medium containing thermal material and magnetic field, first considering a pure compression of

both thermal density and field, and then including three- and two-dimensional stretching (“draping”) of the field lines along the direction of the radio jets (Sects. 5.6 and 5.7). Both of the mechanisms are able to generate anisotropic RM structure.

11. To reproduce the straightness of the iso-RM contours, a two-dimensional field structure is needed. In particular, a two-dimensional draped field, whose lines are geometrically described by a family of ellipses, and associated with compression, reproduces the RM bands routinely for any inclination of the sources to the line-of-sight (Sec. 5.7.3). Moreover, it might explain the high RM amplitude and low depolarization observed within the bands.
12. The invariance of the magnetic field along the axis perpendicular to the forward expansion of the lobe suggests that the physical process responsible for the draping and stretching of the magnetic field must act on scales larger than the lobe itself in this direction. It is not possible to constrain yet the scale size along the line-of-sight.
13. In order to create RM bands with multiple reversals, more complex field geometries such as two-dimensional eddies are needed (Section 5.7.4).
14. I have interpreted the observed RM’s as due to two magnetic field components: one draped around the radio lobes to produce the RM bands, the other turbulent, spread throughout the surrounding medium, unaffected by the radio source and responsible for the isotropic and random RM fluctuations (Section 5.8.3). I tested this model for 0206+35, assuming a typical variation of field strength with radius in the group atmosphere, and found that a magnetic field with central strength of  $B_0 = 1.8 \mu\text{G}$  reproduced the RM range quite well in both lobes.
15. I have suggested two reasons for the low rate of detection of bands in published RM images: our line of sight will only intercept a draped field structure in a minority of cases and rotation by a foreground turbulent field with significant power on large scales may mask any banded RM structure.

These results therefore suggest a more complex picture of the magneto-ionic environments of radio galaxies than was apparent from earlier work. I find three distinct types of magnetic-field structure: an isotropic component with large-scale fluctuations, plausibly associated with the undisturbed intergalactic medium; a well-ordered field draped around the leading edges of the radio lobes and a field with small-scale fluctuations in the shells of compressed gas surrounding the inner lobes, perhaps associated with a mixing layer. In addition, I have emphasised that simple compression by the bow shock should lead to enhanced RM’s around the leading edges, but that the observed patterns depend on the pre-shock field.

MHD simulations should be able to address the formation of anisotropic magnetic-field structures around radio lobes and to constrain the initial conditions.



## Chapter 6

# Faraday rotation in two extreme environments<sup>‡</sup>

In this Chapter I will present polarization analyses of two radio galaxies embedded in very different environments. The sources are: B2 0755+37, located in a very sparse group, and M 87, located at the centre of the cool core Virgo cluster. I will describe the results of two-dimensional analyses of the RM and depolarization distributions. In both sources, the geometry of the surrounding X-ray emitting gas appears to be complex than for the sources studied in Chapters 4 and 5, so a three-dimensional analysis will be deferred to a later study.

### 6.1 The sources

The general parameters of the sources are listed in Table 6.1, while Table 6.2 shows the X-ray parameters taken from the literature and the equipartition parameters derived from radio data in this work. I refer to parts of the sources by the abbreviations N, S, E, W (for North, South, East, West).

#### 6.1.1 B2 0755+37

B2 0755+37 (hereafter 0755+37) is an extended FRI radio source whose optical counterpart, NGC 2484, is a D-galaxy, classified as central member of a nearby and very poor group of galaxies (Mulchaey et al. 2003). The source is one of the most isolated radio galaxies in the B2 catalogue. Here I briefly summarize the radio properties of 0755+37, which are described in detail in the Appendix of this thesis along with a description of the VLA observations. At a resolution of

---

<sup>‡</sup>Guidetti et al. in prep

1.3 arcsec the source shows a very bright core and two-sided jets embedded in an diffuse halo of low surface brightness. The jet E of the nucleus is the brighter one and the jets inclination to the line-of-sight is estimated to be about  $30^\circ$  (Bondi et al. 2000; Laing & Bridle in preparation) The radio source is highly polarized.

0755+35 has been observed with both the PSPC and HRI instruments on *ROSAT* (Worrall & Birkinshaw 1994, 2000) and with *Chandra* (Worrall, Birkinshaw & Hardcastle 2001).

The X-ray emission has extended thermal and partially resolved non-thermal components, respectively associated with the hot medium on group and galactic scales, and with the core and jets (Canosa et al. 1999; Worrall & Birkinshaw 2000; Mulchaey et al. 2003; Wu, Feng & Xinwu 2007). However, the X-ray surface brightness profile (the sum of a  $\beta$  model and a point component) is very poorly constrained. The extent of the thermal X-ray emission is relatively small with respect to other poor groups, particularly along the EW axis of the large-scale source structure, and its luminosity is low (Worrall & Birkinshaw 2000). These arguments together with the “isolation” of 0755+37 suggest that the diffuse emission, at least on the scale of the radio emission, is mainly due to the hot atmosphere surrounding the galaxy.

### 6.1.2 M 87

M 87 is one of the most famous radio galaxies and resides in the gas-rich Virgo cluster, which is the nearest, bright X-ray emitting cluster. This source provides the opportunity to study the magnetic field fluctuations with excellent spatial resolution. It is a popular target of multiwavelength studies, because of its one-sided jet observed at radio (*e.g.* Owen 1989 (VLA); Kovalev 2007 (VLBA), optical Biretta, Sparks & Macchetto 1999) and X-ray frequencies (*e.g.* Forman et al. 2005, 2007; Harris et al. 2006; Churazov 2008). The morphology of the jet is similar at all these wavelengths, suggesting a common synchrotron radiation mechanism.

M 87 is classified as an FR I source. On scales larger than the radio jet ( $\sim 2$  kpc), it has a complex radio structure mapped out to linear scales of about 40 kpc, showing inner and outer lobes, curved “ears”, and filaments (Fig. 6.2, Owen, Eilek & Kassim 2000). The jet inclination is estimated to be about  $22^\circ$  (Biretta, Zhou & Owen 1995).

In this work, I used VLA datasets at 5 and 8 GHz (6 cm and 3 cm respectively), which were generously provided by F. N. Owen. The VLA observations in the 6 cm band and their reduction were presented by Owen, Eilek & Keel (1990) while the 3 cm data have not been published. At these frequencies and at 0.4 arcsec resolution the source is highly polarized. The images show the main jet, pointing to NW, and two “inner lobes” extending about 4 kpc from the core (Owen, Eilek & Keel 1990).

Table 6.1: General optical and radio properties: Col. 1: source name; Cols. 2, 3: position; Col. 4: redshift; Col. 5: conversion from angular to spatial scale with the adopted cosmology; Col. 6: Fanaroff-Riley class; Col. 7: the largest angular size of the radio source; Col. 8: radio power at 1.4 GHz; Col. 9: angle to the line of sight of the jet axis.

source	RA [J2000]	DEC [J2000]	$z$	kpc/arcsec	FR class	LAS [arcsec]	$\theta$ [degree]
0755+37	07 58 28.1	+37 47 12	0.0428	0.833	I	139	30
M 87	12 30 49.4	+12 23 28	0.00436	0.089	I	489	22

Table 6.2: X-ray and radio equipartition parameters for all the sources. Col. 1: source name; Col. 2: X-ray energy band; Col. 3: average thermal temperature; Cols. 4,5,6 and 7,8,9 best-fitting core radii, central densities and  $\beta$  parameters for the outer and inner  $\beta$  models, respectively; Col. 10: average thermal pressure at the midpoint of the radio lobes; Cols. 11&12: minimum synchrotron pressure and corresponding magnetic field; Col.13: references for the X-ray models.

source	band [keV]	$kT$ [keV]	$r_{cx,out}$ [kpc]	$n_{0,out}$ [cm <sup>-3</sup> ]	$\beta_{out}$	$r_{cx,in}$ [kpc]	$n_{0,in}$ [cm <sup>-3</sup> ]	$\beta_{in}$	$P_0$ [dyne cm <sup>-2</sup> ]	$P_{syn}$ [dyne cm <sup>-2</sup> ]	$B_{P_{syn}}$ [ $\mu$ G]	ref.
0755+37	0.2-2.5	$0.73^{+0.32}_{-0.45}$	159	$6.4 \times 10^{-4}$	0.9				$1.7 \times 10^{-12}$	$3.14 \times 10^{-13}$	4.4	1
M 87	0.7-2.7	$1.68^{0.04}_{-0.05}$	23.4	0.011	0.47	1.86	0.13	0.42	$2.7 \times 10^{-10}$	$2.11 \times 10^{-10}$	55	2

References: (1) Worrall & Birkinshaw (2000); (2) Matsushita et al. (2002).

Fields in the Virgo cluster centred on M 87 have been observed by several X-ray satellites. The extent of the X-ray emission is larger than  $2^\circ$ , which is the field of view of the *ROSAT* PSPC, and is centrally peaked, implying that M 87 harbours a cool core.

At the *ROSAT* and XMM-Newton resolutions, the morphology of the X-ray emission appears regular and smooth, but deep *Chandra* observations (*e.g.* Forman et al. 2007 and references therein) have revealed a very complex structure suggesting interaction between the radio source and the hot gas on several spatial scales (Fig. 6.3). In particular, Forman et al. (2007) detected multiple cavities, some of which coincide with the inner radio lobes, rims of enhanced X-ray emission, loops, rings, and filaments. The cavities resemble the outer large-scale radio structure and have been interpreted as a system of buoyant bubbles produced in AGN outbursts. At distances of about 10-20 kpc from the core, temperature and density jumps are apparent. These correspond to weak shocks with Mach numbers  $\mathcal{M} \approx 1.4$ .

## 6.2 Two-dimensional analysis: rotation measure and depolarization

I produced RM images and related rms errors by weighted least-squares fitting to the polarization angle maps  $\Psi(\lambda)$  as a function of  $\lambda^2$  (Eq. 3.1) at respectively three and eight frequencies for 0755+37 and M 87 (Table 6.3) by using a version of the RM task in the AIPS package modified

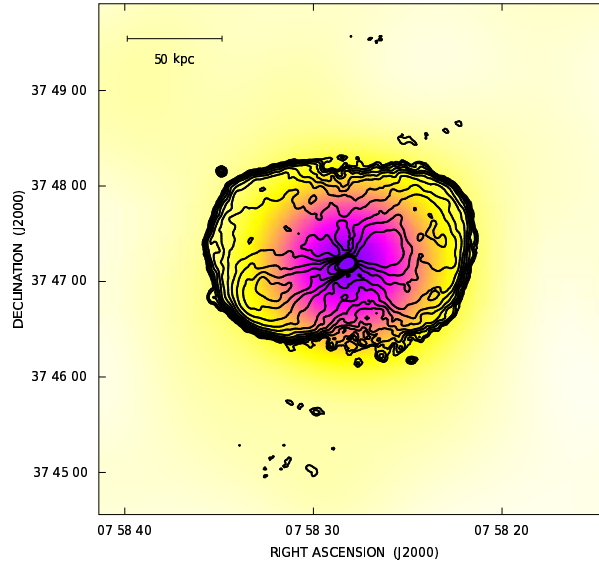


Figure 6.1: Overlay of the X-ray emission (*ROSAT* PSPC) around 0755+37 on radio contours at 1.385 GHz at 4.0 arcsec resolution.

Table 6.3: Frequencies, bandwidths and angular resolutions used in the RM and Burn law  $k$  images. Details of the 0755+37 dataset are given in the Appendix.

source	$\nu$ [MHz]	$\Delta\nu$ [MHz]	beam [arcsec]
0755+37	1385.1	12.5	1.3-4.0
	1464.9		
	4860.1	100	
M 87	4635.1	50	0.4
	4735.0		
	4835.1		
	4935.0		
	8085.1		
	8335.1		
	8535.1		
	8785.1		

by G.B. Taylor. The RM maps were calculated only at pixels with polarization angle uncertainties  $\leq 10^\circ$  at all frequencies. The RM maps have not been corrected for the Galactic contribution. For 0755+37, this is estimated to be negligible ( $-1 \pm 2 \text{ rad m}^{-2}$ ; Simard-Normandin et al. 1981). For M 87, the value is less well-determined, but the source is at very high Galactic latitude, and the associated RM must be very small compared with the measured values (see below). Values of  $\sigma_{\text{RM}}$  integrated over the maps are not corrected for the fitting error  $\sigma_{\text{RM}_{\text{fit}}}$ .

I produced Burn law  $k$  images at the same resolutions and using the same frequencies as the RM maps. Weighted least-squares fits were made to the fractional polarization maps  $\ln p(\lambda)$  as a

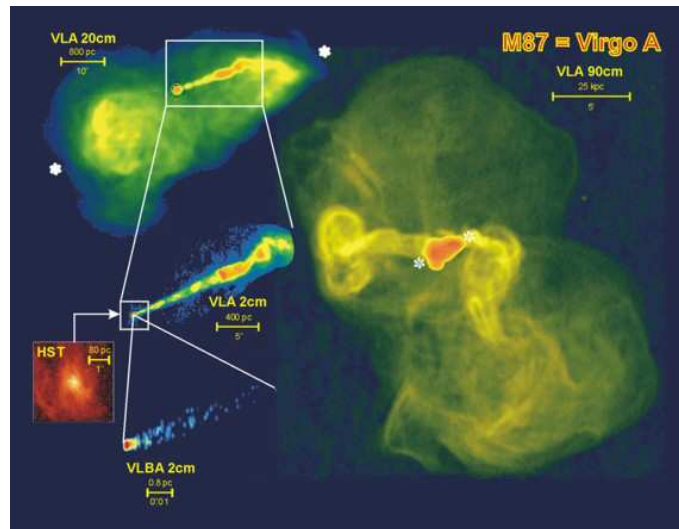


Figure 6.2: Composite radio image of M87 showing the complex structure on multiple spatial scales and at several frequencies. In the present work, the RM from the central cone-like structure, shown in more detail in the top-left panel, has been analysed. Image courtesy of NRAO/AUI.

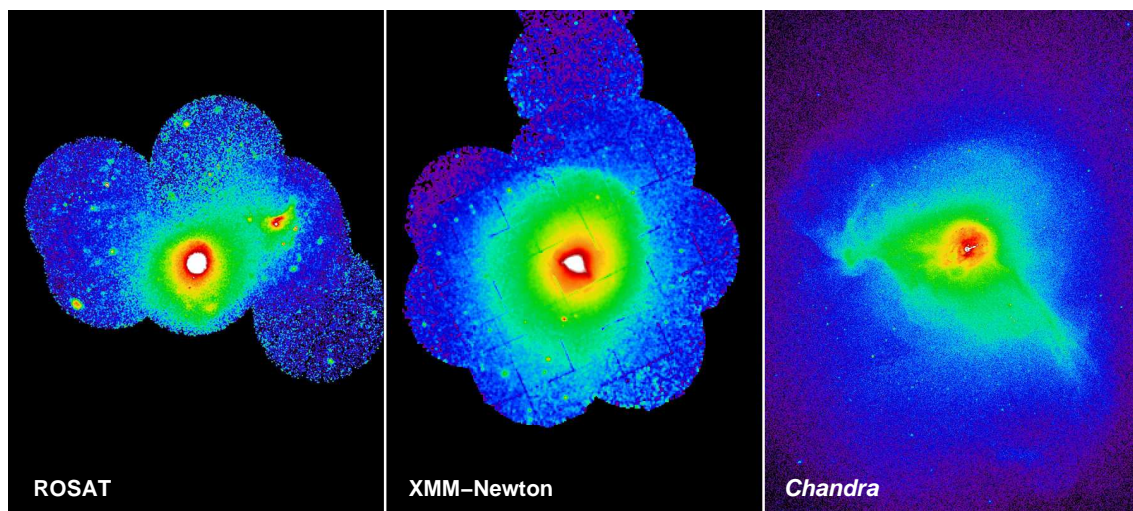


Figure 6.3: X-ray images of the centre of the Virgo cluster showing different scales: *ROSAT* (left) *XMM-Newton* (middle) *Chandra* (right). The increasing resolution has shown a complex structure in the hot gas. Courtesy of W. Forman.

function of  $\lambda^4$  (Eq. 3.5), using a modified version of AIPS RM task. Only data with  $p > 4\sigma_p$  at each frequency were included in the fits.

### 6.2.1 0755+37: images

Two RM images have been produced, at resolutions of 1.3 and 4.0 arcsec. Both of the fits are very good, showing no evidence for deviations from  $\lambda^2$  rotation, although the total range of rotation is quite small. The RM maps are both shown in Fig. 6.4.

At 4.0 arcsec the RM distribution has a mean of  $-5.4 \text{ rad m}^{-2}$  with  $\sigma_{\text{RM}} = 5.1 \text{ rad m}^{-2}$  and an average fitting error  $\sigma_{\text{RM}_{\text{fit}}} = 0.8 \text{ rad m}^{-2}$ . At 1.3 arcsec the mean RM is  $-0.1 \text{ rad m}^{-2}$  with  $\sigma_{\text{RM}} = 6.0 \text{ rad m}^{-2}$  and  $\sigma_{\text{RM}_{\text{fit}}} = 2.0 \text{ rad m}^{-2}$ .

The small amplitude of the RM fluctuations is consistent with an origin in the IGM of the isolated host galaxy, rather than the atmosphere of a more extended group.

There is a clear asymmetry in RM structure between the E and W lobes at both resolutions. Firstly, most of the E (approaching) lobe is characterized by a fairly uniform, positive RM, and the largest RM fluctuations, of both signs, are seen in the W (receding) lobe. Secondly, both lobes show anisotropic features, but with different characteristics. In the E lobe there is a thin, straight structure elongated parallel to the source axis with almost zero  $\langle \text{RM} \rangle$ . This “stripe” is very striking on the 1.3 arcsec map and appears to be almost coincident with the main jet axis, extending beyond the apparent termination of the jet as far as the boundary of the lobe. It is probably the clearest known example of kpc-scale, jet-related RM structure. It can be interpreted in at least two possible ways:

1. the jet is mostly in front of the Faraday screen. This might happen if the jet has displaced a relatively large amount of hot gas or if it is bending along the line-of-sight.
2. The jet lies behind a Faraday screen with an intrinsically low RM along the stripe, *i.e.*, the magnetic field is feeble and/or preferentially aligned in the plane of the sky on the projected jet axis.

The latter point requires that the Faraday screen somehow knows about the jet.

The 4.0-arcsec RM map reveals arc-like features at the leading edge of the W lobe. These have alternating signs and must therefore be associated with field reversals. They are confirmed by the higher resolution map, where the iso-RM contours appear to be fairly straight and perpendicular to the jet axis. The resemblance to the RM bands discussed in Chapter 5 is obvious. It is possible that these features are also caused by draping of the magnetic field around the leading edge of the lobe.

The Burn law  $k$  maps are shown in Fig. 6.5. At 4.0 arcsec resolution, the mean value of  $k$  is  $106 \text{ rad}^2 \text{ m}^{-4}$ , corresponding to a depolarization  $DP_{6cm}^{21cm} = 0.79$ . The mean observed  $k$  values for sub-regions of 0755+37 at both the angular resolutions are listed in Table 6.4. From this table, but also by visual inspection of Fig. 6.5 (left), it is evident that at 4.0 arcsec the highest depolarization is observed in the W (receding) lobe. This is consistent with a higher path length through the X-ray emitting gas (Laing-Garrington effect; Laing 1988; Garrington et al. 1988). In contrast, the Burn law  $k$  distribution at 1.3 arcsec is very symmetrical and has a much lower overall mean, implying that the RM fluctuations are mostly resolved, consistent with a foreground screen.

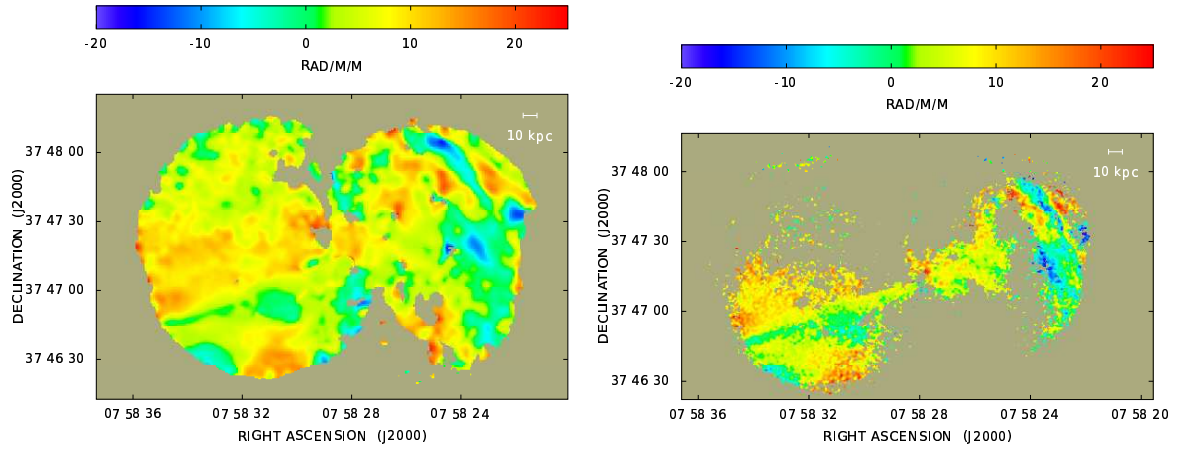


Figure 6.4: Images of the rotation measure for 0755+37, computed from weighted least-squares fits to the position angle –  $\lambda^2$  relation at frequencies of 1385.1, 1469.1 and 4860.1 MHz. The angular resolutions are 4.0 arcsec FWHM (**left**) and 1.3 arcsec FWHM (**right**).

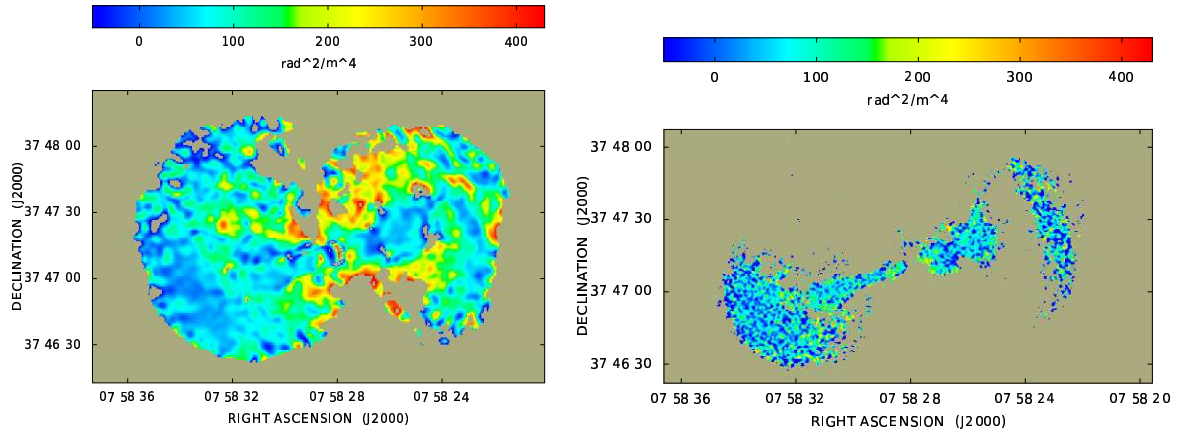


Figure 6.5: Images of Burn law  $k$  for 0755+37 computed from weighted least-squares fits to the relation  $p(\lambda) = p(0)\exp(-k\lambda^4)$  at frequencies of 1385.1, 1469.1 and 4860.1 MHz. The angular resolutions are 4.0 arcsec FWHM (**left**) and 1.3 arcsec FWHM (**right**).

This scenario is confirmed by the profiles of  $\langle k \rangle$  across the source (Fig. 6.6): at lower resolution the profile is asymmetrical, with less depolarization at a given distance from the core in the E lobe and a peak which is displaced slightly W of the nucleus. In contrast, the  $\langle k \rangle$  profile at 1.3 arcsec resolution is symmetrical and lies significantly below that at 4.0 arcsec.

The high  $k$  values in the W lobe at the lower resolution are mostly seen in a cone-like structure (Fig. 6.5 left), as was already pointed out by Bondi et al. (2000). It is possible that the origin of such structure may be gas and field compression or the development of a mixing layer as discussed for M 84 and 3C 270 (Sec. 5.8.5). To confirm this picture, higher resolution X-ray observations are needed. In contrast, a region with very low and almost constant depolarization is observed at the leading edge of the W lobe, beyond the end of the approaching jet.

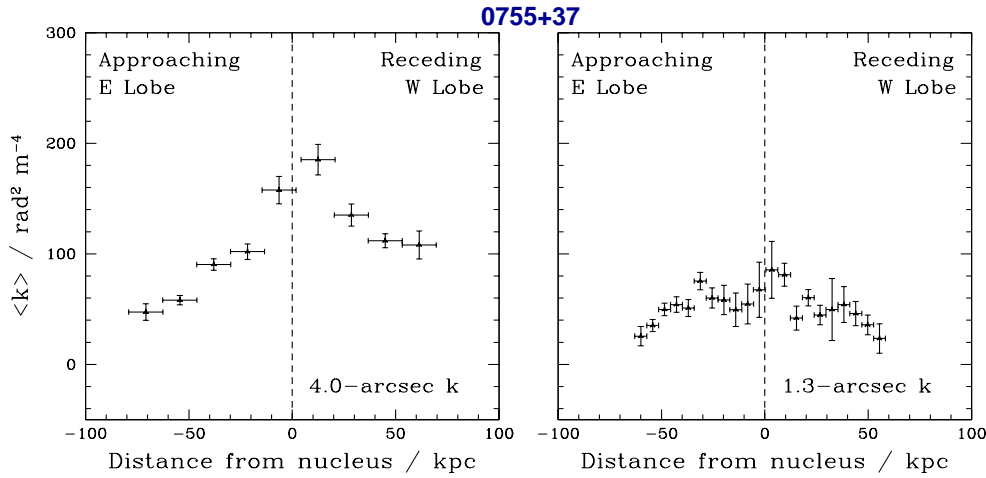


Figure 6.6: Profiles of Burn law  $k$  for 0755+37 parallel to the jet direction, plotted against distance from the nucleus. The angular resolutions are 4.0 (**left**) and 1.3 arcsec FWHM (**right**).

Apart from the cone-like structure in the E lobe no correlation of depolarization with source morphology is apparent. Together with the absence of significant deviations from  $\lambda^2$  rotation, this is again consistent with a Faraday rotating medium mostly external to the source.

### 6.2.2 M 87: images

I made the RM image of M 87 at a resolution of 0.4 arcsec. The `rmfit` task did not solve correctly for the  $n\pi$  ambiguities in position angle at some locations. In order to remove these ambiguities, the RM map was produced using the following steps:

1. Fit to the four frequencies in the 3 cm band using the Greg Taylor version of the `rmfit` program in `RMFIT`. This produced a noisy, but smooth RM image.
2. Run `smooth` in `RMFIT` on this RM image, to apply a median-weight filter with a 15-pixel (1.5 arcsec) smoothing kernel.
3. Correct all of the polarization angle maps (in the 6 and 3 cm bands) using the filtered RM image.
4. Run a modified version of `rmfit` task which minimises the absolute differences between the polarization angle maps at adjacent frequencies (i.e. assumes that there are no  $n\pi$  ambiguities).
5. Add the result back to the filtered RM image.

The resulting RM map essentially confirms the results of the 4-frequency, C-band fit made by Owen, Eilek & Keel (1990), but is significantly improved both in noise level and overall reliability.

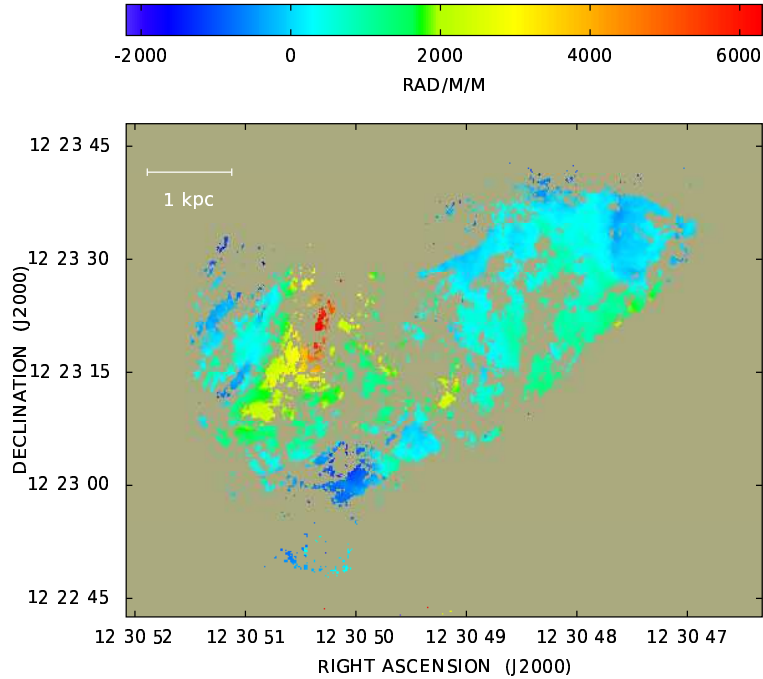


Figure 6.7: Rotation measure of M 87 computed from fits to the position angle –  $\lambda^2$  rotation at eight frequencies as described in the text. The angular resolution is 0.4 arcsec FWHM.

The new map, shown in Fig. 6.7, has an average fitting error  $\sigma_{\text{RM}_{\text{fit}}} = 15 \text{ rad m}^{-2}$ . The RM distribution has a mean of roughly  $650 \text{ rad m}^{-2}$  with  $\sigma_{\text{RM}} \approx 900 \text{ rad m}^{-2}$ .

The main features of the RM image are as follows.

- The RM values are large and almost always positive, requiring a magnetic field pointing towards us across most of the source. They range from  $\approx -2000$  up to  $\approx 6000 \text{ rad m}^{-2}$ . This compares with the much larger range of  $-1000$ - $8000 \text{ rad m}^{-2}$  found by Owen, Eilek & Keel (1990). The most extreme positive values found by Owen, Eilek & Keel (1990) not consistent with the X-band position angles.
- The highest RM values ( $\approx 3500$ - $6000 \text{ rad m}^{-2}$ ) are seen only in a restricted patch in the E lobe.
- The jet appears as a uniform RM structure characterized by low values ( $\approx 100 \text{ rad m}^{-2}$ ), as already pointed out by Owen, Eilek & Keel (1990).
- The RM distribution is asymmetrical: positive and smoothly varying in the W lobe, patchier and associate with field reversals in the E lobe.

As in 0755+37, the low RM seen across the jet is surprising. Similar explanations may hold for the two sources.

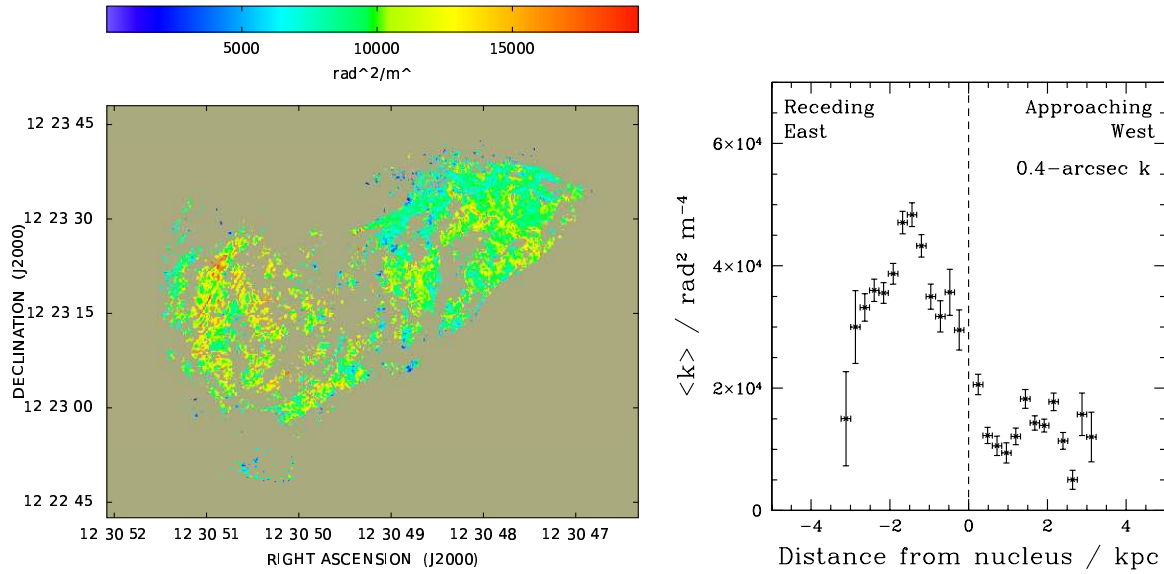


Figure 6.8: **Left:** Image of Burn law  $k$  for M87 computed from weighted least-squares fits to the relation  $p(\lambda) = p(0)\exp(-k\lambda^4)$  at the eight frequencies listed in Table 6.3. **Right:** Profiles of Burn law  $k$  along the jet direction, plotted against distance from the nucleus. The angular resolution is 0.4 arcsec FWHM.

The Burn law  $k$  map for M87 is shown in Fig. 6.8. At 0.4 arcsec resolution the overall  $k$  distribution has a mean of  $9820 \text{ rad}^2 \text{ m}^{-4}$ , corresponding to a depolarization  $DP_{3cm}^{6cm} = 0.85$ . The mean observed  $k$  values for the two lobes are listed in Table 6.4. The highest depolarization occurs in patchy structures in the E (receding) lobe, consistent with the Laing-Garrington effect (Laing 1988; Garrington et al. 1988). These structures appear filamentary and are likely to be caused by steep (and therefore unresolved) RM gradients. Indeed, they are in the same areas as the highest absolute values of RM and  $\nabla\text{RM}$  (Fig. 6.7).

In addition to low and constant RM, the jet also shows uniformly low  $k$ . The profile of  $\langle k \rangle$  across the source (Fig. 6.8, right) is qualitatively similar to that observed in 0755+37, but more extreme: it increases monotonically from W to E across the core, peaks in the E lobe and then decreases at larger distances. Except in the region of the jet, no detailed correlation of depolarization with source morphology is apparent. Together with the absence of significant deviations from  $\lambda^2$  rotation, this again requires a Faraday rotating medium mostly external to the source.

### 6.3 Two-dimensional analysis: structure functions

I used the RM structure function (Eq. 3.13) to quantify the two-dimensional fluctuations of Faraday rotation measure on scales larger than the observing beamwidth for 0755+37 and M87.

## 0755+37

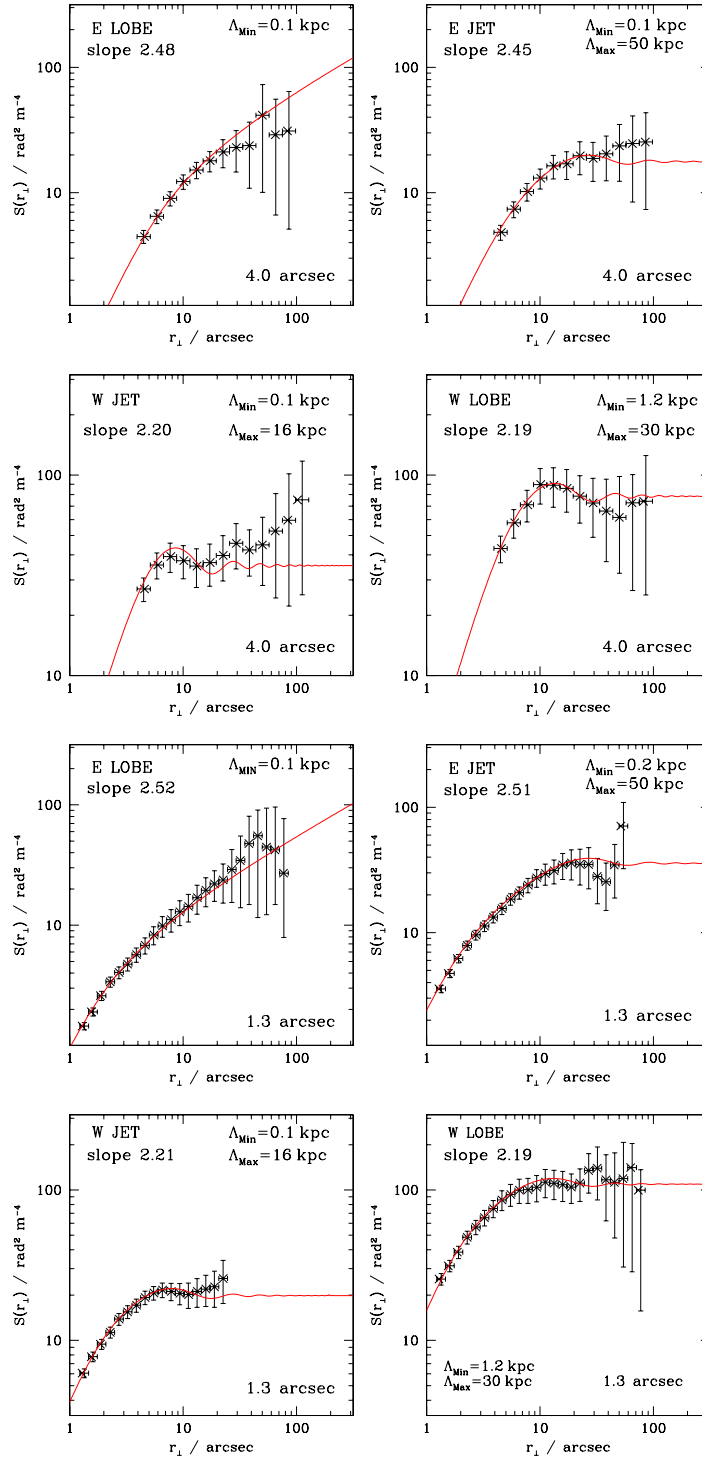


Figure 6.9: RM structure functions for the sub-regions of 0755+37 indicated in the panels at 4.0 and 1.3 arcsec FWHM. The horizontal bars represent the bin widths and the crosses the mean separation for data included in the bins. The red curves are the best fits, including the effects of the convolving beam. The error bars represent the rms variations for structure functions derived from multiple realizations of the indicated power spectrum on the observed grid.

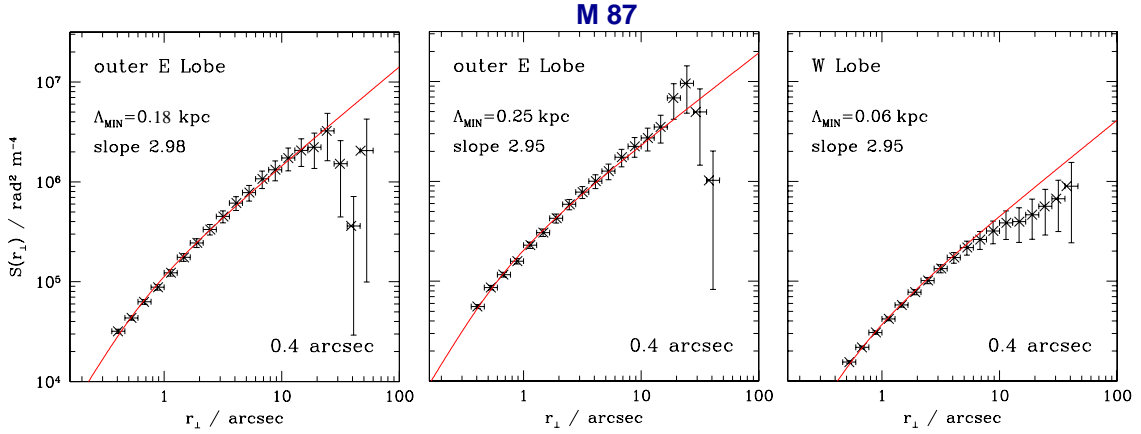


Figure 6.10: RM structure functions for the sub-regions of M 87 indicated in the panels at 0.4 arcsec FWHM. The horizontal bars represent the bin widths and the crosses the mean separation for data included in the bins. The red curves are the best fits including the effects of the convolving beam. The error bars represent the rms variations for structure functions derived for multiple realizations of the indicated cut-off power-law power spectra on the observed grid for each region.

Structure functions have been computed at the resolutions of the RM images and binned by separation over four areas of 0755+37 (the two jets and the two lobes), and in three areas of M 87 (the inner and outer E lobe and the W lobe). The reason for splitting the E lobe of M 87 into two sub-regions was that the structure function derived for the whole lobe showed a decrease at large separation which probably indicates the presence of significant spatial variations in the field and/or density (cf. 3C 449, Chapter 4). All of these sub-regions have enough data points to ensure that the structure functions are robustly determined. A first-order correction for uncorrelated random noise,  $\sigma_{\text{fit}}$ , evaluated in each sub-region, has been applied to all of the structure functions. A cut-off power law (CPL) power spectrum (see also Eq. 4.3)

$$\begin{aligned}
 \widehat{C}(f_{\perp}) &= 0 & f_{\perp} < f_{\min} \\
 &= C_0 f_{\perp}^{-q} & f_{\perp} \leq f_{\max} \\
 &= 0 & f_{\perp} > f_{\max} .
 \end{aligned} \tag{6.1}$$

gives model structure functions in very good agreement with the data for both sources (Figs. 6.9 and 6.10). The values of  $f_{\max}$  have also been estimated by fitting the mean values of  $k$  for the sub-regions. I produced multiple RM realisations corresponding to the CPL model power spectrum on the observed grid, including the effects of the convolving beam, to evaluate the rms deviations of their structure functions. These take into account the effects of undersampling and are plotted as error bars attached to the observed points. The best-fitting parameters are quoted for each sub-region separately in Table 6.4, together with the observed and predicted values of

Table 6.4: Best-fitting power spectrum parameters for the individual sub-regions of 0755+37 and M 87.

Source	Region	FWHM [arcsec]	$q$	$f_{\max}$ [arcsec <sup>-1</sup> ]	$f_{\min}$ [arcsec <sup>-1</sup> ]	$k_{obs}$ [rad <sup>2</sup> m <sup>-4</sup> ]	$k_{syn}$ [rad <sup>2</sup> m <sup>-4</sup> ]
0755+37	E LOBE	4.0	2.48	8.33	$\infty$	64±3	69±3
	E JET		2.45	''	0.017	112±5	119±4
	W JET		2.20	''	0.052	156±7	164±5
	W LOBE		2.19	0.69	0.028	109±5	104±5
	E LOBE	1.3	2.52	8.33	$\infty$	41±3	37±4
	E JET		2.51	4.16	0.017	63±4	57±5
	W JET		2.21	8.33	0.052	58±5	55±5
	W LOBE		2.19	0.69	0.028	38 ±6	40±4
M 87	E <sub>out</sub> LOBE	0.4	2.98	0.5	$\infty$	12900±600	13400±100
	E <sub>in</sub> LOBE	''	2.91	0.35	''	15800 ±800	16400±250
	W LOBE	''	2.95	1.5	''	9300 ±500	10250±250

Burn law  $k$ . In M 87, the slopes and cut-off frequencies derived for the individual sub-regions are mutually consistent. A combined fit, weighting all of the sub-regions equally and allowing their normalizations to vary, gives  $q = 2.95$  and  $f_{\max} = 2.75 \text{ arcsec}^{-1}$ . The slopes for the different parts of 0755+37 differ significantly from each other, and no combined fit has been attempted.

The structure functions for the lobes of M 87 show little firm evidence for any levelling off at large separations (the points at  $\geq 15 \text{ arcsec}$  in the East lobe have very large errors). In the W lobe, the field outer scale must be  $\geq 30 \text{ arcsec}$  ( $\approx 2.7 \text{ kpc}$ ). The fits therefore assume  $f_{\min} = \infty$  for this source. In contrast, the structure functions for both of the jets and the W lobe of 0755+37 level off and clearly show the suppression of the RM fluctuations above some outer scale. Better fits to these structure functions are provided by setting a finite value for  $f_{\min}$  of 0.017-0.052  $\text{arcsec}^{-1}$ , corresponding to a maximum field fluctuations on scales  $\Lambda_{\max} \approx 15 - 50 \text{ kpc}$ . The situation is more ambiguous in the E lobe of 0755+37, because of the large errors, and in this case the fit with  $f_{\min} = \infty$  is shown. Further work on the outer scale will require a three-dimensional analysis which takes into account the spatial variations of density and path length across the sources.

## 6.4 Preliminary conclusions

I have studied in detail the images of linearly polarized emission from the FR I radio galaxies 0755+37, in a sparse group, and M 87 at the centre of the cool-core Virgo cluster. I have produced images of RM and Burn law  $k$  with resolutions of 4.0 and 1.3  $\text{arcsec}$  FWHM for 0755+37, and 0.4  $\text{arcsec}$  FWHM for M 87. The spatial variations of the RM distributions in both sources have been investigated using a structure-function technique.

The results of this analysis can be summarized as follows:

- The polarization position angles accurately follow the  $\lambda^2$  relation. Together with the observed low depolarization, this confirms yet again that the Faraday rotation is primarily in front of the radio emission. The residual depolarization is consistent with unresolved RM fluctuations.
- The amplitude of the RM fluctuations in 0755+37 is smaller than for FRI sources embedded in groups of galaxies (Chapter 5) and comparable to that in NGC 315, which is also in a very sparse environment (Laing et al. 2006a). This reinforces the hypothesis the most of the Faraday rotating material is due to the hot atmosphere of the associated galaxy.
- In M 87 the amplitude of the RM fluctuations is typical of that found in other cool-core clusters such as Cygnus A and Hydra A (*e.g.* Carilli & Taylor 2002; Laing et al. 2008).
- The profiles of  $\sigma_{\text{RM}}$  (which is not shown) and  $\langle k \rangle$  for both sources have higher average values for the receding lobes. Thus both resolved and sub-beam fluctuations of RM are higher on the receding side (the Laing-Garrington effect; Laing 1988; Garrington et al. 1988).
- Both approaching jets show low and uniform rotation measures. In M 87, the associated depolarization is also anomalously low.
- There is other evidence for anisotropic RM fluctuations in 0755+37: the leading edge of the W lobe shows arc-like RM structures with sign reversals. These are reminiscent of the RM bands discussed in Chapter 5. The RM structures of both 0755 +37 and M 87 appear reasonably isotropic elsewhere.
- Except in the restricted areas showing obvious anisotropic structure, it is reasonable to treat the RM as a Gaussian, random, isotropic variable and to estimate its power spectrum. The power spectra are well described by power laws with slopes ranging from 2.2 to 2.5 in 0755+37 and slightly steeper ( $\approx 3.0$ ) in M 87. These are comparable with the slopes deduced for 3C 449, 3C 31 (Laing et al. 2008) and the regions not dominated by RM bands in 0206+35, 3C 270 and 3C 353 (Chapter 5). They are all significantly flatter than the value of 11/3 expected for Kolmogorov turbulence.
- These power spectra are consistent with the observed depolarization for minimum field scales of 0.1 kpc in 0755+37 and 0.06-0.25 kpc in M 87. The nearby location and high surface brightness of M 87 have allowed an accurate determination of its RM power spectrum on scales smaller than those accessible for other objects.

- The derived magnetic-field auto-correlation lengths  $\lambda_B$  are 0.1-1.4 kpc in 0755+37 (depending on the sub-region), and 0.2 kpc in M 87.
- The central magnetic field strength required to match the RM fluctuations, deduced from the single-scale approximation including cavities and assuming these values of  $\lambda_B$  as scale-lengths, is  $\approx 1.0 \mu\text{G}$  in 0755+37 and  $\approx 35 \mu\text{G}$  in M 87. This confirms the trend for stronger fields to be seen in richer environments (Carilli & Taylor 2002), although subject to confirmation by three-dimensional modelling.

Significant imprecision is certainly introduced by the assumption of constant integration path required to interpret the RM structure functions over limited sub-regions. This can be corrected in future three-dimensional simulations, but better constraints on the source geometries and the distributions of hot gas will be required. This will be particularly challenging for M 87, where the hot-gas structure is extremely complicated (Forman et al. 2007).



# Summary and conclusions

The goal of this thesis was to constrain the strength and structure of the magnetic field associated with the extragalactic medium surrounding radio galaxies located in a variety of environments by using observations of Faraday rotation and depolarization. To interpret the RM structure, I have derived analytical models and performed two- and three-dimensional Monte Carlo simulations.

The picture that emerges is that the magneto-ionic environments of radio galaxies are significantly more complicated than was apparent from earlier work. The unique feature of this thesis is that the target radio galaxies are all large and highly polarized, enabling the determination of Faraday rotation and depolarization at a large number of independent points with high signal-to-noise ratio. This in turn allows global variations across the sources to be determined, as well as accurate estimates of spatial statistics.

In Section 6.5, I summarize the main results obtained in Chapters 4, 5 and 6. The general conclusions are given in Sec. 6.6 as a set of answers to the questions posed in the Abstract and finally Sec. 6.7 briefly lists some topics for further work.

## 6.5 Summary

### 6.5.1 The tailed source 3C 449

The RM and depolarization across the source both appear to be consistent with a pure, mostly resolved foreground Faraday screen. The RM structure shows no preferred direction anywhere in the radio source. This is consistent with an isotropic, turbulent magnetic field fluctuating over a wide range of spatial scales. I quantified the statistics of the magnetic-field fluctuations by deriving RM structure functions, which have been fitted using models derived from theoretical power spectra. The errors due to undersampling have been estimated by making multiple two-dimensional realizations of the best-fitting power spectrum. Depolarization measurements have also been used to estimate the minimum scale of the magnetic field variations. I then developed three-dimensional models with a gas density distribution derived from X-ray observations and

a random magnetic field with the previously-determined power spectrum. By comparing the simulations with the observed Faraday rotation images, the strength of the magnetic field and its dependence on density could be estimated. The RM and depolarization data are consistent with a broken power-law magnetic-field power spectrum, with a break at about 11 kpc and slopes of 2.98 and 2.07 at smaller and larger scales, respectively. The minimum scale of the fluctuations is  $\approx 0.2$  kpc. A particularly interesting result is the determination of the outer scale,  $\Lambda_{\max} \approx 65$  kpc, which gives the driving scale of turbulence. This is the first time that this quantity has been estimated unambiguously.

The average magnetic field strength at the group centre is  $3.5 \pm 1.2 \mu\text{G}$ , decreasing linearly with the gas density within  $\approx 16$  kpc of the nucleus. At larger distances, the dependence of field on density appears to flatten, but this may be an effect of errors in the density model. The ratio of the thermal and magnetic-field pressures is  $\approx 30$  at the nucleus and  $\approx 400$  at the core radius of the group gas. Therefore, the intra-group magnetic field is not energetically important.

These results indicate a magnetized foreground medium very similar to that in 3C 31 (Laing et al. 2008), as was expected from the close similarity between the environments, radio morphologies and redshifts of the two sources. The RM fluctuation amplitudes are comparable, as is the derived central magnetic field ( $B_0 \approx 2.8 \mu\text{G}$  for 3C 31) and the magnetic field power spectrum which in both sources can be fit by a broken power law steepening at higher spatial frequencies. The low-frequency slopes are similar ( $q = 2.3$  for 3C 31), but the high-frequency slope for 3C 31 is consistent with the value for Kolmogorov turbulence ( $q = 11/3$ ). Because of uncertainties in the density distribution around 3C 31, Laing et al. (2008) could only estimate a lower limit to the outer scale of magnetic-field fluctuations,  $\Lambda_{\max} \gtrsim 70$  kpc, likely set as in 3C 449 by interactions with companion galaxies in the group.

### 6.5.2 The lobed radio galaxies 0206+35, 3C 270, M 84 and 3C 353

In contrast to 3C 449, all of the sources show highly anisotropic banded RM structures with contours of constant RM perpendicular to the major axes of their radio lobes. The bands have widths of 3-10 kpc and amplitudes of  $10\text{-}50 \text{ rad m}^{-2}$ . In several cases, they are associated with field reversals. All of the sources except M 84 also have regions in which the RM fluctuations have lower amplitude and appear isotropic. Structure function and depolarization analyses for these areas have shown that flat power-law power spectra with low amplitudes and high-frequency cut-offs give good descriptions of the spatial statistics. The strength of the field which gives rise to the bands is significantly higher than that of the largest-scale component in the band-free regions. The wavelength behavior of the polarization position angles and the almost complete absence of depolarization imply, as usual, that a mostly resolved foreground Faraday screen is

responsible for the observed RM in the bands and elsewhere. I have presented an initial attempt to interpret the banded RM phenomenon as a consequence of interactions between the sources and their surroundings. Synthetic RM images have been produced for the case of compression of a uniformly-magnetized external medium. This simple model of the source-environment interaction predicts RM bands of approximately the right amplitude, but only under special initial conditions. A much better description of the data is provided by a *two-dimensional* magnetic structure in which the field lines are a family of ellipses draped around the leading edge of the lobe. This draped-field model can produce RM bands in the correct orientation *for any source inclination*. Moreover, it might explain the high RM amplitude and low depolarization observed within the bands. The two-dimensional draped-field model may also account for the low rate of detection of RM bands in published observations, since anisotropic RM structures will not be observed unless the line-of-sight intercepts the wrapped field lines. Furthermore, superposed RM fluctuations with significant power on scales comparable with the bands will make them difficult to recognise.

This work has demonstrated *unequivocally* for the first time that the interaction between radio galaxies and their immediate environments affects the magnetisation of the surrounding plasma.

Finally, I have reported rims of high depolarization at the edges of the inner radio lobes of M 84 and 3C 270. Such highly depolarized structures had not been observed in earlier, less detailed work. The magnetic fields responsible for such depolarization must be tangled on small scales, since they produce depolarization without any obvious effects on the large-scale Faraday rotation pattern. The rims are spatially coincident with shells of enhanced X-ray surface brightness, in which both the field strength and the thermal gas density are likely to be increased by compression.

### 6.5.3 The radio galaxies 0755+37 and M 87

I have presented two-dimensional analyses of the RM and depolarization across the radio galaxy 0755+37, in a very poor group, and the inner 5 kpc of the radio structure of M 87, located at the centre of the cool-core Virgo cluster. 0755+37 shows the clearest known example of jet-related RM structure. The amplitudes of the RM fluctuations across 0755+37 and M 87 are typical of their environments: in 0755+37 they are smaller than those detected in sources in groups of galaxies and much more than those in M 87, which are typical of a cool core cluster. The RM structure functions have been evaluated for both sources over sub-regions where the RM fluctuation amplitudes are approximately constant. The structure-function analysis has shown that the best-fitting power spectrum of the RM fluctuations (and thus the magnetic field) is a power law with a cut-off at high spatial frequencies. The best-fitting power spectra are different for the two lobes of 0755+37: the slopes are  $q \approx 2.5$  in the eastern lobe and  $q \approx 2.2$  in the west. The minimum field scale derived from depolarization measurements is 0.1 kpc and the maximum field fluctuation scale is  $\approx 50$  kpc.

In M 87, a power spectrum with slope  $q \approx 3.0$  fits well everywhere. The minimum scale ranges from 0.06 up to 0.25 kpc. An approximate lower limit to the outer scale is 2.7 kpc.

## 6.6 General conclusions

### 1. Origin of the bulk of the Faraday effect observed across radio galaxies

It is possible to establish that most of the RM is due to material between us and the radio source by verifying that the polarization angles have a  $\lambda^2$  dependence and that the detected depolarization, if any, is consistent with that expected from instrumental effects (beam and bandwidth depolarization). This is the case for all of the radio galaxies analysed in this thesis and in most earlier work.

This is consistent with the idea that radio sources have evacuated cavities in the IGM during their expansion (as observed in X-rays) and that there has been relatively little mixing of thermal and relativistic plasma. The apparent under-pressure in FRI lobes and tails is most easily explained if a small amount of thermal plasma has been entrained and heated, but the densities required are quite small, and consistent with the non-detection of internal Faraday rotation and depolarization at GHz frequencies.

Prior to the work described here, it was generally thought that the observed RM was produced almost exclusively by the distributed hot component of the intra-group or intra-cluster medium and that interactions with the radio source were unimportant. In the present study, three distinct types of magnetic-field structure have been found: a component with large-scale fluctuations, indeed plausibly associated with the undisturbed intergalactic medium; a well-ordered field draped around the leading edges of radio lobes and a field with small-scale fluctuations in the shells of compressed gas surrounding the inner lobes, perhaps associated with a mixing layer.

Foreground Faraday rotation in a spherically symmetrical, undisturbed IGM provides a natural explanation for the systematic asymmetry in RM variance and/or depolarization observed between the approaching and receding lobes (Laing 1988; Garrington et al. 1988; Morganti et al. 1997; Laing et al. 2008). In contrast, some authors (e.g. Bicknell, Cameron & Gingold 1990) have suggested that the RM could be localized in a thin layer around the source, but simple shell models of this type find difficulties in reproducing the observed asymmetries and are unlikely to be important on large scales. It is likely that the spherically-symmetric group component dominates in large, tailed sources such as 3C 449.

The results on banded RM structures presented in this thesis suggest that the magnetised medium producing them must have a scale comparable to that of the lobe width. If the

radio source is expanding supersonically, there will also be a bow shock ahead of the lobe in the hot gas which will naturally produce higher densities and stronger fields in the post-shock material immediately surrounding the lobes. All of the sources which show banded RM structure show evidence of strong interaction with the surrounding medium, either from expansion driven by the jets (0206+35, 3C 270, 3C 353) or from X-ray observations (M 84). The best evidence for mixing between thermal and relativistic plasma comes from the observation of enhanced depolarization in the inner lobes of M 84, 3C 270 and 0755+37. It is in these regions that models like those of Bicknell, Cameron & Gingold (1990) are most likely to apply.

## 2. The connection between magnetic field and thermal gas

The results of this work are consistent with the idea that the RM fluctuation amplitude in galaxy groups and clusters scales roughly linearly with density, ranging from a few  $\text{rad m}^{-2}$  in the sparsest environments (0755+37) through intermediate values of  $\approx 30\text{-}100 \text{ rad m}^{-2}$  in groups (0206+35, 3C 270 and 3C 449) to  $\sim 10^4 \text{ rad m}^{-2}$  in the centres of clusters with cool cores (M 87).

The spatial variation of RM fluctuation amplitude in galaxy groups is consistent with a distribution for the magneto-ionic medium which is spherically symmetric, together with cavities coincident with the radio emission. The radial dependence of the field strength can be approximated by  $B(r) = \langle B_0 \rangle \left( \frac{n_e(r)}{n_0} \right)^\eta$ , with  $1 \gtrsim \eta \gtrsim 0.5$ . The central magnetic-field strength  $B_0$  is typically a few  $\mu\text{G}$  and the magnetic field is never dynamically dominant over the modeled volumes.

Thus the relation between magnetic field strength and density in galaxy groups appears to be a continuation of the trend observed in galaxy clusters (*e.g.* Brunetti et al. 2001; Dolag et al. 2006; Guidetti et al. 2008; Bonafede et al. 2010): the radial variations have similar functional forms and the normalization scales with density.

## 3. Magnetic-field structure

In this thesis, two types of RM structures have been found: one with RM variations reasonably approximated as isotropic and random (3C 449, M 87, the western lobe of 3C 353) and one with two-dimensional banded RM patterns (0206+35, 3C 270, M 84, the eastern lobe of 3C 353 and perhaps 0755+37). The first type of structure is well reproduced by a Gaussian isotropic random magnetic field, as shown by earlier numerical modelling as well as that performed in this thesis. The second type shows evidence for a two-dimensional, ordered magnetic field. One of the major results of this thesis has been to demonstrate that RM enhancements are expected from compression of the surrounding magneto-ionic medium by expanding radio galaxies, but that such structures can have band-like shapes

with the observed properties *only* when the field is wrapped around the radio lobes in a two-dimensional geometry. In order to create RM bands with multiple reversals, more complex field geometries such as two-dimensional eddies are needed.

#### 4. Magnetic field power spectrum: functional form and range of scales

Recent observational work on galaxy clusters has led to claims that the intra-cluster magnetic field has a Kolmogorov-like power spectrum (i.e. a power law with slope  $q = 11/3$ ). Kolmogorov turbulence would be expected over some inertial range if the turbulence is primarily hydrodynamic (Kolmogorov 1941) or for the MHD cascade investigated by Goldreich & Sridhar (1997). However, the assumptions on which the Kolmogorov turbulence relies (homogeneity, isotropic and lack of magnetization) are not satisfied in the intergalactic medium. Numerical simulations predict a wide range of spectral slopes (albeit with some preference for the Kolmogorov value; Dolag 2006), and a comparison between theory and observation therefore seems premature.

None of the RM distributions studied in this thesis show fluctuations compatible with a Kolmogorov power spectrum over the full range of observed scales. Instead, they are consistent with flatter power-law power spectra ( $q \leq 3$ ). A Kolmogorov form on scales below the resolution limit cannot be excluded, although this is not the case on linear scales as low as 60 pc in M 87. Power spectra with slopes flatter than 11/3 have also been found by other authors (Murgia et al. 2004; Govoni et al. 2006; Laing et al. 2008). Similar results come from the analysis of magnetic turbulence in the Galaxy. For example, Regis (2011) found a flatter index ( $q = 2.7$ ) by analysing the fluctuations in the Galactic synchrotron emission (see also Minter & Spangler 1996).

It is worth noting that the power spectra for sources in this thesis appear to be steeper in richer environments. The slopes range from  $q \approx 2$  in groups (0755+37, 0206+35) up to  $q \approx 3$  in clusters (3C 353, M 87). The flatter slopes are found in sources showing anisotropic RM's, but this might be a selection effect. The idea of that the index of the power spectrum is determined by the richness of the environment is probably oversimplified.

In 3C 449, the power spectrum cannot be a single power law, but rather steepens on smaller scales. A broken power law gives a good representation of the data, as found for 3C 31 (Laing et al. 2008), but is not unique: a smoother function would fit just as well. The precise location of the break in the broken power law may not be physically significant, but a change in slope might occur at the typical field reversal scale if the field is produced by a fluctuation dynamo (Schekochihin & Cowley 2006; Eilek & Owen 2002).

It is not clear what determines the minimum and the maximum scales of the magnetic field. Reconnection of field lines is expected to occur on much smaller scales than those sampled

and is therefore not relevant. Energy can be injected on large scales from the interactions between the radio source and the magnetized gas, gas motions (“sloshing”) within the group/cluster potential well (*e.g.* merger-related) and motion of the host galaxy. All of these provide energy input on roughly the outer scale estimated for 3C 449 and 0755+37 (the latter subject to confirmation by three-dimensional modelling). In principle, the origin of the maximum scale could be constrained by observations of the same type of radio source in different environments.

#### 5. RM structure and its connection with the radio source morphology

I pointed out a potential correlation between radio source morphology and RM anisotropy. RM bands have so far been unambiguously detected only in lobed radio galaxies. This is what expected if the process producing bands is related to some form of compression or draping. Radio galaxies with lobes are indeed expected to be more effective than tailed sources in compressing the surrounding gas. Production of RM bands by draped fields in tailed sources is not excluded, provided that there is relative motion between the source and the surrounding gas. This might occur in narrow-angle tail sources (where the host galaxy is moving rapidly through the ICM) or in wide-angle tails if there are sloshing motions of gas in the cluster potential well.

## 6.7 Future prospects

The work described in this thesis raises a number of observational questions, including the following.

1. How common are anisotropic RM structures? Do they occur primarily in lobed radio galaxies with small axial ratios, consistent with jet-driven expansion into an unusually dense surrounding medium? Is their frequency qualitatively consistent with the two-dimensional draped-field picture?
2. Why do we see bands primarily in sources where the isotropic RM component has a flat power spectrum of low amplitude? Is this just because the bands can be obscured by large-scale fluctuations, or is there a causal connection?
3. Are the RM bands suggested in tailed sources such as 3C 465 and Hydra A caused by a similar phenomenon (*e.g.* bulk flow of the IGM around the tails)?
4. Is an asymmetry between approaching and receding lobes seen in the banded RM component? If so, what does that imply about the field structure?

5. How common are the regions of enhanced depolarization at the edges of radio lobes? How strong is the field and what is its structure? Is there evidence for the presence of a mixing layer?

It should be possible to address all of these questions using a combination of observations with the new generation of synthesis arrays (EVLA, e-MERLIN and LOFAR all have wide-band polarimetric capabilities) and high-resolution X-ray imaging. It will be possible to determine rotation measures within a single observing band at high spatial resolution, allowing at the same time a much quicker and more accurate RM determination and the building of larger samples. Higher resolution and improved image quality will allow sampling of a larger range of spatial scales and hence improve the constraints on the RM power spectrum. In particular, it should be possible to determine with certainty whether the power spectrum has the form expected for Kolmogorov turbulence. An alternative to fitting parametrized functions to the power spectrum is provided by Bayesian methods, which are non-parametric and should improved error estimates (Enßlin & Vogt 2005). RM modelling should be conducted in synergy with jet modelling, which provides constraints on the geometry of the sources and estimates of their jet powers, and with X-ray observations. Finally more detailed MHD simulations of radio-source evolution in a surrounding magnetised medium are needed.

# Appendix



# Appendix

## Data reduction and imaging of the radio galaxies 0206+35, 0755+37 and M 84 <sup>‡</sup>

The aim of this appendix is to present the VLA data reduction and high-quality radio imaging of the FRI sources 0206+35, 0755+37 and M 84, which have been performed in collaboration with R. A. Laing, A. H Bridle, P.Parma and M.Bondi.

Here, we describe:

1. details of the observations and data reduction
2. the source morphologies in total intensity at a range of resolutions,
3. images of the degree of polarization and the apparent magnetic field direction, corrected for Faraday rotation.

### .1 Observations and VLA data reduction

We made use of new and archive VLA observations. Deep images with angular resolution ranging from 4.5 down to 0.35 arcsec FWHM have been produced from multi-configuration VLA observations at 1.4 GHz (L-band) and 4.9 GHz (C-band). A journal of the observations is given in Table 5.

The VLA data listed in Table 5 were calibrated and imaged using the AIPS software package, following standard procedures, with a few additions. The flux-density scale was set using observations of 3C 286 or 3C 48 and the zero-point of **E**-vector position angle was determined

---

<sup>‡</sup>part of Laing, Guidetti et al. 2011, in prep.

Table 5: Journal of VLA observations.  $\nu$  and  $\Delta\nu$  are the centre frequencies and bandwidth, respectively, for the one or two frequency channels observed and  $t$  is the on-source integration time scaled to an array with all 27 antennas operational.

Source	Config.	Date	$\nu$ [GHz]	$\Delta\nu$ [MHz]	$t$ [min]	Proposal code
0206+35	A	2008 Oct 13	4885.1, 4835.1	50	486	AL797
	A	2008 Oct 18	4885.1, 4835.1	50	401	AL797
	B	2003 Nov 17	4885.1, 4835.1	50	254	AL604
	C	2004 Mar 20	4885.1, 4835.1	50	88	AL604
	A	2004 Oct 24	1385.1, 1464.9	25	189	AL604
	B	2003 Nov 17	1385.1, 1464.9	25	110	AL604
0755+37	A	2008 Oct 05	4885.1, 4835.1	50	477	AL797
	A	2008 Oct 06	4885.1, 4835.1	50	383	AL797
	B	2003 Nov 15	4885.1, 4835.1	50	332	AL604
	B	2003 Nov 30	4885.1, 4835.1	50	169	AL604
	C	2004 Mar 20	4885.1, 4835.1	50	125	AL604
	D	1992 Aug 02	4885.1, 4835.1	50	55	AM364
	A	2004 Oct 25	1385.1, 1464.9	12.5	450	AL604
	B	2003 Nov 30	1385.1, 1464.9	12.5	160	AL604
M 84	C	2004 Mar 20	1385.1, 1464.9	12.5	21	AL604
	A	1980 Nov 09	4885.1	50	223	AL020
	A	1988 Nov 23	4885.1, 4835.1	50	405	AW228
	A	2000 Nov 18	4885.1, 4835.1	50	565	AW530
	B	1981 Jun 25	4885.1	50	156	AL020
	C	1981 Nov 17	4885.1	50	286	AL020
	C	2000 Jun 04	4885.1, 4835.1	50	138	AW530
	A	1980 Nov 09	1413.0	25	86	AL020
	B	1981 Jun 25	1413.0	25	29	AL020
	B	2000 Feb 09	1385.1, 1464.9	50	30	AR402

using 3C 286 or 3C 138, after calibration of the instrumental leakage terms. The main deviations from standard methods were as follows.

Firstly, we used the routine `calphase` to compute closure corrections for the 4.9 GHz observations. This was required to correct for large closure errors on baselines between EVLA and VLA antennas in the most recent observations (VLA Staff 2010), but also improved a number of the earlier datasets. Whenever possible, we included observations of the bright, unresolved calibrator 3C 84 for this purpose; if it was not accessible during a particular run, we used 3C 286. We found that it was not adequate to use the standard calibration (which averages over scans) to compute the baseline corrections, as phase jumps during a calibrator scan caused serious errors in the derived corrections. We therefore self-calibrated the observations in amplitude and phase with a solution interval of 10 s before running `calphase`. We assumed a point-source model for 3C 84 and the well-

determined model supplied with the AIPS distribution for 3C 286.

Secondly, we imaged in multiple facets to cover the inner part of the primary beam at L-band and to image confusing sources at large distances from the phase centre in both bands. Before combining configurations, we subtracted in the  $(u, v)$  plane all sources outside a fixed central field. For 0755+37, this procedure failed to remove sidelobes at the centre of the field from a bright confusing source close to the half-power point of the primary beam. The reason for this is that the VLA primary beam is not azimuthally symmetric, so the effective complex gain for a distant source is not the same as that at the pointing centre and varies with time in a different way. We used the AIPS procedure to remove the offending source from the  $(u, v)$  data for each configuration before combining them.

Finally, we corrected for variations in core flux density and amplitude scale between observations as described in Laing et al. (2006b).

J2000 coordinates are used throughout this work. The astrometry for each of the sources was set using the A-configuration observations, referenced to a nearby phase calibrator in the usual manner. Thereafter, the position of the compact core was held constant during the process of array combination. If positions from archival data were originally in the B1950 system, then  $(u, v, w)$  coordinates were recalculated for J2000 before imaging. The C-band data were usually taken in two adjacent 50 MHz frequency channels, which were imaged together. We also made  $I$  images at L-band using the data from both channels; these were used for spectral-index analysis which will be presented elsewhere.

In order to avoid the well-known problems introduced by the conventional algorithm for well-resolved, diffuse brightness distributions, total-intensity images at the higher resolutions were produced using either a maximum-entropy algorithm (Leahy & Perley 1991) or the multi-scale algorithm as implemented in the AIPS package (Greisen et al. 2009). In the former case, bright, compact core and jet components were first removed. The maximum-entropy images were then convolved with a Gaussian beam and the components restored. We found very few differences between the images produced by the two methods. The standard single-resolution was found to be adequate for the lowest-resolution  $I$  images. Stokes  $Q$  and  $U$  images were produced using one or more resolutions (we found few differences between single and multiple-resolution, for these images, which have little power on large spatial scales). All of the images were corrected for the effects of the antenna primary beam.

In general, the 4.9 GHz images have off-source rms levels very close to those expected from thermal noise in the receivers alone. The integrations for the L-band images are shorter than at the higher frequency, and the noise levels are correspondingly higher. As a check on the amplitude calibration and imaging of the  $I$  images used in spectral-index analysis, we have integrated the

Table 6: Resolutions and noise levels for the images used in this work. Col.1 source name; Col.2 angular resolution; Col.3 observing frequency; Col.4 VLA configurations; Col.5 imaging method; Col.6 off-source noise level on the  $I$  image ( $\sigma_I$ ) and the average of the noise levels for  $Q$  and  $U$  ( $\sigma_P$ ). Col.7 approximate maximum scale of structure imaged reliably (Ulvestad, Perley & Chandler 2009). Col.8 corrected single-dish flux densities put in the standard scale of Baars et al. (1977), as used at the VLA. Col.9 references.

Source	FWHM [arcsec]	Freq [GHz]	Config.	Method		rms noise level [ $\mu\text{Jy beam}^{-1}$ ]		Max scale [arcsec]	Image	$I_{\text{int}}/\text{Jy}$ SD	Ref.
				$I$	$QU$	$\sigma_I$	$\sigma_P$				
0206+35	1.20	4860.1	BC	MR	MR	12	12	300	$0.90 \pm 0.02$	$0.98 \pm 0.12$	1
	1.20	1464.9	AB	MR	MR	21	22	300	$2.12 \pm 0.04$	2.13	3
	1.20	1385.1	AB	MR	MR	21	23	300	$2.12 \pm 0.04$	2.22	3
	1.20	1425.0	AB	MR	–	19	–	300	$2.12 \pm 0.04$	2.18	4
	4.50	4860.1	BC	MR	–	18	–	300	$0.90 \pm 0.02$	$0.98 \pm 0.12$	1
	4.50	1425.0	AB	MR	–	38	–	300	$2.13 \pm 0.04$	2.18	4
0755+37	1.30	4860.1	BCD	MR	MR	7.8	7.9	300	$1.26 \pm 0.03$	$1.27 \pm 0.02$	2
	1.30	1464.9	ABC	MR	MR	28	28	300	$2.60 \pm 0.05$	$2.53 \pm 0.09$	2
	1.30	1385.1	ABC	MR	MR	27	26	300	$2.74 \pm 0.05$	$2.62 \pm 0.09$	2
	1.30	1425.0	ABC	MR	–	20	–	300	$2.64 \pm 0.05$	$2.57 \pm 0.09$	2
	4.00	4860.1	BCD	MR	MR	14	12	300	$1.25 \pm 0.03$	$1.27 \pm 0.02$	2
	4.00	1464.9	ABC	MR	MR	44	42	300	$2.59 \pm 0.05$	$2.53 \pm 0.09$	2
	4.00	1385.1	ABC	MR	MR	46	36	300	$2.73 \pm 0.05$	$2.62 \pm 0.09$	2
	4.00	1425.0	ABC	MR	MR	32	–	300	$2.65 \pm 0.05$	$2.57 \pm 0.09$	2
M 84	1.65	4860.1 <sup>a</sup>	ABC	MR	MR	15	11	300	$2.94 \pm 0.06$	$2.88 \pm 0.08$	3
	1.65	1413.0	AB	MR	MR	140	140	120	$6.03 \pm 0.12$	$6.44 \pm 0.24$	3
	4.5	4860.1 <sup>a</sup>	C	MR	MR	23	20	300	$2.98 \pm 0.06$	$2.88 \pm 0.08$	3
	4.5	1464.9	B	MR	MR	120	70	120	$6.14 \pm 0.12$	$6.32 \pm 0.24$	3
	4.5	1413.0	AB	MR	MR	210	150	120	$5.99 \pm 0.12$	$6.44 \pm 0.24$	3
	4.5	1385.1	B	MR	MR	130	69	120	$6.46 \pm 0.13$	$6.51 \pm 0.24$	3

References: 1 Gregory & Condon (1991); 2 Kühr et al. (1981); 3 Laing & Peacock (1981); 4 White & Becker (1992).

<sup>a</sup>Although the 1980 and 1981 observations have a centre frequency of 4885.1 MHz, the weighted mean for the combined dataset is still close to 4860.1 MHz.

flux densities using the AIPS verb `imcom`. We estimate that the errors are dominated by a residual scale error of  $\approx 2\%$ . All of the results are in excellent agreement with single-dish measurements (Table 6).

The configurations, resolutions, deconvolution algorithms and noise levels for the final images are listed in Table 6. The noise levels were measured before correction for the primary beam, and are appropriate for the centre of the field.

## .2 Images

Our conventions are as follows:

1. images of total intensity are show as grey-scales, over a range indicated by the labelled wedges.

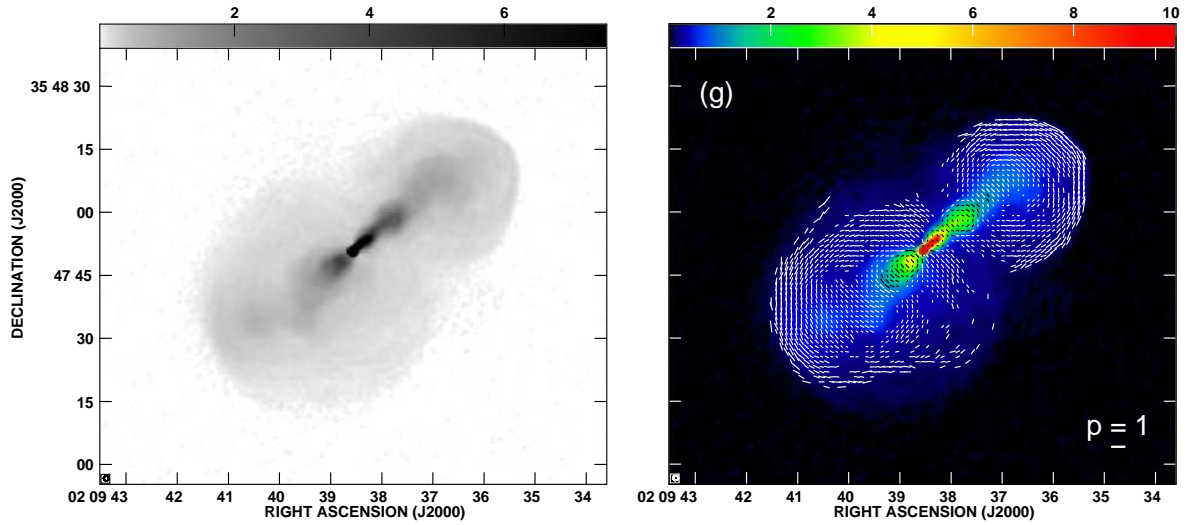


Figure 11: 0206+35 at 4.9 GHz with angular resolution of 1.2 arcsec FWHM. **Left:** total intensity distribution  $I$  in  $\text{mJy (beam area)}^{-1}$ . **Right:** apparent  $\mathbf{B}_a$  vectors with lengths proportional to  $p_{4.9}$  derived from the 3-frequency RM fit, superimposed on a false-colour display of  $I$ .

2. We also show intensity gradient for 0755+37 and M 84,  $|\nabla I|$ , derived using a Sobel filter (Sobel & Feldman, 1968).
3. Linear polarization is illustrated by plots in which vectors have lengths proportional to the degree of polarization at 4.9 GHz ( $p_{4.9}$ ) and directions along the apparent magnetic field ( $\mathbf{B}_a$ ). They are superposed on false-colour images of either  $I$  (again with a labelled wedge indicating the range) or  $|\nabla I|$ .  $\mathbf{B}_a$  vectors are plotted where  $I \geq 5\sigma_I$ . A value of  $p = 1$  is indicated by the labelled bar. The apparent field direction is  $\chi_0 + \pi/2$ , where  $\chi_0$  is the  $\mathbf{E}$ -vector position angle corrected to zero-wavelength by fitting to the relation  $\chi(\lambda^2) = \chi_0 + \text{RM}\lambda^2$  for foreground Faraday rotation. In some sources, we used the RM images at lower resolution to correct the position angles. This procedure is valid if the RM varies smoothly over the low-resolution image, and maximises the area over which we can determine the direction of the apparent field.
4. The restoring beam is shown in the bottom left-hand corner of each plot.
5. We refer to parts of the sources by the abbreviations N, S, E, W (for North, South, East, West) etc.
6. We refer to the *main* (brighter) and *counter* (fainter) jets.

## .2.1 0206+35

The left panel of Fig. 11 shows the total intensity distribution over all of 0206+35 at 4.9 GHz, 1.2 arcsec resolution.

At this resolution, both lobes are circular in cross-section and show sharp outer boundaries, particularly to the NW and SE of the source, plus some fainter diffuse emission to the N and S. If the orientation of  $\theta \approx 40^\circ$  determined for the inner jets (Laing & Bridle, in preparation) also applies to the lobes, then they are presumably ellipsoidal with an axial ratio  $\approx 1$ . The figure also shows internal structure in both jets. NW jet has the brighter base, and both bends and brightens as it enters its lobe, after which its path meanders. The SE counter-jet appears to expand more rapidly initially, then also meanders as it enters its lobe. The right panel of Fig. 11 illustrates that the magnetic field configuration in both lobes is well ordered and basically circumferential, while near the central lines of the jets it is predominantly perpendicular to their axis, with evidence for parallel field at the jet edges. The southern edge of the source is strongly polarized with magnetic field tangential to the source boundary.

## .2.2 0755+37

Figs. 12(a) and (b) show the total intensity distribution over all of 0755+37 at two resolutions and frequencies. Fig. 12(a) at 1.4 GHz, 4.0 arcsec resolution, shows that the large scale structure consists of two lobes, again roughly circular in projection, with well-defined but not particularly sharp outer edges to the W and E, plus fainter diffuse emission to the N and S. The E lobe has a series of narrow rings and brightness steps in the region where the brighter jet appears to terminate. They are recessed from the eastern boundary of this lobe and some may be the edges of thin shells. The structure of the W lobe is unusual, containing some arc-like features, and other structure suggestive of a rapidly decollimating counter-jet W of the nucleus, as previously described by Bondi et al. (2000), with a “hole”, or deficit of emission in the region where the counter-jet might be expected to terminate. Although partially resolved out, all of these internal structures are confirmed by the higher resolution image at 4.9 GHz, 1.3-arcsec resolution (Fig. 12(b)).

Figs. 12(c) and (d) show that the magnetic field in both lobes is exceptionally well organised, and mainly tangential to the lobe boundaries, at both the angular resolutions. At the lower resolution, the degree of linear polarization  $p \leq 0.6$  over much of both lobes. Noteworthy is the excellent alignment between the field vectors and the ridges of high brightness gradient on both sides of the source.

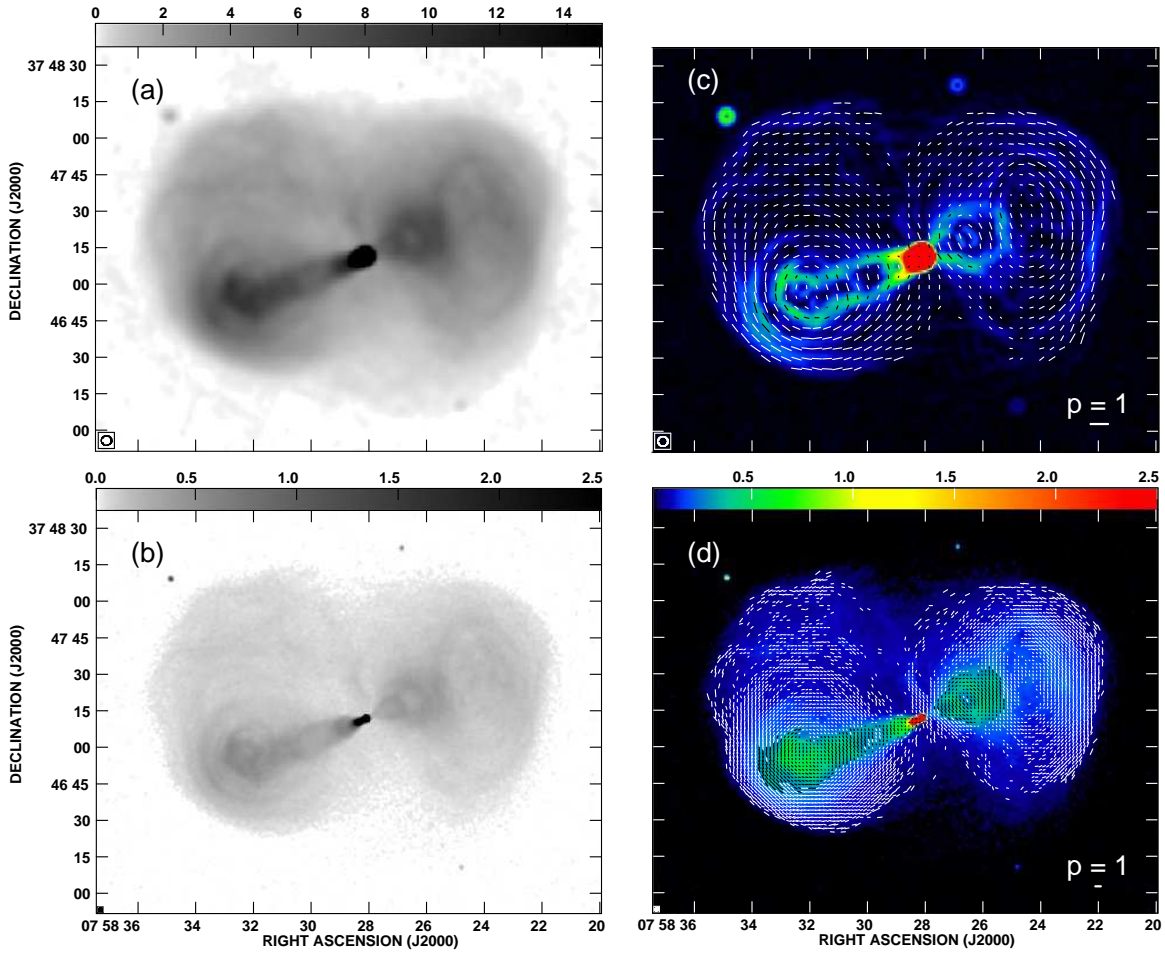


Figure 12: images of 0755+37 at 4.0 arcsec (panels a and c) and 1.3 arcsec (panels b and d). **(a)** Total intensity at 1.4 GHz in  $\text{mJy beam}^{-1}$ . **(b)** Total intensity at 4.9 GHz in  $\text{mJy beam}^{-1}$ . Apparent  $\mathbf{B}_a$  vectors with lengths proportional to  $p_{4.9}$  from the 3-frequency RM fits, superimposed on a false-colour display at 4.9 GHz of the intensity gradient **(c)** and the total intensity **(d)**. The panels show identical areas.

### .2.3 M 84

The left panel of Fig. 13 shows the total intensity distribution over M 84 at 1.65 arcsec FWHM resolution. The source appears to be an intermediate case between lobed and tailed sources: the lobes, in particular the NE one, more closely resemble the inner plumes in FRI sources (3C 31, Laing et al. 2008), albeit on a much smaller linear scale ( $\sim 6$  kpc) and somewhat rounder shape. On the other hand, the spectral gradients (Laing et al. in preparation) are more characteristic of lobed sources, with no hint of steepening outwards. Both jets expand rapidly and deflect within about 1 arcmin of the nucleus. They are surrounded by diffuse emission, at least in projection, everywhere except perhaps within a few arcsec of the nucleus. The North jet is brighter at its base and forms a plume-like structure without well-defined edges after deflecting though approximately

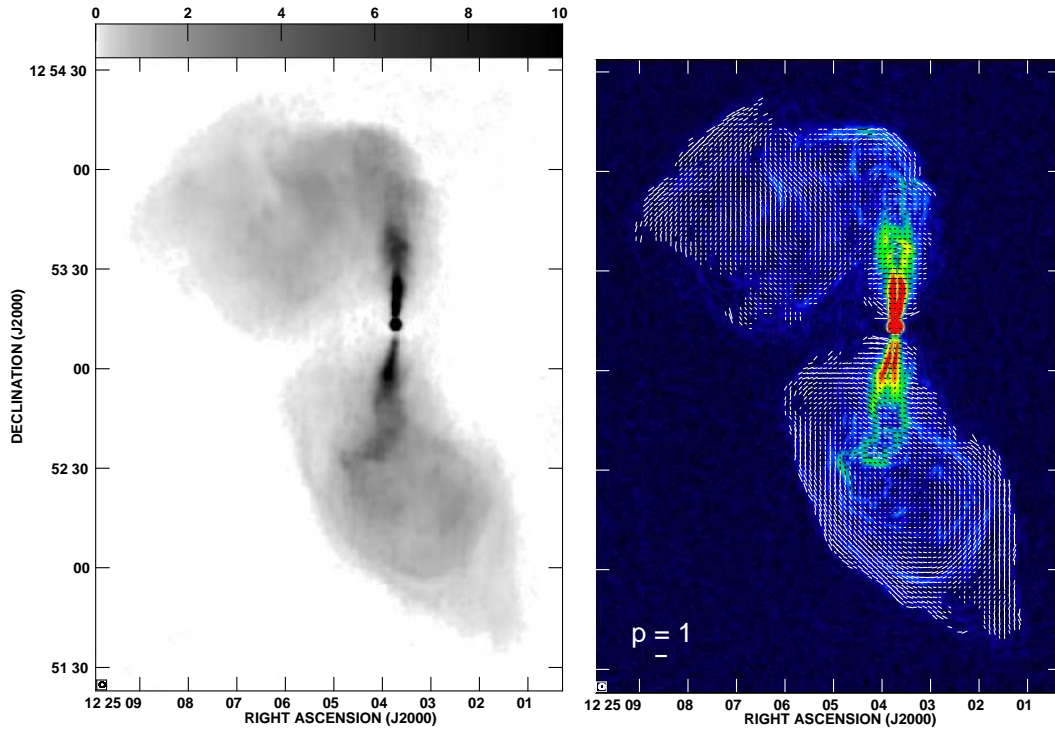


Figure 13: Images of M84 at 1.65 arcsec resolution. **Left:** Total intensity at 4.9 GHz in  $\text{mJy} (\text{beam area})^{-1}$ . **Right:** Apparent  $\mathbf{B}_a$  vectors with lengths proportional to  $p_{4.9}$  derived from the 4-frequency RM fits at 4.5 arcsec, superimposed on a false-colour display of the total intensity gradient at 4.9 GHz.

$90^\circ$  in projection. Lower-resolution observations were previously shown by Laing & Bridle (1987) so are not repeated here.

The right panel of Fig. 13 shows the apparent magnetic field structure. In the N lobe, the magnetic field is predominantly perpendicular to the presumed path of the jet along its mid-line. The magnetic field in the S lobe is broadly circumferential and a sudden increase in the degree of polarization at the edge of the lobe is apparent.

# Bibliography

- Ackermann, M., Ajello, M., Allafort, A., Baldini, L., et al., 2010, ApJ, 717, 127
- Allen, S. W., Taylor, G. B., Nulsen, P. E. J., Johnstone, R. M., et al. 2001, MNRAS, 324, 842
- Andernach, H., Feretti, L., Giovannini, G. et al. 1992, A&A, 93, 331
- Antonucci, R., 1993, ARA&A, 31, 473
- Baars J.W.M., Genzel R., Pauliny-Toth I.I.K., Witzel, A., 1977, A&A, 61, 99
- Balbus, S. A. 2000, ApJ, 534, 420
- Barthel, P., 1989, SciAm, 260, 20
- Bagchi, J., Durret, F., Lima Neto, G.B., Paul, S. 2006, Science, 314, 791
- Baum, Stefi Alison, Heckman, Timothy M., Bridle, Alan, van Breugel, Wil J. M., Miley, George K, 1988, ApJS, 68, 643
- Beck R., 1996, ASPC, 97, 475
- Beck R. & Krause M., 2005, AN, 326, 414
- Bicknell, G.V., 1994, ApJ, 422, 542
- Bicknell, G.V., Cameron, R.A. & Gingold, R.A., 1990, ApJ, 357, 373
- Biermann, P., Kronberg, P. P. & Madore, B. F., 1982, ApJ, 256, 37
- Binney, J., Tabor, G., 1995, MNRAS, 276, 663
- Biretta J.A., Zhou F. & Owen F.N., 1995, ApJ, 447, 582
- Biretta, J.A., Sparks, W.B. & Macchetto, F., 1999, ApJ, 520, 621
- Birkinshaw, M., Laing, R. A. & Peacock, J. A. 1981, MNRAS, 197, 253

- Bîrzan, L., Rafferty, D. A., McNamara, B. R., Wise, M. W., Nulsen, P. E. J., 2004, *ApJ*, 607, 800
- Bîrzan, L., McNamara, B.R., Nulsen, P.E.J., Carilli, C.L., Wise, M.W., 2008, *ApJ*, 686, 859,
- Blanton, E.L., Sarazin, C. L., McNamara, B. R. Wise, M. W., 2001, *ApJL*, 558, L15
- Blanton, E.L., Gregg, M.D., Helfand, D.J., Becker, R.H., White, R.L., 2003, *AJ*, 125, 1635
- Blasi, P., 2000, *ApJ*, 532, 9
- Bogdanović, T., Reynolds, C. S., Balbus, S. A. & Parrish, I. J. 2009, *ApJ*, 704, 211
- Bonafede, A., Giovannini, G., Feretti, L., Govoni, F. & Murgia, M., 2009, *A&A*, 494, 429
- Bonafede, A., Feretti, L., Murgia, M., Govoni, F., et al., 2010, *A&A*, 513, 30
- Bondi, M., Parma, P., de Ruiter, H., Fanti, R., Laing, R.A., Fomalont, E.B., 2000, *MNRAS*, 314, 11
- Bower, G.A., Heckman, T.M., Wilson, A.S., Richstone, D.O., 1997, *ApJ*, 483, 33
- Bower, G. A., Green, R. F., Quillen, A. C., Danks, A., et al., 2000, *ApJ*, 534, 189
- Brentjens M. A. & de Bruyn A. G., 2005, *A&A*, 441, 1217
- Bridle, A. H. & Perley, R. A, 1984, *ARA& A*, 22, 319
- Brüggen M., Ruszkowski M., Simionescu A., Hoeft M., Dalla Vecchia C., 2005, *ApJ*, 631, L21
- Brunetti, G., Setti, G., Feretti, L. & Giovannini, G. 2001, *MNRAS*, 320, 365
- Brunetti, G. & Lazarian, A., 2007, *MNRAS*, 378, 245
- Burn, B.J., 1966, *MNRAS*, 133, 67
- Canosa, C. M., Worrall, D. M., Hardcastle, M. J., Birkinshaw, M., 1999, *MNRAS*, 310, 30
- Carilli, C. L., Perley, R. A. & Harris, D. E., 1994, *MNRAS*, 270, 173
- Carilli, C.L., Perley, R.A. & Dreher, J.W., 1988, *ApJL*, 334, L73
- Carilli, C.L. & Taylor, G.B., 2002, *ARAA*, 40, 319
- Cassano, R. & Brunetti, G., 2005, *MNRAS*, 357, 1313
- Cavagnolo, K. W., McNamara, B. R., Nulsen, P. E. J. Carilli, C. L., et al. 2010, *ApJ*, 720, 1066
- Cavaliere A. & Fusco-Femiano R., 1976, *A&A*, 49, 137

- Churazov, E., Forman, W.R., Vikhlinin, A., Tremaine, S., et al., 2008, MNRAS, 388.1062
- Clarke T. E., 2004, JKAS, 37, 337
- Clarke, T.E. & Ensslin, T.A. 2006, AJ, 131.2900
- Croston, J. H., Hardcastle, M. J., Birkinshaw, M., Worrall, D. M. 2003, MNRAS, 346, 1041
- Croston, J. H., Birkinshaw, M., Hardcastle, M. J., Worrall, D. M., 2004, MNRAS, 353, 879
- Croston, J. H., Hardcastle, M. J., Birkinshaw, M., 2005, MNRAS, 357, 279
- Croston, J. H., Kraft, R. P., Hardcastle, M. J, 2007, ApJ, 660, 191
- Croston, J.H., Hardcastle, M.J., Birkinshaw, M., Worrall, D.M., Laing, R.A., 2008, MNRAS, 386, 1709
- Croston, J. H., Hardcastle, M. J., Mingo, B., Evans, D. A., Dicken, D., Morganti, R., Tadhunter, C. N., 2010arXiv1011.6405
- de Vaucouleurs, G, de Vaucouleurs, A., Corwin, Jr. H.G., Buta, R.J., Paturel, G., Fouqué P., 1991, Third Reference Catalogue of Bright Galaxies, Springer, New York, NY (USA).  
<http://adsabs.harvard.edu/abs/1995yCat.7155....0D>
- De Young, D. S., 2006 ApJ, 648, 200,
- Dineen, P. & Coles, P. 2005, MNRAS, 362,403
- Dolag, K., 2006, Astronomische Nachrichten, 327, 575
- Dolag, K., Schindler, S., Govoni, F., Feretti, L., 2001, A&A, 378, 777
- Dolag K., Bartelmann M., & Lesch H., 2002, A&A, 387, 383
- Dolag K., Bykov A. M. & Diaferio A., 2008, SSRv, 134, 311
- Dreher, J.W., Carilli, C.L. & Perley, R.A., 1987, ApJ, 316, 611
- Dursi, L.J. & Pfrommer, C., 2008, ApJ, 677, 993
- Eckert, D., Produit, N., Paltani, S., Neronov, A., Courvoisier, T. J.-L., 2008, A&A, 479, 27
- Eilek, J. A., Burns, J. O., O’Dea, C. P., Owen, F. N., 1984, ApJ, 278, 37E
- Eilek, J.A. & Owen, F.N., 2002, ApJ, 567, 202
- Enßlin, T.A., Biermann, P.L., Klein, U. & Kohle, S. 1998, A&A, 332, 395

- Ensslin, T.A. & Gopal-Krishna 2001, A&A, 366, 26
- Enßlin T.A. & Vogt C. 2003, A&A, 401, 835
- Enßlin, T.A., Vogt, C., 2005, A&A, 434, 67
- Fabian, A. C., Sanders, J. S., Ettori, S., Taylor, G. B. et al., 2000, MNRAS, 318, 65
- Fabian, A. C., Sanders, J. S., Allen, S. W., Crawford, C. S., et al. 2003, MNRAS, 344, 43
- Fanaroff, B.L., Riley, J.M., 1974, MNRAS, 167, 31P
- Faraday, M., 1846, Experimental Researches in Electricity. Nineteenth Series Phil. Trans. R. Soc. Lond., 136:1-20
- Felten J.E., 1996, in Trimble V., Reisenegger A., eds, ASP Conf. Ser. 88, Clusters, Lensing and the future of the Universe, Astron. Soc. Pac., San Francisco, p. 271
- Feretti, L., Perley, R., Giovannini, G. & Andernach, H. 1999a, A&A, 341, 29
- Feretti, L., Dallacasa, D., Govoni, F., et al. 1999b, A&A, 344, 472
- Feretti, L., Orrú, E., Brunetti, G., Giovannini, G., et al., 2004, A&A, 423, 111
- Ferrari, C., Govoni, F., Schindler, S., Bykov, A. M., Rephaeli, Y., 2008, SSRv, 134, 93
- Finoguenov, A. & Jones, C., 2001, ApJ, 547, 107
- Finoguenov, A., Davis, D.S., Zimer, M., Mulchaey, J.S., 2006, ApJ, 646, 143
- Finoguenov, A., Ruszkowski, M., Jones, C., Brüggén, M., et al., 2008, ApJ, 686, 911
- Forman, W., Schwarz, J., Jones, C., Liller, W., Fabian, A. C., 1979, 234, 27
- Forman, W.R., Jones, C., 1982, ARA&A, 20, 547
- Forman, W.R., Nulsen, P.E.G., Heinz, S., et al., 2005, ApJ, 635, 894
- Forman W.R., Jones, C., Churazov E., Markevitch, M., et al., 2007, ApJ, 665, 1057
- Fujita, Y., Takizawa, M. & Sarazin, C. L., 2003, ApJ, 584, 190
- Garrington S. T., Leahy J. P., Conway R. G., Laing R. A., 1988, Nature, 331, 147
- Giacintucci, S., Venturi, T., Brunetti, G., Dallacasa, D., et al. 2009, A&A, 505, 45
- Giacintucci, S., O'Sullivan, E., Vrtilik, J. David, et al., 2011 arXiv1103.1364

- Giovannini, G., Feretti, L., Venturi, T., Kim, K.-T., Kronberg, P. P., 1993, *ApJ*, 406, 399
- Giovannini, G. & Feretti L., 2002, *ASSL*, 272, 197
- Gitti, M., O'Sullivan, E., Giacintucci, S., David, L.P., 2010, *ApJ*, 714, 758,
- Goldreich, P. & Sridhar, S., 1997, *ApJ*, 485, 680
- Goodger, J.L., Hardcastle, M.J., Croston, J.H., Kassim, N.E., Perley, R.A., 2008, *MNRAS*, 386, 337
- Govoni, F., Taylor, G.B., Dallacasa, D., Feretti, L. & Giovannini, G. 2001, *A&A*, 379, 807
- Govoni, F. & Feretti, L., 2004, *International Journal of Modern Physics D* 13, 1549
- Govoni F., Murgia M., Feretti L., Giovannini G., et al., 2006, *A&A*, 460, 425
- Gregory, P.C. & Condon, J.J., 1991, *ApJS*, 75, 1011
- Greisen E.W., Spekkens K. & van Moorsel G.A., 2009, *AJ*, 137, 4718
- Guidetti, D., Murgia, M., Govoni, F., Parma, P., et al., 2008, *A&A*, 483, 699
- Guidetti, D., Laing, R. A., Murgia, M., Govoni, F., et al., 2010, *A&A*, 514, 50
- Guidetti, D., Laing, R. A., Bridle, A.H., Parma.P, Gregorin, L., 2011, *MNRAS*, in press
- Guidetti, D., Laing, R. A., Bridle, A.H., Parma.P, Gregorini, L., in prep
- Guidetti, D., Laing, R. A., Bridle, A.H., Parma.P, Gregorini, L., in prep
- Hansen, L., Norgaard-Nielsen, H.U. & Jorgensen, H.E., 1985, *A&A*, 149, 442
- Hardcastle, M. J., Worrall, D. M. & Birkinshaw, M. 1998 *MNRAS*, 296, 1098
- Hardcastle, M. J., Birkinshaw, M., Cameron, R. A. Harris, D. E., et al., 2002, *ApJ*, 581, 948
- Harris, D.E., Stern, C.P., Willis, A.G., Dewdney, P.E. 1993, *AJ*, 105, 769
- Harris, D.E., Cheung, C.C., Biretta, J.A., Sparks W.B., 2006, 640, 211
- Helsdon, S. F. & Ponman, T. J., 2000, *MNRAS*, 315, 356
- Iwasawa, K., Etori, S., Fabian, A. C., Edge, A. C., Ebeling, H., 2000, *MNRAS*, 313, 515
- Isobe, N., Seta, H., Gandhi, P., Tashiro, M. S., 2011, *ApJ*, 727, 82
- Jaffe, W.J., *ApJ*, 1980, 241, 925

- Jeltema, T.E. & Profumo, S., 2011, *ApJ*, 728, 53
- Jetha, N. N., Ponman, T. J., Hardcastle, M. J., Croston, J. H., 2007, *MNRAS*, 378, 384
- Kaiser, C. R. & Alexander, P., 1997, *MNRAS*, 286, 215,
- Kataoka, J. & Stawarz, L., 2005, *ApJ*, 622, 797
- Kolmogorov, A.N., 1941, *Dokl. Nauk. Acad. SSSR*, 30, 301
- Konar, C., Hardcastle, M. J., Croston, J. H. Saikia, D. J., 2009, *MNRAS*, 400, 480
- Kovalev, Y. Y., Lister, M. L., Homan, D. C., Kellermann, K. I. 2007, *ApJ*, 668, 27
- Kraft, R.P., Vázquez, S.E., Forman, W.R., Jones C., et al., 2003, *ApJ*, 592, 129
- Kriss, G. A., Canizares, C. R., McClintock, J. E, Feigelson, E. D., 1980, *ApJ*, 235, 61
- Kuchar, P. & Enßlin, T.A., 2009arXiv0912.3930K
- Kühr, H., Witzel, A., Pauliny-Toth, I.I.K., Nauber, U., 1981, *A&AS*, 45, 367
- Laing, R.A., 1988, *Nature*, 331, 149
- Laing, R.A. & Bridle, A.H., 1987, *MNRAS*, 228, 557
- Laing, R. A., 1993, *ASSL*, 103, 95, Radio observations of jets: large scales, *Astrophysics and Space Science Library*, vol. 103 <http://cdsads.u-strasbg.fr/abs/1993ASSL..103...95L>
- Laing R.A. & Peacock J.A., 1980, *MNRAS*, 190, 903
- Laing, R. A. & Bridle, A. H. 2002, *MNRAS*, 336, 328
- Laing, R. A., Canvin, J. R., Cotton, W. D., Bridle, A. H. 2006, *MNRAS*, 368, 48
- Laing, R.A., Canvin, J.R, Bridle, A.H., Hardcastle, M.J., 2006b, *MNRAS*, 372, 510
- Laing, R.A., Guidetti D. & Bridle, A.H., in prep
- Laing, R.A. & Bridle, A.H., in prep
- Laing, R.A., Bridle, A.H., Parma, P., Murgia, M., 2008, *MNRAS*, 386, 657
- Laing, R.A., Guidetti, D., Bridle, A.H., Parma, P., Bondi, M., *MNRAS*, 2011, in prep.
- Landau, L.D., Lifshitz, E.M., 1987, *Fluid mechanics, Course of theoretical physics, Vol.6* Pergamon Press, Oxford

- Laskar, T., Fabian, A. C., Blundell, K. M., Erlund, M. C., MNRAS, 401, 1500
- Lawler, J.M. & Dennison B., 1982, ApJ, 252, 81
- Leahy J.P. & Perley R.A., 1991, AJ, 102, 537
- Longair, M. S., High energy astrophysics. Volume 2. Stars, the Galaxy and the interstellar medium, Cambridge University Press, Cambridge (UK), 1994 <http://cdsads.u-strasbg.fr/abs/1994hea2.book.....L>
- Lutovinov A. A., Vikhlinin A., Churazov E. M., Revnivtsev M. G., Sunyaev R. A., 2008, ApJ, 687, 968
- Mathews, W. G. & Brighenti, F., 2003, ApJ, 599, 992
- Matsushita, K., Belsole, E., Finoguenov, A., Böhringer H., 2002, A&A, 386, 77
- McNamara, B. R., Nulsen, P. E. J., Wise, M. W., Rafferty, et al., 2005, Nature, 433, 45
- McNamara, B.R. & Nulsen, P. E. J., 2007, ARA&A, 45, 117
- McNamara, B.R., Wise, M., Nulsen, P.E.J., David, L.P., et al., 2000, ApJ, 534, L135
- Meier, D. L., 2002, NewAR, 46, 247
- Miller, N. A., Ledlow, M. J., Owen, F. N., F. N. and Hill, J. M., 2002, AJ, 123, 3018
- Minter, A.H. & Spangler, S.R., 1996, ApJ, 458, 194
- Morganti, R., Fanti, R., Gioia, I. M., Harris, D. E. Parma, P., de Ruiter, H., 1988, A&A 189, 11
- Morganti, R., Parma, P., Capetti, A., Fanti, R., de Ruiter, H.R., 1997, A&A, 326, 919
- Mulchaey, J.S., Davis, D.S., Mushotzky, R.F., Burstein, D. 2003, ApJS, 145, 39
- Murgia, M., Govoni, F., Feretti, L., Giovannini, G., et al., 2004, A&A, 424, 429
- Murgia, M., Eckert, D., Govoni, F., Ferrari, C., et al., 2010, A&A, 514, 76
- Nulsen P.E.J., David, L. P., McNamara, B. R. Jones, C., Forman, W. R., Wise, M., 2002, ApJ, 568, 163
- Nulsen P.E.J., McNamara B.R., Wise M.W., David L.P., 2005, ApJ, 628, 629
- Nulsen, P. E. J., Hambrick, D. C., McNamara, B. R., Rafferty, D., et al., 2005, ApJ, 625, 9
- O'Dea, C. P. & Owen, F. N., 1986, ApJ, 301, 841

- Owen, F.N., 1989, BAPS, 34.1278
- Owen, F.N., Eilek, J.A. & Keel, W.C., 1990, ApJ, 362, 449
- Owen, F.N., Eilek, J.A. & Kassim, N.E. , 2000, ApJ, 543, 611
- Perley, R. A., Willis, A. G. & Scott, J. S. 1979, Nature, 281, 437
- Petrosian V., 2001, ApJ, 557, 560
- Petrosian V., 2003, ASPC, 301, 337
- Pfrommer, C., Enßlin, T. A. & Springel, V., 2008, MNRAS, 385.1211
- Regis, M., 2011, arXiv1101.5524
- Rephaeli Y., 1977, ApJ, 218, 323
- Rephaeli Y., Gruber D. & Arieli Y., 2006, ApJ, 649, 673
- Rice, S.O., Bell System Technical Journal 24 (1945) 46
- Röttiger, K., Burns, J.O. & Stone, J.M. 1999, ApJ, 518, 603
- Rybicki, G. B. & Lightman, A. P., 1986, rpa, book, Radiative Processes in Astrophysics, Wiley-VCH, <http://cdsads.u-strasbg.fr/abs/1986rpa..book.....R>
- Sarazin, C.L. 1988, X-ray emission from clusters of galaxies, (Cambridge University Press)
- Scheuer, P. A. G., 1974, MNRAS, 166, 513
- Schekochihin, A.A., Cowley, S.C., 2006, Phys. Plasmas, 13, 56501
- Schlickeiser, R., Sievers, A., Thiemann, H, 1987, A&A, 182, 21
- Simard-Normandin, M., Kronberg, P. P., Button, S., 1981, ApJS, 45, 97
- Simonetti, J.H., Cordes, J.M. & Spangler, S.R., 1984, ApJ, 284, 126
- Slee, O. B., Roy, A. L., Murgia, M., Andernach, H., Ehle, M., 2001, AJ, 122.1172
- Stokes, G.C., 1856, On the composition and resolution of streams of polarized light from different sources, Cambridge Philosophical Society Transactions, IX:399-416, 1856.
- Swain, M.R., 1996, PhD. Thesis, University of Rochester, NY, USA
- Swain, M. R., Bridle, A. H. & Baum, S., 1998, ApJ, 1998, 507, 29

- Taylor, G.B. & Perley, R.A. 1993, ApJ, 416, 554
- Timokhin, A. N., Aharonian, F. A., Neronov, A.Yu, 2004, A&A, 417, 391
- Trager, S. C., Faber, S. M., Worthey, G., González, J. J, 2000, AJ, 119, 1645
- Tribble, P.C., 1991, MNRAS, 250, 726
- Trinchieri, G., Fabbiano G., & Kim, D.-W., 1997, A&A ,318, 361
- Trussoni, E., Massaglia, S., Ferrari, R., Fanti, R., et al., 1997, A&A, 327, 27
- Ulvestad J.S., Perley R.A., Chandler C.J. 2009, The Very Large Array Observational Status Summary, NRAO, Socorro, <http://www.vla.nrao.edu/astro/guides/vlas/current/>
- Urry, C. M & Padovani, P., 1995, PASP, 107, 803
- van Weeren, R. J., Röttgering, H. J. A., Brüggén, M. & Hoefl, M., 2010, Sci, 330, 347
- VLA Staff, 2010, EVLA Transition for Observers,  
<http://www.vla.nrao.edu/astro/guides/evlareturn/vla-evla/>
- Wardle, J. F. C. & Kronberg, P. P. 1974, ApJ, 194, 249
- White, R.L. & Becker, R.H., 1992, ApJS, 79, 331
- Wik, D. R., Sarazin, C. L., Finoguenov, A., Baumgartner, W. H., et al., 2011, ApJ, 727, 119
- Wilson, A. S., Young, A. J. & Shopbell, P. L., 2001, ApJ, 547, 740
- Wilson, A.S., Smith, D.A., Young, A.J., 2006, ApJ, 644, 9
- Worrall, D. M. & Birkinshaw, M., 1994, ApJ, 427, 134
- Worrall, D. M. & Birkinshaw, M., 2000, ApJ, 530, 719
- Worrall, D. M., Birkinshaw, M. & Hardcastle, M. J., MNRAS, 2001, 326, 7
- Worrall, D. M., Birkinshaw, M., O'Sullivan, E., Zezas, A., et al., MNRAS, 2010, 408, 701
- Wu, Q., Feng Y. & Xinwu C., 2007, ApJ, 669, 96
- Xue, S.-J. & Wu, X.-P., 2002, ApJ, 576, 152
- Zwicky, F. & Kowal, C. T., 1968, Catalogue of Galaxies and of Clusters of Galaxies, Vol. 6.  
California Institute of Technology, Pasadena



# Acknowledgments

Probably the most important result is that during this PhD I have grown not only as scientist but as person. For this, I owe many people a debt of gratitude for all my life.

I am privileged for having Robert Laing as supervisor, this thesis would not have been possible without his help and patience. I have learned many valuable things from him, and I also wish to express gratitude for believing in me. One simply could not wish for a better supervisor.

I thank Paola Parma and Loretta Gregorini for their help and support.

I would like to acknowledge ESO (Garching) for the award of a ESO Studentship that allowed me to breath a wide spirit of research and to grow.

I wish to thank Matteo Murgia, Federica Govoni and the staff of the Astronomical Observatory of Cagliari for their hospitality and support during the development of the work on 3C 449. The work on this radio galaxy is part of the “Cybersar” Project, which is managed by the COSMOLAB Regional Consortium with the financial support of the Italian Ministry of University and Research (MUR), in the context of the “Piano Operativo Nazionale Ricerca Scientifica, Sviluppo Tecnologico, Alta Formazione (PON 2000-2006)”. I wish to thank Luigina Feretti for providing the excellent VLA dataset of 3C 449 and Greg Taylor for the use of his rotation measure code. I also thank M. Swain for providing the VLA dataset for 3C 353, J. Eilek for a FITS image of 3C 465 and J. Croston, A. Finoguenov and J. Goodger for the FITS images of 3C 270, M 84 and 3C 353, respectively.

I am grateful to M. Bondi, G. Brunetti, A. Shukurov and J. Stöckl for many valuable comments. I also acknowledge the use of HEALPIX package (<http://healpix.jpl.nasa.gov>) and the provision of the models of Dineen & Coles (2005) in `format`.

The last but certainly not least words are for all of You which “see all my light and love my dark”.

*“And thus I stand”.*